NONLINEAR ANALYSIS OF STEEL BUILDINGS WITH RC SHEAR WALLS USING IMPROVED APPLIED ELEMENT METHOD

HAN QINGER

M.Sc., DTU

B.Eng. (Hons.), ZJU

A THESIS SUBMITTED FOR

THE DEGREE OF DOCTOR OF PHYLOSOPHY

DEPARTMENT OF CIVIL & ENVIRONMENTAL ENGINEERING

NATIONAL UNIVERSITY OF SINGAPORE

2015

This page is intentionally left blank.

Declaration

I hereby declare that this thesis is my original work and it has been written by me in its entirety. I have duly acknowledged all the sources of information which have been used in the thesis.

This thesis has also not been submitted for any degree in any university previously.

Han Qinger

29 July 2015

This page is intentionally left blank.

Acknowledgement

First, I would like to express my sincere appreciation and gratitude to my supervisor, Professor Koh Chan Ghee, for his constant support and guidance throughout the challenging path of this research. His breadth of knowledge, patience and dedication are invaluable.

In addition, I would like to extend my gratitude to National University of Singapore for providing me with the scholarship, without which this research work would not have been possible.

I also wish to thank the constant assistance and companionship of colleagues in room E1A-02-06 especially Dr. Tay Choon Guan for his comments and helpful discussions.

Finally, I would like to thank my parents, sister, husband for their unceasing moral support and encouragement.

All errors, omissions and interpretations are my own.

This page is intentionally left blank.

Table of Contents

Summary

Increasing attention has recently been focused on the design of buildings to resist progressive collapse which requires nonlinear analysis. To this end, the improved applied element method (iAEM) has great potential for efficient and accurate simulation. Nevertheless, currently iAEM is limited to analyse idealized steel structures without considering initial imperfections and semi-rigid connection behavior. These two features should not be ignored as they have considerable implications on the accuracy in simulating the resistance and stability of real steel structures. In addition, there is no application of iAEM for modelling of reinforced concrete (RC) shear walls to capture the shear-flexure interaction, whereas the RC shear walls are extensively used as the lateral resisting systems in the steel buildings. This thesis therefore focuses on enhancing the modelling features of iAEM towards an efficient and accurate nonlinear analysis of steel buildings with RC shear walls.

First, the explicit modelling methods are used to consider the residual stresses and initial geometric imperfections in iAEM. Non-rectangular joint elements are introduced to accommodate the beam and column members with geometric imperfections. The capability of the proposed approaches is demonstrated through several numerical examples. Next, the component method is adopted to model the semi-rigid bolted-angle connections in the framework of iAEM, and the method is consistent with the usage of springs in iAEM. The approach is validated through several numerical examples. To model the RC shear walls by iAEM, the nonlinear beam-truss model is employed with compression-only diagonal truss elements. A biaxial material model for concrete that accounts for the effect of lateral tensile strain on the stress-strain relationship of concrete in compression is used. The verification studies show that compression-shear failure of squat walls can be captured by the

proposed approach. Compared with the conventional AEM, both efficiency and accuracy for analyzing squat walls is achieved by iAEM analysis. Finally, system-level case studies of two multi-storey buildings reveal that the developed modelling features in iAEM can readily be integrated for nonlinear analysis of buildings.

List of Tables

This page is intentionally left blank.

List of Figures

List of Symbols

Abbreviations

ACI	American Concrete Institute, USA
AEM	Applied element method
APM	Alternate path method
ASCE	American Society of Civil Engineers
DEM	Discrete element method
DoD	Department of Defense, USA
DOF	Degree of freedom
ECCS	European Convention for Constructional Steelwork
EDEM	Extended discrete element method
ELR	Enhanced local resistance
FEM	Finite element method
FEMA	Federal Emergency Management Agency, USA
GCS	Global coordinate system
GSA	General Services Administration, USA
HMG	Her Majesty's Government
iAEM	improved applied element method
LCS	Local coordinate system
MP	Menegotto-Pinto
NIST	National Institute of Science and Technology, USA
OC	Occupancy category
RC	Reinforced concrete
RBSM	Rigid body spring model
SHC	Square hollow section

STM	Strut and tie model
TSA	Top and seat angle
TSWA	Top and seat angle with double web angles
MVLE	Multiple vertical line element
UDL	Uniformly distributed load
WTC	World Trade Center, New York City

Symbols

a	Length of the representative area
b	Strain hardening ratio of steel
$b_{eff,a}$	Effective width of the angle
b_w	Thickness of the concrete panel
c_f	Friction coefficient of the bolts
d	Distance between springs
d_b	Bolt diameter
d_{hole}	Bolt-hole diameter
f	Stress
f^*	Effective stress in the Menegotto-Pinto model
f_0	Stress at the point where two asymptotes of the branch under consideration meet in the Menegotto-Pinto model
$f_c^{'}$	Compressive strength of concrete
f_{cc}	Compressive strength of confined concrete
f_r	Stress at the point where the last strain reversal with stress of equal sign took place in the Menegotto-Pinto model
f_{res}	Maximum residual stress
f_{st}	Stress shift in the Menegotto-Pinto model

f_t	Tensile strength of concrete
f_y	Yield strength of steel
f_{yb}	Yield strength of bolts
f_u	Ultimate strength
f_{ub}	Ultimate strength of bolt material
f_{up}	Ultimate strength of the plate steel
g	Gravitational acceleration
g_1	Horizontal gauge length
h_b	Depth of the beam section
h_c	Depth of the column section
k_d	Axial stiffness of the diagonal truss
m	Distance between the two plastic hinges
n_b	Number of bolts
p_{pf}	Bolt pretension force applied during the tightening process
r_a	Radius of the angle fillet
t	Time
t_a	Angle thickness
t_p	Plate thickness
u	Horizontal displacement
v	Vertical displacement
w	Magnitude of the uniformly distributed load
A	Total area of the cross section
A_b	Area of the bolt shank
A_d	Area of the diagonal truss
A_g	Gross section area of the wall

A_s	Shear area
B	Width of the concrete panel
$B_{T,Rd}$	Tensile resistance of the bolts
D	Depth of the concrete panel
E	Elastic modulus of the material
E_c	Elastic modulus of concrete
E_p	Elastic modulus of the plate steel
E_s	Elastic modulus of steel
E_{sec}	Secant modulus of concrete
E_u	Unloading modulus of concrete
F_b	Bearing force
$F_{br,Rd}$	Bearing resistance
F_s	Bolt slip resistance
F_u	Ultimate resistance of the angle
$F_{T,Rd}$	Yield resistance of the angle
$F_{V,Rd}$	Shear resistance of the bolt
G	Shear modulus of the material
G_p	Shear modulus of the plate steel
I	Second moment of inertia
K_b	Bending stiffness
K_{br}	Bearing stiffness
K_e	Initial elastic stiffness of the bolted angle
$K_{i,br}$	Initial stiffness of plate in bearing
$K_{i,V}$	Initial stiffness of bolt in shear

K_{ie}	Transition inelastic stiffness of the bolted angle
K_n^i	Normal stiffness of the i^{th} pair of springs for the normal case
K_{py}	Post-yield inelastic stiffness of the bolted angle
K_s^i	Shear stiffness of the i^{th} pair of springs for the shear case
K_v	Shear stiffness
L	Length
L_b	Beam length
L_e	Distance from bolt center to plate edge
L_w	Wall length
L_R	Reference length of each beam or truss
M	Bending moment
N	Vertical load
P_c	Initial load supported by the middle column
P_{cr}	Elastic buckling load of the column
P_y	Squash load of the column
R	A parameter that defines the shape of the transition curve in the Menegotto-Pinto model
R_0	Value of parameter R during first loading in the Menegotto-Pinto model
T	Fundamental time period
T_n^i	Thickness of the i^{th} pair of springs for the normal case
T_s^i	Thickness of the i^{th} pair of springs for the shear case
V	Shear force
$\mathbf{f}(t)$	Applied force vector
$\mathbf{C}$	Damping matrix
$\mathbf{F}$	Externally applied load vector

$\mathbf{K}$	Stiffness matrix
$\mathbf{M}$	Mass matrix
$\mathbf{R}$	Internal force vector contributed from the spring stresses to the centroid of iAEM elements
$\mathbf{U}$	Displacement vector
$\dot{\mathbf{U}}$	Velocity vector
$\ddot{\mathbf{U}}$	Acceleration vector
$\Delta\mathbf{f}$	Incremental applied load vector
$\Delta\mathbf{F}$	Incremental force vector
$\Delta\mathbf{R}$	The out-of-balance (residual) forces
$\Delta\mathbf{R}_m$	Residual force vector due to cracking and incompatibility between strain and stress of each spring
$\Delta\mathbf{R}_G$	Residual force vector due to geometrical changes in structure during loading
$\Delta\mathbf{U}$	Incremental displacement vector
β	Reduction factor of concrete compressive stress due to the lateral strain
δ_0	Initial out-of-straightness
δ_m	Plastic displacement of the bolted angle
δ_{slip}	Slip displacement
δ_u	Ultimate failure displacement of the bolted angle
δ_v	Shear displacement
δ_y	First yield displacement of the bolted angle
ε	Strain
ε^*	Effective strain in the Menegotto-Pinto model
ε_0	Strain at the point where two asymptotes of the branch under consideration meet in the Menegotto-Pinto model
ε_{c0}	Compressive strain of concrete
ε_{cc}	Compressive strain of confined concrete

ε_{cs}	Strain when concrete softening initiates
ε_{cu}	Ultimate strain of concrete
ε_{D}	Displacement convergence tolerance
ε_{int}	Intermediate lateral strain
$\varepsilon_{\max}$	Absolute maximum strain at the instant of strain reversal in the Menegotto-Pinto model
ε_{n}	Lateral strain
ε_{r}	Strain at the point where the last strain reversal with stress of equal sign took place in the Menegotto-Pinto model
ε_{res}	Residual lateral strain
ε_{y}	Yield strain
ε_{u}	Ultimate strain
γ	Load factor
η	Coefficient considers the interactions between the strengths of the angle legs and the bolts
μ	Strain hardening ratio
ν	Poisson's ratio
θ_{y}	Yield chord rotation of the beam
ρ	Material density
ξ	A parameter updated following a strain reversal in the Menegotto-Pinto model
ψ_{0}	Angle of initial out-of-plumbness
Δ_{0}	Initial out-of-plumbness
Δ_{b}	Bearing displacement
Λ	A factor that considers the effect of unloading on the concrete fracture energy in compression
Θ	Drift ratio of the wall
Ω_{N}	Dynamic increase factor prescribed by the guide for the static analysis

Δt	Time step
$\Delta \delta$	A small incremental displacement

1 Introduction and Literature Review

1.1 Introduction

Since the 1968 chain-reaction failure of the Ronan Point apartment in London, UK triggered by an accidental gas explosion (Pearson and Delatte, 2005), the phenomena of progressive collapse has been recognized and discussed in engineering practice and research communities worldwide. This issue has again been brought to the fore after the terrorism-caused building collapses in the US: the destruction of Alfred P. Murrah Federal Building in 1995 due to a truck bomb attack (FEMA, 1996) and the collapse of the World Trade Center towers in 2001 caused by the impact of large passenger jetliners (NIST, 2005).

Progressive collapse is defined as "the spread of an initial local failure from element to element, resulting eventually in the collapse of an entire structure or a disproportionate part of it" (ASCE, 2010). The disproportionality refers to the situation in which failure of one or more primary load-carrying members causes a major collapse, with a magnitude disproportionate to the initial event. Thus, "progressive collapse" is an incremental type of failure wherein the total damage is out of proportion to the initial cause. In some countries, the term "disproportionate collapse" is used to describe this type of failure (Ellingwood et al., 2007).

Progressive collapse is triggered by extreme loading events. These low-probability high-consequence events include intentional explosions, accidental explosions, vehicle impacts, earthquakes, fire, or other abnormal load events (NIST, 2006). Though structural safety is assured implicitly in the current Load and Resistance Factor Design (LRFD) through reliability-based loads and resistance factors, such provision does not take into account these unforeseen events. The availability of

advanced structural analysis software leads to highly optimized use of construction materials. Very limited or insufficient reserve capacity may be available for unexpected loads. The redistribution of loads caused by loss of primary load-carrying members may cause materials to exceed their limits (Mohamed, 2006). As a result, local structural damage or failure cannot be absorbed by the inherent continuity and ductility of the structural system, and it initiates a chain reaction of failures that propagates vertically or horizontally through the structural system, leading to an extensive partial or total collapse (Ellingwood and Dusenberry, 2005).

In order to minimize the consequences of extreme loading events, progressive collapse of the building should be mitigated. Building codes, standards and guidelines have specified quantitative design requirements against progressive collapse. Different acceptance criteria in terms of force and deformation have been set for different types of structures (DoD, 2009; GSA, 2013). Allowable damage area has also been specified by UK Building Regulations 2000 (HMG, 2013) and US GSA guidelines (GSA, 2013) (see Figure 1-1). But the difficulty lies in how to properly predict damage area of a structure during collapse.

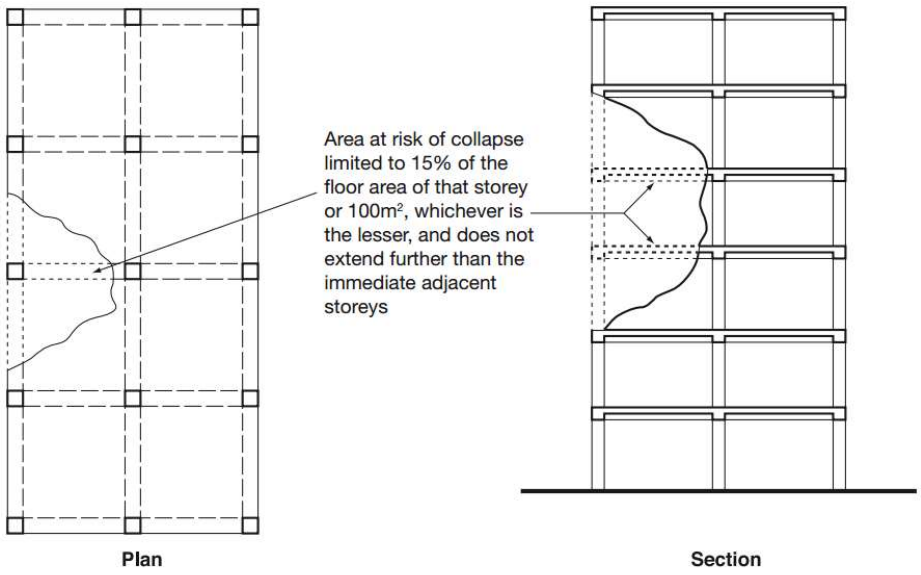

Figure 1-1 Area at risk of collapse in the event of an accident (HMG, 2013)

1.2 Research gaps

To assess the vulnerability of progressive collapse, and determine the post-collapse damage area, several numerical methods are available, and they can be categorized as two main groups. One group is based on continuum including the well-known finite element method (FEM). A number of algorithms have been proposed to model progressive failure, fragmentation and impact under extreme loading conditions during the past few years (Choi and Chang, 2009; Elsanadedy et al., 2014; Kaewkulchai and Williamson, 2006; Peng et al., 2015; Scott and Fenves, 2010; Vlassis et al., 2009). However, they are very difficult or practically impossible to follow the complete collapse behavior by the continuous mechanics approach. The other group is based on discrete element framework, including discrete element method (DEM) (Hakuno and Meguro, 1993) and applied element method (AEM) (Tagel-Din, 1998). Both methods are able to model the whole process of structural collapse, but AEM is superior to DEM in its much higher accuracy (Meguro and Tagel-Din, 2000; Tagel-Din, 1998) .

However, the conventional AEM requires prohibitive computational efforts for collapse analysis of large-scale structures, because it applies the micromodelling approach and a large number of brick-type elements need to be used in the model. Recently, the macromodel-based improved AEM (iAEM) has been developed for collapse analysis of large-scale steel framed structures with high efficiency and reliable accuracy (Elkholy, 2004). In the iAEM, beam-column members are modelled by beam-type elements, resulting in significant reduction of element number in the model and great saving of computational time.

iAEM is good numerical tool for efficient and realistic analysis of progressive collapse, but currently it is limited to analyse idealized steel structures without considering residual stresses and geometric imperfections. Nevertheless, these

imperfections cannot be ignored in real structures, as they have significant implications on the resistance and stability of the structures. Besides, current iAEM assumes rigid connection in the modelling, yet the real connection behavior of steel structures is semi-rigid. Connections become nonlinear with gradual yielding of connection plates and cleats, bolts etc, which would affect the ultimate capacity of the structures (Chen et al., 1996). Furthermore, iAEM has not been used for modelling of steel buildings with reinforced concrete (RC) shear walls. RC shear walls are extensively used as the lateral resisting systems for steel buildings. Flexure-shear interaction (FSI) of the concrete in the multi-axial stress state due to combined axial, flexural and shear forces is especially important for squat walls.

To facilitate better prediction of the collapse behavior of structures, the three features mentioned above have to be included in the modelling.

1.3 Objective and scope of research

The objective of this research is to enhance the modelling features of iAEM for efficient and accurate nonlinear analysis, accounting for the initial material and geometric imperfections, semi-rigid connection behavior, and the contribution of RC shear walls. To accomplish the thesis objective, the study covers the following scope.

1. To consider both initial material and geometric imperfections of steel frames in iAEM by appropriate modelling methods. The modelling methods should not only accurately predict the ultimate load capacity of steel frames, but also be easy to apply without changing the element formulation. The effect of initial imperfections on the structural behavior of the steel frames will be studied.
2. To simulate the semi-rigid bolted-angle connections of the steel frames using iAEM. The connection modelling method should not only be able to predict

the cyclic connection behavior, but also to capture the key responses of bolted-angle connections during progressive collapse. The effect of semi-rigid connections on the structural strength of steel frames will be investigated.

3. To propose an efficient method to model the RC shear walls in iAEM. The method should also be able to consider the FSI so that compression-shear failure for the squat walls can be captured. Comparison between conventional AEM and iAEM in terms of both accuracy and efficiency will be carried out.
4. To integrate the three modelling features in system-level case studies. Case studies are to be performed for multi-storey buildings to assess whether that proposed modelling features in iAEM can readily be integrated for nonlinear analysis of buildings.

1.4 Research significance

The conventional AEM can simulate the entire process of progressive collapse, but it is very computationally expensive. The significance of this study lies in adding three important modelling features to current iAEM for an efficient and accurate nonlinear analysis of steel buildings with RC shear walls. The original contributions of this thesis can be summarized in the following three aspects:

1. Modelling of initial imperfections of steel frames in iAEM. The explicit modelling methods are used to directly and physically account for the residual stresses and initial geometric imperfections. Non-rectangular joint elements are introduced to accommodate the beam and column members with geometric imperfections. When the initial imperfections are considered in iAEM, the earlier yielding, reduced structural strength, buckling and post-buckling behavior can be predicted.

2. Modelling of semi-rigid connections of steel frames in iAEM. The component method is seamlessly applied to model the semi-rigid bolted-angle connections of the steel frames. The monotonic load deformation behavior is described for three connection components. Unloading and reloading paths are also defined to consider the cyclic connection behavior in the dynamic analysis. With consideration of the semi-rigid connection behavior, the key responses of bolted-angle connections during progressive collapse can be simulated.
3. Modelling of RC shear walls in iAEM. The nonlinear beam-truss model is used to represent the RC shear wall using iAEM. FSI is considered by the compression-only diagonal truss elements. A biaxial material model for concrete that accounts for the effect of normal tensile strain on the stress-strain relationship of concrete in compression is used. By use of the beam-truss model, the compression-shear failure of squat walls where significant FSI exists can be captured though several numerical examples.

The following common characteristics of the three modelling features developed in iAEM can be observed:

- **Accuracy:** The proposed modelling features are validated against the published numerical and experimental results and the results obtained from the established commercial software SAP2000, and reasonable accuracy of these features in iAEM can be achieved through a number of examples in the study. The developed modelling features in iAEM can readily be integrated for nonlinear analysis of buildings.
- **Efficiency:** Compared with the conventional AEM, the iAEM is very efficient in the analysis. Significant reduction of number of elements and consequently number of degrees of freedom in iAEM compared with the conventional AEM is

observed for the RC shear wall modeling, which makes iAEM well suited for nonlinear analysis of large-scaled structures.

- **Consistency:** The three enhanced modelling features in the study utilize the nonlinear springs in iAEM to model the steel frames, RC shear walls and the connections. As a result, the distinct behaviors of various main structural components of the building are consistently modelled. The consistent nature makes the iAEM easy to use, and therefore, it is suitable for routine office use.

1.5 Outline of the thesis

The thesis comprises seven chapters as follows:

Chapter 1: Introduction and literature review. This chapter firstly provides an introduction to the thesis, where the general background of progressive collapse, research objective, scope and significance, and outline of the thesis are described. Then the chapter presents a literature review on the milestone events of structural collapse, and the numerical methods and modelling approaches used for progressive collapse analysis.

Chapter 2: Benchmark examples of improved applied element method. This chapter presents benchmark examples of the current iAEM. Firstly, the element formulation of iAEM and solution strategies for nonlinear analysis are described. The capability of the iAEM is demonstrated through seven benchmark examples from simple first-order elastic static analysis to the sophisticated second-order inelastic dynamic analysis. The validation study of iAEM in this chapter serves as the basis for modelling of the initial imperfections, semi-rigid connections and RC shear walls in the subsequent chapters of the thesis.

Chapter 3: Modelling of initial imperfections of steel frames. This chapter shows the explicit modelling of residual stresses and initial geometric imperfections of steel

frames using iAEM. The first part of the chapter describes the explicit modelling approaches, and the later part of the chapter presents the four numerical examples for verification.

Chapter 4: Modelling of semi-rigid connections of steel frames. This chapter employs the component method to simulate the semi-rigid connection behavior of steel frames using iAEM. First, the importance of modelling semi-rigid connection of steel structures is explained. Then the component method for the bolted-angle connections in iAEM is described. Finally, the component method is validated against the experimental results through three numerical examples.

Chapter 5: Modelling of reinforced concrete shear walls. This chapter applies the beam-truss modelling approach to model RC shear walls. Firstly the chapter reviews several modelling methods of RC shear walls. Then the macromodel-based beam-truss modelling approach using iAEM is described, and FSI is considered through the compression-only diagonal truss elements. Finally, the modelling approach is verified through five tested shear walls with shear span ratios ranging from 0.45 to 3 and the compression-shear failure due to significant FSI are captured for squat RC shear walls.

Chapter 6: System level case studies. This chapter presents case studies of two multi-storey buildings by integrating the three developed modelling features at the system level. The first building is the 6-storey 2-bay Vogel steel frame for which the initial imperfections and semi-rigid connections are considered. The second building is a 14-storey hybrid structure for which the steel frames and RC shear wall are modelled together using iAEM.

Chapter 7: Conclusions and recommendations. This chapter summarizes the conclusions drawn from the research study, and provides recommendations for future research on progressive collapse analysis.

1.6 Literature Review

In this section, firstly, three well-known progressive collapse events in the past few decades are described. Secondly, the design methods to prevent progressive collapse are introduced. Thirdly, three numerical methods for progressive collapse analysis are discussed. Finally, the multi-scale modelling methods including macromodels and micromodels are presented and compared.

1.6.1 Milestone events of progressive collapse

The evolution of modern design codes for structural safety and robustness is driven significantly by the past collapse events. In this section, three milestone events of progressive collapse are described with emphasis on the lessons learnt from these unfortunate failures.

1.6.1.1 Ronan Point apartment, 1968

Figure 1-2 Ronan Point after collapse (Pearson and Delatte, 2005)

In the early morning of May 16, 1968, a dramatic partial collapse occurred to the Ronan Point apartment building in London, England due to an accidental gas stove

explosion on the 18th floor of a 22-storey precast concrete building. The collapse generated the widespread concern for potential collapse of high-rise buildings in a chain-reaction mode, triggered by a local failure. The investigation panel (Griffiths, 1968) reported that, the explosion blew out the exterior bearing wall of the apartment that caused the upper floor slab to fall on the floor below, thereby initiating the collapse of one corner of the building "progressively" almost to the ground (see Figure 1-2). Five people died, and many people survived as they were fortunately still in bed in the early morning whereas the explosion caused damage to the living rooms. The lack of structural redundancy was found to be the main cause of Ronan Point apartment failure. The Larsen-Nielson building system, developed in Denmark in 1948, consisted of precast panels jointed together without a structural frame, and the connections relied, in large part, on friction. The apartment tower lacked the alternate load paths to redistribute forces in the event of a partial collapse.

The Ronan Point disaster initiated changes to building codes throughout the world, and many countries began to adopt structural integrity or "robustness" provisions. One of the outcomes was the development of the "fifth amendment" to the U.K. building regulations in 1970. Limits of damage are laid down and if these would be exceeded by removal of a partial member, that member must be designed to resist a pressure of 34 kN/m^2 from any direction. The provisions remain unchanged and are known as the "direct design method" in the British Code (HMG, 2013). The Portland Cement Association and the Prestressed Concrete Institute also issued guidelines on tying structural elements together to increase its ductility (Ross, 1984).

1.6.1.2 Alfred P. Murrah federal building, 1995

On April 19, 1995, Alfred P. Murrah federal building in Oklahoma City incurred significant damage, and partially collapsed due to blast loading. The structural system of Murrah building was a nine-storey cast-in-place ordinary moment resisting frame. The lateral load resisting system comprised reinforced concrete shear walls located

within the stair and elevator system on the south side of the building (Corley et al., 1998; FEMA, 1996). On the north side of the building, a transfer girder was used at the 3rd level to allow 12.2 m column spacing for the first two levels, and 6.1 m column spacing for the upper levels. A truck carrying approximately 1.8 tons of TNT detonated at approximately 4.3 m from the north face of the building. The blast shock wave disintegrated one of the ground columns and caused brittle failures of two others. Subsequently, the transfer girder above these columns failed, and the upper-storey floors collapsed in a progressive manner. Approximately 70 percent of the building experienced dramatic collapse in both the vertical and horizontal directions (see Figure 1-3). One hundred sixty-eight people died, many of them as a direct result of progressive collapse (ASCE, 2010).

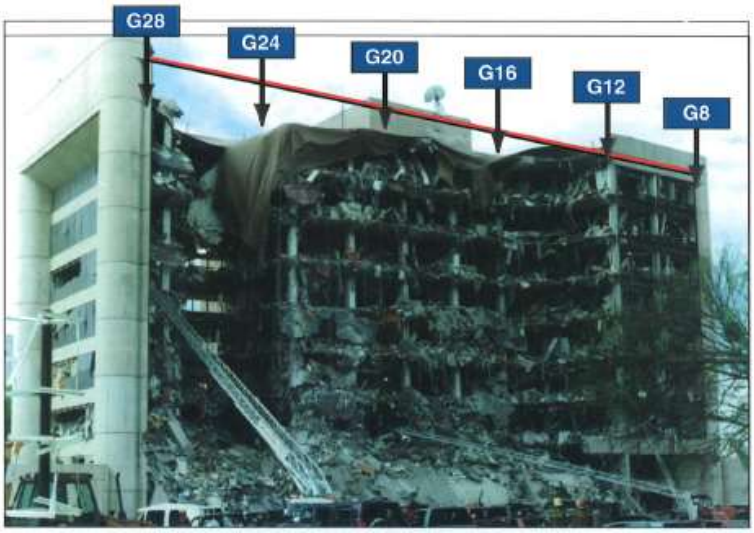

Figure 1-3 Damage to north and east sides of Murrah Building (FEMA, 1996)

The effects of seismic strengthening measures on Murrah building's capacity to resist blast effects and progressive collapse was investigated. It was found that using special moment frame detailing could reduce the collapse area of the building by 50% to 85% (Corley et al., 1998; FEMA, 1996). Using the pier-spandrel, the exterior special moment frame, and the re-detailed original frame, floor area loss could be approximately 90% less than that in the actual 1995 attack (Hayes Jr et al., 2005).

However, seismic design details cannot replace specific measures to mitigate blast and progressive collapse vulnerabilities as there will be instances in which known threats will justify specific design for blast and progressive collapse (Hayes Jr et al., 2005).

1.6.1.3 World Trade Center towers 1 and 2, 2001

Figure 1-4 Impact, explosion and fire in the twin towers (FEMA, 2002)

The total collapse of World Trade Center (WTC) twin towers in New York City on September 11, 2001 was among the worst building disasters and loss of life from any single building event in the world. In this event, a total of 2830 people lost their lives. The structural system of the twin towers consisted of an exterior load-bearing tube formed by closed spaced columns of 1.015 m on center and deep spandrel plates. Interior cores, formed by larger, more widely spaced steel columns, housed elevator shafts and stairwells. Double trusses spanned between the exterior wall spandrel plates and interior core columns (Corley, 2004). The collapse event was initiated by the impact of two hijacked Boeing 767-200ER series airplanes. The first plane crashed into the north face of WTC 1 (north tower) at a velocity of about 760 km/h between 94th and 98th stories. After only 16 minutes, the second plane crashed into the

south face of WTC 2 (south tower) at a velocity of about 950 km/h between 78th and 84th stories (FEMA, 2002). Despite massive damage to a significant number of perimeter columns on several floors of the building due to large aircraft impact, these buildings remained erected long enough for most occupants to escape safetly. WTC 1 stood for 103 min and WTC 2 stood for 56 min after the collisions. The twin towers were destroyed by a combination of the tremendous plane impact, explosion of the engines and fire ignited by the fuel in each plane. A significant number of preimeter columns on several floors were completely destroyed. Then the high-temperature fires from burning aviation fuel and plane debris softened the steel core of the sturcture. Eventally, the loss of strength and stiffness of the materials resulting from the fire combined with the initial impact caused the collapse of the towers (see Figure 1-4). Many researchers including Quintiere et al. (2002), Usmani et al. (2003), and Bažant and Verdure (2007) have used different methods for simulating the collapse of those towers to understand and prevent progressive collapse of high-rise buildings. Detailed investigation by FEMA (2002) and NIST (2005) concluded that remarkable robustness and redundancy contained in the steel framing systems sustained the towers until their global collapse. The towers collapsed in a progressive manner, but the collapse cannot be viewed as disproportionate collapse since the initial damage due to the two extreme actions from aircraft and fire was also huge. It is practically impossible to prevent such collapse with simple changes to the structural design.

1.6.2 Design approaches to prevent progressive collapse

Methods of mitigating progressive collapse are incorporated in many building codes or standards, especially in Europe and North America. Both direct and indirect design approaches are included in these codes. The indirect design approach places minimum requirements on strength, continuity, and ductility for providing resistance

to progressive collapse. The direct design approach includes alternate path method and key element method.

1.6.2.1 Indirect approach - Tie force method

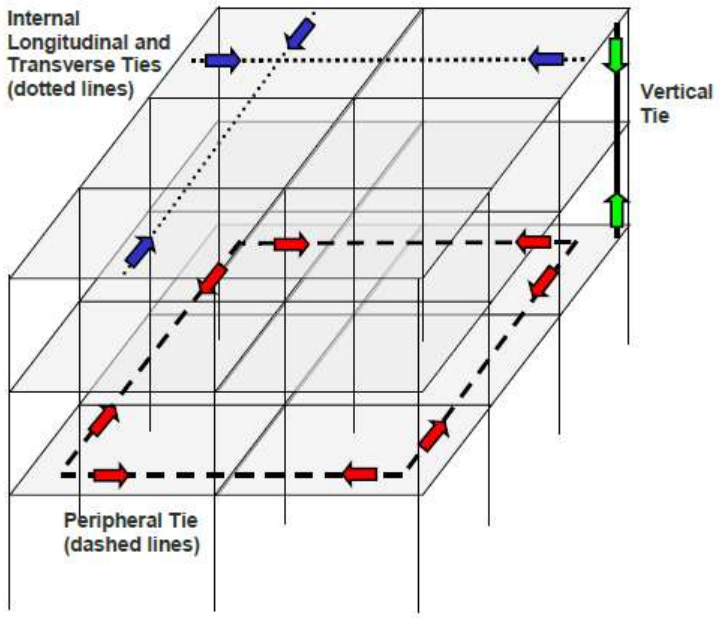

Figure 1-5 Tie force in a frame structure DoD (2009)

The term "general structural integrity" is used to describe the indirect design method by some researchers (Breen, 1975; Fintel and Schultz, 1979; McGuire and Leyendecker, 1974), and this approach has been integrated into general building codes and standards (ACI, 2014; ASCE, 2010). ASCE (2010) presented a few examples of design concepts and details: good plan layout, catenary action of floor slab, ductile detailing, redundant structural systems, etc.

In UK Building Regulations (2013), Eurocode (2006) and DoD (2009), the indirect method is expressed in terms of tie force requirements, including horizontal and vertical ties. The provision of ties increases structural continuity, thereby creating a structure with a higher degree of redundancy, should part of the structure be removed by an accidental action. Generally, ties are provided by steel members or reinforcement. Besides, the beam-column joints can also aid in the transfer of tying

forces. There are three kinds of horizontal ties (DoD, 2009): (i) longitudinal, (ii) transverse and (iii) peripheral. Vertical ties must be present in columns and load-bearing walls. Different tie strengths are required for framed structures and vertical load-bearing wall structures. There are also requirements for continuity of ties around the building's plan geometry and throughout the height. A schematic of different types of ties applicable in typical frame construction is presented in Figure 1-5.

Although this indirect design method can reduce the risk of progressive collapse (Corley et al., 1998; Corley, 2004; FEMA, 1996; Sozen et al., 1998), estimation of post-failure performance of structures designed based on such a method is not readily available.

1.6.2.2 Direct approach - Alternate path method

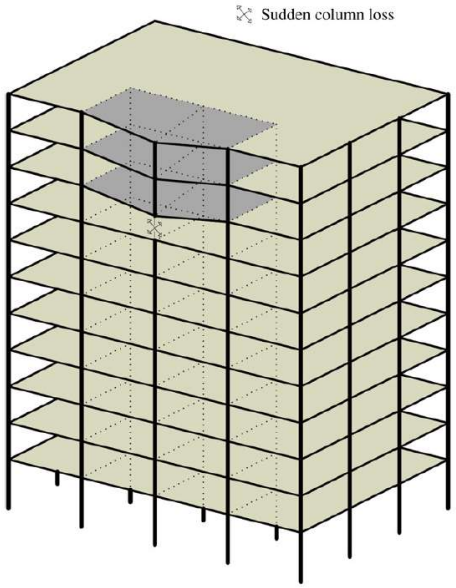

Figure 1-6 Multi-storey building subjected to sudden column loss (Izzuddin et al., 2008)

The direct alternate path method (APM) has been adopted by a number of design codes including Eurocode (2006), GSA (2013) and DoD (2009). APM is a threat-independent methodology, meaning that it does not consider the type of triggering event, but rather, considers building system response after the triggering event has

destroyed critical structural members. This methodology is generally applied in the context of a "missing column" scenario to assess the vulnerability of progressive collapse (see Figure 1-6); i.e. it is used to check if a building can successfully absorb loss of a critical column without propagated damage. The portion of building at risk of collapse should be limited to 15% of the floor area, or 100 m^2 at the relevant storey, whichever is less (Eurocode, 2006).

As for the analysis procedure, Eurocode (2006) does not explicitly require dynamic analysis on APM, while GSA (2013) and DoD (2009) recognize the dynamic nature of progressive collapse events, and they recommend three types of analyses, i.e. linear static, nonlinear static and nonlinear dynamic analyses. The current version of GSA (2013) utilizes the APM analysis procedure of DoD (2009). When the static analysis is used, the recommended accidental load combination is:

$$G_{ND} = \Omega_N \left[1.2D + \left(0.5L \quad \text{or} \quad 0.2S \right) \right] \tag{1-1}$$

where G_{ND} = gravity loads for inelastic dynamic analysis; D = dead load including façade loads; L = live load; S = snow load; Ω_N = dynamic increase factor prescribed by the guide for the static analysis. If the dynamic analysis is adopted, Ω_N should be unity. Depending on the structural materials, members, and analysis types, different demand-to-capacity criteria and deformation criteria are presented.

Advantage of APM is that it is independent of the initiating load, so that the solution is presumably valid for any type of hazard that causes member loss. Most of the published progressive collapse analyses for the entire building (Fu, 2009; Galal and El-Sawy, 2010; Khandelwal et al., 2008; Kim and Kim, 2009), or their components (Khandelwal and El-Tawil, 2006; Lee et al., 2009; Sadek et al., 2011) are based on APM. However, as summarized in a state-of-the-practice article (Dusenberry and Juneja, 2002), building codes, reference standards and guidelines have not provided

an effective and quantitative design goal for increased robustness. Performance expectations are generally not well quantified or elaborated in most documents. There is a general lack of information on procedures, particularly numerical modelling (nonlinear dynamic analysis) guidelines, to carry out simple yet reliable progressive collapse studies of structures.

1.6.2.3 Direct approach – Key element method

For any critical structural elements over which the building cannot bridge, the elements must be designed as "key" or "protected" elements to resist an accidental static pressure of 34 kN/m^2 applied in the horizontal and vertical directions (in one direction at a time) . Such accidental loading should be assumed to act simultaneously with other design loadings (i.e. wind and imposed loading) in accidental loading combination (Eurocode, 2006). The key element method in DoD (2009) is called enhanced local resistance (ELR) which is required for buildings of Occupancy Category (OC) II Option 1, OC III, and OC IV. Depending on the occupancy category, requirements for ELR location and extent, shear and flexural demand should be satisfied.

1.6.3 Numerical methods for progressive collapse analysis

Due to high cost of the experimental programs for assessing the structural response and complex interactions between the various factors of a real structure during collapse, application of numerical models and computer simulation is inevitable. Currently, the available numerical methods for progressive collapse analysis can be classified into two categories: one is based on the continuum-mechanics theorem, i.e. finite element method (FEM), and the other is based on the discrete element technique, e.g., discrete element method (DEM), and applied element method (AEM). In this section, the applicability, advantages and disadvantages of FEM, DEM and AEM for progressive collapse analysis are discussed and compared.

1.6.3.1 Finite element method

The continuum-based finite element method (FEM) has been most widely used for progressive collapse analysis. The FEM software include SAP2000 (SAP2000, 2002), ABAQUS (ABAQUS, 2005), LS-DYNA (Hallquist, 2005), and OpensSees (McKenna et al., 2000), etc. In most of the studies, the progressive collapse analysis is carried out in the framework of APM involving both linear and nonlinear or static and dynamic analyses. A large amount of efforts have been taken by the researchers on studying important characteristics for progressive collapse behavior such as catenary action (Kim and An, 2009; Samuel Tan and Abolhassan Astaneh-Asl, 2003), beam-column connection (Khandelwal et al., 2008; Yim and Krauthammer, 2012), slab effect (Pham and Tan, 2013; Yu et al., 2010) and impact or debris loading (Kaewkulchai and Williamson, 2006; Vlassis et al., 2009). Some useful recommendations have been made based on their analysis.

However, there is a limitation associated with FEM that these analysis tools typically assume that the analysed structures remain continuous, meaning that even if a collapse occurs, the structure still maintains its continuity. As a result, most of the literature focuses on collapse initiation, and the separation of elements of real collapse cannot be simulated. In order to overcome this disadvantage, LS-DYNA and ABAQUS have developed a so-called element deletion (or erosion) technique, by which the corresponding elements will be deleted from the model after reaching failure criteria. This technique has been applied by some researchers in their finite element models for progressive collapse analysis. For example, models of multi-storey steel framed buildings were built by Kwasniewski (2010) and Szyniszewski and Krauthammer (2012) with element deletion in LS-DYNA to study the applicability of detailed modelling for progressive collapse analysis, and energy flow during collapse, respectively. Models of single tower and transmission tower-line system were established to simulate wind-induced progressive collapse by birth-to-

death element technique (or element deletion) in ABAQUS by Zhang et al. (2013). However, deleting the failed elements will remove mass and energy from the whole system. If the analysis has substantial element removal, the contact-collision and pile-up of the rest of the structure will be very different from a real collapse case, largely affecting the accuracy of the simulation.

1.6.3.2 Discrete element method

The discrete element method (DEM) is another method used for collapse analysis of buildings. This method was originally developed by Cundall (1971) to study progressive movements of rock masses as 2D rigid block assemblages. In the original DEM, material is considered to be assembly of circular and rigid particles with deformable contacts (or springs) (see Figure 1-7), and the equation of motion based on the Newton's second law is solved by the explicit time integration algorithm. The model behaves as a continuous medium while the springs are intact; after the breakage of some of the springs, it can trace the movement of the individual fragments. Since then, DEM was mainly used for simulating collapse of granular materials such as rock and soil. Later, Lorig and Cundall (1989) applied the DEM to model the cracking and failure of reinforced concrete through both static and dynamic numerical tests on beams. Hakuno and Meguro (1993) proposed the Extended Discrete Element Method (EDEM) based on the original DEM. In their work, concrete aggregate is modelled as circular particles, mortar is represented as pore springs that bind the aggregate, and whole process of structural collapse of a reinforced concrete frame from its crack initiation till fragmentation was simulated under earthquake loading. Nakagawa et al. (2011) used 3D-EDEM to establish a basic quantitative simulation method to test the collapse process of a brick masonry house. For progressive collapse analysis, the DEM was used by Masoero et al. (2010) to model the collapse of three-dimensional reinforced concrete framed structures after sudden loss of a column.

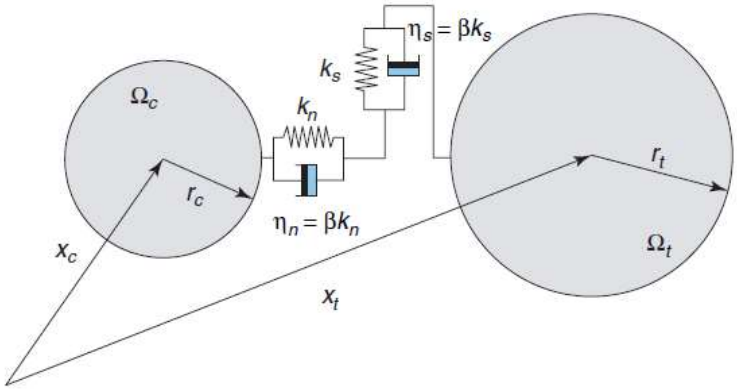

Figure 1-7 Discrete element bodies (particles) in contact (Groger et al., 2002)

DEM has its merit for structural collapse analysis in that it is able to simulate the whole process of structural collapse including fragmentation, collision and pile-up of debris by a number of contact-collision models available. However, DEM is not as accurate as FEM for modelling continuum materials such as concrete. It relies on calibration processes to determine the correct inter-element parameters for a specific problem for modelling continuum behavior and fracture, so it is only able to explain qualitatively the collapse sequence of structures made of continuum materials. If DEM is used to model the continuum materials, adoption of the inter-element parameters based on continuum mechanics are needed. Furthermore, the explicit DEM does not have a stiffness matrix or accurate element connectivity, the solution is conditionally stable and very small time step is required in the computation. Also contact search for the neighboring elements at every time step is very computationally demanding once the number of elements becomes large, making DEM much slower (Bićanić, 2004).

1.6.3.3 Applied element method

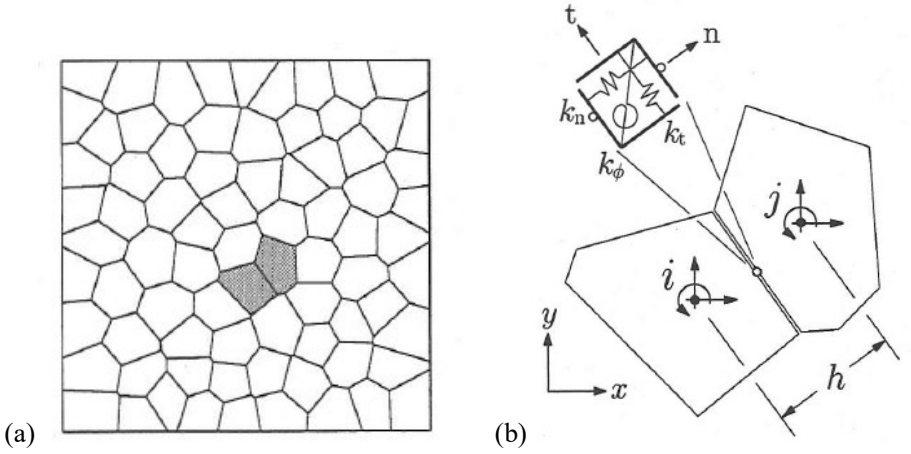

Figure 1-8 Rigid Body Spring Model: (a) partitioning of a domain using a Voronoi diagram; (b) element unit (Bolander et al., 1999)

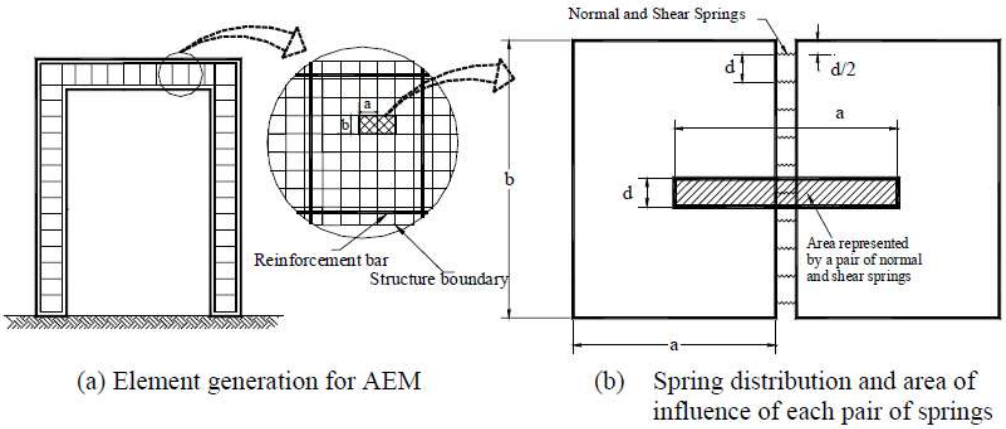

Figure 1-9 Modelling of structure using AEM (Meguro and Tagel-Din, 2001)

In recent years, the applied element method (AEM), a discrete element variant, has emerged for progressive collapse analysis. It is developed from the rigid body spring model (RBSM) proposed by Kawai (1977). In RBSM, the structure is modelled as assemblage of rigid elements interconnected along their boundaries by springs. In the two dimensional version of RBSM, each element has three degrees of freedom (DOFs) defined at its centroid, i.e. two translational and one rotational DOFs. At the boundary midpoint, one set of axial, shear and rotational springs is used to connect two adjacent elements (see Figure 1-8). The initial properties of springs are set to approximate the

elastic properties of the continuum. The global structural stiffness matrix can be obtained using the direct stiffness method by adding the stiffness contributions from each two-adjacent-element assembly. RBSM is very suited for simulating crack initiation and propagation of concrete since the springs can break after reaching the failure criteria. However RBSM is so far only used in small deformation range, and it is mainly used for limit plastic analysis (Kunieda et al., 2011). By contrast, in AEM, the rigid elements are connected with pairs of normal and shear springs distributed along the element boundary (see Figure 1-9), and each pair of springs totally represents stress and deformations of a certain area (hatched area in Figure 1-9(b)) of the studied elements. Like RBSM, the spring will also break after reaching the failure criteria. In AEM, the axial and flexure are coupled, the spread of yielding across steel section and crack opening or closure across concrete section can be modelled. AEM can model the full structural behavior from application of the load, crack initiation and propagation, separation of structural elements until total collapse in reasonable computational time with reliable accuracy (Tagel-Din, 1998).

Since the development of AEM, it has been successfully used for collapse analysis in different engineering fields such as reinforced concrete (Meguro and Tagel-Din, 1997; Meguro and Tagel-Din, 2001; Tagel-Din and Meguro, 2000), steel (Elkholy and Meguro, 2004), soil (Ramancharla and Meguro, 2001; Worakanchana and Meguro, 2006), and masonry (Guragain et al., 2006; Mayorca and Meguro, 2003). In recent years, AEM has been extended to 3D case (Worakanchana et al., 2008). Commercial software Extreme Loading for Structures ELS (2006) based on this method has been used by researchers to simulate the progressive collapse process of structures (Galal and El-Sawy, 2010; Helmy et al., 2012; Sasani, 2008).

Nevertheless, there are limitations associated with AEM. Use of springs with specified orientation in AEM implies that the responses being modelled are primarily uniaxial, which complicates modelling of multi-axial phenomena, e.g., associated

plasticity or accounting for the triaxial effect on the fracture strain of steel (Chao et al., 2006). Application of the continuum-based computational plasticity as adopted in FEM is not straightforward, and improvement is needed.

1.6.4 Multi-scale modelling approaches for progressive collapse analysis

Appropriate structural models in terms of modelling complexity and ways of response interpretation must be used when the nonlinear version of APM is employed for progressive collapse analysis. These models can be broadly classified as micromodels and macromodels. Micromodels use continuum finite elements to capture both local and global responses. Macromodels, on the other hand, utilize a combination of shell, beam-column, and discrete spring finite elements to simulate the overall response of a structure. The former focuses on the pointwise constitutive response, e.g. stress versus strain behavior, as opposed to the generalized strain stress behavior in the latter, e.g. curvature versus bending moment behavior. In this section, both micromodels and macromodels for progressive collapse analysis by some researchers are presented, and it is found that macromodels are indispensable for efficient progressive collapse analysis.

1.6.4.1 Micromodels

Some micromodels have been established by researchers to study both global and local behaviors of structures in progressive collapse analysis.

Kwasniewski (2010) presented a case study of progressive collapse analysis of a selected multi-storey building, using finite element software LS-DYNA (Hallquist, 2005). A detailed 3D FE model was developed for an existing 8-storey (22m high) building at the Cardington Large Building Test Facility (LBTF) in the UK. Nonlinear dynamic analysis using the alternate path method recommended by GSA (2013) was

adopted. All beams and columns including the flush and fin plate connections were modelled using shell elements. Such approach substantially increases the number of finite elements in the model but it allows for capturing effects initiated by large structural deformations such as an inelastic bending of end plates or local buckling of compressed flanges. The bolts were represented by 1D beam elements. The simplified steel model proposed by Galambos (2000) with Von Mises criterion was used to model the behavior of all the structural steel members. The orthotropic slab was modelled using four-node shell elements and it was divided into two types of strips, with different overall cross-sectional properties, and positioned alternatively side by side. The first strip has a total thickness of 130 mm and the second 70 mm. Each strip was modelled as a multilayer composite using an isotropic elastic-plastic material model with different responses for tension and compression (MAT 124 (Hallquist, 2005)). The complete FE model of the entire structure consisted of 1.08 million of finite elements. Three cases of notional column removal were considered in the analysis, i.e. removal of a corner column, removal of a perimeter column and removal of an internal column. The results in all the three cases showed low potential for progressive collapse of the structure. Although the explicit solution method took advantage of parallel processing on multiprocessor computers, this approach still required large computational time. The parallel computation took 19 days on 60 processors for the largest FE model.

Yu et al. (2010) simulated the progressive collapse of a single-storey steel frame with composite floor slabs due to sudden removal of a perimeter column using the finite element software LS-DYNA (Hallquist, 2005). The influence of the joints and the concrete slabs on the effective tying of steel beams was investigated. The composite-floor steel frame was one of the specimens tested by Samuel Tan and Albolhassan Astaneh-Asl (2003) at UC Berkeley. The floor slabs were made of reinforced concrete over metal deck that was supported by longitudinal and transverse beams.

Fin plate shear connection was used for all beam-to-column connections. In the finite element model, all the beams and columns were modelled by beam elements, while the metal deck and concrete slab were modelled by the shell and the constant-stress 8-node solid elements, respectively. Kinematic hardening model was used for steel material, while the HJC model in LS-DYNA (Hallquist, 2005) was used for the concrete. In the analysis, the slip between the metal deck and the concrete was ignored, and three types of joints were considered, i.e. pin joints, semi-rigid joints and hinged joints. From the analysis results, effective tying of joints can be improved by using a more rigid connection, and the tensile capacity of concrete in composite slabs contributes significantly to the effective tying. The numerical results show that retrofitting a steel beam with a steel cable is effective, and the effective tying can be further enhanced by attaching the cable to the beam at intermediate locations.

Sasani (2008) constructed two numerical models for the south annex of Hotel San Diego using the finite element method (SAP2000, 2002) as well as the applied element method (AEM) (ELS, 2006) to study its progressive collapse resistance with two adjacent exterior columns suddenly removed. The annex building was a six-storey non-ductile reinforced concrete frame structure with hollow clay tile exterior infill walls. The floor system consisted of one-way joists running in the longitudinal direction. In the 3D AEM model, structural elements were modelled with cubical sub-elements (cuboids). Beam and column cuboids were connected by 200 concrete spring triples at each cross section as an array of 10 (over the width) by 20 over the height). Floor joists were modelled in a similar manner. Slab between joists and the infill walls were also modelled using cuboid elements. Reinforcement bars of all the structural members were explicitly modelled according to their position. The AEM model results showed good agreement with experimental data in terms of the vertical displacement histories of selected joints and strain histories of selected beams and columns.

Micromodels aim at producing accurate local and global structural behaviors, but substantial computational resources are required to execute such models. In addition, micromodels are usually difficult to build as they involve detailed modelling of structural components and appropriate nonlinear constitutive models. Hence they should only be exercised by competent analysts with expertise in nonlinear dynamic modelling. As a result, micromodels are generally not suitable for routine office use for progressive collapse analysis.

1.6.4.2 Macromodels

Compared to micromodels, macromodels are fairly simpler to build and more efficient to run. They have been popular among researchers in the earthquake engineering field, e.g. Jin and El-Tawil (2005), and their applications are increasing in collapse research.

Kaewkulchai and Williamson (2004) developed a beam-column element for progressive collapse analysis of frame structures. The beam-column element utilized a multi-linear, lumped plasticity model with axial-bending interaction. Strength and stiffness degradation were included through a damage-dependent constitutive relationship. A damage index was used to determine the onset of member failure. A two-bay, two-storey plane frame with fixed supports was modelled and analysed under column-removal scenarios. The nonlinear static analysis missed some failure modes and underestimated the deformation demands, therefore, dynamic effects should be considered for progressive collapse problem.

Bao and Kunnath (2010) presented a macromodel-based approach for progressive collapse analysis of reinforced concrete frame-wall structure. A simplified shear wall model with partial damage was developed based on the multiple vertical line element method (MVLEM) proposed by Kabeyasawa et al. (1983). By comparing simulated results from the detailed finite element model in DIANA (DIANA, 2007) with those

from the developed macromodel in OpenSees (McKenna et al., 2000), it was demonstrated that the simplified model had the capability to represent the failure mechanism as well as the local effects in the overall response under given damage pattern. Then simplified models were developed for two frame-wall systems which were designed for different seismic requirements (SDC-C and SDC-D), and numerical simulations of sudden partial loss of 1st-storey wall were conducted. There was no collapse in either system, but load redistribution and variation of forces in critical structural members indicated system SDC-D was more robust than system SDC-C because of its enhanced seismic design and resulting structural layout.

Liu et al. (2015) developed a component-based model to study the dynamic response of bolted-angle connections subjected to sudden column removal. A failure criterion determined from quasi-static test results by Yang and Tan (2012a) was introduced into the model to predict the tension resistance of the bolted-angle component under large tension. The hysteric behavior of each component under cyclic load was included for dynamic analysis under free-fall scenarios. Thereafter, the model was implemented as a fiber element for simulation of the beam-to-column connection. Numerical validations demonstrated the capabilities of the component-based model in predicting the connection performance including its peak resistance and the deformation capacity. Applications of the component-based model for the analysis of the web cleat connections in two 4-storey 2D steel frame structures were studied: one was unbraced, and the other braced. The analysis results showed that a value of up to 2.9 should be used as the dynamic increase factor for both structures when dynamic effects are incorporated into the nonlinear static load resistances. It was also shown that the ultimate load capacity of unbraced frame was much smaller than that of the braced frame due to horizontal movements of its adjacent columns under catenary action.

Elkholy and Meguro (2004) proposed the improved applied element method (iAEM) to simulate the global collapse behavior of large-scale steel frames under hazardous loads. The main feature of iAEM is that each beam or column is modelled as a series of fiber beam elements as in FEM along its length (see Figure 1-10). Thickness of each pair of normal and shear springs varies across the section, and they are equal to the thickness of the section at the contact location (see Figure 1-11). The areas of normal and shear springs are differentiated by the shear factor of the cross section. As a result, only one element is used across the section instead of many as in the conventional AEM which assumes uniform thickness of the springs along the element edges (see Figure 1-12). This achieves a significant reduction of element number in the model. Some commonly used steel sections can be conveniently modelled in this method (see Figure 1-13). The efficiency and accuracy of iAEM were verified through ultimate load capacity prediction by elastic-plastic analysis of a long span beam, and a portal frame. Furthermore, a nine-storey steel building was modelled by only 477 iAEM elements, and analysed under the 1995 Kobe earthquake. Failure mode of the steel building agreed well with a recorded collapse case of multi-storey steel buildings due to this earthquake. The proposed iAEM has overcome the limitation of conventional AEM on extensive computational time and demanding computer capacity.

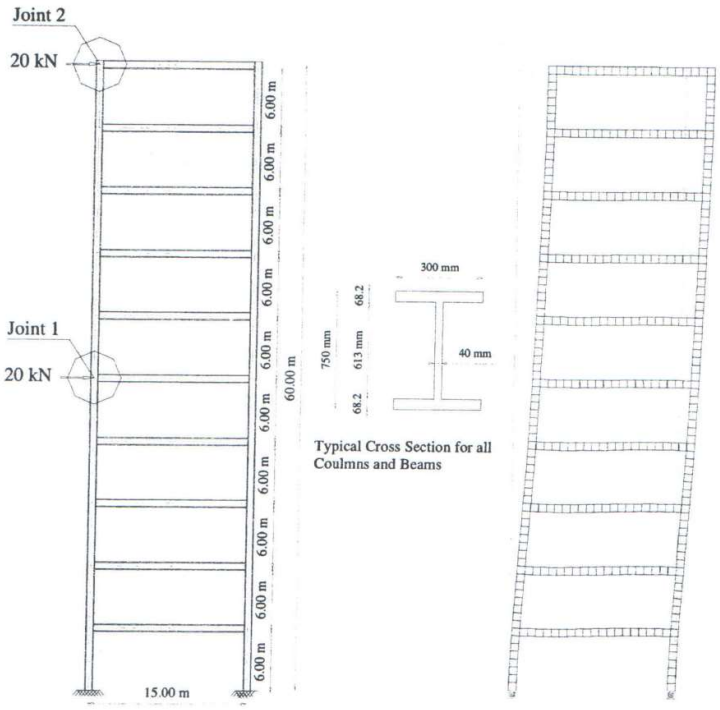

Figure 1-10 iAEM modelling of the ten-storey steel frame (Elkholy, 2004)

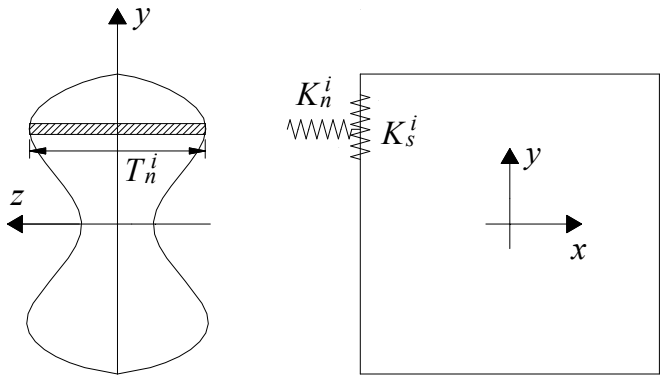

General cross section New element type for iAEM

Figure 1-11 New element type for iAEM (Elkholy, 2004)

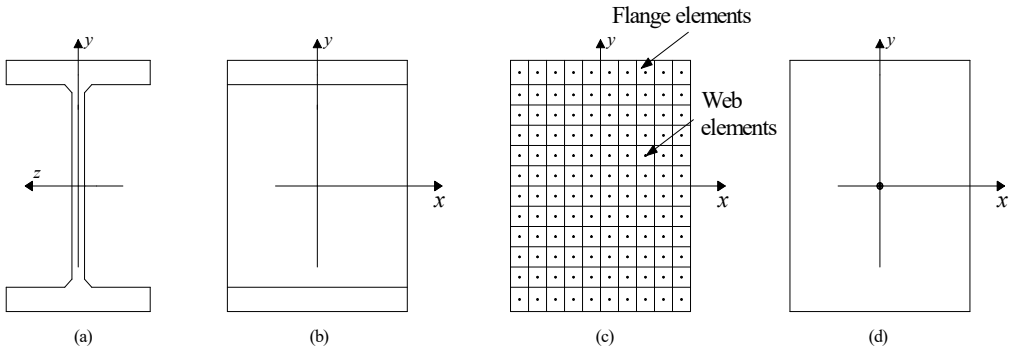

Figure 1-12 Simulation of I-shaped section: (a) cross section (b) part of the I-section to be modelled (c) modelling using conventional AEM and (d) modelling using iAEM

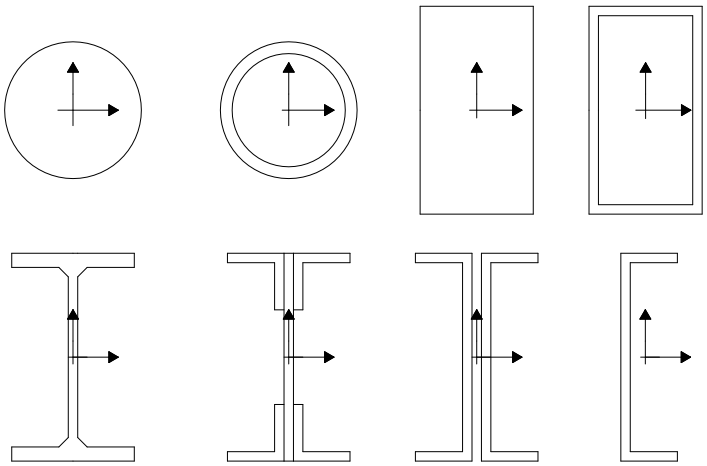

Figure 1-13 Some cross sections can be directly used in iAEM

1.6.4.3 Micromodels versus macromodels

Both micromodels and macromodels have their advantages and disadvantages. Researchers have studied the effects of different modelling methods on the progressive collapse analysis.

Liu (2010b) investigated the post-attack performance of catenary action for both original and retrofitted beam-to-column connection geometries. One-dimensional beam models, two-dimensional solid models, and there-dimensional shell models were built by means of the ABAQUS (ABAQUS, 2005) finite element package.

Numerical simulations of catenary action through four examples revealed that the global behavior of the one-dimensional beam element model is close to that corresponding to the two-dimensional solid or the three-dimensional shell models. The comparison of simulation results before and after strengthening highlighted the effectiveness of the retrofitting scheme proposed in the companion paper (Liu, 2010a).

Alashker et al. (2011) studied the effect of some commonly employed approximations in collapse modelling by using four different types of models. The models were built in LS-DYNA (Hallquist, 2005) based on a 10-storey seismically designed steel building. Model M1 is a detailed micromodel of the full 3D system; Model M2 is the full 3D system composed of macroelements for beams, columns, connections and shell elements for the slab; Model M3 is a 2D micromodel of a single frame in the system; and model M4 is the macromodel of model M3. After model validation, the ability of all four models to predict collapse response was compared using the APM. Comparison between M1/M2 and M3/M4 showed that both macro and micromodels produced similar responses, and well calibrated macromodels can be relied on for accuracy when modelling progressive collapse. But a key conclusion drawn from this study is that significant computational benefits can be gained by using the macromodels such as M2 or M4. For example, model M1 took 208,564 seconds (58 hours) with 766,935 elements, while model M2 took only 903 seconds (15 minutes) with 62,554 elements. The latter was much more computationally efficient.

From these comparative studies, it is concluded that appropriate macromodels can be executed rapidly without loss of accuracy, facilitating implementation in models of entire structural systems. Therefore, when only the global progressive collapse response of the structure is examined, macromodelling is a better choice. iAEM is promising for efficient and accurate progressive collapse simulation.

However, currently there are limitations in iAEM. Firstly, it is limited to analyse idealized steel structures without considering the effects of residual stresses and geometric imperfections. These imperfections cannot be ignored in real steel structures, as they have considerable implications on the resistance and stability of the structures. Furthermore, iAEM currently assumes rigid connection in the modelling, yet the real connection behavior is semi-rigid, which affects the ultimate capacity of the structures. In addition, under the macromodel framework there has been no application of iAEM in reinforced concrete shear walls which are often needed for lift cores and stairwells and are used to enhance the lateral resistance of the building. Therefore, in order to conduct efficient and accurate progressive collapse of steel-frame RC-shear wall structures using iAEM method, further developments are essential to include the effects of imperfections, semi-rigid connection behavior and macromodelling of shear walls.

1.6.5 Summary

There are three main families of numerical methods to simulate progressive collapse, i.e. finite element method (FEM), discrete element method (DEM), and applied element method (AEM). With these methods, both macromodels and micromodels can be constructed to simulate progressive collapse. The macromodel-based improved AEM (iAEM) is able to model the whole process of progressive collapse with high efficiency and reliable accuracy. However, this method currently is limited to analyse idealized steel structures without considering initial material and geometric imperfections, and semi-rigid connection behavior. In addition, there is no published application of this method in modelling the RC shear walls. Therefore, it is essential to develop such features in iAEM in order to perform efficient and realistic progressive collapse analysis.

2 Benchmark Examples of Improved Applied Element Method

In the previous chapter, the theoretical background of the conventional AEM and main features of iAEM is briefly introduced. In this chapter, firstly, the element formulation of iAEM is presented. Subsequently, the solution techniques for both static and dynamic nonlinear analysis used by iAEM are described. Finally, capability of the iAEM is demonstrated through some benchmark examples from the simple first-order elastic static analysis to second-order inelastic dynamic analysis.

2.1 Improved applied element method

2.1.1 Element formulation

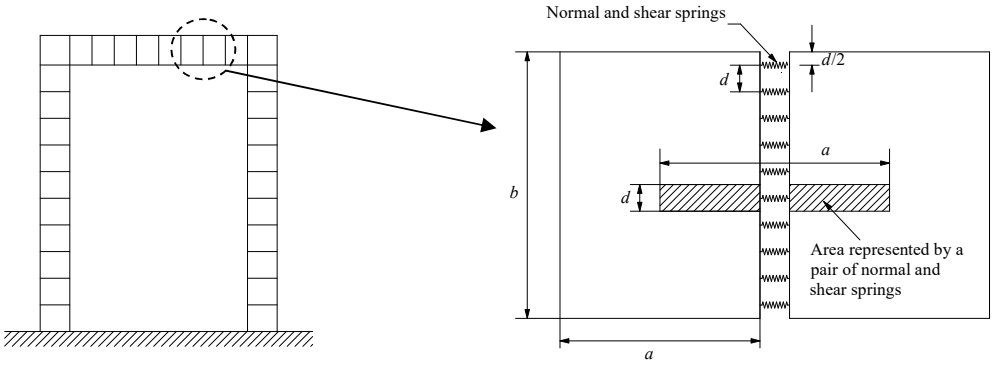

(a) Element generation for iAEM (b) Spring distribution

Figure 2-1 Modelling of structure using iAEM

Based on the conventional AEM, the iAEM was developed by Elkholy (2004) to simulate the progressive collapse behavior of large-scale steel frames under earthquake and fire scenarios. Compared with the conventional AEM, the main feature of iAEM is that it uses macromodelling technique to model beams and

columns. This achieves significant reduction of element number in the model, making structural collapse analysis much more efficient with adequate accuracy. In iAEM, each beam column is divided virtually into a string of rigid elements which are connected by pairs of normal and shear springs that are distributed along the element edges (see Figure 2-1). Each pair of springs totally represents stress and deformation of a certain area (hatched area in Figure 2-1(b)) of the studied elements. The springs carry the microscopic material properties, such as stiffness and yield strength. The spring stiffness is determined according to Equation (2-1).

$$K_n^i = \frac{E \cdot d \cdot T_n^i}{a};\ K_s^i = \frac{G \cdot d \cdot T_s^i}{a} \tag{2-1}$$

where

d is the distance between springs,

a is the length of the representative area,

E and G are Young's modulus and shear modulus of the material, respectively,

T_n^i and T_s^i are the thicknesses of the i^{th} pair of springs for normal and shear cases, respectively.

The variation in the values of thickness used in calculating the stiffness values of normal and shear springs owes to the change in effective area for both normal and shear directions. The ratio of T_n^i and T_s^i is assumed to be the ratio of the total area and effective shear area.

The above equation indicates that each spring represents the stiffness of an area of $d \cdot T_n^i$ (for normal spring) and $d \cdot T_s^i$ (for shear spring) with the length a of the studied material. Each of the elements has three DOFs in the 2D model. These DOFs represent the rigid body motion of the element. Although the element moves as a rigid body, its internal deformations are represented by the spring deformation around each element. This means each element shape does not change during analysis but the element assembly is deformable.

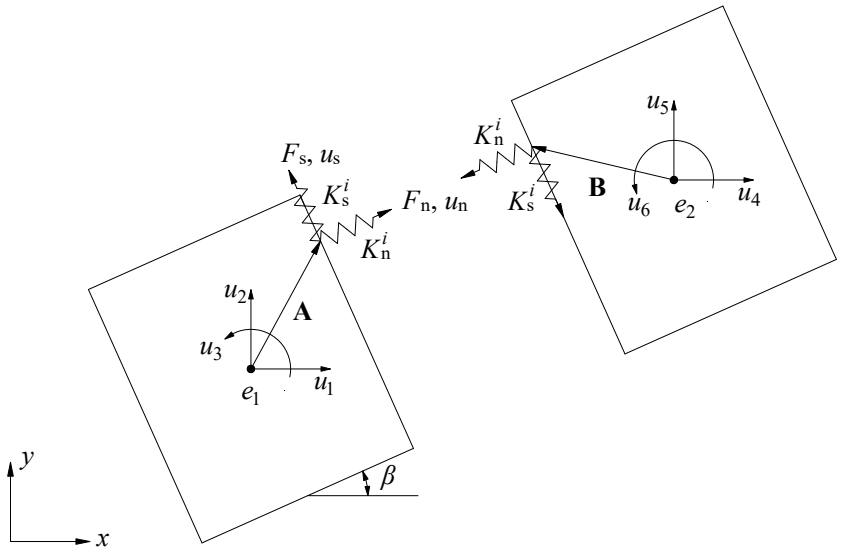

Figure 2-2 Parameters for the formulation of iAEM

To construct a general stiffness matrix, the locations of element and contact springs are assumed to be in a general position. The components of stiffness matrix corresponding to a certain DOF are the forces induced at the centroid of each element by a unit displacement in the direction of the studied DOF. The two elements shown in Figure 2-2 are assumed to be connected by the i^{th} pair of normal and shear springs for visualization purpose. The deformation of this pair of springs as a function of the element DOFs in the global coordinate system (GCS) is:

$$\begin{Bmatrix} u_x \\ u_y \end{Bmatrix} = \begin{Bmatrix} u_4 \\ u_5 \end{Bmatrix} - \begin{pmatrix} 1-\cos u_6 & \sin u_6 \\ -\sin u_6 & 1-\cos u_6 \end{pmatrix} \begin{Bmatrix} B_x \\ B_y \end{Bmatrix} - \begin{Bmatrix} u_1 \\ u_2 \end{Bmatrix} + \begin{pmatrix} 1-\cos u_3 & \sin u_3 \\ -\sin u_3 & 1-\cos u_3 \end{pmatrix} \begin{Bmatrix} A_x \\ A_y \end{Bmatrix} \tag{2-2}$$

where A_x, A_y, B_x and B_y are the x and y components of vectors $\mathbf{A} = \begin{Bmatrix} A_x & A_y \end{Bmatrix}^T$ and $\mathbf{B} = \begin{Bmatrix} B_x & B_y \end{Bmatrix}^T$, respectively, and vectors **A** and **B** are directed to the coordinates of i^{th} pair of springs from centroid of elements e_1 and e_2, respectively.

Considering the small deformation theory, i.e., $\sin\alpha = \alpha$ and $\cos\alpha = 1$, Equation (2-2) can be reduced to:

$$\begin{Bmatrix} u_x \\ u_y \end{Bmatrix} = \begin{Bmatrix} u_4 - u_6 B_y - u_1 + u_3 A_y \\ u_5 + u_6 B_x - u_2 - u_3 A_x \end{Bmatrix} \tag{2-3}$$

Written in the matrix form, Equation (2-3) becomes

$$\begin{Bmatrix} u_x \\ u_y \end{Bmatrix} = \mathbf{D} \begin{Bmatrix} u_1 \\ u_2 \\ u_3 \\ u_4 \\ u_5 \\ u_6 \end{Bmatrix} \tag{2-4}$$

where $\mathbf{D} = \begin{pmatrix} -1 & 0 & A_y & 1 & 0 & -B_y \\ 0 & -1 & -A_x & 0 & 1 & B_x \end{pmatrix}$.

Then, the deformation of the i^{th} pair of springs in the local coordinate system (LCS) can be expressed by

$$\begin{Bmatrix} u_n \\ u_s \end{Bmatrix} = \mathbf{T} \begin{Bmatrix} u_x \\ u_y \end{Bmatrix} \tag{2-5}$$

where $\mathbf{T} = \begin{pmatrix} \cos\beta & \sin\beta \\ -\sin\beta & \cos\beta \end{pmatrix}$ and β is the angle between LCS and GCS assuming anticlockwise is positive.

The normal and shear forces of the pair of springs then can be calculated by

$$\begin{Bmatrix} F_n \\ F_s \end{Bmatrix} = \mathbf{k} \begin{Bmatrix} u_n \\ u_s \end{Bmatrix} \tag{2-6}$$

where $\mathbf{k} = \begin{pmatrix} K_n^i & 0 \\ 0 & K_s^i \end{pmatrix}$ and K_n^i and K_s^i are the normal and shear stiffnesses of the i^{th} pair of springs, respectively.

In order to balance the normal and shear forces at the location of the i^{th} pair of springs, the forces developed at the centroid of the elements can be obtained by

$$\begin{Bmatrix} f_1 \\ f_2 \\ f_3 \\ f_4 \\ f_5 \\ f_6 \end{Bmatrix} = \mathbf{L} \begin{Bmatrix} F_n \\ F_s \end{Bmatrix} \tag{2-7}$$

where $\mathbf{L} = \begin{pmatrix} -\cos\beta & \sin\beta \\ -\sin\beta & -\cos\beta \\ -A_x \sin\beta + A_y \cos\beta & -A_x \cos\beta - A_y \sin\beta \\ \cos\beta & -\sin\beta \\ \sin\beta & \cos\beta \\ B_x \sin\beta - B_y \cos\beta & B_x \sin\beta + B_y \cos\beta \end{pmatrix}$.

Finally, the relationship between the force and displacement can be expressed as

$$\begin{Bmatrix} f_1 \\ f_2 \\ f_3 \\ f_4 \\ f_5 \\ f_6 \end{Bmatrix} = \mathbf{LkTD} \begin{Bmatrix} u_1 \\ u_2 \\ u_3 \\ u_4 \\ u_5 \\ u_6 \end{Bmatrix} \tag{2-8}$$

The stiffness matrix is therefore

$$\mathbf{K} = \mathbf{LkTD} \tag{2-9}$$

$$\mathbf{K}_1 = \begin{pmatrix} K_{11} & K_{12} & K_{13} \\ \vdots & K_{22} & K_{23} \\ sym. & \cdots & K_{33} \end{pmatrix} \tag{2-10}$$

where

$\mathbf{K}_1$ is the upper left quarter of stiffness matrix $\mathbf{K}$,

$K_{11} = K_n^i \cos^2\beta + K_s^i \sin^2\beta$,

$K_{12} = \left(K_n^i - K_s^i\right)\sin\beta\cos\beta$,

$$K_{13} = K_n^i \cos\beta\left(A_x \sin\beta - A_y \cos\beta\right) - K_s^i \sin\beta\left(A_x \cos\beta + A_y \sin\beta\right),$$

$$K_{22} = K_n^i \sin^2\beta + K_s^i \cos^2\beta,$$

$$K_{23} = K_n^i \sin\beta\left(A_x \sin\beta - A_y \cos\beta\right) + K_s^i \cos\beta\left(A_x \cos\beta + A_y \sin\beta\right),$$

$$K_{33} = K_n^i \left(A_x \sin\beta - A_y \cos\beta\right)^2 + K_s^i \left(A_x \cos\beta + A_y \sin\beta\right)^2.$$

It is clear that the stiffness matrix depends on the contact spring stiffness and the spring location. The stiffness matrix in Equation (2-9) is for only one pair of contact springs. However, the global stiffness matrix is determined by summing up the stiffness contributions of individual pair of springs around each element. Consequently, the developed stiffness matrix has total effects from all pairs of springs, according to the stress situation around the element (Meguro and Tagel-Din, 2001).

2.1.2 Material models

As fragmentation process of the structure is not modelled in this study, it is assumed that normal and shear springs do not fail or break even when they undergo very large deformations. In iAEM, normal spring and shear spring are uncoupled, and independent stress-strain models are used without considering the influence on each other. The material models of reinforcement and concrete for modelling the reinforced concrete shear walls are presented in Chapter 5.

2.1.2.1 Normal spring

The material model employed for the normal spring in this chapter, unless specifically noted, is the uniaxial bilinear stress-strain model with kinematic strain hardening (see Figure 2-3), where E is the initial modulus of elasticity, f_y is the yield strength and μ is the strain hardening ratio. This model can capture the principal characteristics of the steel material under cyclic loadings, and it is convenient for programming. If unloading occurs before hardening, E is used as

loading or unloading stiffness and the Bauschinger effect is ignored, but if unloading occurs after hardening, E is used as unloading stiffness and the Bauschinger effect is considered.

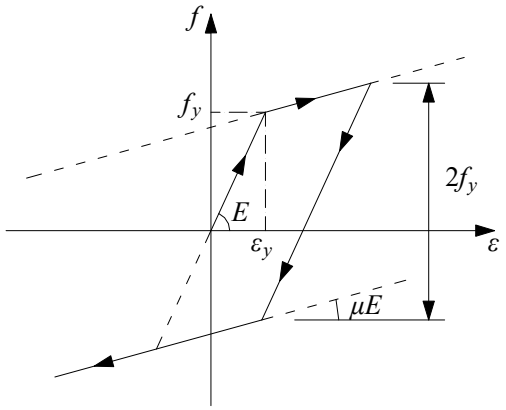

Figure 2-3 Bilinear kinematic model for normal spring

2.1.2.2 Shear spring

For simplification, the shear spring utilizes the linear elastic model as shown in Figure 2-4. The shear deformation often is not dominant, and it can be much smaller than the bending deformation. The nonlinear shear stress-strain relationship has little influence on the structural behavior, and thus simplified linear behavior is adopted.

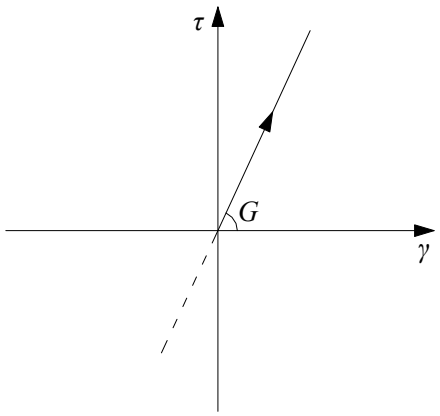

Figure 2-4 Linear elastic model for shear spring

2.1.3 Algorithm for geometric nonlinearity analysis

In iAEM, the algorithm for geometric nonlinearity (or large displacement) analysis introduced by Meguro and Tagel-Din (2002) is adopted. The basic idea of the algorithm is to add two vectors $\Delta\mathbf{R}_m$ and $\Delta\mathbf{R}_G$ to the general equations of motion in both static and dynamic loading cases, where $\Delta\mathbf{R}_m$ represents the residual force vector due to cracking and incompatibility between strain and stress of each spring, and $\Delta\mathbf{R}_G$ represents the residual force vector due to geometrical changes in structure during loading. Equation (2-11) shows the new equations of motion in the static loading case:

$$\mathbf{K}\Delta\mathbf{U} = \Delta\mathbf{f} + \Delta\mathbf{R}_m + \Delta\mathbf{R}_G \tag{2-11}$$

where

$\mathbf{K}$ is the nonlinear stiffness matrix,

$\Delta\mathbf{U}$ is the incremental displacement vector,

$\Delta\mathbf{f}$ is the incremental applied load vector.

For each incremental step, Equation (2-11) is solved in an iterative way as follows:

1) In the first iterative step, $\Delta\mathbf{R}_m$ and $\Delta\mathbf{R}_G$ are assumed to be null, Equation (2-11) is solved to get $\Delta\mathbf{U}$.
2) Update the structural geometry according to the calculated incremental displacements.
3) Modify the direction of the spring force vectors according to the new element configuration.
4) Verify whether cracking has occurred and calculate $\Delta\mathbf{R}_m$. In this study, as the springs will not fail, $\Delta\mathbf{R}_m$ is zero.
5) Calculate the element force vector $\mathbf{R}_m$ by summing the forces of the springs around each element.

6) Calculate geometrical residuals using Equation (2-12):

$$\Delta \mathbf{R}_G = \mathbf{f}(t) - \mathbf{R}_m \tag{2-12}$$

where $\mathbf{f}(t)$ is the applied force vector. $\Delta \mathbf{R}_G$ accounts for incompatibility between the externally applied forces and internal forces due to modification of the structure's geometry.

7) Calculate the stiffness matrix for the structure with the new configuration considering stiffness changes due to cracking or yielding.
8) Repeat the entire iterative process till convergence is reached for this incremental step.

2.2 Solution strategies for nonlinear analysis

With the element formulation and material constitutive models of the iAEM presented in the previous section, static and dynamic solution techniques can be employed to solve nonlinear static and dynamic problems respectively, as described in this section.

2.2.1 The nonlinear static problem

Various incremental-iterative numerical schemes can be implemented for the nonlinear static problems. Two of the most widely-used schemes, i.e. load control and displacement control with Newton-Raphson iteration, are used in this thesis by means of iAEM.

2.2.1.1 Load control

The basic equations to be solved in nonlinear static analysis are, at time $t + \Delta t$,

$$^{t+\Delta t}\mathbf{F} - {}^{t+\Delta t}\mathbf{R} = 0 \tag{2-13}$$

where

${}^{t+\Delta t}\mathbf{F}$ are the externally applied loads at the centroid of iAEM elements,

${}^{t+\Delta t}\mathbf{R}$ are the forces at the centroid of iAEM elements that are equivalent to the element stresses.

Iterations should be carried out to solve Equation (2-13) since ${}^{t+\Delta t}\mathbf{R}$ depends nonlinearly on the nodal point displacements. In the load control method, the Newton-Raphson iteration is carried out within each load step (or increment), and the iteration loop is shown below.

For $i = 1, 2, 3, \ldots$

$$\Delta\mathbf{R}^{(i-1)} = {}^{t+\Delta t}\mathbf{F} - {}^{t+\Delta t}\mathbf{R}^{(i-1)} \tag{2-14}$$

$${}^{t+\Delta t}\mathbf{K}^{(i-1)}\Delta\mathbf{U}^{(i)} = \Delta\mathbf{R}^{(i-1)} \tag{2-15}$$

$${}^{t+\Delta t}\mathbf{U}^{(i)} = {}^{t+\Delta t}\mathbf{U}^{(i-1)} + \Delta\mathbf{U}^{(i)} \tag{2-16}$$

with $${}^{t+\Delta t}\mathbf{U}^{(0)} = {}^{t}\mathbf{U}; \qquad {}^{t+\Delta t}\mathbf{R}^{(0)} = {}^{t}\mathbf{R} \tag{2-17}$$

where

$\Delta\mathbf{R}^{(i-1)}$ are the out-of-balance (residual) forces,

${}^{t+\Delta t}\mathbf{K}^{(i-1)}$ is the current tangent stiffness matrix,

$\Delta\mathbf{U}^{(i)}$ are the displacement increments,

${}^{t+\Delta t}\mathbf{U}^{(i)}$ are the current displacements.

These equations are obtained by linearizing the response of the structural system about the conditions at time $t+\Delta t$, iteration $(i-1)$. In each iteration, the out-of-balance forces are calculated using Equation (2-14), and then an increment in displacements is obtained by Equation (2-15). The iteration is continued until the out-of-balance forces $\Delta\mathbf{R}^{(i-1)}$ or the displacement increments $\Delta\mathbf{U}^{(i)}$ are sufficiently small. The process of solution strategy is illustrated in Figure 2-5.

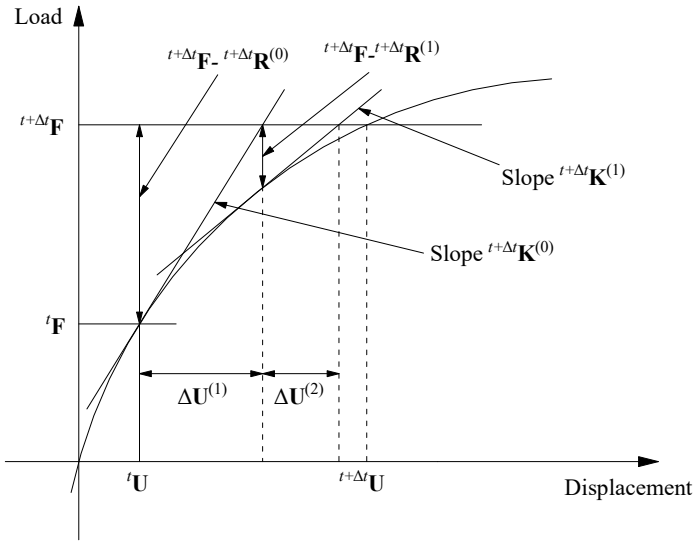

Figure 2-5 Solution process of load control with Newton-Raphson iteration (Bathe, 1996)

2.2.1.2 Displacement control

Apart from load control method, displacement control method is adopted in iAEM to trace the nonlinear load displacement paths where there is a load decrease due to structural behaviors such as snap-through, or buckling etc. The basic idea of displacement control method is to introduce a load multiplier that increases or decreases the intensity of the applied loads, so as to obtain fast convergence in each load step, in order to traverse the collapse point and evaluate the post collapse response. In this study, the displacement control scheme with Newton-Raphson iteration proposed by Batoz and Dhatt (1979) is adopted and their algorithms are presented below.

Suppose that a solution corresponding to a load level $^{t}\lambda$ at time t has been obtained. Let this solution correspond to the initial solution at time $t+\Delta t$, i.e.

$$^{t+\Delta t}\lambda^{(0)} = {}^{t}\lambda \quad \text{and} \quad {}^{t+\Delta t}\mathbf{U}^{(0)} = {}^{t}\mathbf{U} \tag{2-18}$$

The q^{th} component of ${}^{t+\Delta t}\mathbf{U}^{(0)}$ is increased by ΔU_q, thus the initial solution vector is redefined as

$$ {}^{t+\Delta t}\mathbf{U}^{(0)} = {}^{t}\mathbf{U} \text{ where } {}^{t+\Delta t}U_q^{(0)} = {}^{t+\Delta t}U_q^{(0)} + \Delta U_q \tag{2-19} $$

For the i^{th} iteration, a Newton-Raphson iteration is employed to obtain ${}^{t+\Delta t}\mathbf{U}^{(i)}$ and ${}^{t+\Delta t}\lambda^{(i)}$ with $U_q^{(i)}$ considered as fixed ($\Delta U_q^{(i)} = 0$), and the basic equations to be solved are

$$ {}^{t+\Delta t}\mathbf{K}^{(i-1)}\Delta\mathbf{U}^{(i)} = \Delta\mathbf{F}^{(i)} \tag{2-20} $$

where $\Delta\mathbf{F}^{(i)}$ are the force increments for the i^{th} iteration.

The load increment i^{th} is composed of two components, i.e.

$$ \Delta\mathbf{F}^{(i)} = \Delta\mathbf{R}^{(i)} + \Delta\lambda^{(i)}\mathbf{P} \tag{2-21} $$

where

$\Delta\mathbf{R}^{(i)}$ is the residue vector with $\Delta\mathbf{R}^{(i)} = {}^{t+\Delta t}\lambda^{(i-1)}\mathbf{P} - {}^{t+\Delta t}\mathbf{R}^{(i-1)}$,

$\Delta\lambda^{(i)}$ is the load factor increment,

$\mathbf{P}$ is the applied basic load vector.

Therefore, Equation (2-20) can be decomposed into

$$ \begin{aligned} {}^{t+\Delta t}\mathbf{K}^{(i-1)}\Delta\mathbf{U}^{a(i)} &= \Delta\mathbf{R}^{(i)} \\ \Delta\lambda^{(i)}\,{}^{t+\Delta t}\mathbf{K}^{(i-1)}\mathbf{U}^{b(i)} &= \Delta\lambda^{(i)}\mathbf{P} \end{aligned} \tag{2-22} $$

where

$\Delta\mathbf{U}^{a(i)}$ is the displacement increment due to $\Delta\mathbf{R}^{(i)}$,

$\mathbf{U}^{b(i)}$ are the displacements due to $\mathbf{P}$.

The displacement increment is thus

$$ \Delta\mathbf{U}^{(i)} = \Delta\mathbf{U}^{a(i)} + \Delta\lambda^{(i)}\mathbf{U}^{b(i)} \tag{2-23} $$

$$ \Delta U_q^{(i)} = \Delta U_q^{a(i)} + \Delta\lambda^{(i)}U_q^{b(i)} = 0 \tag{2-24} $$

Therefore,

$$\Delta\lambda^{(i)} = -\Delta U_q^{a(i)} / U_q^{b(i)} \; \Delta\lambda^{(i)} = -\Delta U_q^{a(i)} / U_q^{b(i)} \tag{2-25}$$

and

$$\begin{aligned} {}^{t+\Delta t}\mathbf{U}^{(i)} &= {}^{t+\Delta t}\mathbf{U}^{(i-1)} + \Delta\mathbf{U}^{(i)} \\ {}^{t+\Delta t}\lambda^{(i)} &= {}^{t+\Delta t}\lambda^{(i-1)} + \Delta\lambda^{(i)} \end{aligned} \tag{2-26}$$

The algorithms are summarized as follows. For each cycle:

3 Choose an incremental displacement component ΔU_q at iteration level $i = 1$.

4 Modify the initial displacement vector ${}^{t+\Delta t}\mathbf{U}^{(0)}$ such that ${}^{t+\Delta t}U_q^{(0)} = {}^{t+\Delta t}U_q^{(0)} + \Delta U_q$.

5 Calculate the residue vector $\Delta\mathbf{R}^{(i)}$ and tangent matrix ${}^{t+\Delta t}\mathbf{K}^{(i-1)}$.

6 Using equations (2-22) to solve for $\Delta\mathbf{U}^{a(i)}$ and $\mathbf{U}^{b(i)}$ simultaneously.

7 From equations (2-25) and (2-26), calculate ${}^{t+\Delta t}\mathbf{U}^{(i)}$ and ${}^{t+\Delta t}\lambda^{(i)}$.

8 Repeat steps 3-5 until a desired accuracy is achieved.

2.2.2 The nonlinear dynamic problem

For the nonlinear dynamic analysis, the Newmark's constant-average-acceleration method (also called trapezoidal rule) together with the Newton-Raphson iteration is adopted in this study using iAEM. Using the implicit time integration, the governing equilibrium equations of the system at the i^{th} iteration at time $t + \Delta t$ are:

$$\mathbf{M}\,{}^{t+\Delta t}\ddot{\mathbf{U}}^{(i)} + \mathbf{C}\,{}^{t+\Delta t}\dot{\mathbf{U}}^{(i)} + {}^{t+\Delta t}\mathbf{K}^{(i-1)}\Delta\mathbf{U}^{(i)} = {}^{t+\Delta t}\mathbf{F} - {}^{t+\Delta t}\mathbf{R}^{(i-1)} \tag{2-27}$$

$${}^{t+\Delta t}\mathbf{U}^{(i)} = {}^{t+\Delta t}\mathbf{U}^{(i-1)} + \Delta\mathbf{U}^{(i)} \tag{2-28}$$

where

$\mathbf{M}$ is the mass matrix,

$\mathbf{C}$ is the damping matrix,

${}^{t+\Delta t}\ddot{\mathbf{U}}^{(i)}$ is the acceleration vector,

${}^{t+\Delta t}\dot{\mathbf{U}}^{(i)}$ is the velocity vector.

Using the trapezoidal rule of time integration, the following assumptions are employed:

$$ {}^{t+\Delta t}\mathbf{U} = {}^{t}\mathbf{U} + \frac{\Delta t}{2}\left({}^{t}\dot{\mathbf{U}} + {}^{t+\Delta t}\dot{\mathbf{U}} \right) \tag{2-29} $$

$$ {}^{t+\Delta t}\dot{\mathbf{U}} = {}^{t}\dot{\mathbf{U}} + \frac{\Delta t}{2}\left({}^{t}\ddot{\mathbf{U}} + {}^{t+\Delta t}\ddot{\mathbf{U}} \right) \tag{2-30} $$

Using the relations in Equations (2-28) to (2-30), the ${}^{t+\Delta t}\ddot{\mathbf{U}}^{(i)}$ can be obtained as

$$ {}^{t+\Delta t}\ddot{\mathbf{U}}^{(i)} = \frac{4}{\Delta t^2}\left({}^{t+\Delta t}\mathbf{U}^{(i-1)} - {}^{t}\mathbf{U} + \Delta\mathbf{U}^{(i)} \right) - \frac{4}{\Delta t}{}^{t}\dot{\mathbf{U}} - {}^{t}\ddot{\mathbf{U}} \tag{2-31} $$

Substituting equation (2-31) into (2-27), the iterative equations in nonlinear dynamic analysis can be obtained.

For $i = 1, 2, 3, \ldots$

$$ \begin{aligned} \left(\frac{4}{\Delta t^2}\mathbf{M} + \frac{2}{\Delta t}\mathbf{C} + {}^{t+\Delta t}\mathbf{K}^{(i-1)} \right)\Delta\mathbf{U}^{(i)} = {}^{t+\Delta t}\mathbf{F} - {}^{t+\Delta t}\mathbf{R}^{(i-1)} \\ -\mathbf{M}\left(\frac{4}{\Delta t^2}\left({}^{t+\Delta t}\mathbf{U}^{(i-1)} - {}^{t}\mathbf{U} \right) - \frac{4}{\Delta t}{}^{t}\dot{\mathbf{U}} - {}^{t}\ddot{\mathbf{U}} \right) \\ -\mathbf{C}\left(\frac{2}{\Delta t}\left({}^{t+\Delta t}\mathbf{U}^{(i-1)} - {}^{t}\mathbf{U} \right) - {}^{t}\dot{\mathbf{U}} \right) \end{aligned} \tag{2-32} $$

2.2.3 Convergence criteria and re-solution strategy

In the analysis, iterations are continued until a convergence criterion based on the incremental displacements is satisfied at the end of each load or time step. The displacement convergence criterion is defined as:

$$ \frac{\left\| \Delta\mathbf{U}^{(i)} \right\|_2}{\left\| {}^{t+\Delta t}\mathbf{U} \right\|_2} \le \varepsilon_D \tag{2-33} $$

where ε_D is a displacement convergence tolerance.

The vector ${}^{t+\Delta t}\mathbf{U}$ is not known. The last calculated value ${}^{t+\Delta t}\mathbf{U}^{(i)}$ is used as an approximation to ${}^{t+\Delta t}\mathbf{U}$, and tolerance ε_D is set to be 10^{-4}.

A re-solution strategy is incorporated in the solution techniques described above. If convergence is not achieved within a reasonable number of iterations, the increment cutting is activated. The current step is restarted with a reduced increment size until an increment that satisfies convergence and complies with the applied displacement history is found.

2.2.4 Program composition

Flow chart of the nonlinear static analysis with load control in the study is shown in Figure 2-6. In the program, the element location and spring data is generated before the analysis. Spring stiffness matrices are assembled into the global stiffness matrix. Then the equilibrium path is followed by the load control method with the required convergence criteria. In the same way, the nonlinear static analysis with displacement control and nonlinear dynamic analysis with trapezoidal rule are implemented.

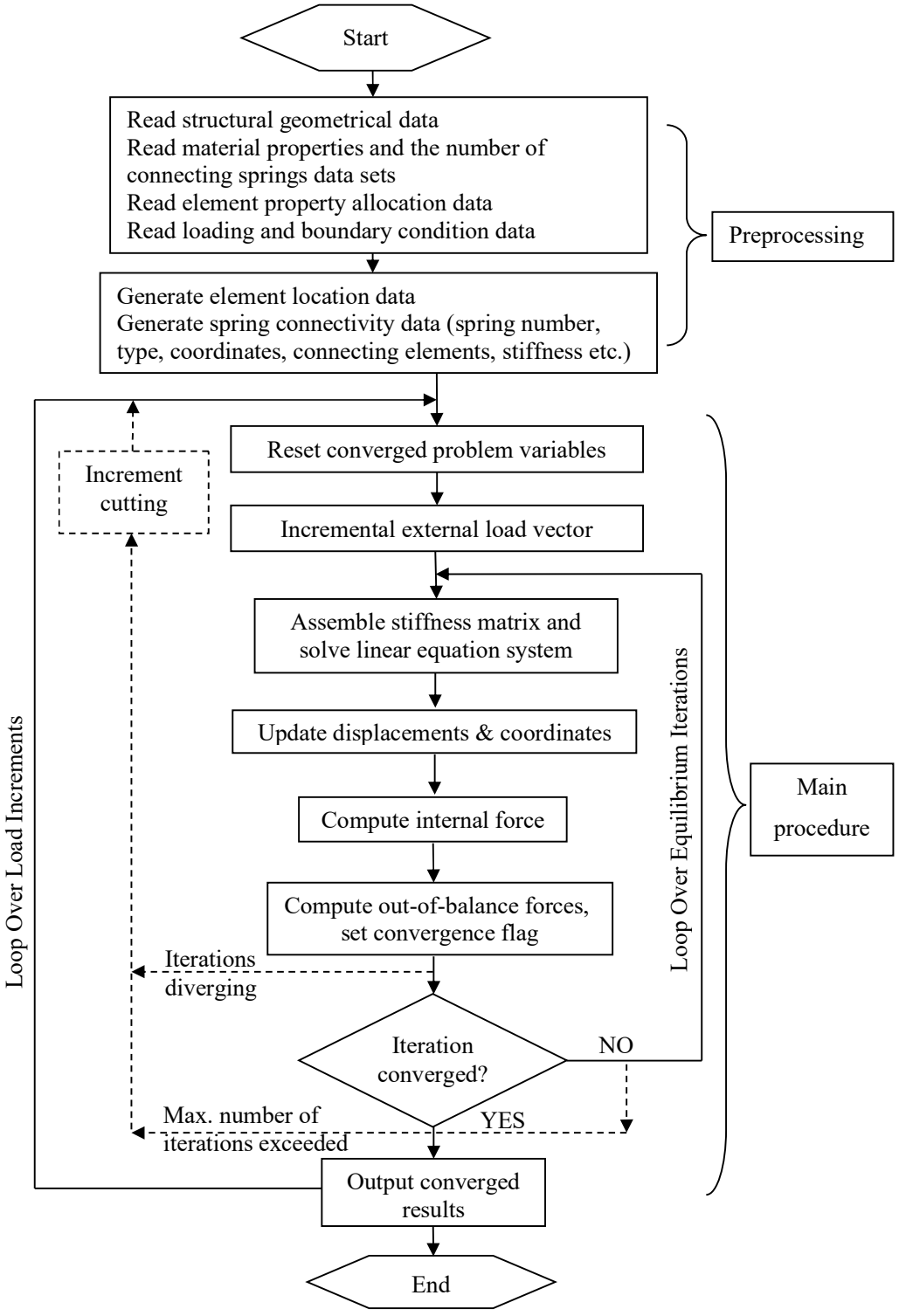

Figure 2-6 Flow chart of the program using load control

2.3 Benchmark examples

In this section, verification of the iAEM program is carried out through a series of benchmark examples in the nonlinear static or dynamic analysis. In each type of analysis, whether static or dynamic, four types of analyses are included, i.e. first-order elastic, first-order inelastic, second-order elastic and second-order inelastic analyses. For clarity, first-order herein means large displacement is not considered while second-order means large displacement is considered. The accuracy of the results produced by iAEM is validated by comparing with other sources, such as theoretical values, published results, or results from finite element analysis.

2.3.1 Static analysis of a tip-loaded cantilever column

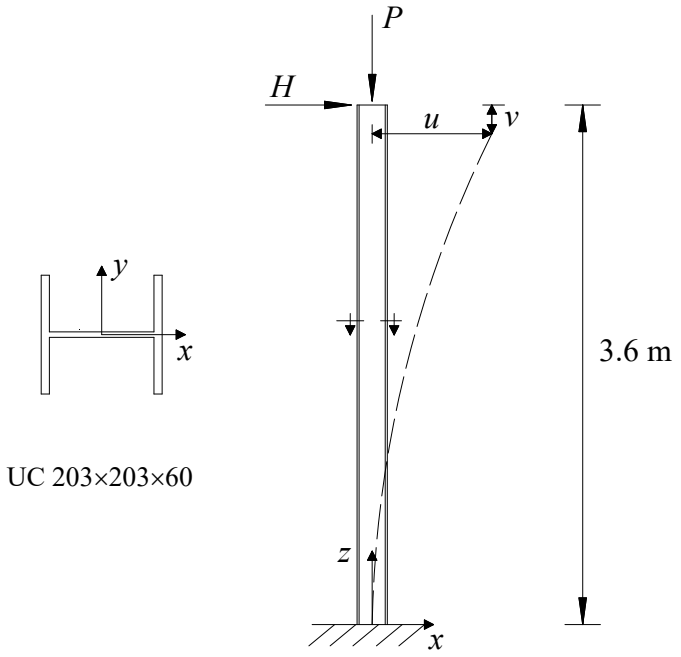

Figure 2-7 A tip-loaded cantilever column

A 3.6 m long cantilever column shown in Figure 2-7 is loaded at its tip by a horizontal load H and a vertical load P. Cross section of the column is UC203×203×60. The slenderness ratio $(2L)/r$ is 80. The elastic modulus of the

material is $E = 200$ GPa and the yield strength is $f_y = 250$ MPa. It can be obtained that the squash load of the column is $P_y = f_y A = 1887$ kN, and the elastic buckling load of the column is $P_{cr} = \left(\pi^2 EI\right)/\left(2L\right)^2 = 2306$ kN ($> P_y$). In the following analysis, the vertical load is varied at $P = 0$, $P = 0.1P_y$, $P = 0.2P_y$ and $P = 0.4P_y$.

8.1.2.1 First-order elastic analysis

For the first-order elastic analysis of the column, convergence study is carried out by varying the number of elements and connecting springs in the model, so that a reference mesh size can be adopted for modelling beams and columns using iAEM.

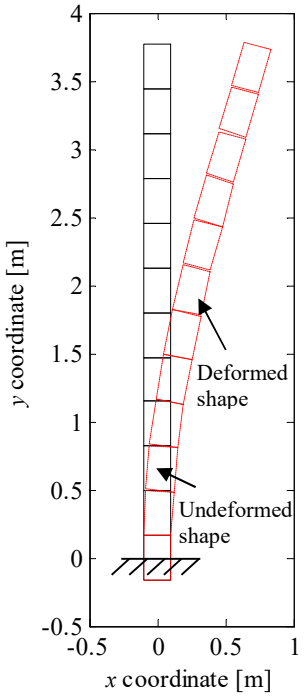

Figure 2-8 Deformed and undeformed shapes of the column (scale factor=15)

1) Varying the number of elements

In order to study the effect of number of elements on the column behavior, the number of normal and shear spring pairs connecting two adjacent elements is fixed as $nspr = 10$, i.e. 1 pair at each flange and 8 pairs at the web. In the modelling, initial

centroid coordinates of the bottom and top elements are located right at the bottom and top of the column, respectively (see Figure 2-8). $P = 0.2P_y = 377$ kN and $H = 50$ kN are used for the analysis.

The computed horizontal displacement u and vertical displacement v for different number of elements at the tip in the model are listed in Table 2-1. They are compared with the theoretical values u_t (= 65.49 mm) and v_t (= 0.9 mm) which are calculated according to the formulae below:

$$u_t = \frac{HL^3}{3EI} + \frac{HL}{A_s G} \tag{2-34}$$

$$v_t = \frac{PL}{EA} \tag{2-35}$$

where

E is the Young's modulus,

G is the shear modulus,

L is the column length,

I is the second moment of inertia,

A_s is the shear area,

A is total area of the cross section.

Table 2-1 Horizontal and vertical displacements at the tip with different number of elements

No. of elements	2	4	6	12	24	48	100
u (mm)	61.64	64.66	65.22	65.56	65.64	65.66	65.67
Error of u (%)	-5.87	-1.26	-0.41	0.11	0.24	0.27	0.28
v (mm)	0.9	0.9	0.9	0.9	0.9	0.9	0.9
Error of v (%)	0	0	0	0	0	0	0

As shown in Table 2-1, it can be seen that the vertical displacement v is the same as the theoretical value, but the horizontal displacement u converges to theoretical value

with an error of 0.28% when 100 elements are used. This is because vertical displacement is determined from the exact representation of the column axial stiffness contributed from the normal springs across the section, while the horizontal displacement due to flexure is determined from the inexact representation of the column flexural stiffness. In this case, the second moment of inertia contributed discretely from the normal springs across the section is $I_{spr} = \sum A_i y_i^2 = 6.0377 \times 10^{-5}$ m^4 which is 0.28% smaller than that of the real section $I_{real} = 6.0548 \times 10^{-5}$ m^4. Since the horizontal displacement is predominated by the flexural behavior, it will be 0.28% larger than the theoretical one. It can be also seen that when 6 elements are used for this column, the error of the calculated horizontal displacements is already less than 1%, which indicates that 6 elements are sufficient for the first-order elastic static analysis.

2) Varying the number of spring pairs

In order to study the effect of number of spring pairs connecting two adjacent elements on the column behavior, the number of elements is fixed as $nel = 6$. $P = 0$ and $H = 50$ kN are used in this case. The number of spring pairs consists of the number of spring pairs at the two flanges and that at the web, and in each flange or web, the spring pairs are uniformly distributed.

Table 2-2 Horizontal displacements at the tip with different number of web spring pairs and total spring pairs

No. of spring pairs/flange	1	1	1	1	1	1	1
No. of web spring pairs	**2**	**4**	**6**	**8**	**18**	**38**	**98**
Total no. of spring pairs	4	6	8	10	20	40	100
u (mm)	66.40	65.45	65.28	65.22	65.16	65.15	65.15
Error of u (%)	1.39	-0.05	-0.31	-0.41	-0.50	-0.52	-0.52

Table 2-3 Horizontal displacements at the tip with different number of flange spring pairs and total spring pairs

No. of web spring pairs	8	8	8	8	8	8
No. of spring pairs/flange	**1**	**2**	**4**	**8**	**16**	**46**
Total no. of spring pairs	10	12	16	24	40	100
u (mm)	65.22	65.14	65.12	65.12	65.12	65.12
Error of u (%)	-0.41	-0.52	-0.55	-0.56	-0.56	-0.56

In the analysis, first it is assumed that there is only one pair of springs per flange, and the number of web spring pairs is increased. The horizontal displacements at the tip with different number of web spring pairs and total number of spring pairs are listed in Table 2-2. Then it is assumed that there are eight pairs of web springs, and the number of spring pairs per flange is increased. The horizontal displacements at the tip with different number of flange spring pairs and total number of spring pairs are listed in Table 2-3. According to these two tables, it can be seen that with the increase of number of either web or flange spring pairs, the horizontal displacement at the tip converges to 65.15 mm and 65.12 mm, respectively. When one spring pair per flange and eight web spring pairs are used in the model, the error of horizontal displacement at the tip is smaller than 0.5%. This kind of spring distribution for the first-order elastic analysis is deemed appropriate. It can be also noticed that when the total number of spring pairs is 40, the combination of 8 web and 32 flange spring pairs gives less error than the combination of 38 web and 2 flange spring pairs, that is because the contribution to the flexural stiffness are mainly from the flanges, for the combination with more flange springs, more accurate approximation of the flexural stiffness will be obtained, which results in more accurate displacement than the combination with less flange springs.

8.1.2.2 First-order inelastic analysis

In the first-order inelastic analysis, three load cases are considered with a fixed axial (or vertical) load P, i.e. $P = 0$, $P = 0.2P_y$ and $P = 0.4P_y$, and an increasing horizontal load H at the column tip. When $H =$ 50 kN, the load factor $\gamma = 1.0$. The material model is the bilinear stress-strain model with the strain hardening ratio of 1.5%.

Ten normal and shear spring pairs are used to connect the two adjacent elements in the iAEM model. When $P = 0$, the load factor versus horizontal displacement curves with different number of elements are plotted in Figure 2-9. The result from the finite element software SAP2000 is also plotted for comparison. In the SAP2000 model, the nonlinear fiber-section or plastic-zone model for frame analysis as proposed by Tay (2013) for efficient progressive collapse analysis is adopted. As recommended by Tay (2013), for the beam member with a length of L, the plastic zone length should be greater than $L/2$, while the element length within the plastic zone should be lesser than $L/24$. For this column, as the material yielding starts only from its bottom, six fiber-beam elements are used at the bottom of the column with a total of 1/4 column length, and six elastic beam elements are used for the rest of the column. According to Figure 2-9, it can be seen that with the increase of the horizontal load, the column behaves elastically until around $\gamma = 0.9$ when it begins to yield with a much gentler slope. It can also be seen that the load displacement curve converges with the increase of element number, and when 11 elements are used in the model, the load factor displacement curve already compares fairly well with the one from finite element analysis by SAP2000.

Therefore, the model with 11 elements is deemed appropriate for the first-order inelastic analysis, and it is also used for the other two load cases when $P = 0.2P_y$ and $P = 0.4P_y$. The load factor versus horizontal displacement curves with different axial

loads are shown in Figure 2-10. It can be seen that results from iAEM agrees well with those from SAP2000. It can also be found that, with the increase of axial load, the horizontal load factor of the column reduces significantly at the same horizontal displacement.

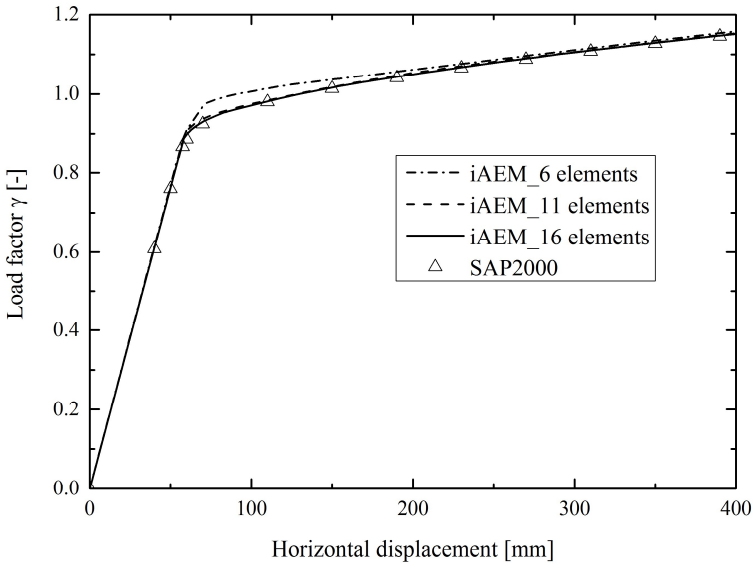

Figure 2-9 Load factor versus horizontal displacement curves with different number of elements

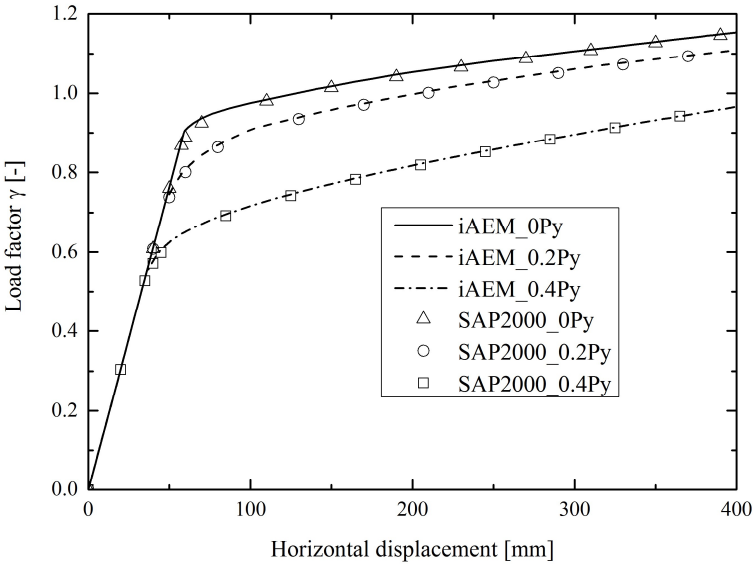

Figure 2-10 Load factor versus horizontal displacement curves with different axial loads

8.1.2.3 Second-order elastic analysis

For the second-order elastic analysis, the same three load cases in first-order inelastic analysis are used. When $P = 0$, the load factor versus horizontal displacement curves with different number of elements from iAEM analysis are plotted in Figure 2-11. The result from finite element analysis in SAP2000 is also plotted for comparison. Six elastic beam elements are used to model this column in SAP2000. From this figure, it can be seen that the load factor displacement curve converges with the increase of the element number, and when 6 iAEM elements are used in the model, the load factor-displacement curve compares very well with that from SAP2000 analysis. Therefore, only a few elements are needed in the second-order elastic analysis to capture the geometric nonlinearity behavior of the column using iAEM. 6 elements are then used for the other two load cases where $P = 0.2P_y$ and $P = 0.4P_y$. The load factor versus horizontal and vertical displacement curves with different axial loads are shown in Figure 2-12 and Figure 2-13, respectively. It can be seen that the curves from iAEM agree well with those from SAP2000. It can also be found that, with the increase of the axial load, the horizontal load factor of the column reduces significantly at the same horizontal displacement.

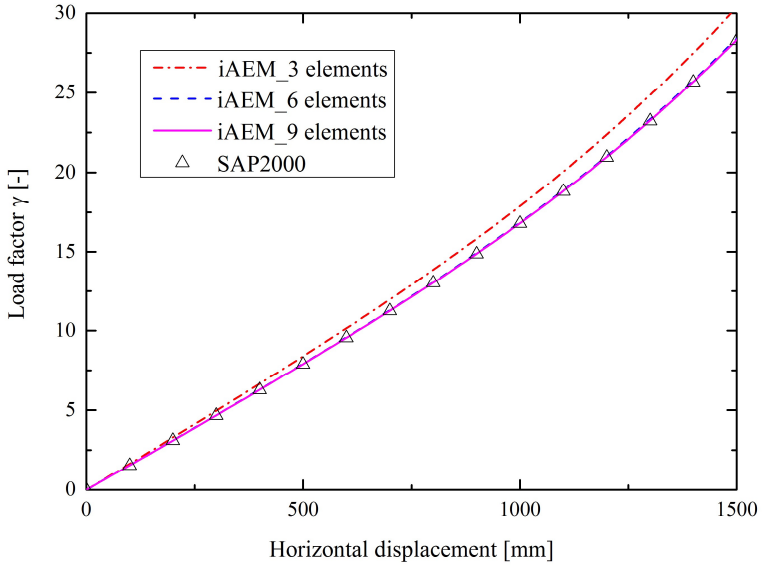

Figure 2-11 Load factor versus horizontal displacement curves with different number of elements

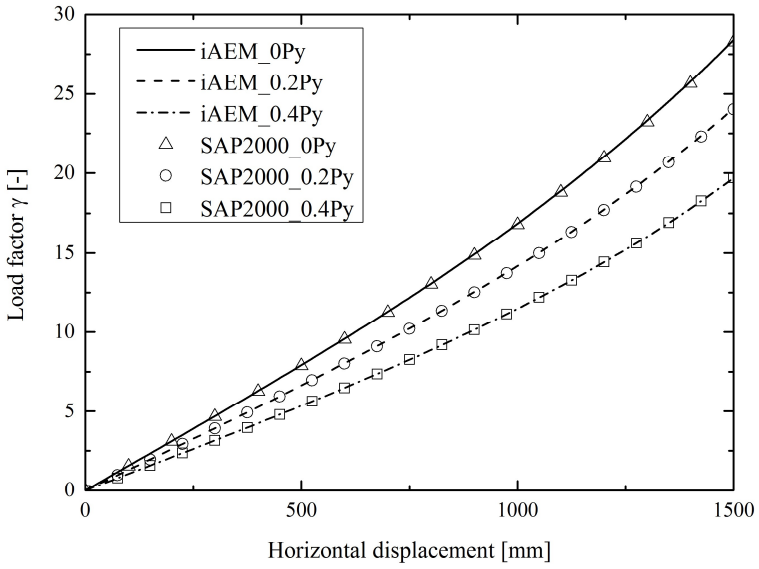

Figure 2-12 Load factor versus horizontal displacement curves with different axial loads

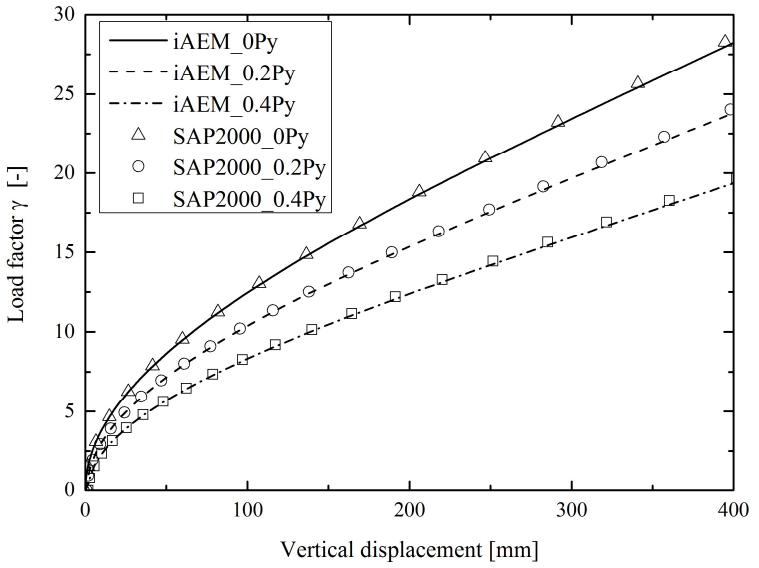

Figure 2-13 Load factor versus vertical displacement curves with different axial loads

8.1.2.4 Second-order inelastic analysis

In the second-order inelastic analysis, the fixed axial load P at the column tip for the three load cases are: $P = 0$, $P = 0.1P_y$ and $P = 0.2P_y$. When the load factor is $\gamma = 1.0$, the horizontal load at the column tip is $H = 50$ kN. The material model is the bilinear stress-strain model with the strain hardening ratio of 1.5%.

The load factor versus horizontal displacement curves with different number of iAEM elements are plotted in Figure 2-14. The result from the plastic-zone model proposed by Tay (2013) for efficient progressive collapse analysis in SAP2000 is also plotted. It can be seen that the load factor displacement curve converges with the increase of the element number, and when 11 elements are used in the model, the curve from iAEM compares very well with the one from SAP2000 analysis. Therefore, 11 elements are used for the other two load cases where $P = 0.1P_y$ and $P = 0.2P_y$, and the load factor versus horizontal and vertical displacement curves with different axial loads are shown in Figure 2-15 and Figure 2-16, respectively. According to these two figures, it can be seen that the load factor displacement curves from iAEM compare well with those from SAP2000. It can be also noticed that due to existence of the axial load, the horizontal load will first increase to a peak point, and then it decreases. The larger the axial load is, the smaller the horizontal load capacity of the column is and the faster the horizontal load after the peak point reduces.

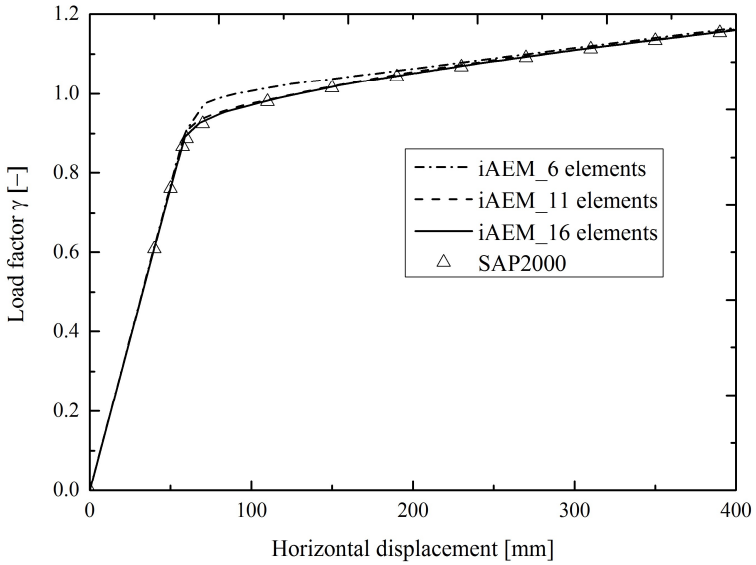

Figure 2-14 Load factor versus horizontal displacement curves with different number of elements

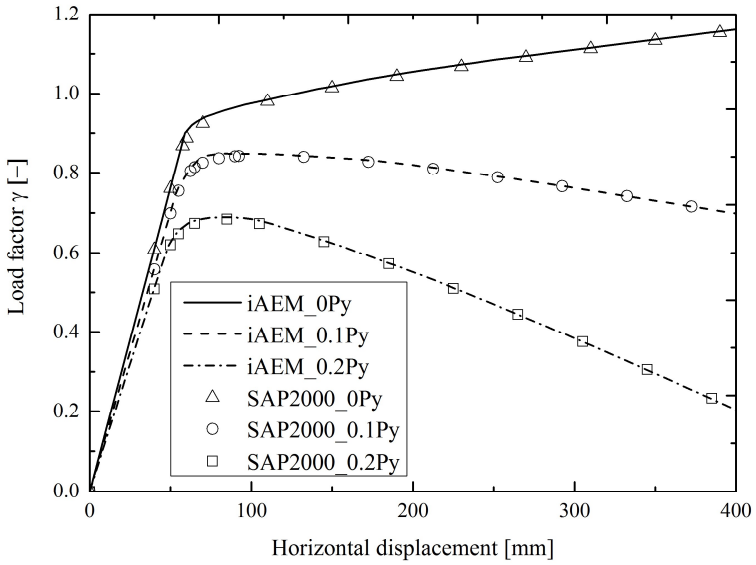

Figure 2-15 Load factor versus horizontal displacement curves with different axial loads

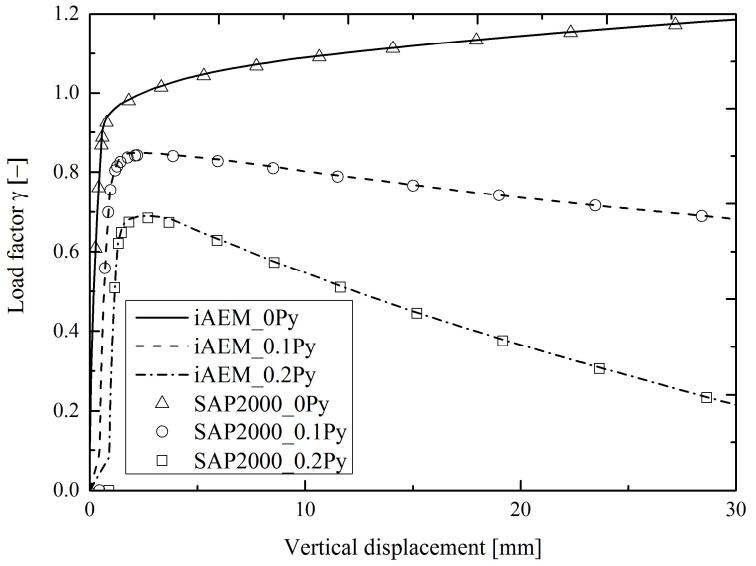

Figure 2-16 Load factor versus vertical displacement curves with different axial loads

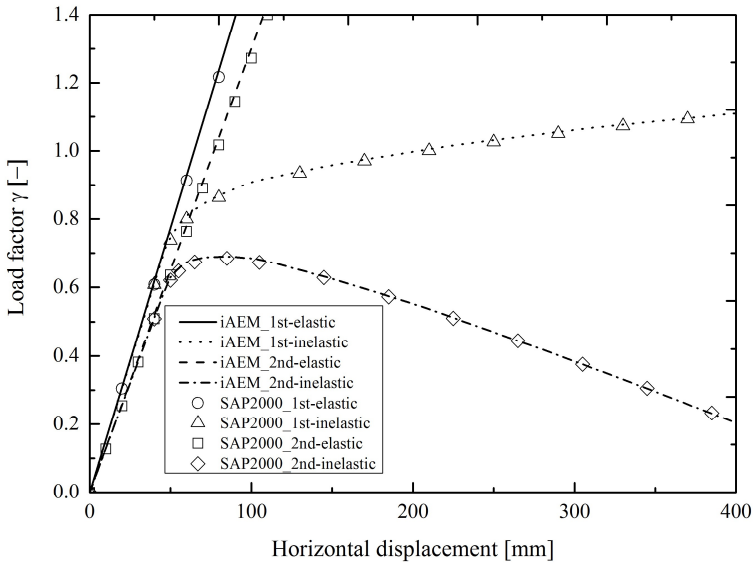

Figure 2-17 Load factor versus horizontal displacement curves in different levels of analysis

The load factor versus horizontal displacement curves from the four types of static analysis are plotted together in Figure 2-17. In this case, the axial load is $P = 0.2P_y$, and the horizontal load $H = 50$ kN at $\gamma = 1.0$. Strain hardening ratio of 1.5% for the bi-linear material model is used for the nonlinear material. According to Figure 2-17, it can be seen that slopes of the curves before material yielding in the first-order elastic and inelastic, or second-order elastic and inelastic analyses are the same, but the slope in the second-order-type analysis is smaller than that in the first-order-type analysis. This is because the geometric effect is accounted for in the former. It can also be seen that when material nonlinearity is considered, the horizontal load will increase at a slower rate (first-order inelastic) or even decrease due to column buckling (second-order inelastic) after material yielding. The difference between the curves of first-order elastic and second-order inelastic analyses is so significant that it is necessary to include both material and geometric nonlinearities in the analysis in order to simulate the real structural behavior.

2.3.2 Static analysis of a long-span steel beam

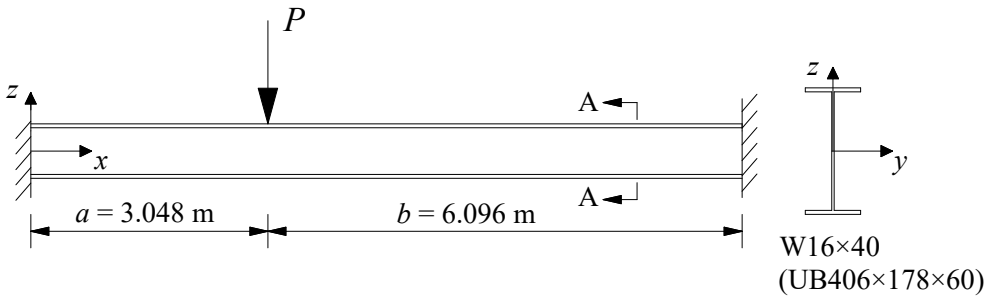

Figure 2-18 A long-span steel beam (Salmon and Johnson, 1996)

A 9.14 m (30 ft) long steel beam shown in Figure 2-18 is fixed at both ends. The cross section of the beam is the wide flange section W16×40 (equivalent UB 406×178×60), and it is loaded at 1/3 of its span. The beam has a modulus of elasticity of $E =$ 205 GPa (29,700 ksi) and yield strength is $f_y =$ 248 MPa (36 ksi).

8.1.2.5 First-order elastic analysis

In the first-order elastic analysis, the vertical load P is 20kN. In the iAEM model, initial centroid coordinates of the elements at the two ends are right located at the two ends of the beam (see Figure 2-19).

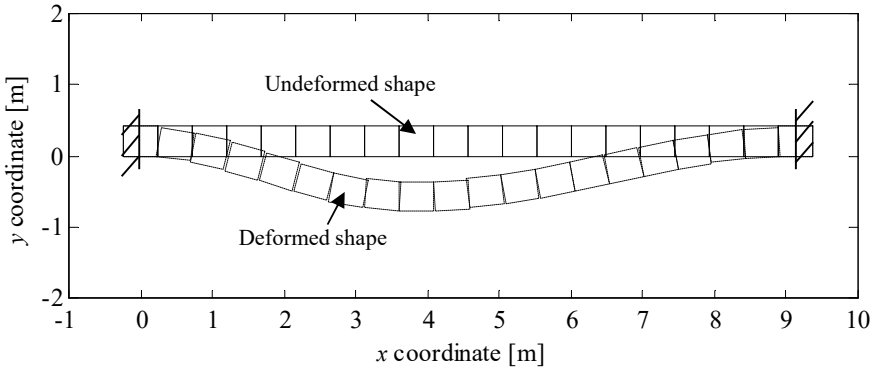

Figure 2-19 Undeformed and deformed shapes of the beam

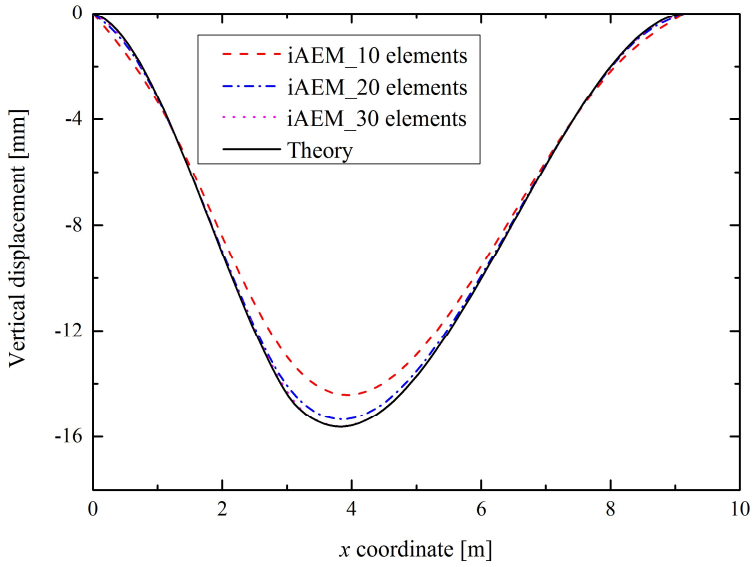

Figure 2-20 Vertical displacement distribution along the beam span

The vertical displacement distribution curves along the beam span with different number of elements are plotted in Figure 2-20 and they are compared with the theoretical vertical displacement calculated by the formula below:

when $x \le a$,

$$u_t = \frac{-Pb^2x^2(3aL-3ax-bx)}{6EIL^3} - \frac{2Px}{27}\frac{(10L^2-3Lx+2x^2)}{GA_sL^2}$$

when $x > a$, (2-36)

$$u_t = \frac{-Pa^2}{6EIL^3}(-(a+2b)Lx^2+(a+3b)x^3+3xL^3-aL^3)$$

$$-\frac{P}{27}\frac{(-7xL^2-6Lx^2+4x^3+9L^3)}{GA_sL^2}$$

According to Figure 2-20, it can be seen that with the increase of element number in the analysis, the deflection converges to the theoretical value, and the model with 20 elements produces sufficiently accurate results.

8.1.2.6 First-order inelastic analysis

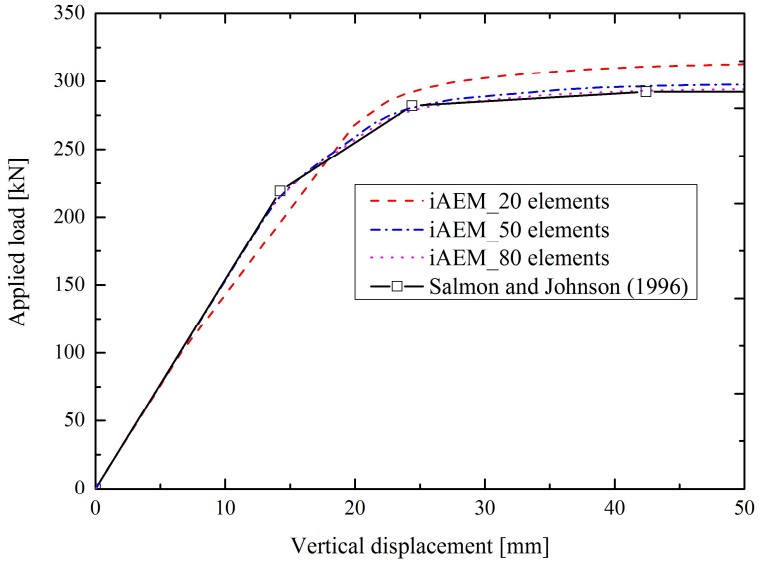

Figure 2-21 Applied load verses vertical displacement curves of the beam with different number of elements

For the first-order inelastic analysis, in order to compare the iAEM result with the theoretical one from the plastic analysis by Salmon and Johnson (1996), the material is assumed to be elastic-perfectly-plastic (EPP), and the shear deformation is excluded in the analysis by multiplying the shear modulus by 1000.

The applied load versus vertical displacement (at 1/3 span) curves with different number of elements using iAEM are plotted in Figure 2-21. The load displacement curve converges with the increase of the elements, and when 50 elements are used in the model, the iAEM result has already approached the result by Salmon and Johnson (1996). However, it should be noted that the curves from iAEM analysis are smooth while the theoretical curve is not. This is because the theoretical curve is obtained with the concentrated plastic hinge assumption but iAEM can realistically simulate the distributed plasticity along the beam span.

2.3.3 Snap-through of a two-bar truss system

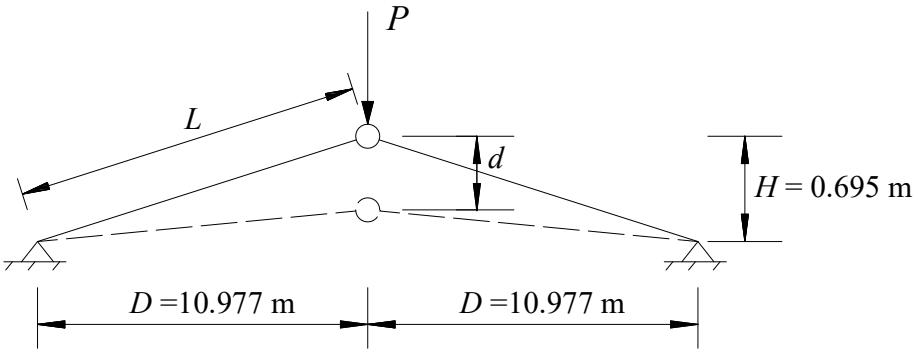

Figure 2-22 Two-bar truss system (Liew et al., 1997)

A two-bar truss system, shown in Figure 2-22, consists of square bars of 0.254 m × 0.254 m size with member slenderness ratio L/r of 150. The modulus of elasticity of the material is $E = 206$ GPa and yield strength is $f_y =$ 235 MPa. The truss supports are restrained against translations. The structure is subjected to a concentrated downward load P, applied at the crown joint resulting in compressive forces in both members (Liew et al., 1997). The truss system is analysed using iAEM for the second-order elastic analysis. Due to symmetry, only half of the structure is modelled. 11 elements are used in the model.

The theoretical relationship between the bar axial force S, applied load P and vertical displacement d at the crown joint can be obtained from Equations (2-37) and (2-38) in which the geometric parameters L, H and D are shown in Figure 2-22.

$$S = \frac{EA}{L}\left(L - \sqrt{D^2 + \left(H - d\right)^2}\right) \tag{2-37}$$

$$P = 2S\frac{\left(H - d\right)}{\sqrt{D^2 + \left(H - d\right)^2}} \tag{2-38}$$

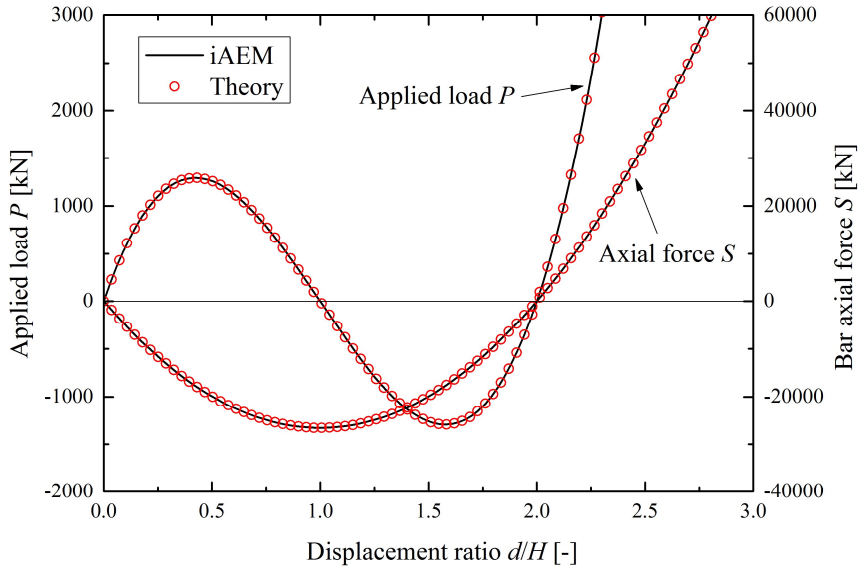

Figure 2-23 Applied load and axial force versus displacement ratio curves of the two-bar truss system

The applied load P and bar axial force S versus displacement ratio d/H curves of the two-bar truss from iAEM analysis with the corresponding theoretical ones are plotted in Figure 2-23. From the figure, it can be seen that the load displacement curves from iAEM analysis agree very well with the theoretical ones. The bar during deformation passes through the following stages:

(1) After the loading is applied, the bar length is decreased, hence, bar compressive force is increased. When the bar is horizontal, the shortest bar length and maximum bar compressive force are achieved, but the applied load is zero.

(2) After the horizontal position, with the increase of the displacement, the bar length is increased, and hence, bar compressive force is reduced. The applied load direction is reversed.

(3) When displacement ratio d/H reaches 2, the bar has the same length as it is at the initial position, bar axial force and applied load are zero.

(4) Further application of the load leads to the increased bar tensile force.

2.3.4 Dynamic analysis of a simply supported beam

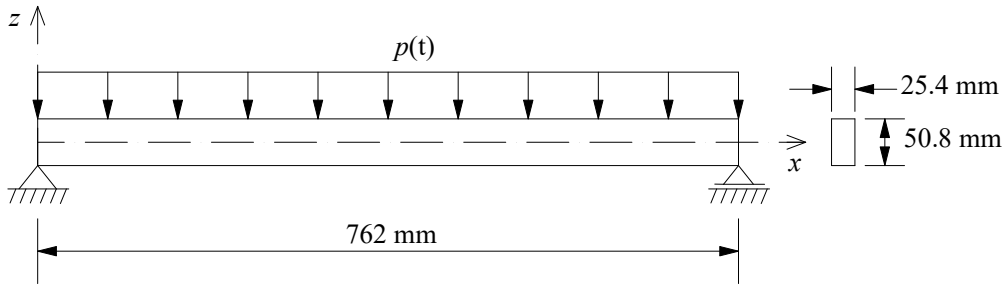

Figure 2-24 A simply supported beam under uniformly distributed load

A simply supported beam under uniformly distributed load is shown in Figure 2-24. The beam is 762 mm (30 in) long with a rectangular cross section of 25.4 mm × 50.8 mm (1 in × 2 in). The modulus of elasticity of the material is $E =$ 207 GPa (30 × 10^6 psi), the yield strength is $f_y =$ 345 MPa (50,000 psi), Poisson's ratio is $\nu =$ 0.3, and the material density is $\rho =$ 15.667 ton/m^3 (1.466 × 10^{-3} lb·s^2/in^4). The material model is the bilinear kinematic model with a strain hardening ratio of μ. For the first-order inelastic dynamic analysis, two types of load history are considered: (a) a step load of $p(t) =$ constant and (b) an exponentially decaying load of $p(t) = 2p_0 e^{(-t/t_0)}$.

8.1.2.7 A step load

Firstly the beam is subjected to the step lateral loads of different magnitudes with the strain hardening ratio $\mu = 0$, i.e. $p(t) = 0.5p_0$, $p(t) = 0.625p_0$ and $p(t) = 0.75p_0$, where p_0 is the static collapse load defined as the load causing a plastic hinge to occur at the midspan of the beam. Damping is ignored, and a time step of $\Delta t =$ 0.681×10^{-4} s, 1/72 of the fundamental period of the beam, is used in the analysis. The deflection of the midspan, δ, is normalized with respect to Δ, the static elastic deflection corresponding to the load p_0. The results by Liu and Lin (1979), SAP2000

and iAEM analysis are shown in Figure 2-25 together with the elastic analysis when $\mu = 1$ and $p(t) = 0.5p_0$. In the analysis by Liu and Lin (1979), elastic-plastic dynamic responses of those structures was analysed with known elastic solutions. Only one quarter of beam was analysed and an 8 × 5 grid system was used to calculate the stress and strain distributions. In the SAP2000 analysis, the plastic-zone model proposed by Tay (2013) for efficient progressive collapse analysis is adopted. For this simply supported beam, as the plasticity occurs in the midspan, six fiber-section beam elements are used at the midspan with a total of 1/4 span length, and three elastic beam elements are used at each end of the beam. It can be seen that the results from iAEM generally compare well with those by Liu and Lin (1979) and SAP2000 analysis. It is observed that the effective period (time to reach maximum deflection) of vibration of the elastic-plastic beam increase with the magnitude of the step lateral load. This is because with the increase of load magnitude, the stiffness of the beam decreases up to the maximum deflection.

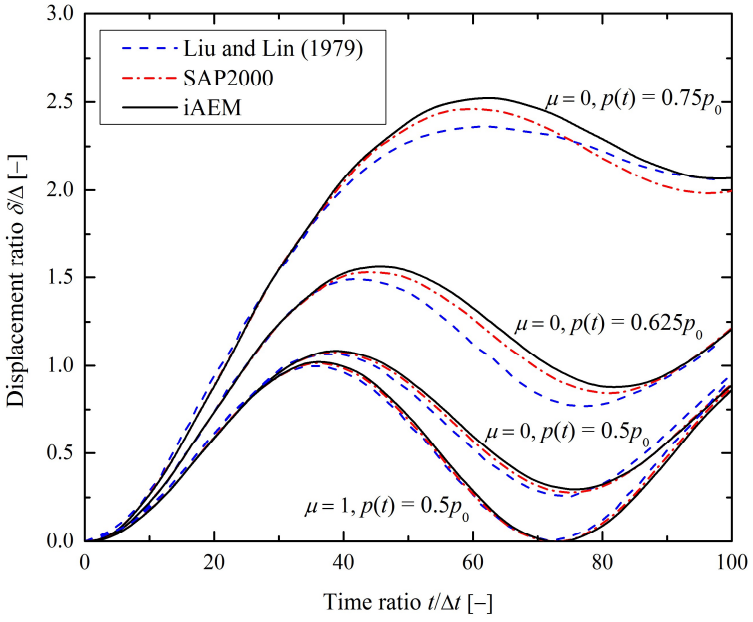

Figure 2-25 Displacement time histories with different load magnitudes

Then the beam is subjected to the same step load of $p(t)=0.625p_0$, but three different strain hardening ratios are used in the analysis, i.e. $\mu=0$, $\mu=0.25$ and $\mu=1$. Damping is also ignored, and a time step of $\Delta t=1.02\times10^{-3}$ s is used in the analysis. The results given by Liu and Lin (1979) and SAP2000 analysis are also shown in Figure 2-26 for comparison. It can be seen that the results from iAEM analysis agree well with the those by Liu and Lin (1979) and SAP2000 analysis. As expected, the effective period and the amplitude of vibration decrease with the increase of the hardening ratio.

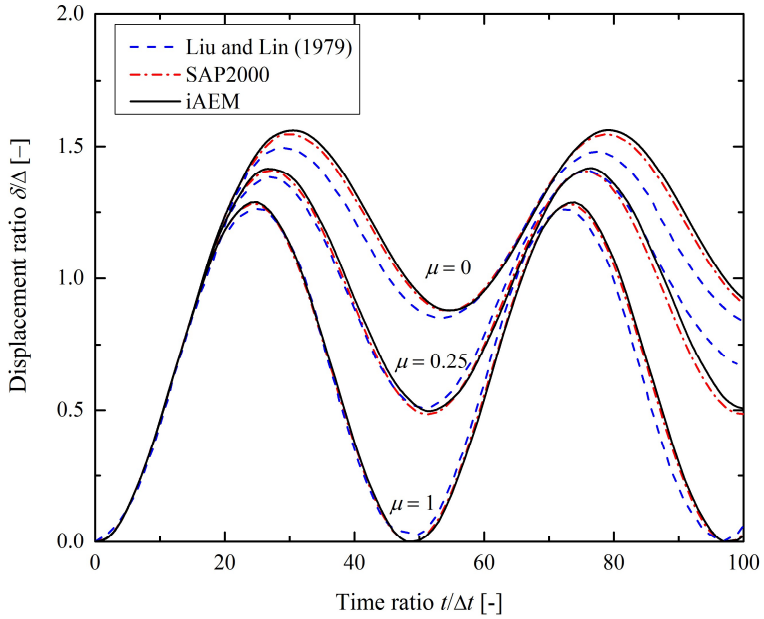

Figure 2-26 Displacement time histories with different strain hardening ratios

8.1.2.8 A decaying load

The beam is subjected to a decaying load of $p(t)=2p_0e^{(-t/t_0)}$, where $t_0=T/2$, T being the fundamental time period. The material is elasto-plastic, i.e. strain hardening ratio $\mu=0$, and damping is ignored. A smaller time step of $\Delta t=1.0\times10^{-5}$ s is used in the analysis, because the exponentially decaying load is more complex than the step load and its Fourier components range over the entire spectrum, thus exciting several

modes of vibration in the beam. The displacement time history of the beam from iAEM analysis is shown in Figure 2-27 together with those by Baron et al. (1961) and Nagarajan and Popov (1974). Baron et al. (1961) used five rigid bars and six plastic hinges to one-half of the beam and the solution was achieved by a finite difference approach. Nagarajan and Popov (1974) used five 10-node quadrilateral isoparametric finite elements to model one quarter of the beam. From Figure 2-27, it can be seen that the result from iAEM agree well with the published results. The maximum displacement ratio from iAEM is 8.34 which is only +0.6% than 8.29 by Baron et al. (1961) and +5.5% than 7.90 by Nagarajan and Popov (1974).

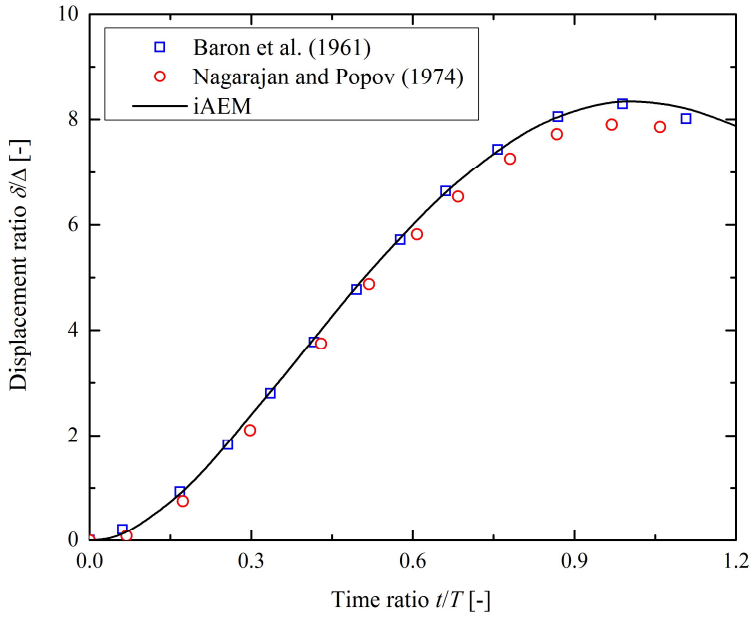

Figure 2-27 Displacement time histories of the beam subjected to a decaying load

2.3.5 Dynamic analysis of a clamped beam

A clamped-clamped beam under a concentrated step load of $p(t) = 2847$ N (640 lbf) acting at the midspan is shown in Figure 2-28. The beam is 508 mm (20 in) long with a rectangular cross section of 25.4 mm × 3.2 mm (1 in × 1/8 in) The modulus of elasticity of the material is $E = 207$ GPa (30×10^6 psi), Poisson's ratio is $\nu = 0$, and the material density is $\rho = 27.8$ ton/m^3 (2.6×10^{-3} lbf·s^2/in^4).

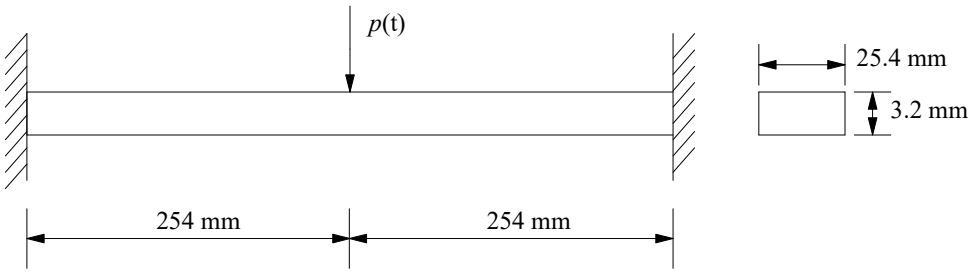

Figure 2-28 A clamped beam under a concentrated step load

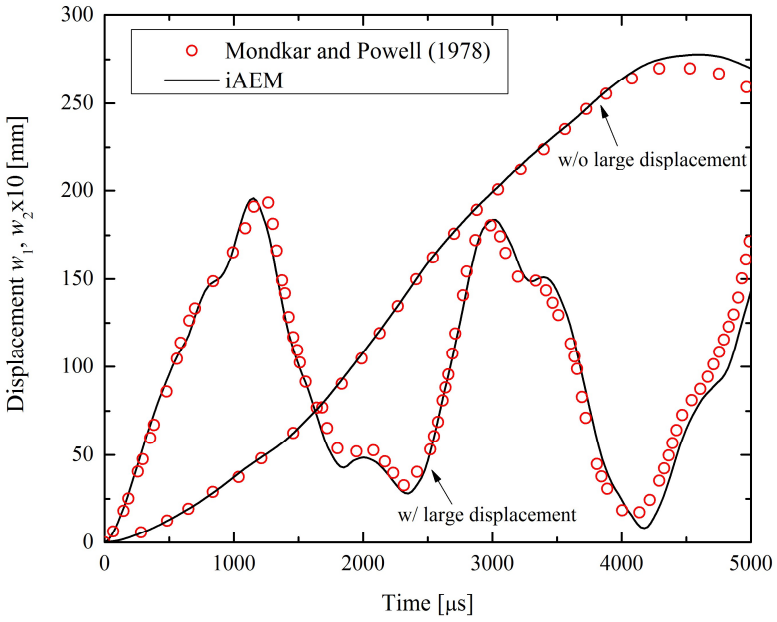

Figure 2-29 Displacement time histories of the beam with and without large displacement

Both first-order and second-order elastic dynamic analyses are conducted for the beam. Due to symmetry, one half of the beam is modelled by 50 elements using iAEM. Damping is ignored, and a time step of $\Delta t = 100$ μs and $\Delta t = 25$ μs are used for the first-order and second-order elastic dynamic analyses, respectively. The vertical displacement time histories at the midspan are plotted in Figure 2-29 in which w_1 is the displacement from first-order analysis and w_2 is the displacement from second-order analysis. It can be seen that the results by the iAEM agree well with those by Mondkar and Powell (1978). Five 8-node plan stress finite elements are used

by Mondkar and Powell (1978) to model the half-span of the beam with automatic stiffness reformulation procedure for calculation. The period of vibration of the first-order elastic dynamic analysis from iAEM analysis is close to the fundamental period of $T = 9056\ \mu$s using the beam formula in the book by Paz and Leigh (2004) , but the first cycle of the nonlinear vibration is seen to be approximately 2300 μs. There is considerable difference in the maximum displacements of the first-order and second-order solutions. This is due to the highly stiffening behavior of the beam when geometric effect is considered. The results of the elastic static analysis by Mondkar and Powell (1978) show that the displacement from first-order analysis is several times larger than that from second-order analysis when the load is 2847 N (640 lb).

2.3.6 Swing of a stiff pendulum

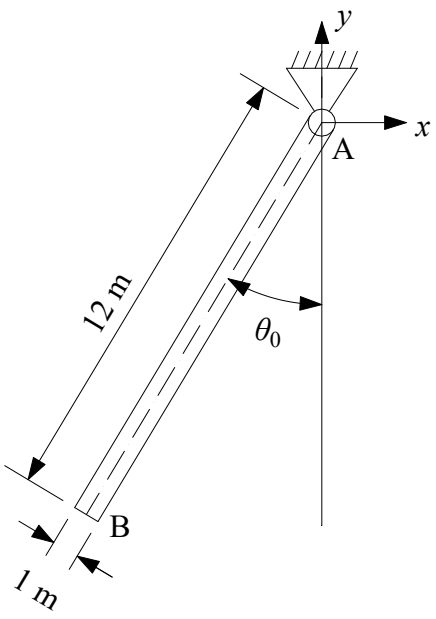

Figure 2-30 Shape and dimensions of a stiff pendulum

The stiff pendulum shown in Figure 2-30 is used for the second-order elastic analysis. The pendulum is 12 m long with a cross section of 1 m × 1 m. It is pinned at end A and inclined with an initial angle of θ_0. The pendulum is set to swing under its own self weight with zero initial velocity. In order to test the ability of geometric

nonlinearity (large displacement) analysis in iAEM, a large initial angle of $\theta_0 = \pi/2$ is assumed. As the pendulum is considered to be rigid, a large value of elastic modulus is used in the model with $E = 3000$ GPa. In order to compare with the theoretical result, shear deformation is ignored in the iAEM analysis by setting the shear modulus G equal to E.

The pendulum is modelled with 13 elements using iAEM with a time step of $\Delta t =$ 0.02 s, and the damping is ignored. As the widely used trapezoidal rule (Newmark's constant-average-acceleration method) does not conserve energy and momentum, it is unstable for this pendulum problem. The time integration method proposed by Bathe (2007) is adopted. The method is a "composite scheme". The time step Δt is assumed to consist of two equal sub-steps of size $\Delta t/2$. For the first sub-step solution, the trapezoidal rule is used, and for the second sub-step solution, the 3-point Euler backward formula is employed.

The inclined angle time history is plotted in Figure 2-31 and the *x* coordinate of end B time history is plotted in Figure 2-32, respectively. The theoretical curves can be obtained by computing the equation of motion of the bar below numerically.

$$\frac{d^2\theta}{dt^2} + \frac{3g}{2L}\sin(\theta) = 0 \tag{2-39}$$

where

θ is the inclined angle of the bar with respect to the *y* axis,

t is the time,

g is the gravitational acceleration,

L is the bar length.

As shown in Figure 2-31 and Figure 2-32, it can be seen that the results from iAEM agree well with those from the theory. The pendulum swings around the *y* axis, and the large geometric effect can be captured using iAEM.

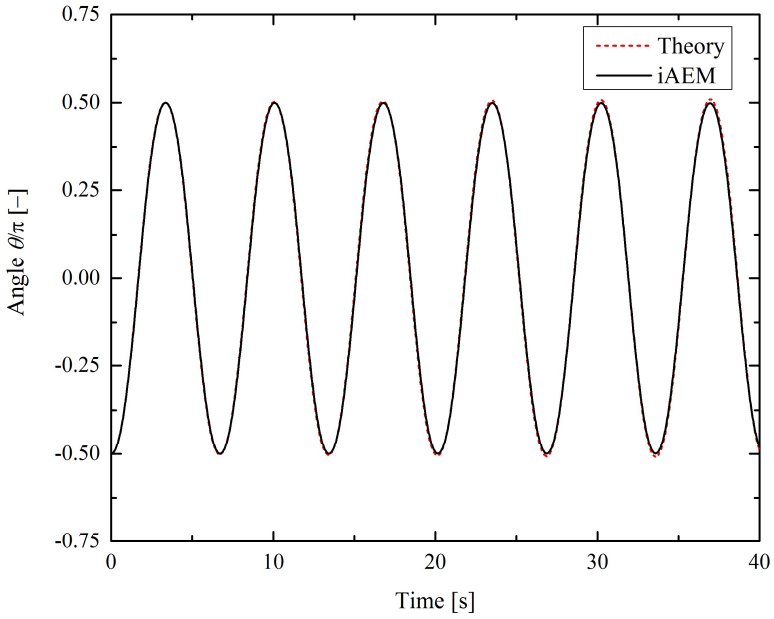

Figure 2-31 Inclined angle time histories of the rigid bar under self weight

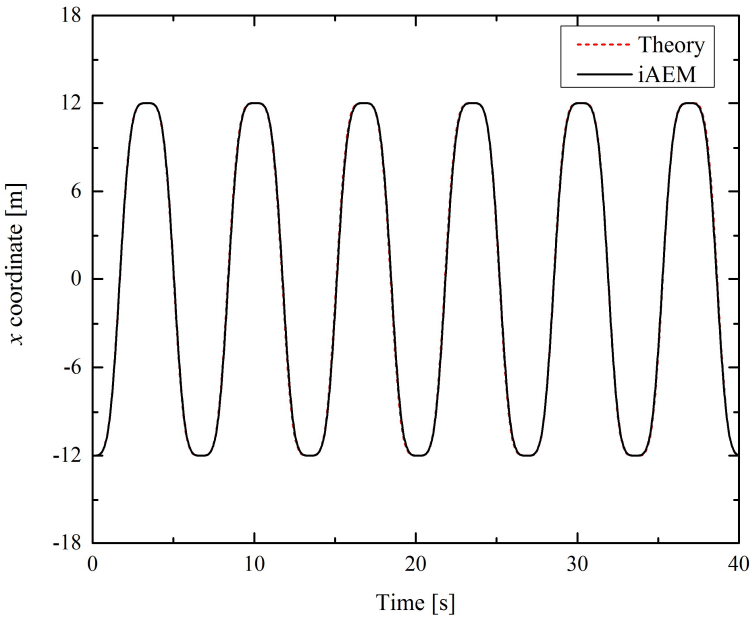

Figure 2-32 *x* coordinate of end B time histories of the rigid bar under self weight

2.3.7 Sudden column removal of moment frames

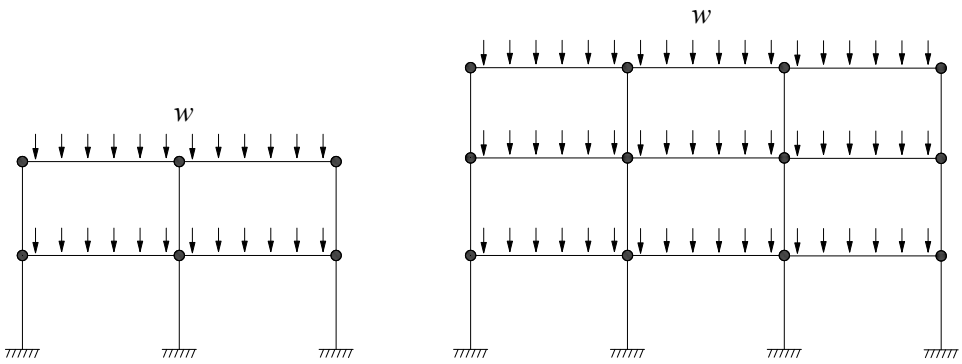

Figure 2-33 Two-bay two-storey and three-bay three-storey moment frames with uniformly distributed load

The second-order inelastic dynamic analysis using iAEM is carried out for the two-bay two-storey and three-bay three-storey moment frames (see Figure 2-33) studied by Kaewkulchai (2003). The analysis follows the alternative path method for progressive collapse analysis, that is, a column is suddenly removed from the structure. The two frames are subjected to the same gravity load of $w =$ 70.051 kN/m (0.4 kips/in) uniformly distributed along the beam lengths. Member properties and dimensions of the frames are listed in Table 2-4. The modulus of elasticity of the material is $E =$ 200 GPa (29,000 ksi), and the yield moment for the columns and beams is $M_y =$ 734.4 kN·m (6,500 kip·in). Lumped mass of 21.713 tons (0.124 kip·s^2/in) is considered at each beam end.

In the study by Kaewkulchai (2003), a beam-column element formulation was adopted and a solution procedure was developed. The beam-column element utilizes a multi-linear, lumped plasticity model, and it also accounts for the interaction of axial force and bending moment. Structural damping is ignored as material yielding is deemed to dominate energy absorption of inelastic response.

Table 2-4 Member properties and dimensions of the frames

	Length, L	Area of cross section, A	Second moment of inertia, I
Beams	6.096 m (240 in)	7.742×10^{-3} m^2 (12 in^2)	8.325×10^{-4} m^4 (2000 in^4)
Columns	3.658m (144 in)	1.290×10^{-2} m^2 (20 in^2)	4.995×10^{-4} m^4 (1200 in^4)

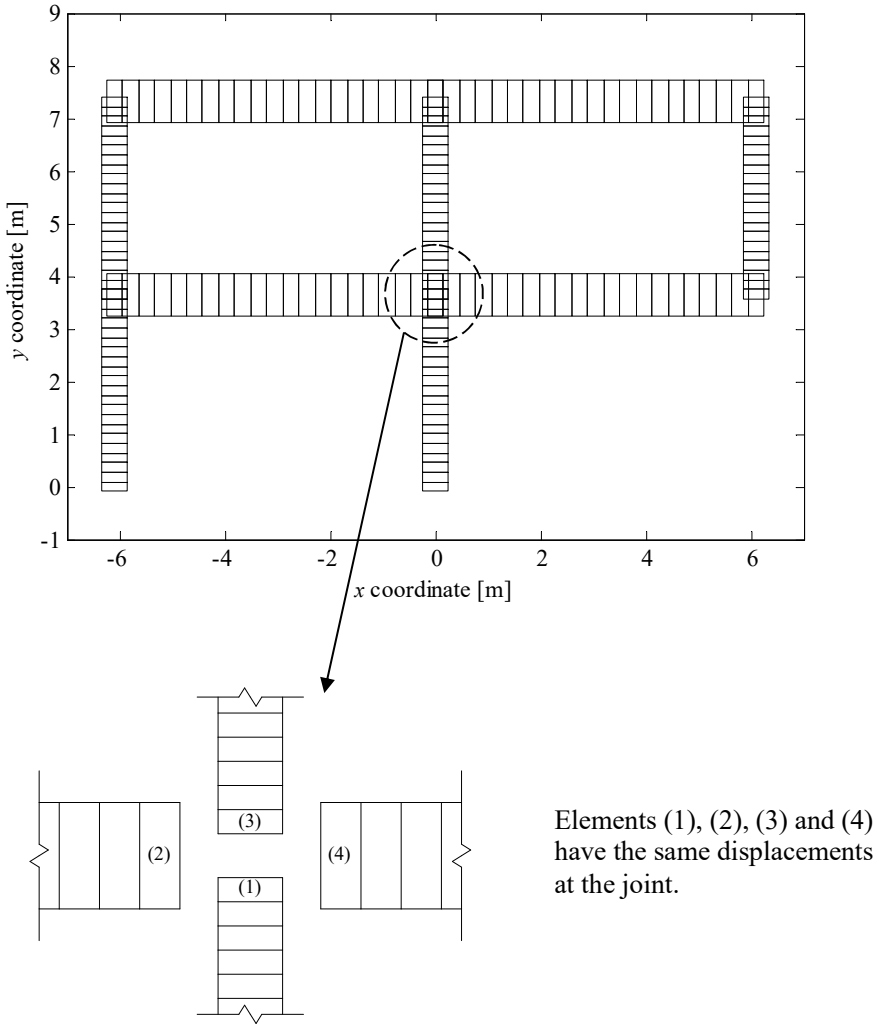

Figure 2-34 Modelling of the two-bay two-storey moment frame using iAEM

Table 2-5 Reaction forces used for simulating sudden column removal of the two-storey and three-storey moment frames

Frames	Case of column removal	P (kN)	V (kN)	M (kN·m)

Two-bay two-storey	Case 1: removal of perimeter column	398.59	28.02	69.36
	Case 2: removal of internal column	910.95	-	-
Three-bay three-storey	Case 1: removal of perimeter column	613.98	30.15	74.89
	Case 2: removal of internal column	1307.66	0.43	1.66

In order to model this frame using iAEM, the physical steel sections with equivalent stiffness and strength are used. This result in the 806 mm square hollow section (SHC) with a thickness of 2.41 mm for the beam member, and the 489 mm SHC with a thickness of 6.7 mm for the column member. Yield strength of $f_y = 315$ MPa is used in the analysis. The bilinear material model with strain hardening ratio of 0.3% is assumed. To model the moment frame using iAEM, all the members are first modelled separately with strings of rigid elements, and then they are assembled by imposing the same displacements for the elements which meet at the same joint (see Figure 2-34). In this way, if small-size elements are used, section plasticity can be extended as near the member ends as possible, and the results from the iAEM can be compared with those by Kaewkulchai (2003) using beam element formulation.

Equivalent reaction forces (i.e. axial force *P*, shear force *V* and bending moment *M*) are used to represent the columns that need to be removed for progressive collapse. These forces are equivalent to the internal forces of the columns before removal, and are tabulated in Table 2-5. In the dissertation of Kaewkulchai (2003), the sudden column removal is simulated in three phases as shown in Figure 2-35. In the first phase, gravity load and reaction forces are applied slowly to full magnitude following a linear ramp function. Then, the loads are kept constant over a period of time to damp out the inertia force effects. In the final phase, reaction forces are removed by reducing the magnitude to zero over a short period of time. The first and second phases of the simulation are not only time-consuming, but also they can lead to

incorrect results if insufficient time step is used. In order to avoid these issues, a two-phase analysis approach is adopted. First the static analysis is performed in place of the first and second phases (shown as dotted lines in Figure 2-35(c)) of the time-history. Then with the developed initial deformation and internal forces of the frame, dynamic time history analysis is carried out by sudden removal of reaction forces over a 0.01 s period. The adopted removal duration is smaller than one tenth of the period associated with the structural response mode for the vertical motion of the bays above the removed column recommended by DoD (2009). In the second-order inelastic dynamic analysis, a time step of 0.0005 s for a period of 2.0 s is adopted in each analysis case. In the analysis, structural damping is ignored as material yielding is deemed to dominate energy dissipation in the inelastic response.

8.1.2.9 The two-bay two-storey frame

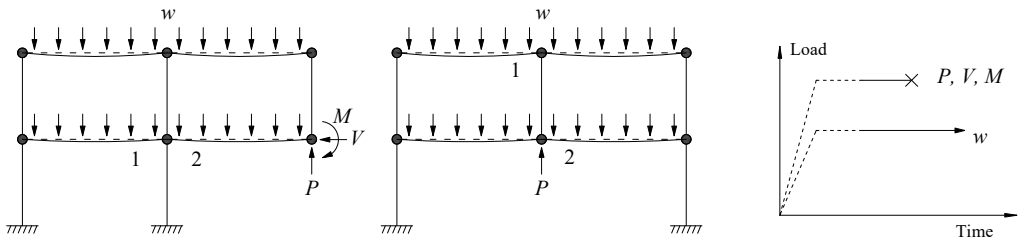

(a) Case 1: removal of perimeter column

(b) Case 2: removal of internal column

(c) Load history for column removal

Figure 2-35 Column removal cases considered for the two-bay two-storey frame

For the two-bay two-storey moment frame shown in Figure 2-35, two cases of sudden column removal are considered, i.e. Case 1 of removing a perimeter column and Case 2 of removing an internal column. The vertical displacement time histories at the column removal position from iAEM analysis are plotted in Figure 2-36 together with those from Kaewkulchai (2003) and SAP2000 for comparison. In the SAP2000 analysis, the plastic-zone model proposed by Tay (2013) for efficient progressive collapse analysis is adopted. For the beam members, twelve fiber-beam elements with

a total of 1/4 beam length, and six fiber-beam elements with a total of 1/8 beam length are used at the midspan and at each beam end, respectively. For the column members, six fiber-beam elements with a total of 1/8 column length are used at each column end. The remaining part of the beam or column members is modeled by the elastic beam elements.

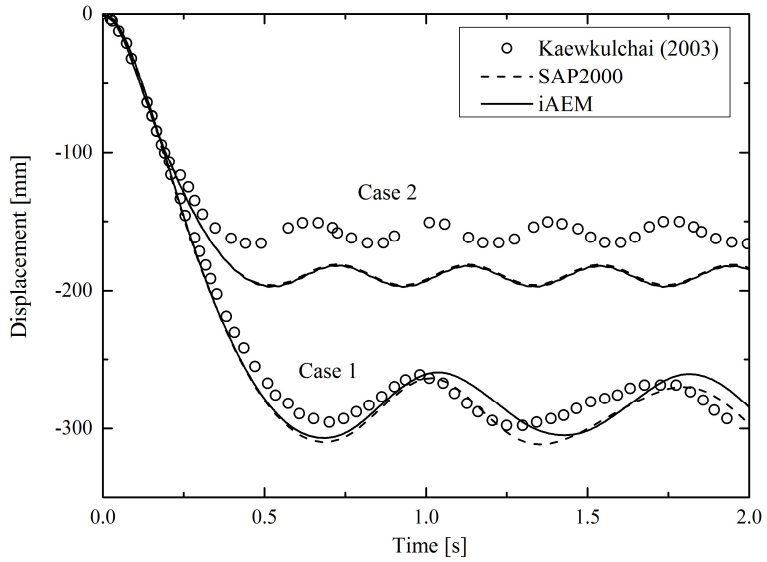

Figure 2-36 Displacement time histories at the column removal position of the two-bay two-storey moment frame

For Case 1, the general trend of the displacement time history from iAEM agrees well with those from Kaewkulchai (2003) and SAP2000. After column removal, the vertical displacement increases rapidly till the maximum value which is followed by the transient vibration. The maximum displacement from iAEM is 307mm which is only 3.0% larger than that from Kaewkulchai (2003) and 1.3% smaller than that from SAP2000. For Case 2, the displacement time histories from iAEM and SAP2000 match very well, both giving a maximum displacement of 197 mm which is 18.7% larger than that from Kaewkulchai (2003). The significant discrepancy of the displacement from Kaewkulchai (2003) with those from iAEM and SAP2000 analysis may imply that the results by Kaewkulchai (2003) for Case 2 of the two-bay two-storey frame are not accurate or incorrectly reported. From this figure, it is

observed that the maximum displacement of Case 2 is 35.8% smaller than that of Case 1 from iAEM analysis. This is because a better load path due to catenary action to redistribute the forces is developed in Case 2 of removing an internal column than that in Case 1 of removing a perimeter column.

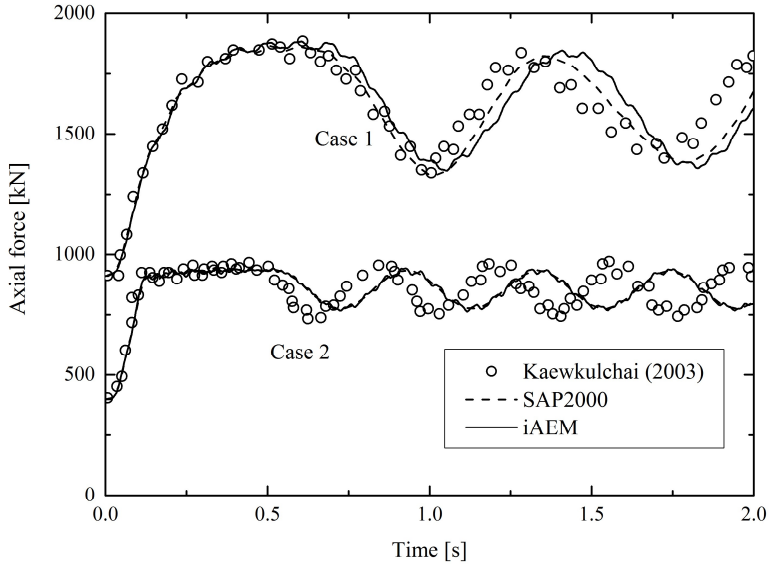

Figure 2-37 Axial force time histories for Case 1 and Case 2 of the two-bay two-storey moment frame

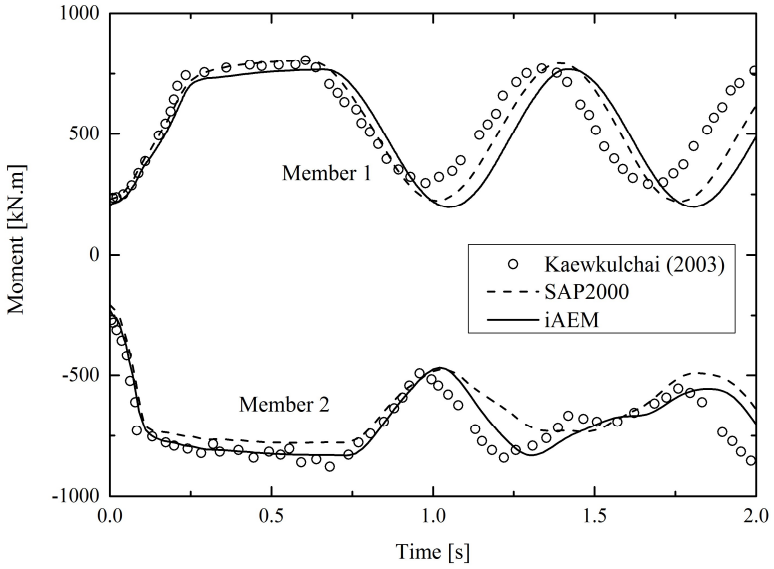

Figure 2-38 Moment time histories of Member 1 and Member 2 for column removal case 1 of two-bay two-storey frame

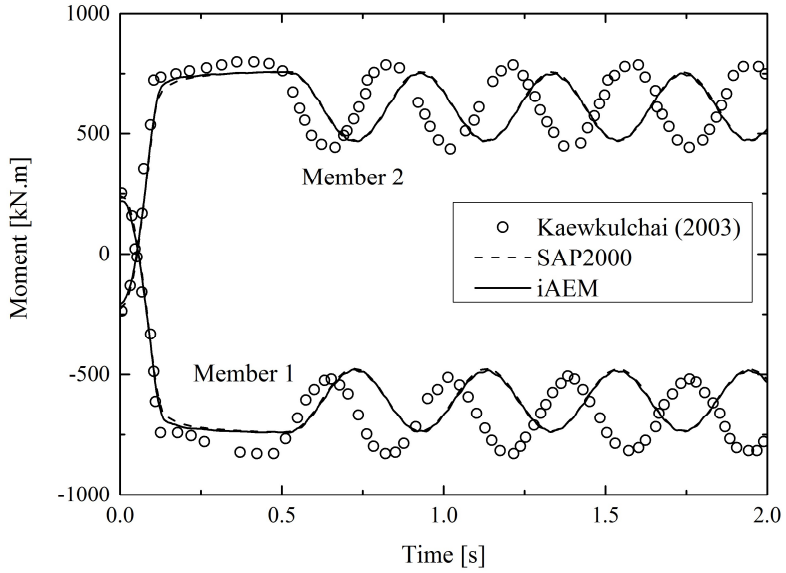

Figure 2-39 Moment time histories of Member 1 and Member 2 for column removal case 2 of two-bay two-storey frame

The axial force time histories at the right column of Case 1 and the middle column of Case 2 from iAEM analysis are presented in Figure 2-37. The bending moments of Members 1 and 2 for Case 1 and Case 2 are presented in Figure 2-38 and Figure 2-39, respectively. The results from Kaewkulchai (2003) and SAP2000 are also plotted in these figures for comparison. For Case 1, the general trend of the axial force and bending moment time histories from iAEM agree well with those from Kaewkulchai (2003) and SAP2000. Due to sudden column removal, the axial forces and bending moments increase significantly. The ratios of maximum and initial axial forces are in good agreement between the three solutions, being 2.07, 2.07 and 2.05 from iAEM, Kaewkulchai (2003) and SAP2000, respectively. The ratios of maximum and initial moments are also in reasonably good agreement, being 3.92, 3.43 and 3.67 for Member 1 and 3.78, 3.26 and 3.66 for Member 2 from iAEM, Kaewkulchai (2003) and SAP2000, respectively. For Case 2, the axial force and bending moment time histories by iAEM and SAP2000 match very well. Though the magnitudes of these forces by iAEM and SAP2000 are fairly close to those by Kaewkulchai (2003), a

phase lag of the vibration results by iAEM and SAP200 can be observed, which is due to the larger effective period predicted in the displacement time histories as shown in Figure 2-36.

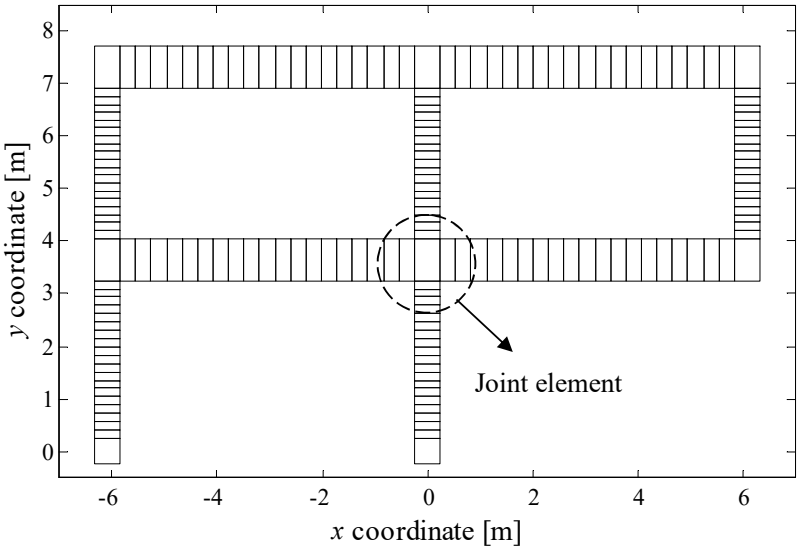

Figure 2-40 Modelling of moment frame considering physical geometries of the joint using iAEM

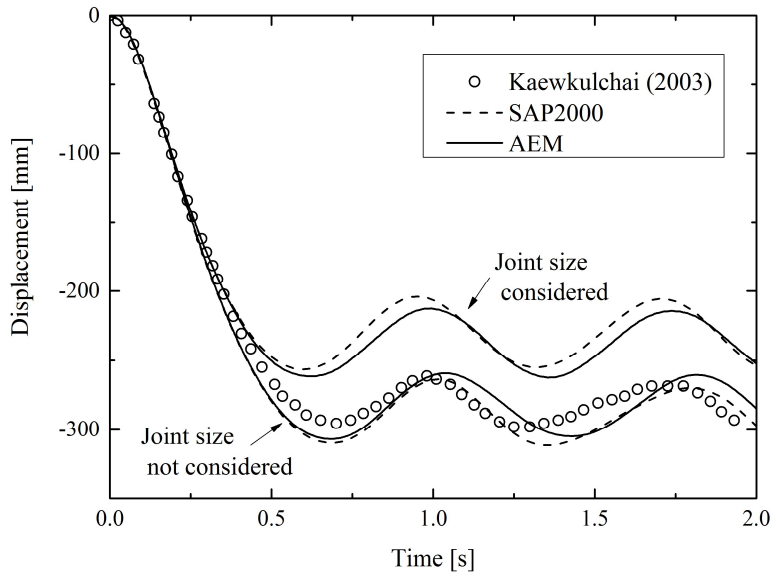

Figure 2-41 Displacement time histories at the column removal position considering the joint size

In the above analysis using iAEM, the physical size of joints is not considered with the model shown in Figure 2-34, and the section plasticity can spread as near as the

joint center. Thus, the results from iAEM analysis can be compared with those by Kaewkulchai (2003).

However, in reality, joints with considerable size enhance the frame stiffness. The global behavior predicted by the previous modelling method with smaller stiffness in Figure 2-34 is not necessarily accurate. An advantage of iAEM modelling is that joint element can be used to account for the effect of finite joint size on the structural behavior in the analysis (see Figure 2-40). To this end, iAEM element with real joint size is used to connect the intersecting beam and column members. The displacement time history from iAEM with the joint element is plotted in Figure 2-41, in comparison with the result from SAP2000 analysis. In SAP2000, the geometry of the joint is considered by setting the "End Length Offsets" with the real joint size. It is seen that the results from iAEM and SAP2000 compare well, and due to stiffening effect of the joints, the maximum displacements are approximately 15% smaller than those previous analysis from iAEM, SAP2000 and Kaewkulchai (2003) when the physical size of joint is not considered. In the later part of the thesis, joint element is used in the modelling of steel frames when necessary.

8.1.2.10 The three-bay three-storey frame

For the three-bay three-storey moment frame shown in Figure 2-42, two cases of sudden column removal are also considered, i.e. Case 1 of removing a perimeter column and Case 2 of removing an internal column. The vertical displacement time histories at the column removal position from iAEM analysis are plotted in Figure 2-43 together with those from Kaewkulchai (2003) and SAP2000 for comparison. The general trend of the displacement time histories from iAEM agrees well with those from Kaewkulchai (2003) and SAP2000. After column removal, the vertical displacement increases rapidly till the maximum value which is followed by the transient vibration. For Case 1, the maximum displacement from iAEM is 236 mm

which is only 1.7% smaller than that from Kaewkulchai (2003) and 0.4% larger than that from SAP2000. For Case 2, the maximum displacements from iAEM is 168 mm which is only 3.1% larger than that from Kaewkulchai (2003) and 1.2% larger than that from SAP2000. The maximum displacement of Case 2 is 28.8% smaller than that of Case 1 from iAEM analysis. This is because a better load path to redistribute the forces is developed in Case 2 of removing an internal column than that in Case 1 of removing a perimeter column.

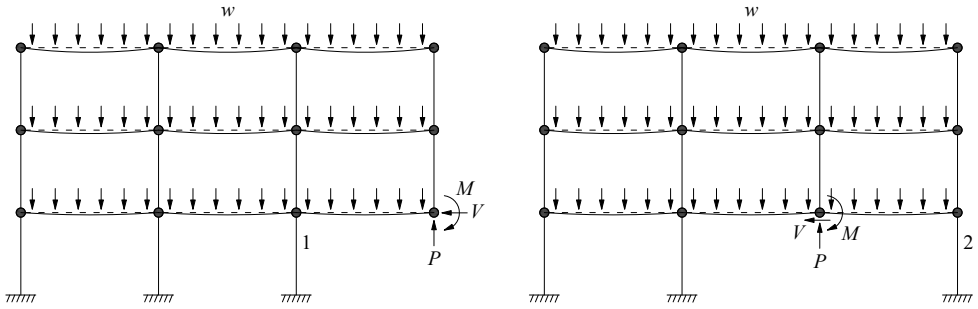

(a) Case 1: removal of perimeter column (b) Case 2: removal of internal column

Figure 2-42 Cases of column removal considered for the three-bay three-storey frame

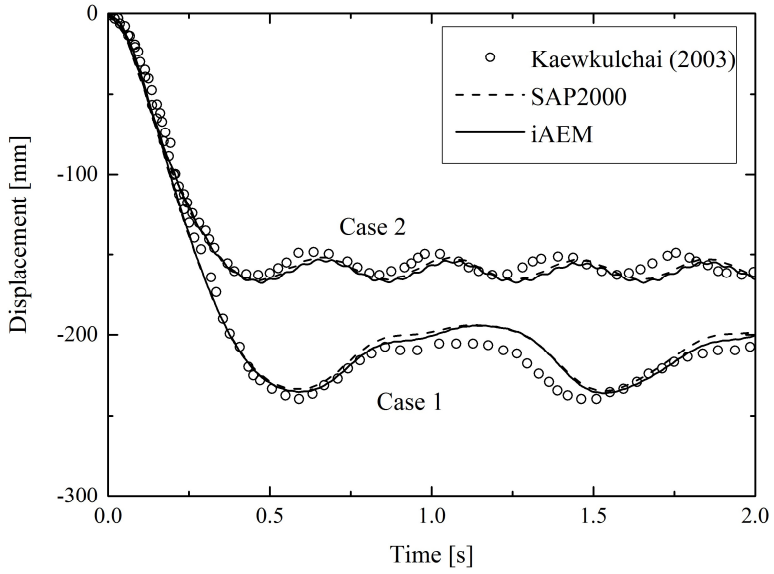

Figure 2-43 Displacement time histories at the column removal position of the three-bay three-storey moment frame

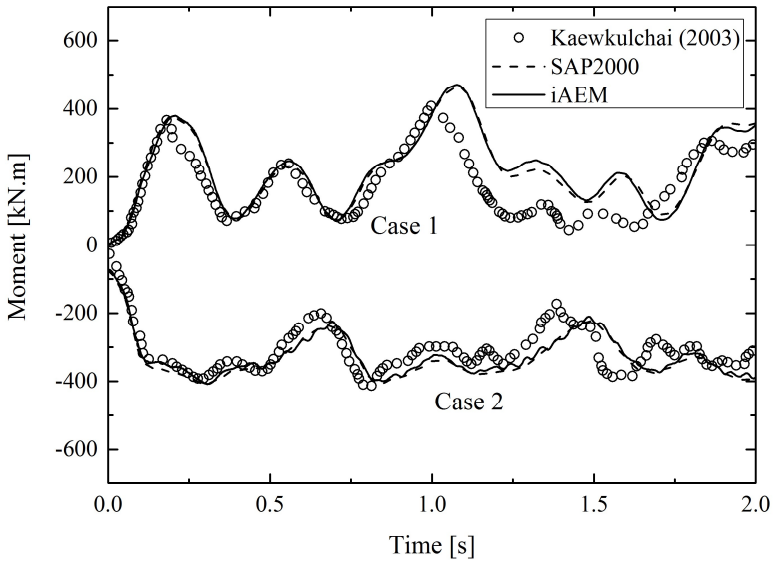

Figure 2-44 Moment time histories for column removal Case 1 and Case 2 of three-bay three-storey frame

The bending moments of Member 1 of Case 1 and Member 2 of Case 2 time histories are plotted in Figure 2-44. The curves from Kaewkulchai (2003) and SAP2000 are also plotted on the same figure for comparison. The general trend of the bending moment time histories from iAEM compares well with those from Kaewkulchai (2003) and SAP2000. For Case 1, the maximum bending moment from iAEM is 470 kN·m which is 15.2% and 1.3 % larger than that from Kaewkulchai (2003) and SAP2000, respectively. For Case 2, the maximum bending moment from iAEM is 408 kN·m which is only 1.4% and 0.2% smaller than that from Kaewkulchai (2003) and SAP2000, respectively.

From the above column removal analysis for these two frames, the results predicted by iAEM compare generally well with those by Kaewkulchai (2003) in terms of the displacements and forces. However, the advantage of iAEM over Kaewkulchai (2003) is also observed that the influence of joint size on the frame behavior can be considered by using the joint element in the model.

2.3.8 Summary

In this chapter, the element formulation of the improved applied element method (iAEM) is first presented. Then the solution strategies of iAEM for both static and dynamic analyses are described. Load control method and displacement control method with Newton-Raphson iterations are used in static analysis, and constant acceleration method with Newton-Raphson iterations is used in dynamic analysis. Finally, seven benchmark examples are presented and four types of analyses are adopted: first-order elastic, first-order inelastic, second-order elastic and second-order inelastic analyses. The results from these examples show that good accuracy of iAEM can be achieved, and material and geometric nonlinearities can be correctly considered. The results from iAEM analysis compare well with other sources, such as theoretical values, published results, or results from finite element analysis. The validation study of iAEM in this chapter serves the basis for the modelling of imperfections, semi-rigid connection and RC shear walls in the following chapters of the thesis.

3 Modelling of Initial Imperfections of Steel Frames

The iAEM is currently limited to analyse idealized steel structures without considering the initial material and geometric imperfections. However, in real steel structures, the initial imperfections often adversely affect the structural stability and post-buckling behavior. Therefore, in order to obtain more accurate behavior of steel frames, the iAEM is extended to consider initial imperfections by the explicit modelling approach. In this chapter, a brief introduction of the initial imperfections is given, followed by the explicit modelling approach to consider the imperfections using iAEM. Finally, modelling of imperfections using iAEM is validated through some numerical examples.

3.3 Modelling of material imperfection using iAEM

3.3.1 Initial material imperfections

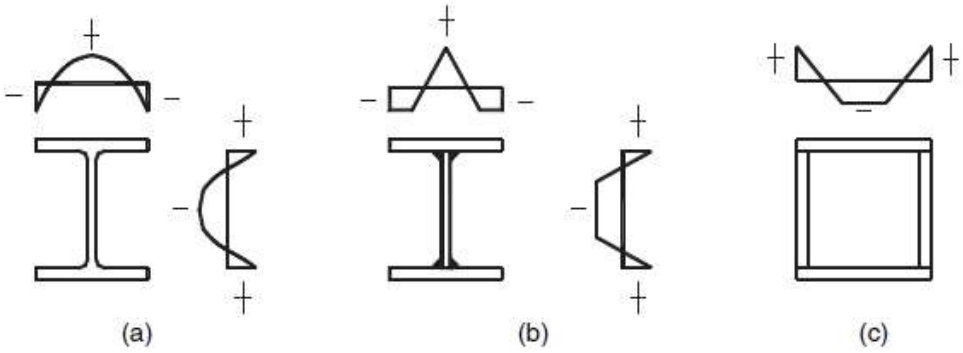

Figure 3-1 Typical distribution of residual stresses for steel members (a) hot-rolled H-type section; (b) welded H-type section; (c) welded box section (Li and Li, 2007)

Initial material imperfections or residual stresses with significant magnitude exist in I-shaped or box-shaped beam and column members of steel structures (see Figure 3-1). Generally, tensile stresses are produced at the cross of flange and web plates or where cooling speed is relatively slow after welding or hot-rolling, self-balanced compression stresses will be produced at the remaining area of the section.

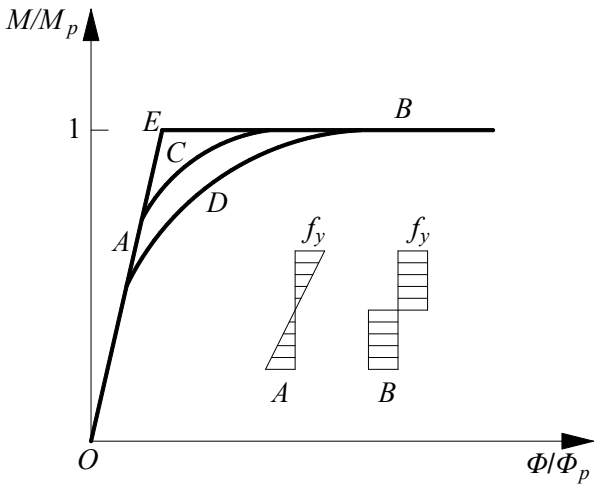

Figure 3-2 Effect of residual stresses on the moment–rotation relationship of steel sections (Li and Li, 2007)

The existence of residual stresses will influence the yielding of the member across the section, thus it affects the structural behavior of steel structures. For example, due to the existence of initial compressive stresses, the part of a section in compression may go into plasticity earlier than section free of residual stresses, although the ultimate plastic strength of the section is the same. As shown in Figure 3-2, for a steel section in bending, the moment-rotation relationships with and without the residual stresses are represented by curves ODB and OCB, and OCB can be simplified to curve OEB. The material property of steel in Figure 3-2 is assumed to be idealized elastic perfectly plastic. From this figure, it can be seen that along with the earlier development of plasticity due to residual stresses, stiffness of the section reduces significantly, resulting in the softer force-deformation behavior of the section. The effects of residual stresses should therefore be incorporated in the analysis by iAEM.

The residual stress distributions for the hot-rolled I-section recommended by ECCS (1984) are shown in Figure 3-3. When the depth-width ratio h/b is less than 1.2, the maximum residual stress is $f_{res} = 0.5 f_y$. When h/b is larger than 1.2, the maximum residual stress is $f_{res} = 0.3 f_y$.

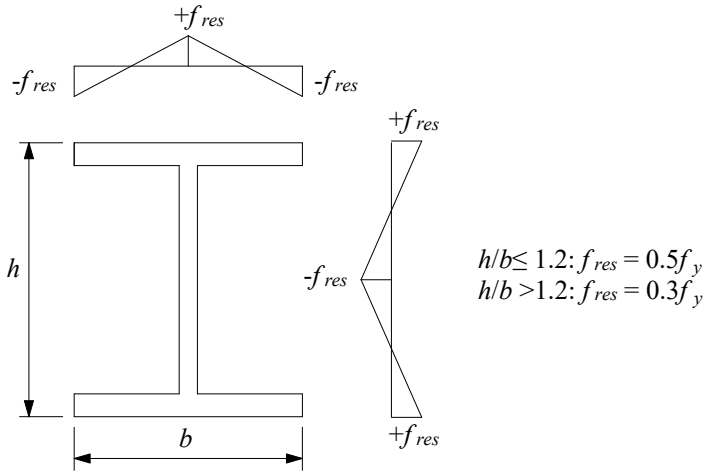

Figure 3-3 Residual stress pattern for rolled I-section (f_{res}/f_y) (ECCS, 1984)

3.3.2 Modelling of residual stresses

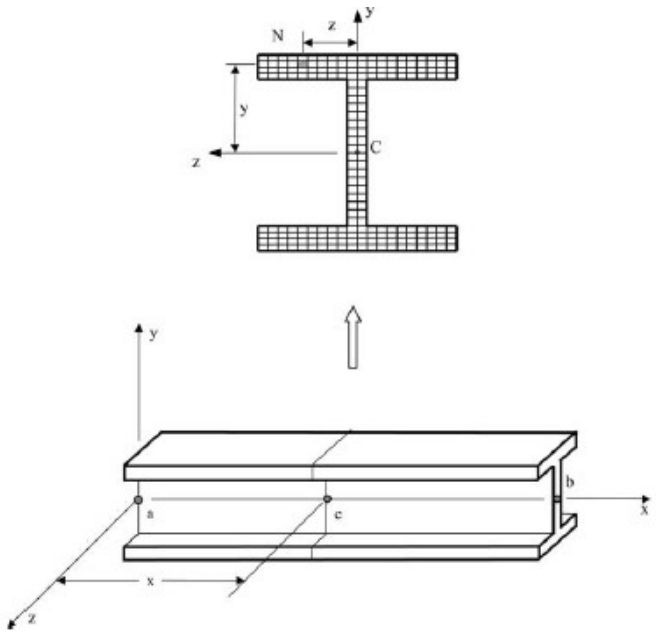

Figure 3-4 Discretization of I-section in the spread-of-plasticity analysis (Jiang et al., 2002)

The explicit modelling approach is adopted to model the residual stresses using iAEM. It is the same modelling method that has been conducted in the plastic-zone or distributed-plasticity method (see Figure 3-4). In plastic-zone method, the element cross section is subdivided into small sections called 'fibers', and each fiber follows the material stress-strain relationship with initial residual stress according to the distribution recommended by ECCS (1984); thus the gradual yielding throughout the cross-section can be captured by incrementally updating the stress state throughout the analysis. In iAEM, instead of fibers, nonlinear springs are used to connect the adjacent rigid elements, and these springs contain initial residual stresses at the start of analysis.

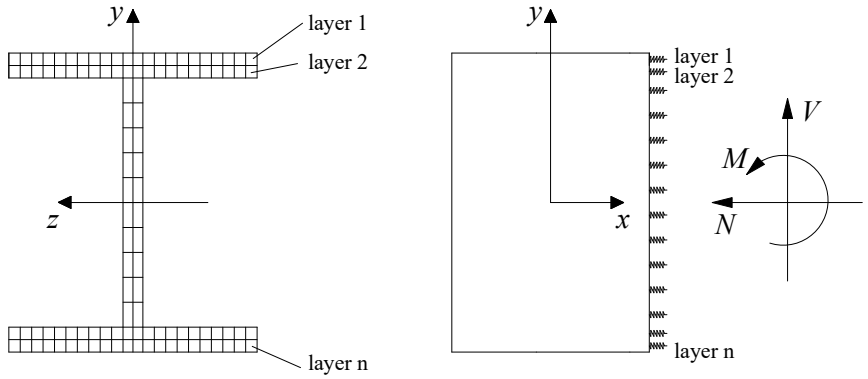

Figure 3-5 Modelling of residual stresses in iAEM

In the 2D version of iAEM, the residual stresses along the web are allocated to the web springs in the *y* direction, and *z* axis is added to define the coordinates of flange springs in the out-of-plane direction, so that the residual stress along the flanges can be allocated to these springs. The analysis is conducted in the 2D framework with the springs on the same layer in the *xy* plane sharing the same deformation, and forces acting on the cross section involve only axial force *N*, shear force *V* and bending moment *M*.

3.4 Modelling of initial geometric imperfections using iAEM

3.4.1 Initial geometric imperfections

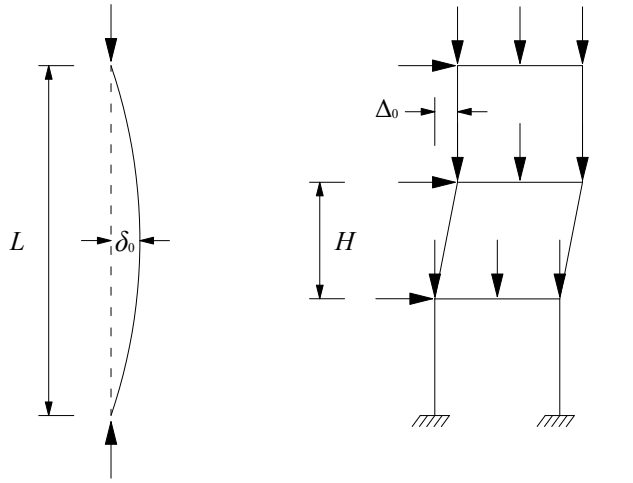

(a) out of straightness (b) out of plumbness

Figure 3-6 Geometric imperfections (Clarke et al., 1992)

Geometric imperfections are also inevitable in real steel members with the potential of significantly influencing their structural behavior. They can be in the forms of member out-of-plumbness and out-of-straightness during erection or cambering (see Figure 3-6). Geometric imperfections amplify the moments in members when second-order effects are considered. The principal effect of an initial out-of-straightness on an individual member is the additional internal moment when the axial load P acts through the initial out-of-straightness δ_0 as shown in Figure 3-6. This moment reduces the maximum axial capacity of a column. The initial out-of-plumbness also affects member strength, with additional moment caused by the axial load P acting through the nonverticality Δ_0. The $P \cdot \Delta_0$ moment also impacts the forces and moments in connecting elements, including connections, beams, base plates, slabs, etc. The effects of geometric imperfections should therefore be incorporated in

analysis by iAEM in order to obtain more accurate structural behavior of real steel structures.

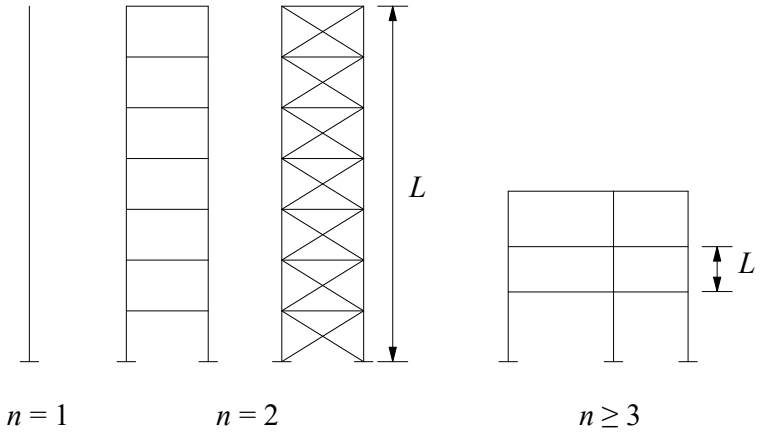

Figure 3-7 Definition of height for geometric imperfection (*n* = no of columns) (ECCS, 1984)

The initial out-of-plumbness recommended by ECCS (1984) is given by the following equation

$$\psi_0 = \frac{1}{300} r_1 r_2 \tag{3-1}$$

where $\psi_0 =$ initial angle of inclination,

$$r_1 = \begin{cases} \sqrt{5/L}; & \text{if } L > 5\text{m} \\ 1; & \text{if } L \le 5\text{m} \end{cases},$$

$$r_2 = \frac{1}{2}\left(1 + \frac{1}{n}\right),$$

$L =$ height of frame (m),

$n =$ number of columns in plane of frame.

It should be noted that when the frame has only one bay ($n \le 2$), the height L should be taken as the overall height of the frame. When the frame has more than 2 bays ($n \ge 3$), L should be taken as a storey height of the frame.

The initial out-of-straightness of members is assumed to have a parabolic configuration with a maximum offset of 0.1% of the member length at midspan.

3.4.2 Modelling of initial geometric imperfections

The explicit modelling approach is adopted to consider the initial geometric imperfections of steel structures using iAEM, and the exact geometry of the structure with out-of-plumbness and out-of-straightness is directly used at the start of analysis.

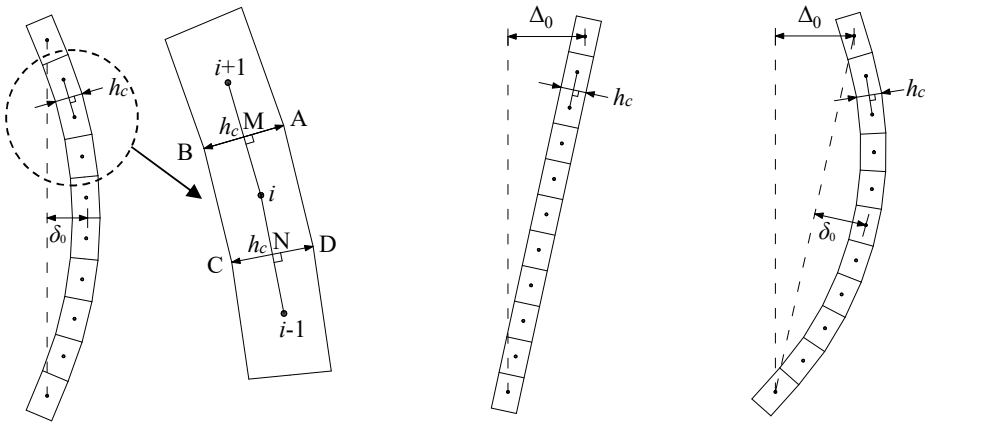

(a) out-of-straightness (b) out-of-plumbness (c) out-of-straightness + out-of-plumbness

Figure 3-8 Modelling geometric imperfections using iAEM

In the modelling of a single member with out-of-straightness using iAEM (see Figure 3-8(a)), the member is first divided into a number of elements with their centroids located at the curved shape of the member. Then the common edges between adjacent elements such as AB and CD in Figure 3-8(a) are drawn perpendicular to the lines connecting centroids of adjacent elements through their midpoints M and N. The lengths of AB and CD are equal to the member depth h_c. Finally, the element edges in the longitudinal directions such as BC and AD are drawn by connecting points B and C, and A and D. The shape of i^{th} element is thus determined. In the same way, shapes of other elements can be determined. With this kind of modelling, distribution

of normal and shear springs along the common edges are still perpendicular to the line connecting centroids of adjacent elements, and the element formulation remains unchanged in iAEM. In the same way, the out-of-plumbness or combined out-of-straightness and out-of-plumbness can be modelled (see Figure 3-8(b) and (c)).

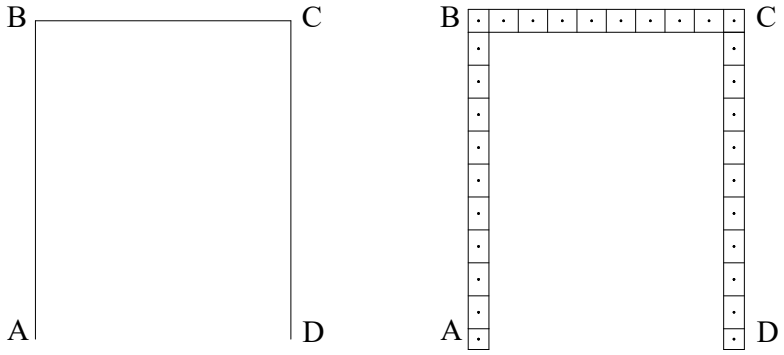

(a) Portal frame (b) iAEM model

Figure 3-9 Portal frame modelling using iAEM without geometric imperfections

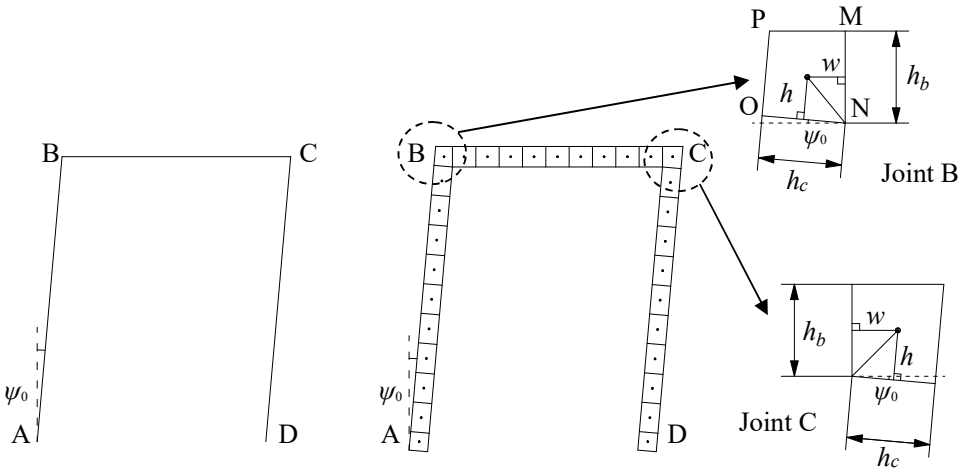

(a) Portal frame (b) iAEM model (c) Joint elements

Figure 3-10 Portal frame modelling using iAEM with out-of-plumbness

When the explicit modelling approach is used in iAEM to account for initial geometric imperfections, employment of rectangular elements to connect the beam and column members as in the modelling of idealized frames without geometric imperfections (see Figure 3-9) becomes impossible. Non-rectangular joint element is

therefore created to accommodate the beam and column members with geometric imperfections. For example, the out-of-plumbness with an angle of ψ_0 is considered for the portal frame shown in Figure 3-10(a). The beam and column elements of the frame employ the conventional rectangular elements (see Figure 3-10(b)). The geometry of the iAEM element at Joint B can be determined as follows. Firstly, the inner edges of the joint element, MN and ON, have a length of sectional depths of the beam and column of h_b and h_c, respectively (see Figure 3-10(c)). MN is perpendicular to the horizontal line, and ON has an inclined angle of ψ_0 with respect to the horizontal line. Then, the outer edges of the joint element, OP and PM can be determined by chamfering the outer shape lines of the frame. Finally it is assumed that the distances from the centroid of joint element B to the common edges between the adjacent beam and column elements are w and h, respectively, which can be determined by solving the following geometric relations (see Figure 3-10(c)):

$$\begin{aligned} &\tan^{-1}\left(\frac{w}{h_b/2}\right)+\tan^{-1}\left(\frac{w}{h_c/2}\right)+\tan^{-1}(\psi_0)=\frac{\pi}{2} \\ &w^2+\left(\frac{h_b}{2}\right)^2=h^2+\left(\frac{h_c}{2}\right)^2 \end{aligned} \tag{3-2}$$

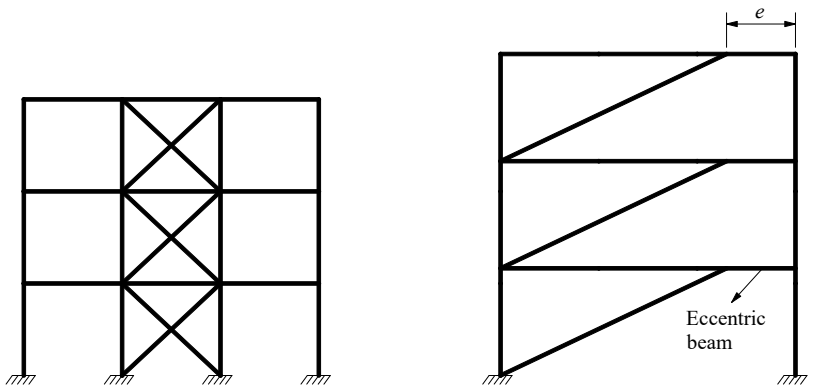

(a) (b)

Figure 3-11 Braced frames: (a) concentrically braced (b) eccentrically braced (Li and Li, 2007)

In the same way, the geometry of the iAEM element at Joint C can also be determined. With this kind of modelling, the element formulation of iAEM remains unchanged, and the initial geometric imperfections of framed structures can be modelled explicitly. Using this joint modelling technique, the members that non-perpendicularly join at a common point as often seen in the braced steel structures (see Figure 3-11) can be readily modelled.

3.5 Numerical examples

3.5.1 A steel column

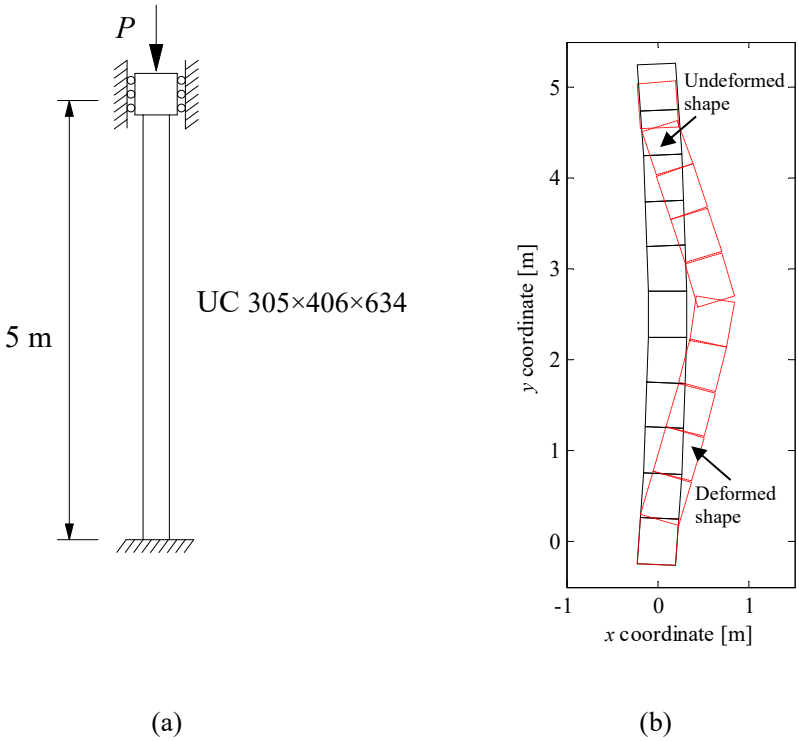

(a) (b)

Figure 3-12 The fixed-fixed column: (a) boundary condition (b) its model with out-of-straightness of 2% in iAEM

The influence of the out-of-straightness on the column buckling capacity is studied for a 5-m long column. As shown in Figure 3-12(a), the column is fixed at the bottom, and horizontal and rotational movements are prevented at the top. The column section is the wide flange section of UC 305×406×634. The elastic modulus of the material is

E = 210 GPa and the yield strength is f_y = 355 MPa. The material model used for the analysis is the bilinear stress-strain model with the strain hardening ratio of 0.3%.

Based on a convergence study, it is found that 11 elements give sufficiently accurate results, and thus used to model the column in iAEM (see Figure 3-12(b)), and out-of-straightness is modelled explicitly using the method described in Section 3.2. Different maximum values of out-of-straightness are introduced at the midspan: 0.1%, 1% and 2% of the column length. The load displacement curves from iAEM analysis are shown in Figure 3-13, and the curves from the finite element analysis in SAP2000 are also plotted for comparison. It can be seen that the results from iAEM analysis agree well with those from SAP2000, and with the increase of out-of-straightness, the buckling load capacity of the column decreases quite significantly from 28,120 kN to 24,580 kN, and further to 21,740 kN.

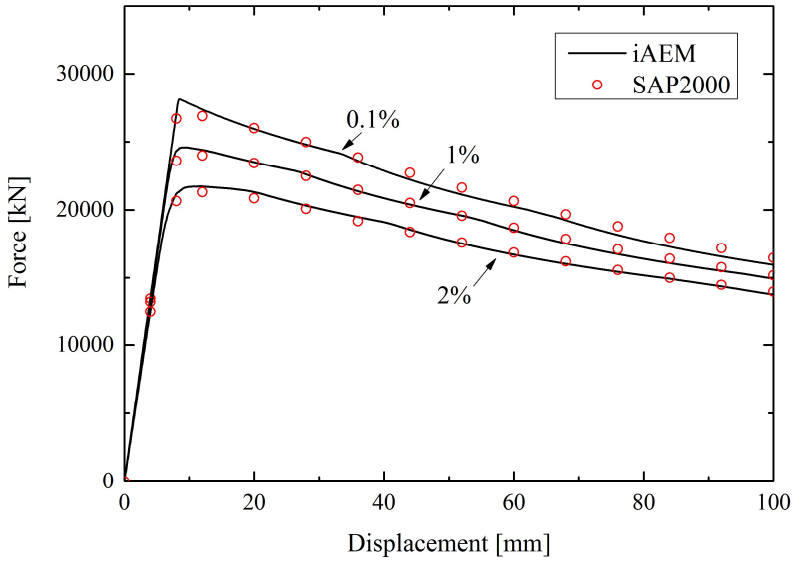

Figure 3-13 Force versus displacement curves of the column with fixed-fixed boundary condition

3.5.2 Vogel portal frame

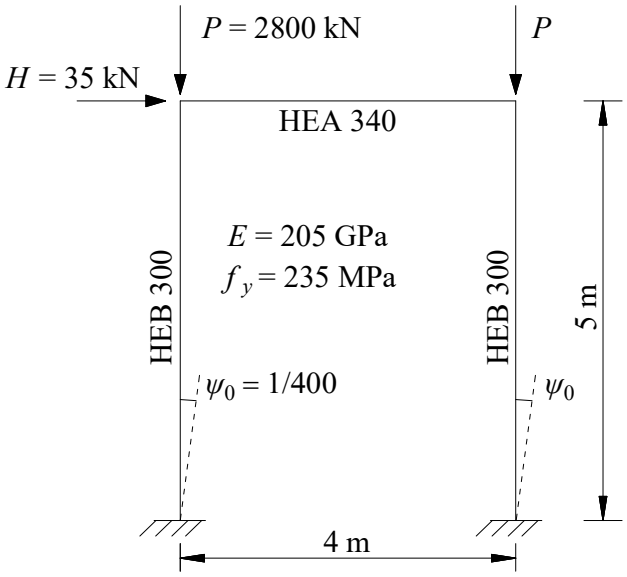

Figure 3-14 European calibration frame, portal frame (Vogel, 1985)

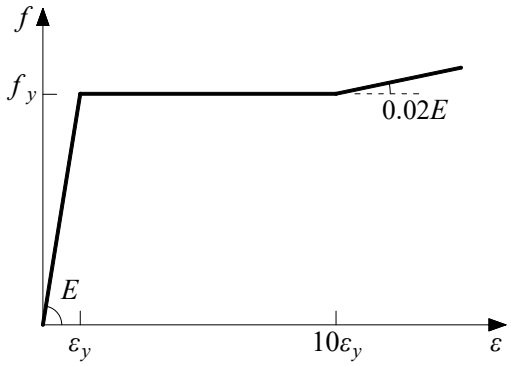

Figure 3-15 Stress-strain relationship of the steel material (Vogel, 1985)

The portal frame as shown in Figure 3-14 is one of the three frames selected by European Convention for Constructional Steelwork (ECCS) for the calibration of second-order inelastic analysis (Vogel, 1985). This frame is fixed at its base, and is subjected to vertical and horizontal loads at its top. The horizontal load produces a side sway, inducing significant second-order $P-\Delta_0$ effect on the members. The loads shown in Figure 3-14 are for the case when the load factor is $\gamma=1.0$, and the

real loads will be these loads multiplied by the load factor γ. A tri-linear stress-strain relationship as illustrated in Figure 3-15 is adopted for the steel material in the analysis. Strain-hardening starts at the strain $\varepsilon = 10\varepsilon_y$, where ε_y is the yield strain, and the hardening modulus is taken as 2% of the elastic modulus E. To account for the residual stresses for the hot-rolled sections of the frame, the residual stress pattern as shown in Figure 3-3 is used. The out-of-plumbness is $\psi_0 =$ 1/400, which is calculated using Equation (3-1) recommended by ECCS (1984). The initial out-of-straightness is a maximum offset of 0.1% of the member length at midspan, but it is not modelled in the iAEM analysis because for this unbraced frame, the $P-\delta_0$ effect is not dominant.

The second order inelastic static analysis is carried out using iAEM. The initial imperfections including residual stresses and out-of-plumbness are explicitly modelled following the methods described in Sections 3.1 and 3.2, respectively. The undeformed and deformed shapes of the iAEM model are shown in Figure 3-16. The load factor versus horizontal displacement curves at top of the frame from iAEM analysis are presented in Figure 3-17. In the same figure, the result obtained by Vogel (1985) using the second-order plastic-zone analysis is also plotted for comparison. It can be seen that when both geometric and material imperfections are considered, the result by iAEM agrees very well with that by Vogel (1985). The predicted ultimate load factor is 0.9840 (-3.7%) compared to 1.022 given by Vogel (1985). From this figure, it can also be seen that when only the residual stresses are considered, the frame has the same initial stiffness as the perfect frame, but it yields earlier. When only the geometric imperfections are considered, the frame has smaller initial stiffness due to geometric effect. Softening of the frame due to these imperfections is prominent. The significant differences in the initial stiffness and ultimate load factor of the two curves with and without imperfections indicate that, in order to simulate

the real behavior of steel structures, it is essential to consider both geometric imperfections and residual stresses.

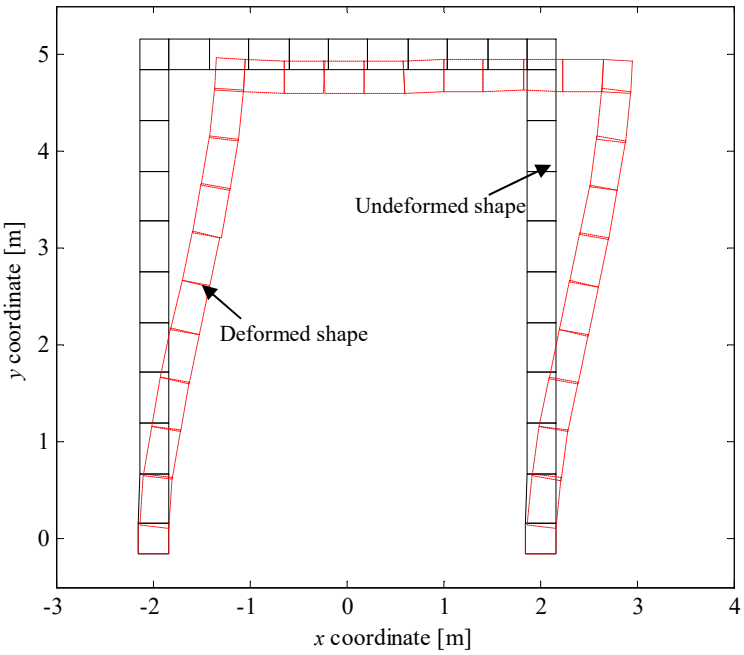

Figure 3-16 iAEM model of the portal frame (scale factor=40)

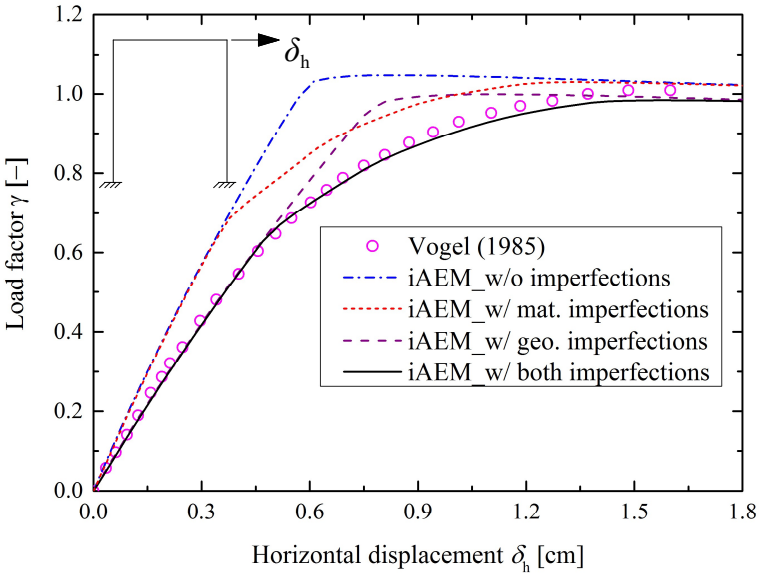

Figure 3-17 Load factor versus horizontal displacement curves of the portal frame

3.5.3 Vogel gable frame

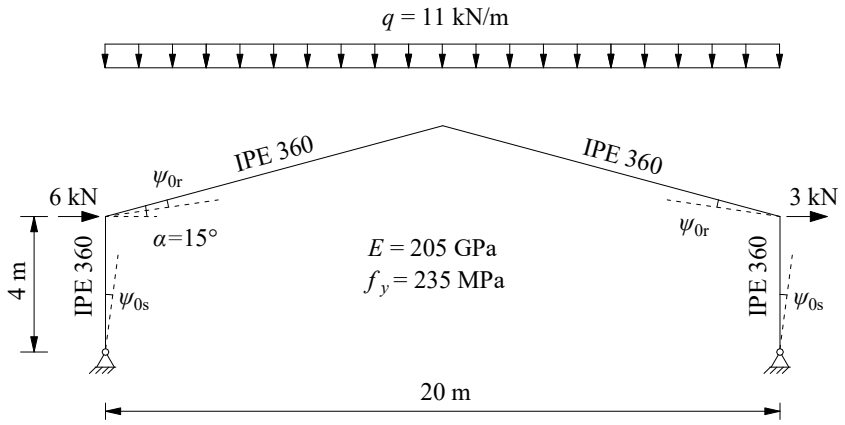

Figure 3-18 European calibration frame, gable frame (Vogel, 1985)

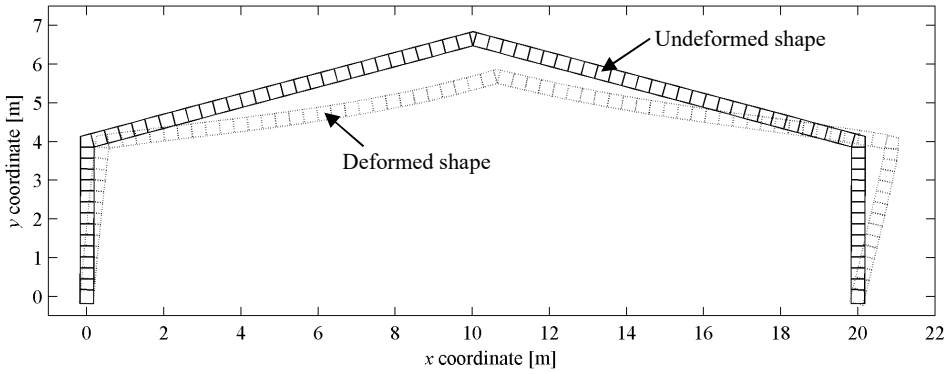

Figure 3-19 iAEM model of the gable frame (scale factor=3)

The gable frame shown in Figure 3-18 is the second frame selected by ECCS for the calibration of second-order inelastic analysis (Vogel, 1985). This frame is pinned at its base. The loads are applied both vertically and horizontally and are shown in Figure 3-18 for the load factor $\gamma = 1.0$. The vertical load is given as uniformly distributed load acting on the projected area of the roof. The horizontal load is assumed such that the wind force at the windward side has double intensity at the leeward side where negative (suction) wind force acts. The same tri-linear steel model and the residual stress pattern as used for the Vogel portal frame are also employed

for this gable frame. The out-of-plumbness of the column and roof members are $\psi_{0s} = 1/300$ and $\psi_{0r} = 1/432$, respectively. The out-of-straightness is a maximum offset of 0.1% of the member length at midspan, but is not modelled as well for this gable frame since the $P-\delta_0$ effect is negligible.

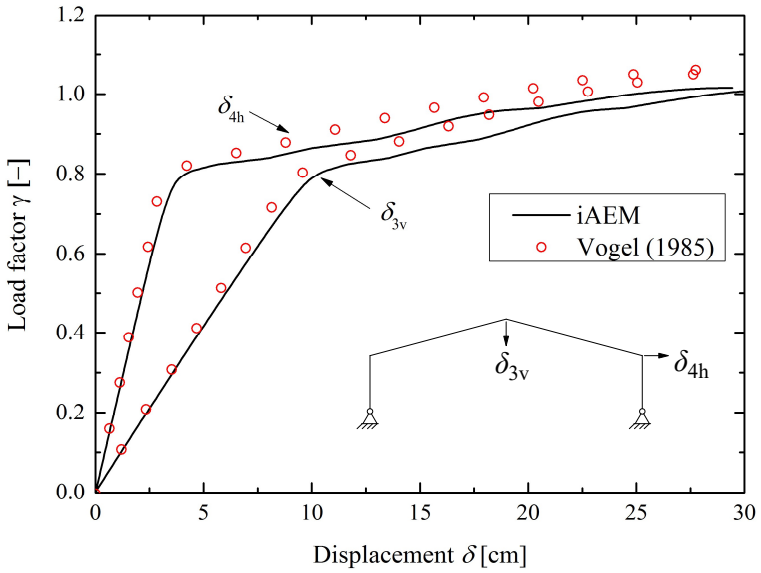

Figure 3-20 Load factor versus displacement curves of the gable frame

To model this gable frame in iAEM, 15 elements per column and 30 elements per roof beam are used, and the initial imperfections are explicitly modelled. After the second-order inelastic analysis in iAEM for this frame, its undeformed and deformed shapes are shown in Figure 3-19. The load displacement curves of the frame for Points 3 and 4 are plotted in Figure 3-20. For comparison purpose, the results by Vogel (1985) using the second-order plastic-zone analysis are also plotted in the same figure. It can be seen that the results from iAEM analysis generally agree with those from Vogel (1985). The predicted ultimate load factor from iAEM analysis is 1.016 (-5.0%) compared to 1.07 given by Vogel (1985).

3.5.4 Vogel six-storey two-bay frame

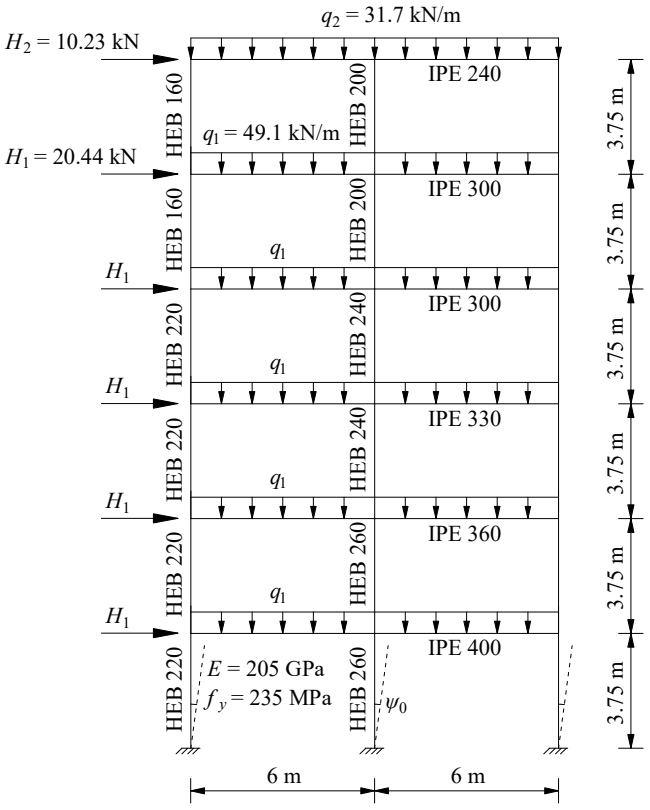

Figure 3-21 European calibration frame, six-storey two-bay frame (Vogel, 1985)

The third European calibration frame selected by ECCS is the six-storey two-bay frame as shown in Figure 3-21. This frame is fixed at its base, and is subjected to horizontal wind and vertical gravity loads. The wind load at the top of the frame is half of that at other intermediate levels because the projected area for the top level is half. Also, the distributed gravity load at the top of the frame is smaller than those on the other floors. The loads shown in Figure 3-14 are for the case when the load factor $\gamma = 1.0$. The sections for columns and beams are such that members at lower stories have larger resistances. For this frame, the same tri-linear steel model and the residual stress pattern as used for the Vogel portal frame are still employed. Based on Equation (3-1) recommended by ECCS (1984), the out-of-plumbness is calculated as $\psi_0 = 1/450$. Again for this unbraced frame, the initial out-of-straightness with a

maximum offset of 0.1% of the member length at midspan is not modelled as the $P-\delta_0$ effect on this structure is insignificant.

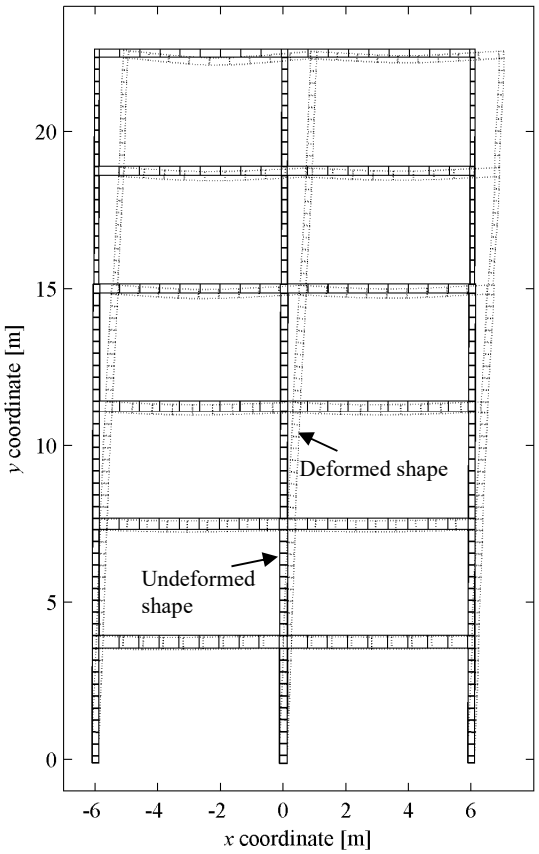

Figure 3-22 iAEM model of the six-storey two-bay frame (scale factor=4)

Ten elements per member are used to model this frame in iAEM, and the initial imperfections are also explicitly modelled as the previous examples. The undeformed and deformed shapes of the iAEM model are shown in Figure 3-22 after the second-order inelastic analysis for this frame. The load factor versus horizontal displacement curves at the 4th and 6th storey of the frame are plotted in Figure 3-23 along with those predicted by Vogel (1985) using the second-order plastic-zone analysis. When both geometric and material imperfections are considered, the results by iAEM compare very well with those from Vogel (1985). The predicted ultimate load factor is 1.113 (+0.2%) compared to 1.111 given by Vogel (1985). The load factor versus horizontal displacement curves at the 6th storey of the frame with

different out-of-plumbness are plotted in Figure 3-24. It can be seen that when the out-of-plumbness increases, the ultimate load factor of the frame reduces significantly from 1.113 to 1.036, and further to 0.951 due to the second-order effect. Therefore, it is important to include the geometric imperfection to model the real behavior of steel structures.

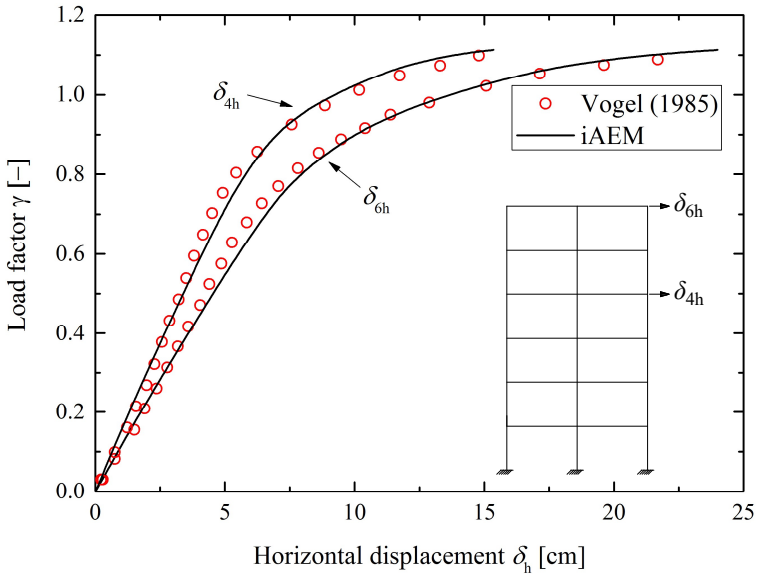

Figure 3-23 Load factor versus horizontal displacement curves of the six-storey two-bay frame

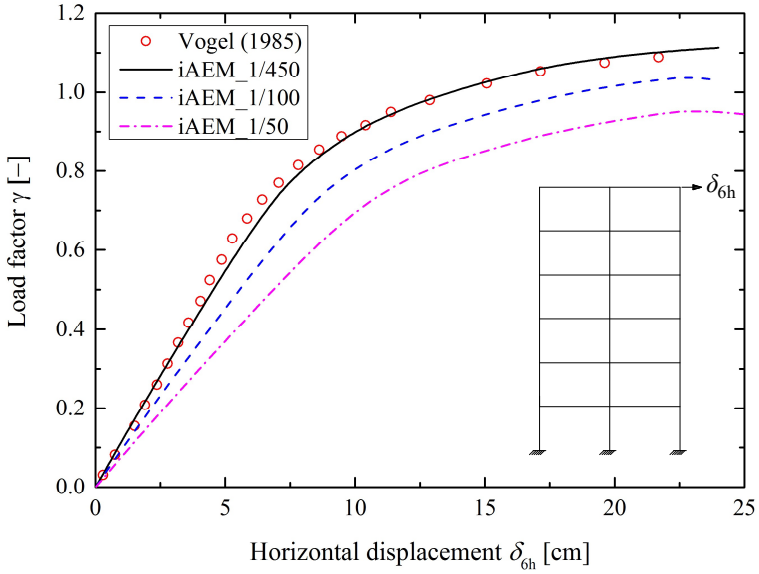

Figure 3-24 Load factor versus horizontal displacement curves at the 6th storey of the six-storey two-bay frame

3.6 Summary

In this chapter, the explicit modelling of initial material and geometric imperfections of real steel structures using iAEM is first proposed. Then the proposed modelling methods are used in the four numerical examples to consider the initial imperfections of steel structures. It is found that the results from iAEM analysis compare generally well with those from finite element analysis and published results, and the structural ultimate load capacity is decreased quite significantly due to residual stress and the second-order effect. Therefore, extension of the iAEM to consider initial material and geometric imperfections is useful to analyse the structural behavior of real steel structures.

4 Modelling of Semi-Rigid Connections of Steel Frames

The iAEM currently assumes rigid beam-to-column connection in the modelling; yet real connections of steel structures are seldom fully rigid. Connections become nonlinear with gradual yielding of connection plates, cleats, and bolts etc, which affects the ultimate capacity of the structures (Chen et al., 1996). Therefore, in order to obtain more accurate behavior of steel frames, the iAEM is extended to consider semi-rigid connection behavior by the component method. In this chapter, the importance of modelling semi-rigid connection of steel structures is first explained. Then the component method to model the bolted-angle connections in iAEM is described. Finally, modelling of bolted angle connections in iAEM is validated through some numerical examples.

4.3 Modelling of semi-rigid connections using iAEM

4.3.1 Why should semi-rigid connections be modelled?

It is a common engineering practice to assume either pinned or fully rigid connections between beams and columns. However, numerous experiments have shown that the actual behavior of a connection can be represented by a nonlinear moment-rotation $M-\phi_c$ curve which can generally be obtained from test results. Typical moment-rotation $M-\phi_c$ curves of several commonly used connections are shown in Figure 4-1. As illustrated from the figure, the two extreme cases are the ideally pinned (i.e. the horizontal line) and perfectly rigid (i.e. the vertical line) connections, and those

connections lie between the two extreme cases are classified as semi-rigid connections.

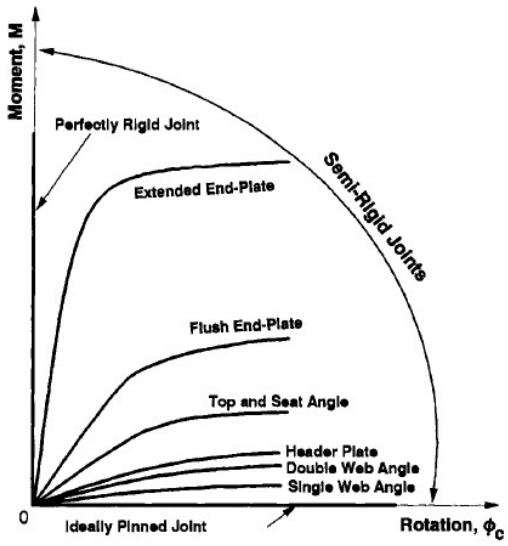

Figure 4-1 Typical moment-rotation curves of common connections (Chan and Chui, 2000)

The structural response of steel frames is closely related to the behavior of beam-to-column connections. The nonlinear characteristics of beam-to-column connections play a very important role in frame resistance and stability, because semi-rigid connections enable larger storey drift than rigid connections. This larger storey drift may influence the *P*-Δ effect and lead to column buckling at earlier stage than assumed otherwise. As a result, the structural behavior may be significantly different for the two steel frames with one considering the semi-rigid connection behavior whereas the other not.

During progressive collapse, failure of structural members initiates at the weakest point of the structure, usually at the semi-rigid connections for steel structures. The failure of connections from the WTC 5 building that partially collapsed on September 11, 2001 (FEMA, 2002) indicates that that modelling of semi-rigid connections is conceptually appropriate to employ in nonlinear dynamic analysis and progressive collapse analysis. Figure 4-2(a) shows a failed connection from the seventh floor of

the building. It is observed that the main failure feature is tear-out at the bolt locations in the web of the connected beam and that substantial rotational, shearing and axial deformation occurs during the failure process. Figure 4-2(b) shows a second failed connection recovered from the eighth floor of the WTC 5 building. The failure mode is different from that in Figure 4-2(a), and it is due to the shearing fracture caused by tear-out of the bolts for the single-angle web connection plate. It is observed that the failure also involves significant axial deformation.

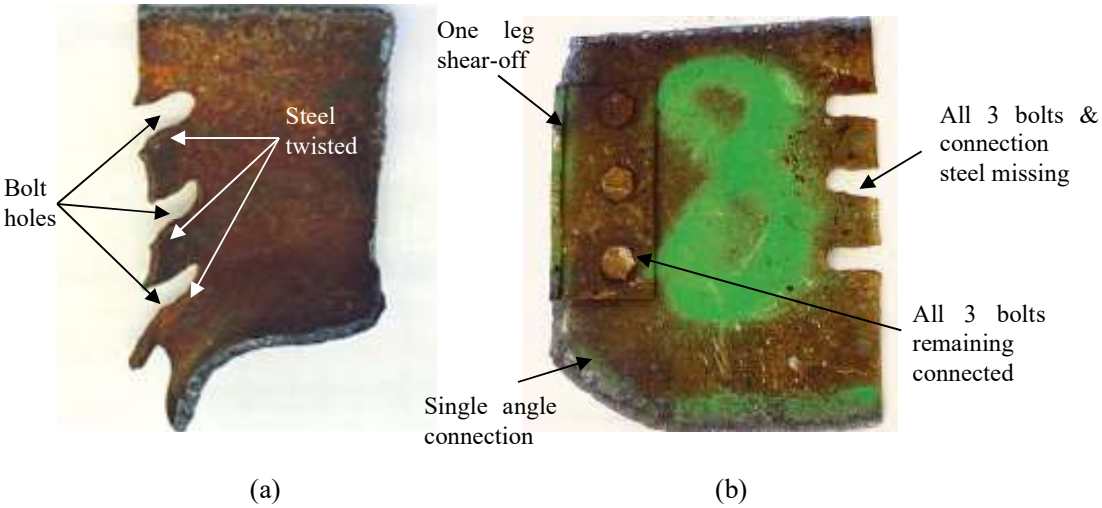

Figure 4-2 Connection failures from the WTC 5 building (FEMA, 2002): (a) Failed connection sample from 7th floor and (b) Failed connection sample from the 8th floor

Therefore, in order to obtain a more accurate prediction of progressive collapse response of steel frames, it is necessary to properly model their semi-rigid connection behavior. Since the current iAEM in the literature assumes rigid connection in the modelling, it is essential to extend this method to realistically account for the semi-rigid connection behavior of the steel frames.

4.3.2 Modelling of bolted-angle connections using the component method

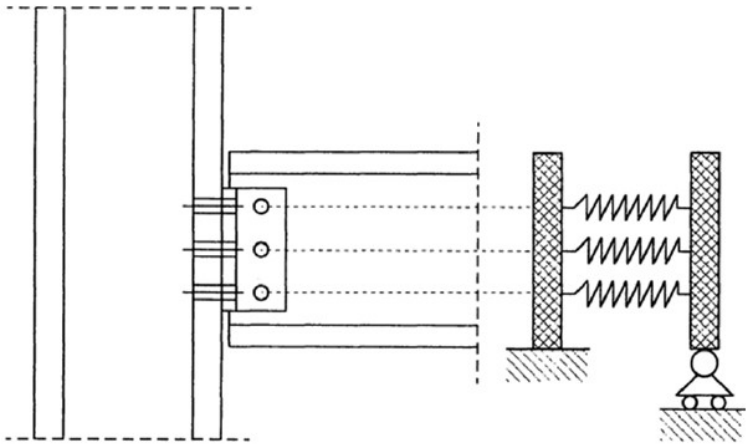

Figure 4-3 Component-based model for web angle connection (Wales and Rossow, 1983)

For steel frames, several methods can be used to model semi-rigid connection behavior, i.e. analytical, empirical, experimental, informational, component and numerical methods (Díaz et al., 2011). The component method models a connection as an assembly of extensional springs (component) and rigid links, and each spring represents a specific part of a connection with its own strength and rigidity (see Figure 4-3). The behavior of the connection is obtained by knowing the mechanical and geometrical properties of each component of the connection. This method was initially developed in the 1980s (Wales and Rossow, 1983), and later introduced in Eurocode 3 Part 1.8 (Eurocode, 2005). Until recently, with the advancement of computer hardware and software and acceptance of performance based design (PBD), the component method has gradually gained great popularity simply because of its advantages over other methods. For instance, it may apply to any connection type, connection configuration and loading condition provided that the description of the load-deflection curve of each component is properly characterized. Compared to the detailed FEM (numerical) model, the component method is easier to use and costs much less computational resources. Therefore, the component method is perhaps the most effective solution to predict the complex connection behavior of the whole structure against progressive collapse. In addition, the component method is

compatible with iAEM as the nonlinear load displacement relationship of the connection component can be easily defined for the connecting springs of iAEM elements. Therefore, in this study, the component method is adopted to model the semi-rigid connection behavior in iAEM.

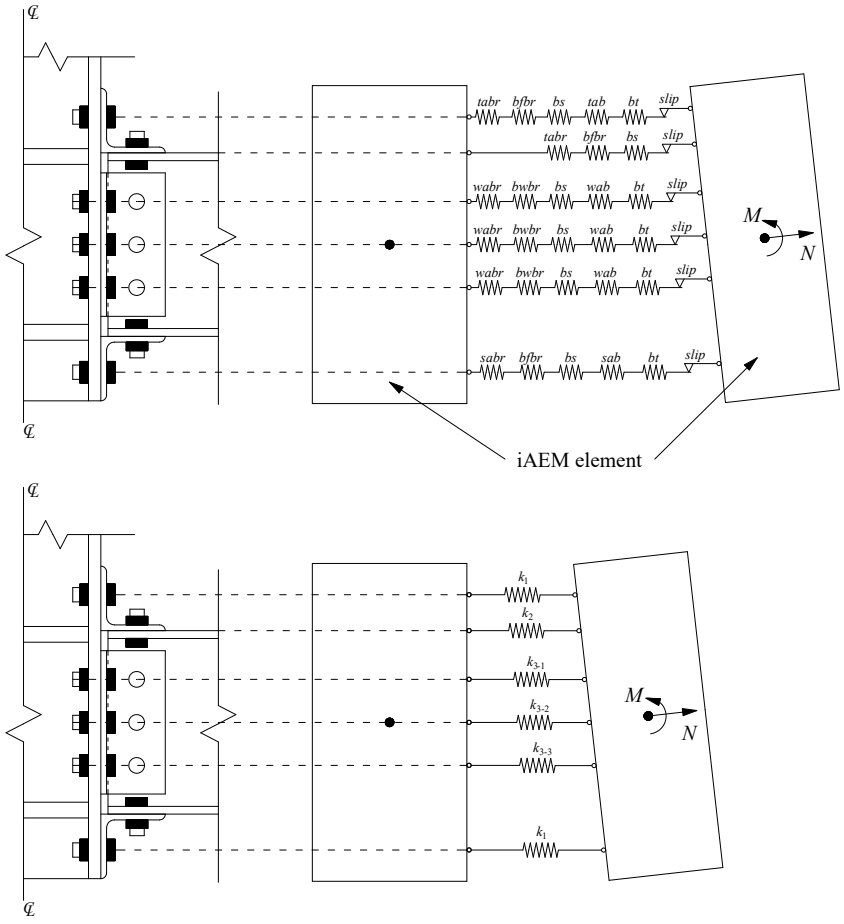

Figure 4-4 Component-based model of bolted-angle connections in iAEM

As to which type of semi-rigid connections to be modelled in iAEM by the component method for progressive collapse analysis, Yang and Tan (2012b) and Yang and Tan (2013a) conducted seven experimental tests on the performance of common types of bolted steel beam-to-column connections subjected to catenary action, and the test results showed that bolted-angle connections, such as web cleats and top and seat with web angles (TSWA) performed better in the development of catenary action than the other types of connections. The better performance was

attributed to extremely high ductility (rotational capacity) through deformation of the connected angles. Therefore, in this study, bolted-angle connections are modelled by the component method in iAEM, and the component-based model proposed by Yang and Tan (2013b) is applied. The basic components of the model (see Figure 4-4) include top, web and seat angle in bearing (*tabr*, *wabr*, *sabr,* respectively); beam flange and beam web in bearing (*bfbr*, *bwbr*, respectively); bolt in shear (*bs*); top, web, and seat angle in bending (*tab*, *wab* and *sab*, respectively); bolt in tension (*bt*); and bolt in slip (*slip*). As shown in Figure 4-4, the component-based model can be further simplified by combining all the components at one bolt row as one equivalent spring. For example, all the components located at the top bolt row, including *tabr*, *bfbr*, *bs*, *tab*, *bt* and *slip*, have been combined as one spring k_1. In this model, it is assumed that k_1, k_{3-1}, k_{3-2}, and k_{3-3} can sustain tensile forces, whereas all the compression forces are sustained by the spring k_2. This assumption is used by most of the proposed component-based model (Eurocode, 2005; Faella et al., 2000; Lemonis and Gantes, 2009; Park and Wang, 2012). In this study, it is also assumed that a rigid shear spring is used to transfer vertical shear forces in the component-based model, and the strain rate effect on the connection behavior is not considered.

For the bolted-angle connections loaded to large deformation during progressive collapse, connection failure is dominated by the interactions between the angles and the bolts under large tension force. Shen and Astaneh-Asl (2000) developed a component-based model to simulate the hysteretic behavior of bolted angles under seismic loading condition. Yang and Tan (2013c) also proposed a component-based model of bolted angles under monotonic tension force. Both models included the interaction between bolts and angles, and considered possible failure modes observed in their tests. Yang and Tan (2013b) later applied the component-based model of bolted angles under tension together with the other components to model the bolted-angle beam-to-column connections. The spring called “bolted angles under tension”

combines the three component springs, i.e. bolt in tension, angle in bending and bolt in slip. In iAEM, this equivalent "bolted angles under tension" spring is also used. It should be mentioned that if the column web is stiffened by horizontal stiffener plates, all the column components are assumed rigid, and do not have to be modelled. They can be modelled if the column deformation cannot be ignored. The individual property of each component is briefly described in the following subsections.

4.3.2.1 Bolted angle under tension

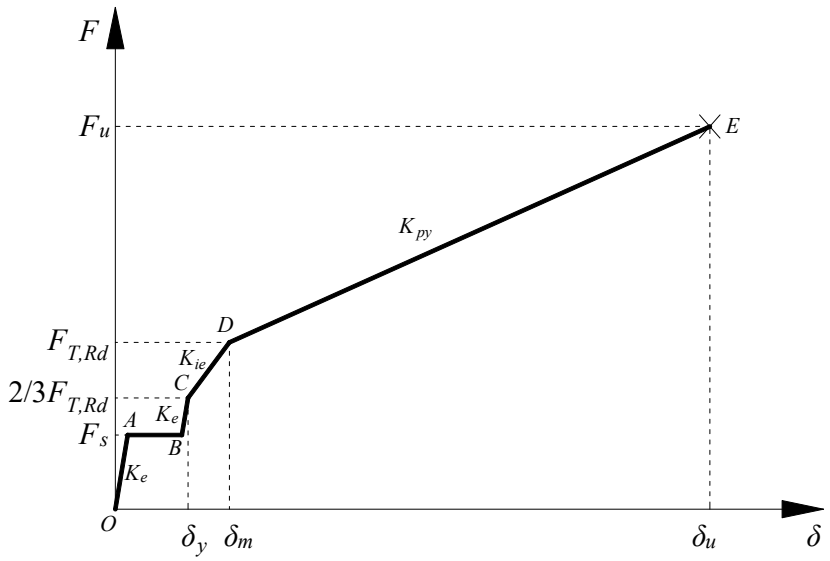

Figure 4-5 Load-displacement relationship of bolted-angle under tension (Yang and Tan, 2013c)

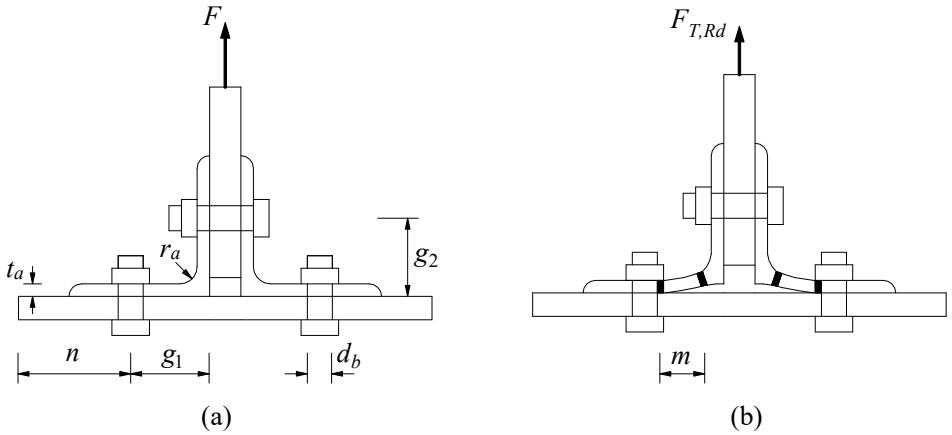

Figure 4-6 Initial yielding of the bolted-angle under tension

To model the nonlinear behavior of the component for bolted angle under tension, the load-displacement relationship proposed by Yang and Tan (2013c) is employed (see Figure 4-5). The deformation history of the angle consists of five stages: (1) elastic stage before bolt slippage (O-A), (2) bolt slippage stage (A-B), (3) elastic stage after bolt slippage (B-C), (4) transition stage (C-D), and (5) post-yielding/large deformation stage (D-E). The terms K_e, K_{ie} and K_{py} are the initial elastic stiffness, transition inelastic stiffness, and post-yield inelastic stiffness of the bolted angle, respectively. The terms δ_y, δ_m and δ_u represent the first yield displacement, plastic displacement and ultimate failure displacement of the bolted angle. As shown in Figure 4-6, when failure of the bolted angle is governed by the complete yielding of T-stub flange, the two plastic hinges can be formed at the angle legs when the displacement reaches δ_m at the load of $F_{T,Rd}$.

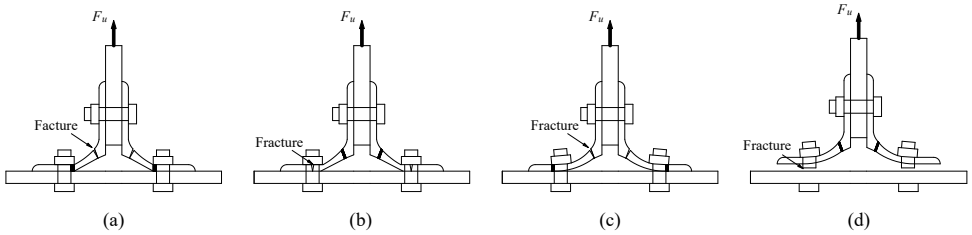

Figure 4-7 Failure modes of the bolted angle observed from Yang and Tan's test results (Yang and Tan, 2013c)

In the small deformation stage ($0 \le F \le F_{T,Rd}$), the values of $F_{T,Rd}$ and K_e are calculated based on Faella's model (Faella et al., 2000):

$$F_{T,Rd} = \frac{4M_{y,Rd}}{m} = \frac{b_{eff,a}t_a^2 f_y}{m} \tag{4-1}$$

$$K_e = \frac{0.5b_{eff,a}t_a^3 E}{m^3}\left(\frac{4\gamma}{4\gamma+3}\right) \tag{4-2}$$

where f_y is yield strength of the angle material, t_a is the angle thickness, $b_{eff,a}$ is the effective width of the angle, and m is the distance between the two plastic hinges

(see Figure 4-6). The equations for determination of $b_{eff,a}$, m and the coefficient γ can be found in the book by Faella et al. (2000). According to the book, the value of K_{ie} is recommended to be $K_e/7$. When failure of the bolted angle is governed by bolt failure with yielding of T-stub flange or bolt failure, calculation of $F_{T,Rd}$ can also be found in this book. The bolt slip resistance F_s is calculated as:

$$F_s = n_b c_f p_{pf} \tag{4-3}$$

where n_b is the number of bolts, c_f is the friction coefficient, and p_{pf} is the bolt pretension force applied during the tightening process. Since the bolt holes in the angles and thick steel plates were 2 mm oversize in the test by Yang and Tan (2013c), the normal gap between the bolt shank and the bolt hole is assumed to be 1 mm. There are two bolt holes in a bolted-angle connection, i.e, one hole at the angle, and the other at the connected element. Thus, the slip displacement δ_{slip} is assumed to be 2 mm. $c_f = 0.2$ and $p_{pf} = 40$ kN recommended by Yang and Tan (2013c) are used in this model.

In the large deformation stage ($F_{T,Rd} < F \le F_u$), the load displacement response of the bolted angles is due to significant material hardening and geometric nonlinearities. With the increase of tensile force, the deformation of the bolted-angle gradually increases until the final failure displacement δ_u is reached (see Figure 4-5). Four failure modes have been observed in the tests by Yang and Tan (2013c) (see Figure 4-7), including (a) angle fracture close to the heel; (b) angle fracture at the bolt hole; (c) angle fracture close to the heel with yielded bolts; and (d) bolt fracture with yielded angle. It has been found that the locations of plastic hinge formed in the angles are significantly influenced by the strength ratio of the angles and the bolts. Therefore, accounting for the four failure modes with interactions between the angles

and bolts, Yang and Tan (2013c) proposed a new method to calculate the ultimate displacement δ_u as below:

$$\delta_u = g_1^*(1+\varepsilon_u)\sin\left(\frac{\varepsilon_u g_1^*}{2t_a}\right) \tag{4-4}$$

$$g_1^* = g_1 - t_a - 0.8r_a + \eta d_b \tag{4-5}$$

where g_1 is the horizontal gauge length, r_a is the radius of the angle fillet, d_b is the bolt diameter (see Figure 4-6), and ε_u is the ultimate tensile strain of the angle material. The coefficient η considers the interactions between the strengths of the angle legs and the bolts, and it can be calculated by the following equations (Yang and Tan, 2013c):

$$\eta = 1.335 - 0.00242\frac{f_{yb}A_b b_{eff,a}}{F_{T,Rd}} \text{ if } \frac{f_{yb}A_b b_{eff,a}}{F_{T,Rd}} < 560 \tag{4-6}$$

$$\eta = -0.22 \text{ if } \frac{f_{yb}A_b b_{eff,a}}{F_{T,Rd}} \geq 560 \tag{4-7}$$

where f_{yb} and A_b are the yield strength of bolts and area of the bolt shank, respectively. After the ultimate displacement δ_u is determined, the ultimate resistance F_u can be calculated by the following incremental equation until the angle displacement reaches the failure displacement δ_u (Yang and Tan, 2013c):

$$F_{i+1} = F_i + \left[\left(b_{eff,a} - n_b d_{hole}\right)t_a f_u\right]\left(\frac{\delta_i + \Delta\delta}{\sqrt{\left(g_1^2 + \left(g_i + \Delta\delta\right)^2\right)}} - \frac{\delta_i}{\sqrt{\left(g_1^2 + \delta_i^2\right)}}\right) \tag{4-8}$$

where n_b is the number of bolts, d_{hole} is the bolt hole diameter, and f_u is the ultimate strength of angle material. The terms F_i and δ_i are the tensile force and angle displacement obtained from the previous step. $\Delta\delta$ is taken as a small incremental

displacement to calculate the tensile force in the current step F_{i+1}. From Equation (4-8), it can be seen that the stiffness K_{py} is not constant in the post-yielding stage.

In addition, the ultimate resistance of the bolted-angle connection should be limited to the tensile resistance of the bolts $B_{T,Rd}$, and it can be calculated by the following equation:

$$F_u \le \frac{2t_a}{\left(2t_a + 0.4g_1^*\right)} \cdot n_b \cdot B_{T,Rd} \tag{4-9}$$

$$B_{T,Rd} = f_{ub} A_b \tag{4-10}$$

where f_{ub} is the ultimate strength of bolt material.

4.3.2.2 Bolt in shear

Generally, shear failure of bolts is not critical for the connection behavior, especially for the connection loaded at ambient temperature. According to EC3: Part 1.8 (Eurocode, 2005), the shear resistance of bolts is given by:

$$F_{V,Rd} = 0.6 n_b f_{ub} A_b \tag{4-11}$$

The behavior of Grade 8.8 M20 bolts in double shear has been investigated experimentally by Yu et al. (2009), and based on their test result, it is proposed that at ambient temperature, bolts are assumed to reach their maximum shear resistance at a displacement of 2 mm, and maintain this resistance up to 3 mm, after which the bolts fracture in a brittle manner. The mathematical description of the shear resistance with the corresponding shear displacement δ_v is given by:

$$\frac{F}{F_{V,Rd}} = \begin{cases} -0.2\delta_v^2 + 0.9\delta_v & 0 \le \delta_v \le 2 \\ 1 & 2 < \delta_v \le 3 \\ 0 & \delta_v > 3 \end{cases} \tag{4-12}$$

4.3.2.3 Plate in bearing

When the bolted angle is under tension or compression, the plate components of the top, web and seat angles, beam flange and beam web will subject to bearing at the edges of bolt holes. Experimental tests have been conducted by Rex and Easterling (2003) to investigate the bearing behavior of a single plate with a single bolt, and they also developed an analytical model for plate in bearing. The proposed model has been successfully applied to the respective component-based model for fin plate (Sarraj, 2007) and bolted T-stub connections (Xu and Ellingwood, 2011). In this study, the analytical model developed by Rex and Easterling (2003) is also used to model the bearing behavior of the connection plates. The relationship between the bearing force F_{br} and the corresponding bearing displacement Δ_{br} is given by:

$$\frac{F_{br}}{F_{br,Rd}} = \frac{1.74\overline{\Delta}}{\left(1+\overline{\Delta}^{0.5}\right)^2} - 0.009\overline{\Delta} \tag{4-13}$$

$$\overline{\Delta} = \Delta_{br} K_{i,br} / F_{br,Rd} \tag{4-14}$$

$$F_{br,Rd} = \min\left(L_e, 2.76 d_b\right) \cdot f_{up} t_p \tag{4-15}$$

where $F_{br,Rd}$ is the bearing resistance, L_e is the distance from bolt center to plate edge, f_{up} is the ultimate strength of the plate steel and t_p is the plate thickness. The initial stiffness $K_{i,br}$ is calculated based on the bearing stiffness K_{br}, bending stiffness K_b and shear stiffness K_v using Young's modulus E_p and shear modulus G_p of the plate steel.

$$K_{i,br} = \frac{1}{1/K_{br} + 1/K_b + 1/K_v} \tag{4-16}$$

The individual stiffness is calculated as follows:

$$K_{br} = 120 t_p f_{yp} \left(d_b / 25.4 \right)^{0.8} \tag{4-17}$$

$$K_b = 32 E_p t_p \left(L_e / d_b - 0.5 \right)^3 \tag{4-18}$$

$$K_v = 6.67 G_p t_p \left(L_e / d_b - 0.5 \right) \tag{4-19}$$

4.4 Numerical examples

In this section, the bolted-angle beam-to-column connections are modelled by the component method in iAEM through three numerical examples, and the predicted results are validated against those from published experimental tests.

4.4.1 Yang and Tan (2013b) – Monotonic static connection test

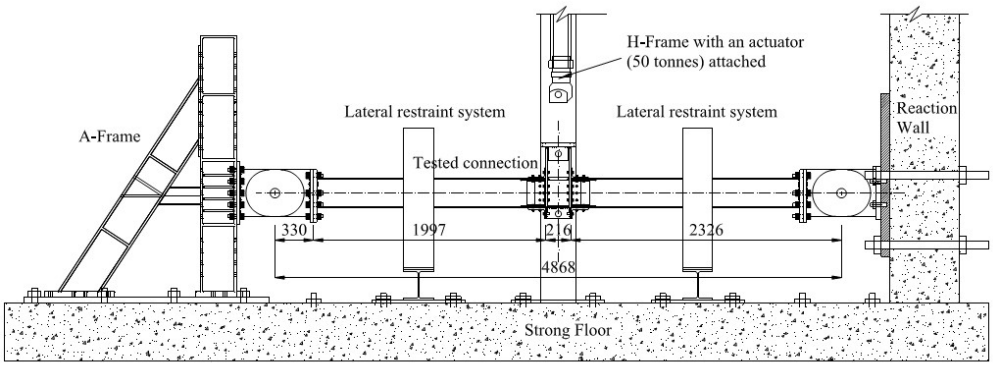

Figure 4-8 Test setup of the monotonic static connection test (Yang and Tan, 2013b)

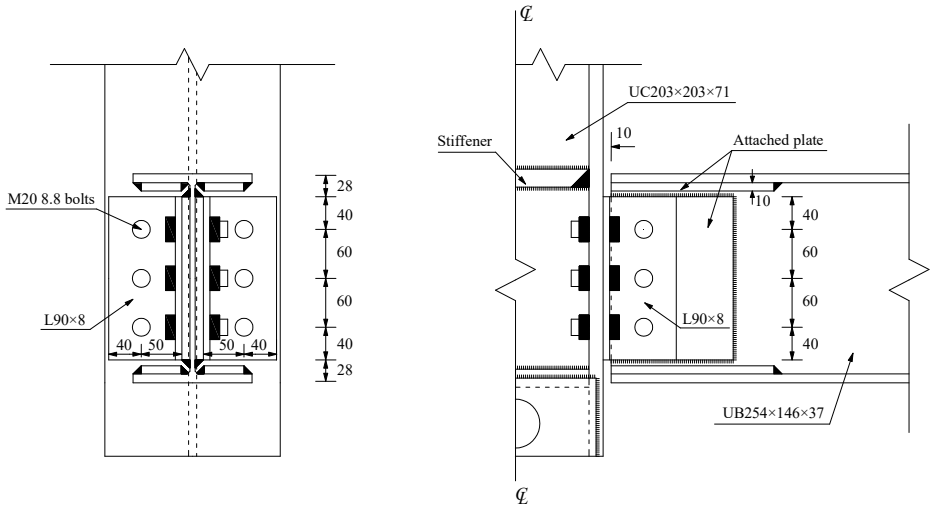

(a) W-8

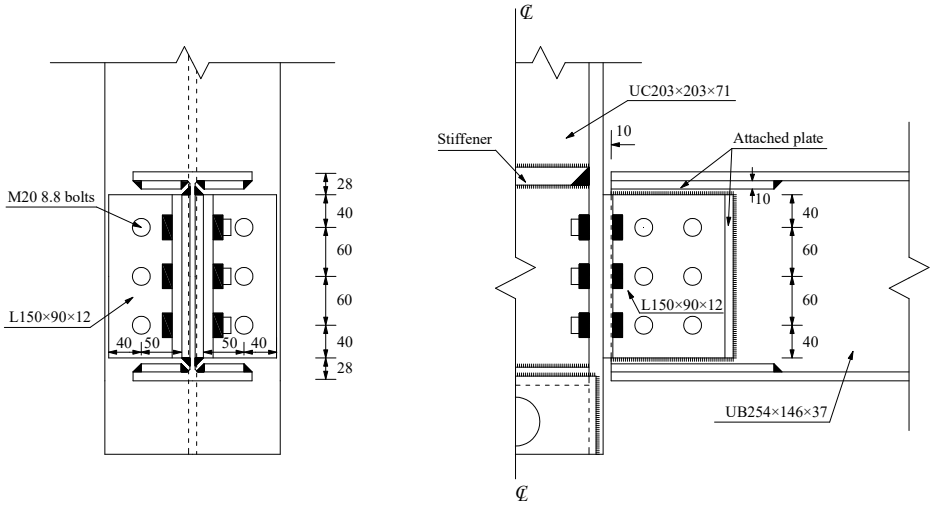

(b) W-12

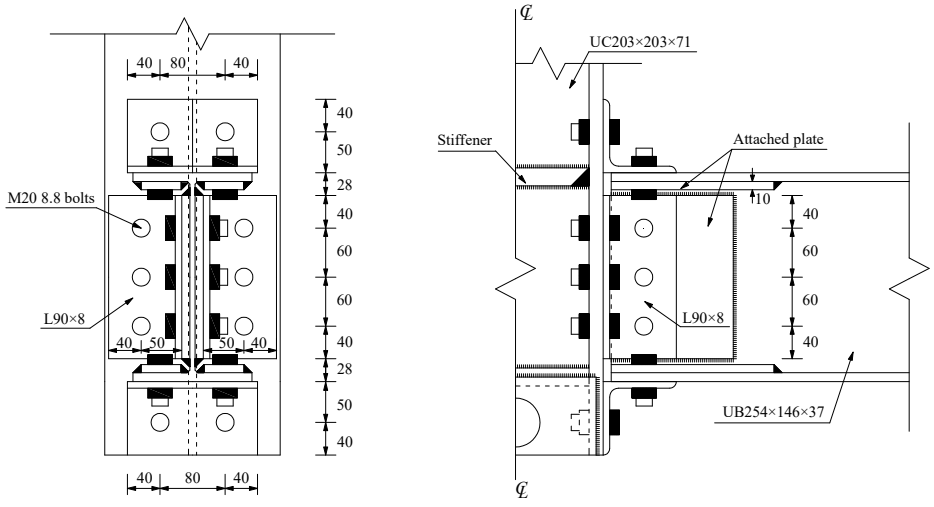

(c) TSW-8

Figure 4-9 Specimen configurations: (a) W-8, (b) W-12, and (c) TSW-8

In the first example, three out of the nine bolted-angle connections tested by Yang and Tan (2013b) are modelled by the component method in iAEM. In their test, monotonic static tests have been carried out for a double-span test beam to study the performance of bolted-angle connections subjected to catenary action under a middle column removal scenario (see Figure 4-8). An UC203×203×71 section and two UB254×146×37 sections were used for the column and beams, respectively. The distance between the two pin supports was 4868 mm as shown in Figure 4-8. The three connection specimens modelled by iAEM shown in Figure 4-9 are: (a) W-8, (b) W-12 and (c) TSW-8. The connection type, angle size, and material type of the modelled connection specimen are listed in Table 4-1. W-8 and W-12 are double web angle connections (WA) with angle thickness of 8 mm and 12 mm, respectively. TSW-8 is the top and seat with double web angle (TSWA) connections with angle thickness of 8 mm. In all the tests, the steel material of both columns and beams were Grade S355, whereas the steel material of angles was Grade S275. Grade 8.8 M20 bolts were used for all the specimens. A Grade-8.8 bolt has a nominal ultimate tensile strength of 800 MPa and a nominal yield strength of 640 MPa. Table 4-2 gives the material properties obtained from the coupon tests.

Table 4-1 Descriptions of test specimens

Specimen	Connection type	Angle size	Angle material type
W-8	Web angle	L90×8	I
W-12	Web angle	L150×90×12	II
TSW-8	TSWA	L90×8	I

Table 4-2 Material properties of tested angles

Connection type	Yield strength f_y (MPa)	Ultimate strength f_u (MPa)	Fracture strain ε_u
I	331	484	0.31
II	280	430	0.31

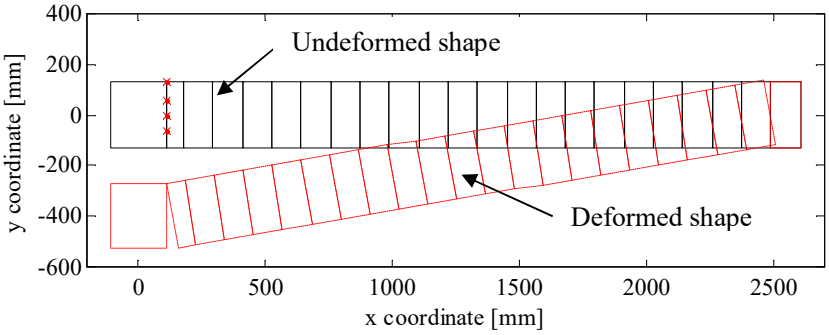

Figure 4-10 iAEM model of connection specimen W-8

Table 4-3 Key properties of connection springs

Specimen	Bolted angle under tension			Bolt in shear		
	K_e (kN/mm)	F_u (kN)	δ_u (mm)	$K_{i,V}$ (kN/mm)	$F_{V,Rd}$ (kN)	δ_u (mm)
W-8	52	200	31.1	233	259	3
W-12	279	261	24.3	466	517	3
TSW-8 (top/seat angle)	62	225	27.2	233	259	3
Specimen	Beam web/flange in bearing			Angle plate in bearing		
	$K_{i,br}$ (kN/mm)	$F_{br,Rd}$ (kN)		$K_{i,br}$ (kN/mm)	$F_{br,Rd}$ (kN)	
W-8	1059	494		594	305	
W-12	2118	989		1523	815	
TSW-8 (top/seat angle)	1683	786		594	305	

The iAEM model of the double-span test beam with connection specimen W-8 is shown in Figure 4-10, and only half of test structure is modelled due to symmetry. Four springs are used to model the beam-to-column connections W-8 and W-12. The bottom three springs represent the three web angle components at each bolt row, and the top spring is a rigid-plastic spring to consider the effect of the beam flange coming into contact with the column flange at large rotation. Six springs are used to model the connection TSW-8 as shown in Figure 4-4. For the web angle connections,

the three components of web angles are working together and influence one another. In the experimental tests, it was observed that the two springs corresponding to the bottom two bolt rows of web angles (k_{3-2} and k_{3-3}) failed simultaneously. Therefore, in the component-based model, in order to get a closer agreement with the test results, it is assumed that once the component k_{3-3} reaches deformation capacity, this spring goes into a plastic plateau stage and fails until k_{3-2} reaches deformation capacity. The key properties of the spring components including its initial stiffness, ultimate force and displacement are listed in Table 4-3.

In the test setup system (see Figure 4-8), there were some gaps between the support pin and the pin holes. These connection gaps have great influence on the development of the catenary action of the test beam. In order to simulate actual boundary conditions, a simplified horizontal restraint model (Yang and Tan, 2013b) as shown in Figure 4-11 is introduced into the component-based model in iAEM.

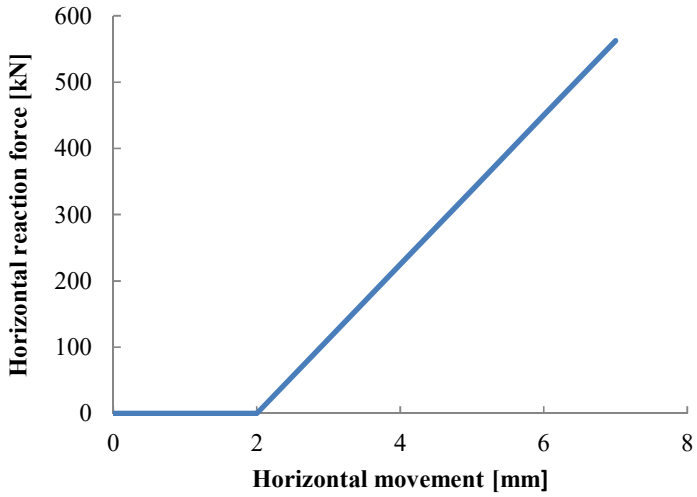

Figure 4-11 Horizontal restraint model

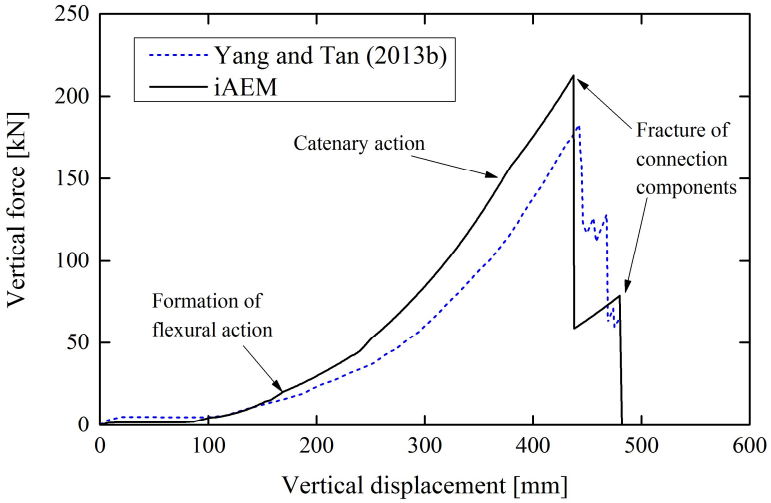

Figure 4-12 Vertical force versus vertical displacement curves of specimen W-8

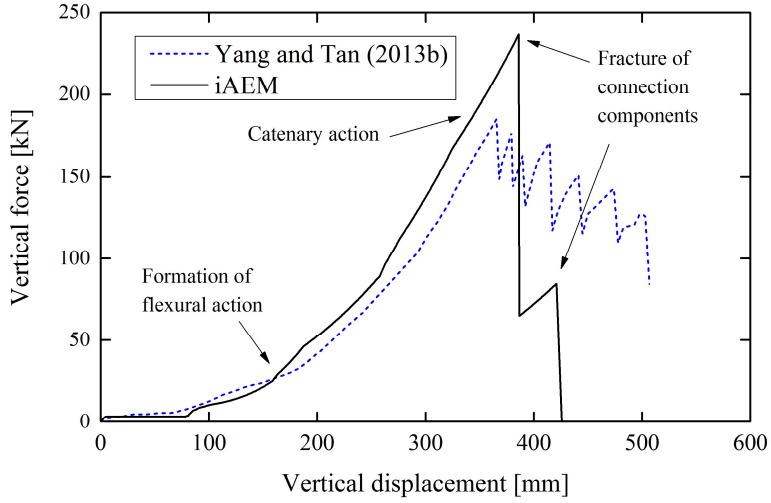

Figure 4-13 Vertical force versus vertical displacement curves of specimen W-12

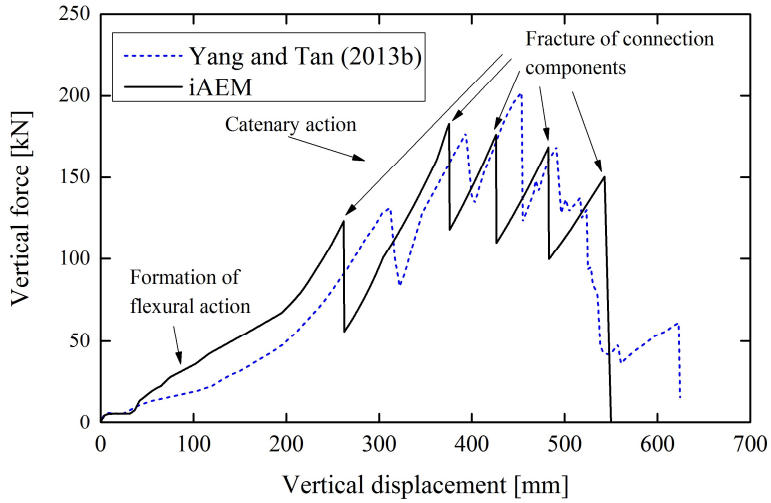

Figure 4-14 Vertical force versus vertical displacement curves of specimen TSW-8

Table 4-4 Comparison between results from component-based model in iAEM and the tests

Specimen	Vertical load (kN)			Displacement (mm)		
	Test	Model	Model/Test	Test	Model	Model/Test
W-8	183	212	1.16	443	437	0.99
W-12	185	236	1.28	365	386	1.06
TSW-8 (first peak load)	136	123	0.90	311	262	0.84

The vertical load versus vertical displacement curves of connection specimens W-8, W-12 and TSW-8 are plotted in Figure 4-12, Figure 4-13 and Figure 4-14, respectively. The test results by Yang and Tan (2013b) are also plotted in these figures for comparison. Table 4-4 summarizes the comparisons between the test results and those predicted by the component method in iAEM. It can be seen that the component-based model predictions in iAEM agree generally well with the experimental results. The component-based models can simulate the key responses of bolted-angle beam-to-column connections under a middle column removal scenario, including the formation of flexural action at small deformation stage, the development of catenary action at large deformation stage, and the fracture of connection components at the last stage. The predicted ultimate loads from iAEM are about 11% larger than those from the test, and the predicted ultimate displacements are quite close to the test results, and are around only 4% larger. The larger ultimate load may be due to the following reasons. Firstly, the effect of shear force and the initial residual stresses in the test specimens are not considered in the component-based model, which may reduce the overall connection resistance. Secondly, the lack of fit due to workmanship in the test introduces additional movement of the test specimen, and the 2 mm horizontal movement of the support pin in iAEM analysis may be smaller than the real movement in the test, making the iAEM result stiffer than the test result. In addition, the assumption in component method that the

behavior of each layer of springs is independent of the others may contribute to inaccuracy of results. Other possible reasons for the discrepancies in the overall shape of the predicted versus experimental curves may be due to different material and geometric properties used in the analysis from the actual properties in the experiment.

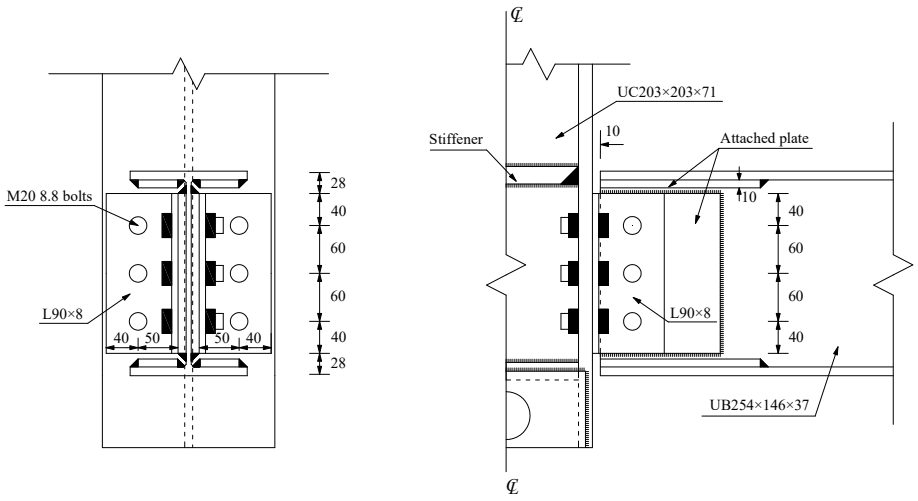

(a) W-8

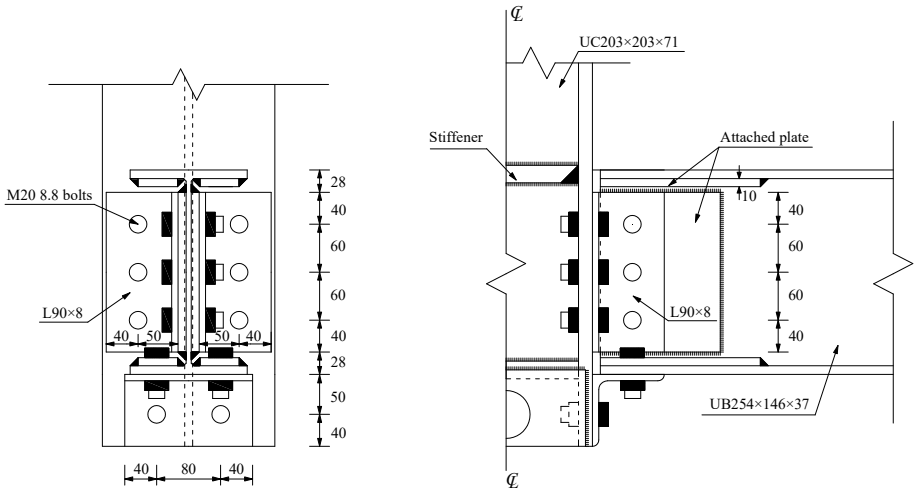

(b) New type

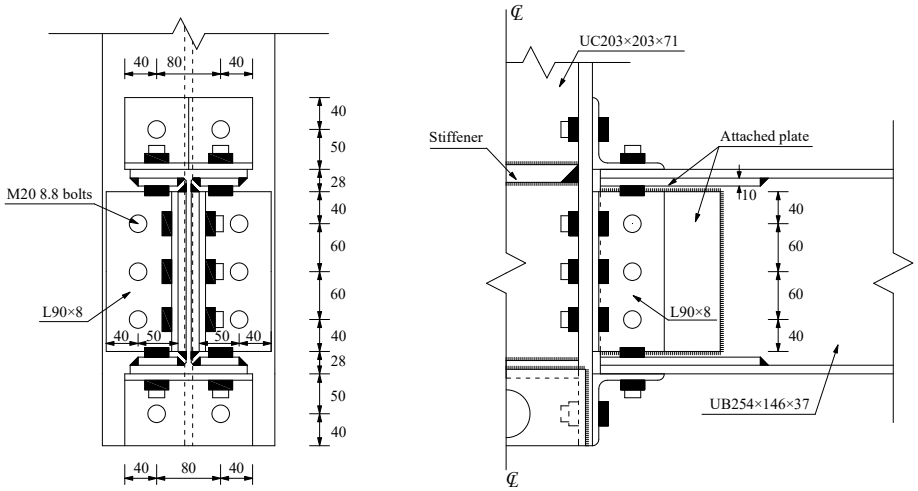

(c) TSW-8

Figure 4-15 Three different connection types: (a) W-8, (b) New type and (c) TSW-8

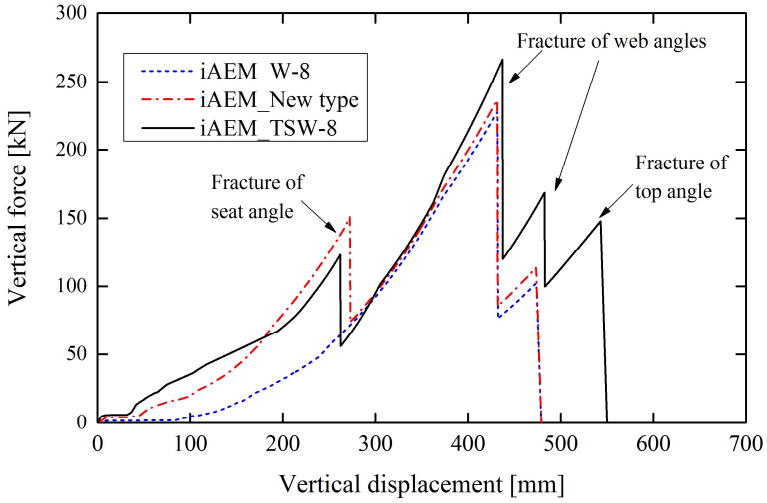

Figure 4-16 Vertical force versus vertical displacement curves of the three connections

In order to test versatility of the component method to predict the connection behavior in iAEM, a new type of bolted-angle connection, i.e., seat angle with double web angles, is modeled. This type of connection as shown in Figure 4-15 is between specimen W-8 and TSW-8. It is assumed that the new type of connection has the same material properties as W-8 and TSW-8. The vertical force versus vertical displacement curves of these three connections from the iAEM analysis using the component method are plotted in Figure 4-16. In the analysis, it is assumed that the

bottom two component springs of the web angles fail simultaneously as observed in the test by Yang and Tan (2013b). From this figure, it can be seen that the initial stiffness of the connections increase with the addition of seat and web angles. The TSW-8 connection has the largest peak vertical load capacity of 266 kN and ultimate vertical displacement of 545 mm. The new type of connection reaches almost the same load capacity of 237 kN and ultimate displacement of 472 mm as W-8 connection, which is reasonable because the new type of connection becomes W-8 connection actually after its seat angle fractures. Therefore, behavior of the new-type connection is reasonably predicted by the component method in iAEM. By simply adding or removing the component springs, the designer can quickly decide the suitable connection type for the desired connection behavior. Therefore, the component method in iAEM is also very suitable for design purpose.

4.4.2 Stelmack et al. (1986) - Cyclic connection test

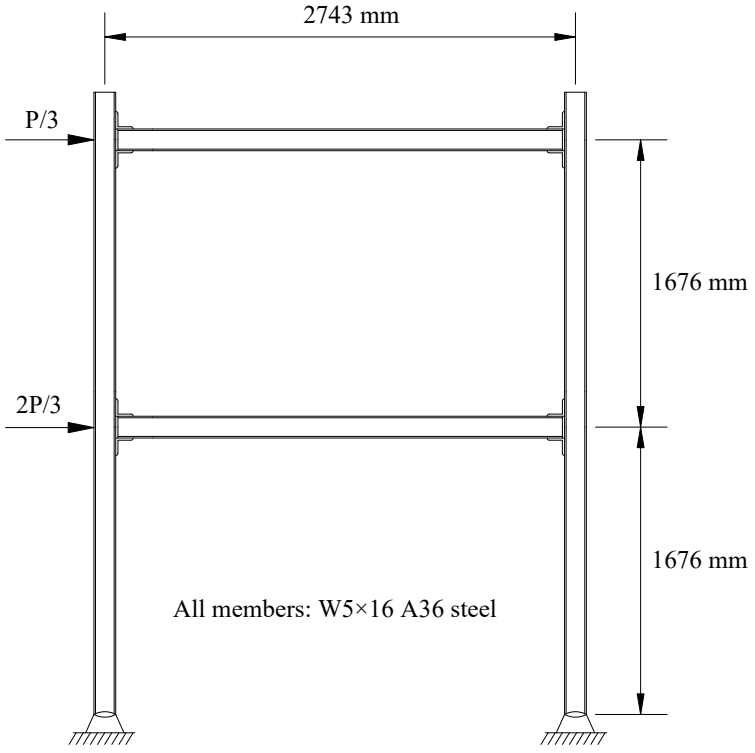

Figure 4-17 Two-storey single-bay test frame

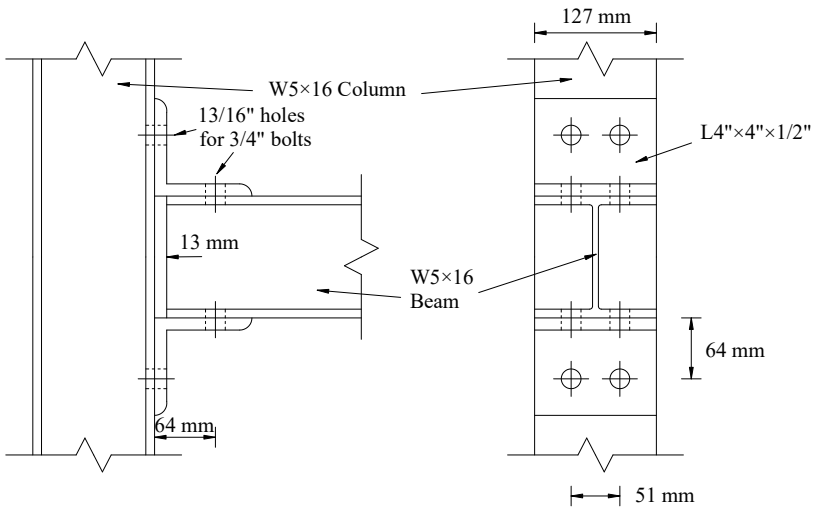

Figure 4-18 Half-inch thick top and seat angle connection

In this example, the two-storey single-bay frame as shown in Figure 4-17, initially tested by Stelmack et al. (1986) is considered. The frame is pin-supported at the two column bases, and fabricated with half-inch thick top and seat angle (TSA) beam-to-column connections. The column length is 1676 mm (5.5 ft), and the beam length is 2743 mm (9 ft). W5×16 wide flange sections (equivalent UC127×127×24) of A36 steel are employed for all the beams and columns. L4"×4"×1/2" angles (equivalent L100×100×12) and high-tensile, friction-type A-325 bolts of 3/4" (19 mm) are used for the TSA connections (see Figure 4-18). Load-indicating washers are used to verify the imposed tension force of 28 kips (125 kN) applied by torque wrench. During the test, cyclic lateral loads of 2P/3 and P/3 are applied at the first storey and the top storey, respectively.

Before modelling the whole frame using iAEM, the half-inch thick TSA connection is modelled alone by the component method using three springs. One spring is located at the tension side, and the other two springs are located at the compression side in case of a change of spring force from compression to tension. The key properties of the spring components including its initial stiffness, ultimate force and displacement are listed in Table 4-5.The moment-rotation curve predicted by iAEM is compared

with those from the monotonic connection tests. As the bolt-slippage was not observed in these tests, it is not considered in the iAEM connection model, but the increase of stiffnesses due to preloading need to be accounted for. In case of the bolt preloading, the stiffness of the top angle is evaluated by the following equation (Faella et al., 2000) :

$$K_{e,ta} = \psi \frac{0.5 b_{eff,ta} t_{ta}^3 E}{m_{ta}^3} \left(\frac{4\gamma_{ta}}{4\gamma_{ta} + 3} \right) \tag{4-20}$$

where the coefficient ψ , accounting for the preloading effects, is given by

$$\psi = 0.57 \left(\frac{t_p}{d_b \sqrt{m_{ta} / d_b}} \right)^{-1.28} \tag{4-21}$$

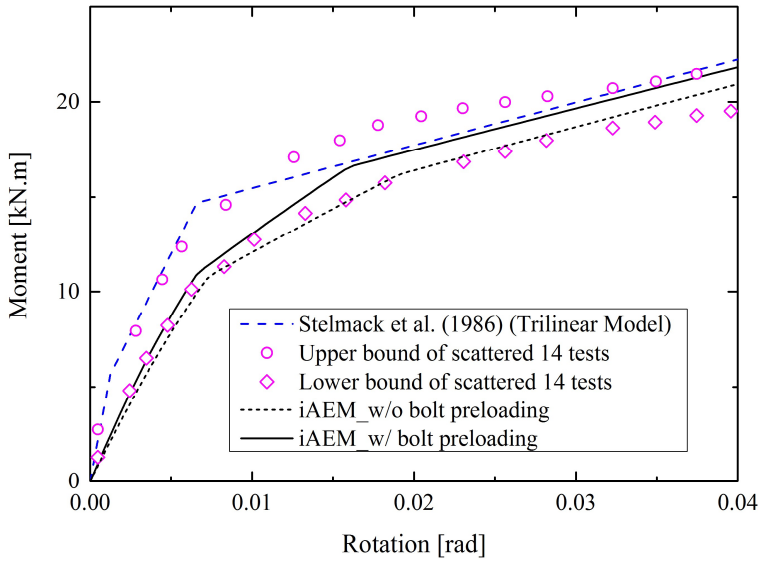

Figure 4-19 Moment rotation curve of the half inch thick TSA connection

Table 4-5 Key properties of connection springs

Bolted angle under cyclic loading			Bolt in shear		
K_e (kN/mm)	F_u (kN)	δ_u (mm)	$K_{i,V}$ (kN/mm)	$F_{V,Rd}$ (kN)	δ_u (mm)
183	217	20.3	210	233	3
Beam flange in bearing			Angle plate in bearing		
$K_{i,br}$ (kN/mm)	$F_{br,Rd}$ (kN)		$K_{i,br}$ (kN/mm)	$F_{br,Rd}$ (kN)	

743	200		910	621

The predicted moment rotation curves of the TSA connection with and without the bolt preloading effects from iAEM analysis is shown in Figure 4-19. For the same size of the TSA connection, fourteen monotonic moment-rotation test results have been reported by Stelmack et al. (1986). The upper and lower bounds of the scattered data along with the mean result represented using a trilinear model by Stelmack et al. (1986) are plotted in Figure 4-19. It can be seen that the mean test result is close to the upper bound curve, whereas the iAEM result with the bolt preloading has a smaller initial stiffness, but overall, by using the component method in iAEM, the moment-rotation curves of the TSA connection can be modelled generally well. This figure also shows that when the bolt preloading effect is not considered, the initial stiffness is smaller and the predicted moment-rotation curve is close to the lower bound of the test data. Therefore, in this case study, it is important to consider the effect of bolt preloading in order to better predict the connection behavior.

After validation of the monotonic connection behavior using the component method, the frame under cyclic lateral loads is then modelled by iAEM. The monotonic load displacement curves of the connection components, i.e., bolted angle under tension, bolt in shear and plate in bearing, are modified to account for the cyclic loading effects. It is assumed now the component springs can take both tension and compression forces. The hysteretic load-displacement curve of the bolted angle under cyclic loading by Liu et al. (2015) is shown in Figure 4-20. The backbone curve of the hysteresis model is the monotonic load displacement curve (Yang and Tan, 2013c) as described in Section 4.1.2, and the bolt slippage is not considered in this example. The unloading and reloading paths are based on the experimental results by Shen and Astaneh-Asl (2000). In compression, the load displacement curve remains virtually elastic under compression load with a large stiffness K_c from the supporting column.

In tension, the unloading stiffness is approximately equal to the initial stiffness K_e, then the angle is linearly pushed back to column flange (i.e. from Point B to Point C), in which the compression load at Point C is assumed to be equal to the tension force where unloading begins at Point A. The reloading curves always return to the point on the envelope where the unloading starts (i.e. OA and EA in Figure 4-20). The secondary loops inside the envelope follows the similar rules, but relate to the primary loops instead, as shown in a typical smaller cycle between O and B in Figure 4-20. The monotonic load displacement curves for components of bolt in shear and plate in bearing have been described in Section 4.1.2. The simplified bilinear models with symmetrical loading and unloading behavior are used for these components as shown in Figure 4-21 (a) and (b), respectively, where $K_{i,V}$ and $K_{i,br}$ are their initial stiffness, and $F_{V,Rd}$ and $F_{br,Rd}$ are their resistance.

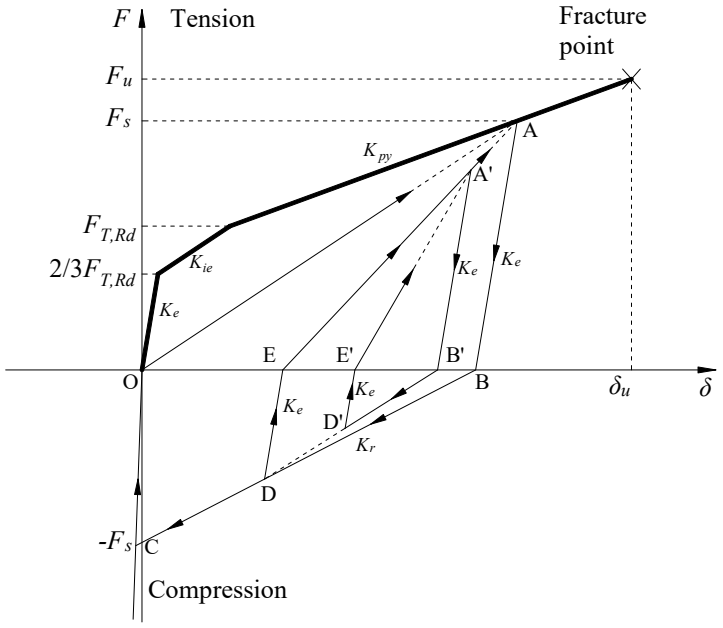

Figure 4-20 Hysteretic load-displacement curve of bolted-angle under cyclic loading

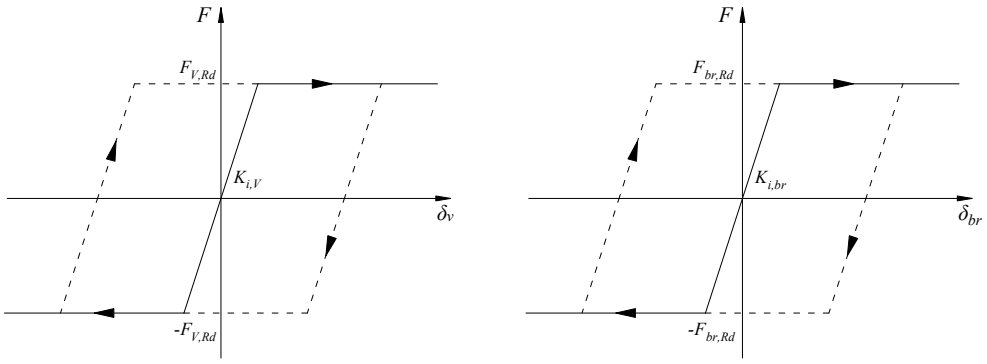

Figure 4-21 Hysteresis models for (a) bolt in shear and (b) plate in bearing

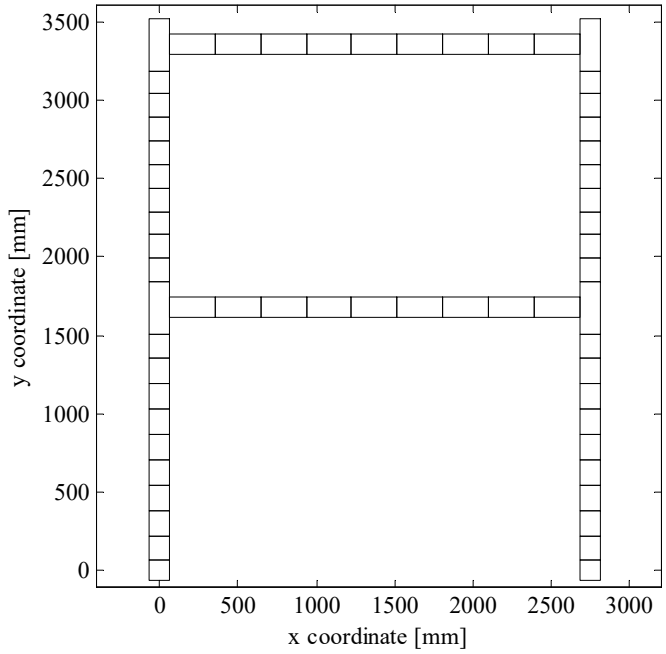

Figure 4-22 iAEM model of the frame

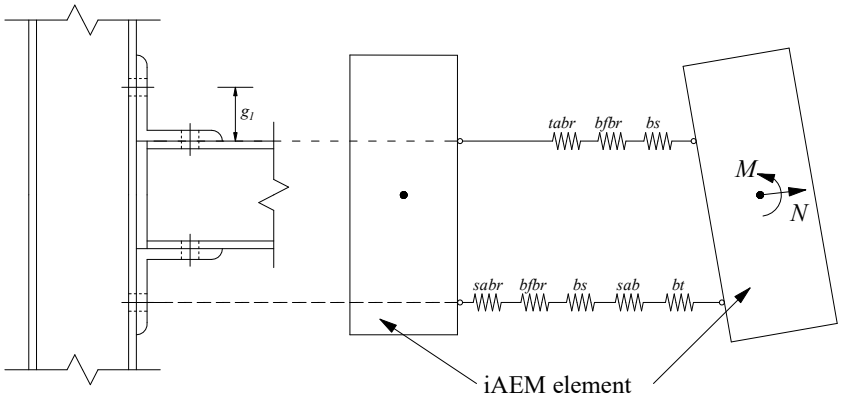

Figure 4-23 Component-based model of TSA in iAEM for the two-storey one-bay frame by Stelmack et al. (1986)

The iAEM model of the two-storey single-bay frame is shown in Figure 4-22. A total of 60 elements are used to model the beams and columns. Two spring rows are now used to connect the beams and columns, and the component springs can take both tension and compression force. The monotonic load displacement curve of each component is directly from the validated monotonic connection test, and to consider the cyclic connection behavior, the aforementioned hysteresis rules for the components are followed. The component-based model at one connection is shown in Figure 4-23 when the bottom side is in tension and the top side is in compression. The bottom springs are acting along the bottom bolt row at the column flange, and the top springs are acting along the beam top flange. When the load reverses, the acting position of the tension and compression force will be shifted by a gauge length g_1 (see Figure 4-23), but the lever arm between the top and bottom spring rows will still be the same. Therefore, in the current analysis, for easy incorporation of the cyclic load displacement curves of the components, the acting positions of the component springs remain unchanged throughout the analysis.

The lateral load P versus first- and top-storey displacement curves from iAEM analysis are shown in Figure 4-24 and Figure 4-25, respectively. The cyclic test results by Stelmack et al. (1986) and the predicted results under monotonic loading assuming rigid connection by iAEM are also plotted for comparison. From these two figures, it can be seen that the iAEM results match well with the test results when semi-rigid connection behavior is considered. The slightly smaller initial stiffness of the load-displacement curves can be attributed to the smaller initial stiffness of the predicted moment rotation curve as shown in Figure 4-19. In addition, it can be found that when the rigid connection is modelled using iAEM, the load displacement curves are much stiffer than those obtained from the tests. Therefore, in order to get more accurate behavior of real steel structures, appropriate modelling of semi-rigid connection is necessary.

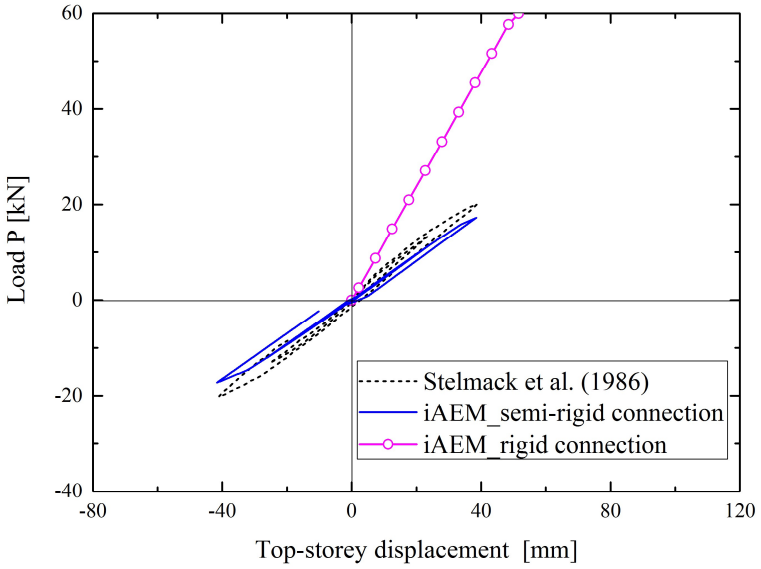

Figure 4-24 Load versus top-storey displacement curves of the frame

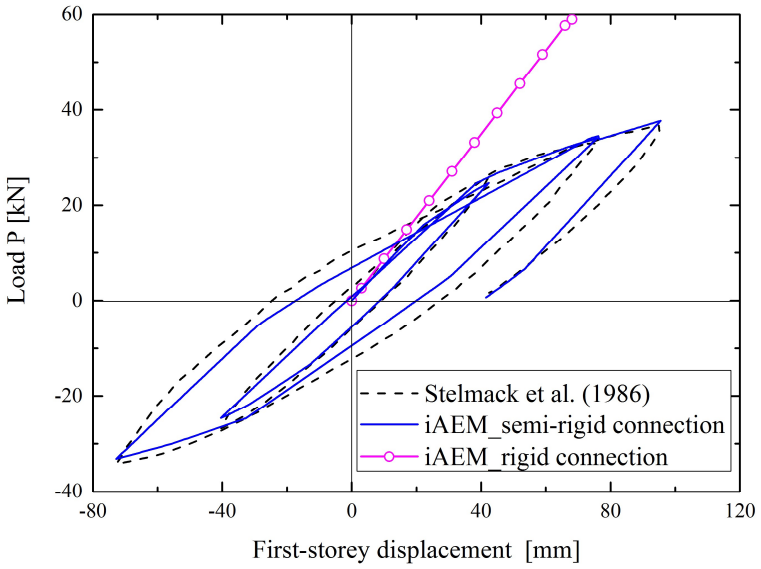

Figure 4-25 Load versus first-storey displacement curves of the frame

4.4.3 Liu et al. (2013) – Dynamic connection test

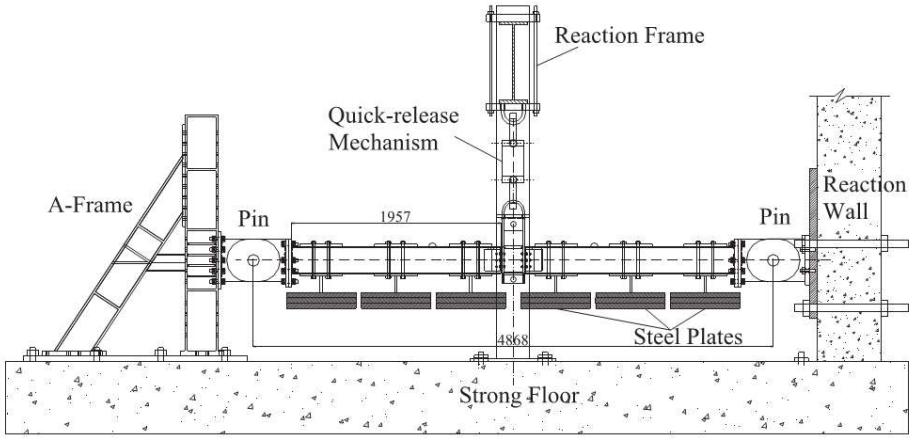

Figure 4-26 Test setup of the connections subjected to sudden column removal scenario (Liu et al., 2013)

In the second example, the component method is used in iAEM to model the web angle connection in the dynamic tests by Liu et al. (2013). The dynamic tests were performed by using a quick release mechanism as shown in Figure 4-26 to simulate a sudden column removal scenario. In the test program, the distance between the two pin supports was 4868 mm as shown in Figure 4-26, and the same UC203×203×71 section and UB254×146×37 sections were used for the column and beams, respectively as in Yang and Tan's test (Yang and Tan, 2013b). The web angle size is L90×8, and web stiffeners were used to stiffen the column and beam webs (see Figure 4-27). The geometries of the connections remained unchanged and the specimens were subjected to different magnitudes of uniformly distributed load (UDL). The steel material of both columns and beams were Grade S355, whereas the steel material of angles was Grade S275. Grade 8.8 M20 bolts were used for all the specimens.

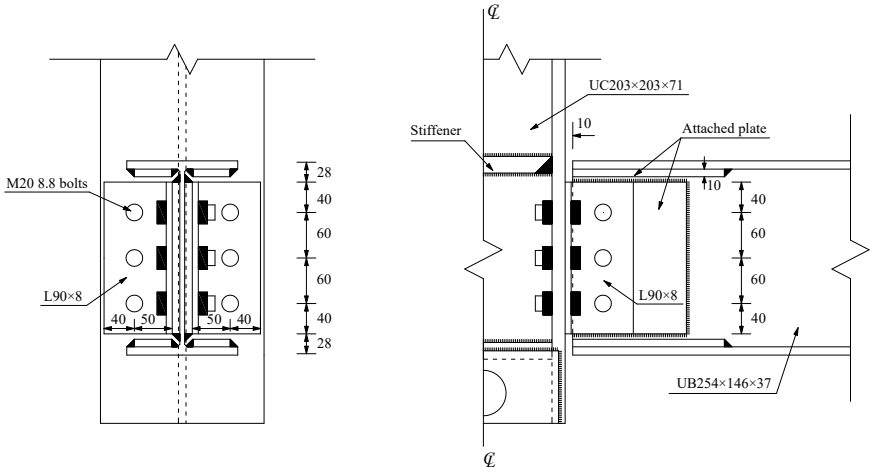

Figure 4-27 Details of the web angle connection

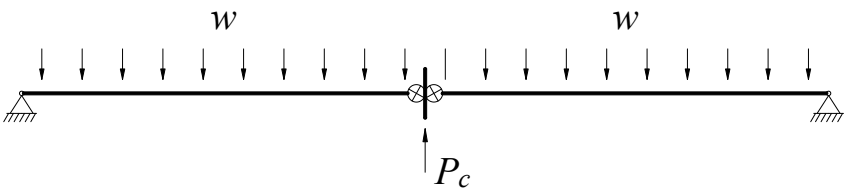

Figure 4-28 Loading method in dynamic analysis

The iAEM model of the double-span test beam is the same as that shown in Figure 4-10, and 23 iAEM elements are used in the model. The loading sequence of the dynamic analysis of this example in iAEM is similar to the one used in sudden column removal analysis of the moment frames in Chapter 2. As shown in Figure 4-28, w is the UDL applied at the two beam spans and P_c is the initial load supported by the middle column. As the first two numerical examples, the connection is also modeled by the component method. Using the hysteresis models proposed in Section 4.2.1, the cyclic connection behavior is incorporated in this frame analysis. Two-phase analysis approach is employed to analyse the structure. Firstly, static analysis is performed until both sets of the forces are gradually increased to the applied amount. Then with the developed initial deformation and internal forces of the structure, dynamic time history analysis is carried out by reducing the column

force P_c to zero within 80 ms. The adopted duration is approximated to be the measured duration in the tests (Liu et al., 2013). In the analysis, the damping ratio of 0.05 is adopted. As in the tests, a number of steel plates were used to represent the applied UDL, which would change the structural mass. Therefore, in the dynamic analysis, density of the beams is adjusted accordingly to achieve the same inertia forces as those in the actual tests.

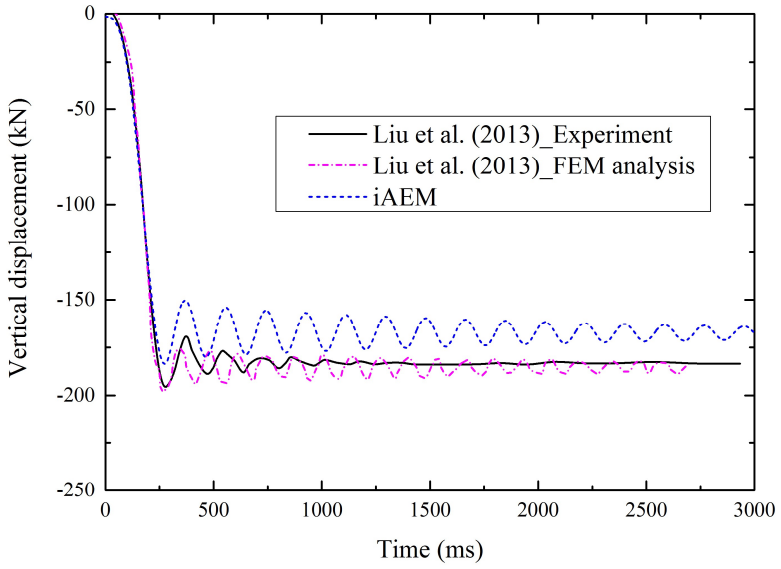

Figure 4-29 Vertical displacement time histories at P_c = 12.7 kN

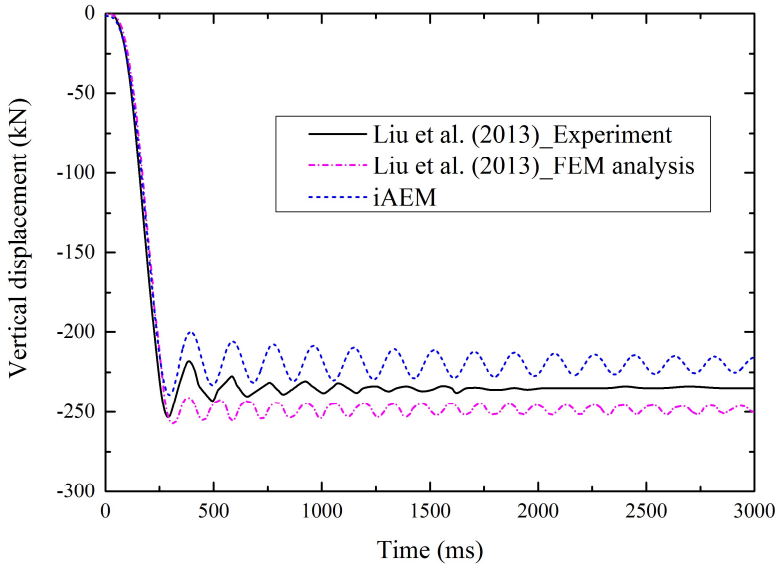

Figure 4-30 Vertical displacement time histories at P_c = 20.9 kN

Table 4-6 Comparison between results from component-based model in iAEM and the experiment and FEM analysis

P_c = 12.7kN	Maximum displacement (mm)	Effective period (ms)	Residual displacement (mm)
iAEM	184(-5.6%)	274	164(-10.4%)
FEM (Liu et al., 2013)	198(+1.5%)	272	187(+2.2%)
Experiment (Liu et al., 2013)	195	284	183
P_c = 20.9 kN	Max. displacement (mm)	Effective period (ms)	Residual displacement (mm)
iAEM	239(-4.8%)	296	217(-7.3%)
FEM (Liu et al., 2013)	257(+2.4%)	314	251(+6.8%)
Experiment (Liu et al., 2013)	251	301	234

The vertical displacement time histories of the middle column at $P_c = 12.7$ kN and $P_c = 20.9$ kN are shown in Figure 4-29 and Figure 4-30, respectively. The results from the test and the detailed FEM analysis using solid elements by Liu et al. (2013) are also plotted in these figures for comparison. The maximum displacements, the effective periods (time to reach maximum deflection of vibration) and the residual displacements are tabulated in Table 4-6, and the difference of the results from the iAEM or detailed FEM analysis with those from the test is also indicated. From these figures and the table, it can be seen that the cyclic connection behavior is captured by iAEM analysis, and the results from the component-based model agree generally well with those from experimental tests. In both load cases, iAEM under-predicts the maximum and residual displacements, which is attributed to the stiffer connection behavior predicted by iAEM. However, the stiffer connection behavior is consistent with that in the static connection test in Section 4.2.1 using the same connection details, i.e., specimen W-8. It can also be found that energy dissipation of iAEM is slower than detailed FEM. This is because in both iAEM and detailed FEM, 5% damping is modeled; while in detailed FEM, additional friction effect due to

interactions of the bolts, angles and the beam plate is modeled which results in faster energy dissipation as in the experiment.

4.5 Summary

In this chapter, the significance of considering semi-rigid connection behavior of real steel structures is first emphasized. Then the component method to model the semi-rigid bolted-angle connections in iAEM is presented. This method is very effective in predicting the complex connection behavior, and it is also consistent with the usage of springs in iAEM. The monotonic load deformation behavior is described for the three components including bolted angle under tension, bolt in shear and plate in bearing. Finally, the component method is applied in iAEM, and verification studies are performed through three numerical examples. For the last two examples, the monotonic load displacement curves of the connection components are modified further by adding the unloading and reloading paths, so that the cyclic and dynamic connection behavior is also captured by iAEM analysis. The cyclic connection test example shows that when semi-rigid connection is modelled, the predicted structural behavior from iAEM analysis agrees generally well with those obtained from the experimental tests, and the structure is more flexible than the case assuming rigid connection. Therefore, the extension of iAEM to consider semi-rigid connection behavior is deemed necessary for efficient and accurate simulation of structural behavior of real steel structures.

5 Modelling of Reinforced Concrete Shear Walls

Reinforced concrete (RC) shear walls have been extensively used for high-rise buildings to resist lateral loads due to wind forces and seismic effects on buildings whereas the vertical loads due to dead and live loads are transmitted by floor systems. Shear walls are thus subjected to axial forces, bending moments and shear forces, resulting in a multi-axial stress state. The responses of RC shear walls are significantly affected by the flexure-shear interaction (FSI) when they are subjected to large-amplitude cyclic loads. By adopting the principle stress criteria, FSI has been considered in the conventional AEM to model RC structures by using many small brick-type elements (Tagel-Din, 1998). However, such kind of modelling is very computationally expensive and it is only suitable for structural analysis at the component level. In this chapter, a macromodelling approach to simulate RC shear walls with consideration of FSI by iAEM is proposed for efficient progressive collapse analysis of high-rise buildings. First, the literature review on the modelling methods for RC shear walls is briefly presented. Next, the methodology of the modelling approach using iAEM is described. Finally, the modelling approach is verified through several numerical examples.

5.3 Literature review on shear wall modelling

The modelling approaches for RC shear walls may be divided into five main categories: (1) lumped plasticity beam-column model; (2) fiber beam-column model; (3) multiple-vertical-line-element model; (4) strut-and-tie model; and (5) multi-layered shell finite element model.

5.3.1 Lumped plasticity beam-column model

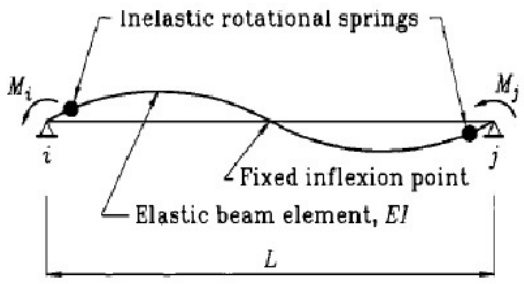

Figure 5-1 Lumped plasticity model (Giberson, 1967)

The lumped plasticity beam-column model was developed by Giberson (1967). It consists of one linear elastic member with two nonlinear rotational springs at the two member ends as shown in Figure 5-1. The member's nonlinear deformations are assumed to be lumped at the zero-length end springs (lumped plasticity). For this model, the deformed shape is assumed to have a double curvature with a fixed point of contraflexture at the middle of the member; plain sections are assumed to remain plain. The lumped plasticity model needs an appropriate hysteretic load-deflection (or moment-curvature) model to be defined. This requires determination of different properties of the member's plastic hinges such as stiffness, strength, ductility, cyclic behavior, etc.

The simple bilinear elasto-plastic model was the first nonlinear hysteresis model developed. Takeda et al. (1970) proposed a trilinear force-displacement primary curve to account for cracking, yielding and strain hardening of the concrete element. The stiffness degradation was considered in the seven-condition hysteretic model of the element. Saatcioglu et al. (1983) included the effect of axial-flexure interaction in the hysteretic behavior of coupled shear walls by shifting the element's primary curve with the increase of axial load level. FSI has been implemented by the empirical calibration of nonlinear hysteresis rules. Hidalgo et al. (2002) developed an analytical

model to predict the inelastic seismic response of RC shear-wall buildings, and both flexural and shear failure models were presented.

5.3.2 Fiber beam-column model

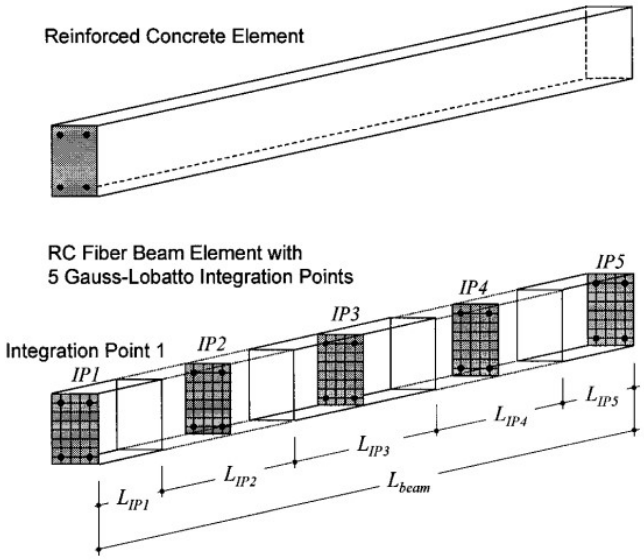

Figure 5-2 Fiber beam-column model with five Gauss-Lobatto integration points (Monti and Spacone, 2000)

Fiber beam-column models were developed in the 1970s (Park and Kent, 1972; Taylor, 1977). In the fiber beam-column model, the member is divided longitudinally into a discrete number of cross sections, and each cross section is subdivided into a series of layers (for a 2D beam) or fibers (for a 3D beam) (see Figure 5-2). For each fiber, uniaxial constitutive models for concrete and steel materials are defined, and then the moment-curvature relationship of the member can be calculated at each load level. This model accounts for the distribution of plasticity along the member length and the axial-flexure interaction.

Chan (1983) used the fiber beam-column model to model the edge beams of the RC shells. Monti and Spacone (2000) accounted for the bond-slip of the reinforcement bars in the fiber beam-beam model. FSI consideration in fiber beam-column models

was implemented using equilibrium, specific assumptions for the shear strain field and biaxial concrete material laws (Petrangeli et al., 1999; Vecchio and Collins, 1988). However, these models have the limitation of using plane-sections-remain-plane assumption of the beam theory. As a result, the predicted structural behavior of squat walls can be significantly different from the real behavior.

5.3.3 Multiple vertical line element (MVLE) model

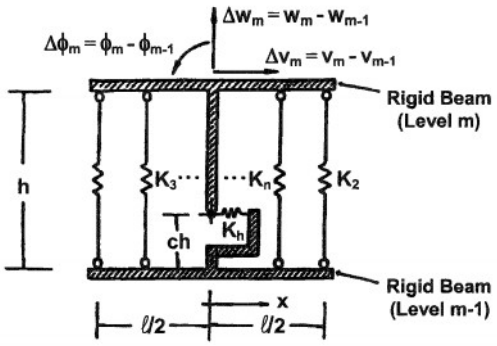

Figure 5-3 MVLE model and wall model (Vulcano et al., 1988)

The macroscopic multiple vertical line element (MVLE) model was introduced by Vulcano et al. (1988) for efficient nonlinear seismic analysis of RC shear walls. In this model, the wall element is represented by a number of uniaxial elements connected in parallel using infinitely rigid bars located at the top and bottom wall ends. The two external elements represent the axial stiffness of the boundary columns, while two or more interior elements represent the axial and flexural behavior of the central panel (see Figure 5-3). A horizontal spring is used to represent the inelastic shear behavior of the wall. The relative rotation of the wall element occurs around the point placed on the central axis of the wall member at height ch ($0 \le c \le 1$). Selection of the parameter c is based on the expected curvature distribution along the inter-storey height h and varies between 0 and 1 for single curvature over the height of an element.

Simpler constitutive laws were introduced by Fischinger et al. (1992) to the MVLE to improve the efficiency of the model in predicting the response of RC shear walls without sacrificing the accuracy. For walls of low to moderate aspect ratios, FSI was considered by Colotti (1993) and Massone (2006) in the MVLE model by adding a shear spring to each vertical line element, and implementing biaxial concrete material laws at the macrofiber (or panel) level.

5.3.4 Strut-and-tie model

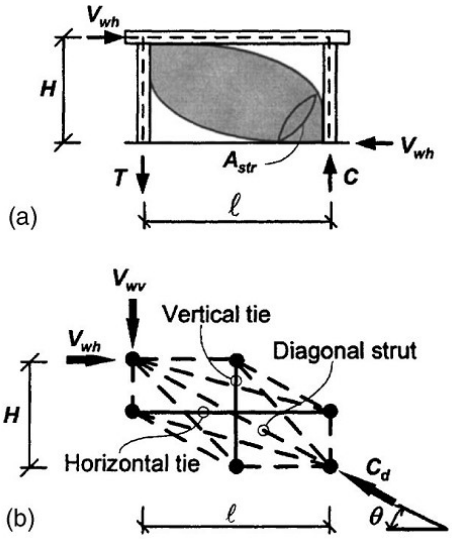

Figure 5-4 Softened strut-and-tie model Yu and Hwang (2005): (a) disturbed stress filed and (b) strut-and-tie idealization

The strut and tie model (STM) was developed by Schlaich and Schäfer (1984) to analyse disturbed regions of the RC structures such as deep beams and corbels, where the magnitude and distribution of stress and strain vary significantly. The STM was used by Oesterle et al. (1984) to analyse the shear capacity of RC structural walls. The STM of the wall assumes that the wall will act as a statically determinate truss. The model consists of diagonal concrete compression struts, horizontal tension ties (representing the shear reinforcement), and two boundary elements at the wall ends to carry the acting moment. Yu and Hwang (2005) used softened STM as shown in Figure 5-4 to predict the shear capacity of RC squat walls.

The STM offers advantages as a design tool: since it uses truss analogy, the modelling of the truss elements and computation of the internal forces by this model are relatively simple. Furthermore, the analytical results expressed as the force–displacement relationship of the elements can be directly used in the design of the members. For these reasons, the strut-and-tie model is adopted in current design codes, including ACI 318-14 (ACI, 2014) and CEB-FIP 2010 (CEB-FIP, 2013).

To et al. (2001) incorporated rational joint force transfer mechanisms to the STM to capture the nonlinear response of the bridge knee joints under monotonic loading. Park and Eom (2007) developed the STM to predict the nonlinear behavior of reinforced concrete members subjected to cyclic loading. However, most of the proposed models for shear behavior consider an uncoupled flexural and shear response. FSI has been considered by Yu and Hwang (2005) to predict shear strength of reinforced concrete squat walls using a softened STM with constitutive laws of cracked concrete.

5.3.5 Multi-layered shell model

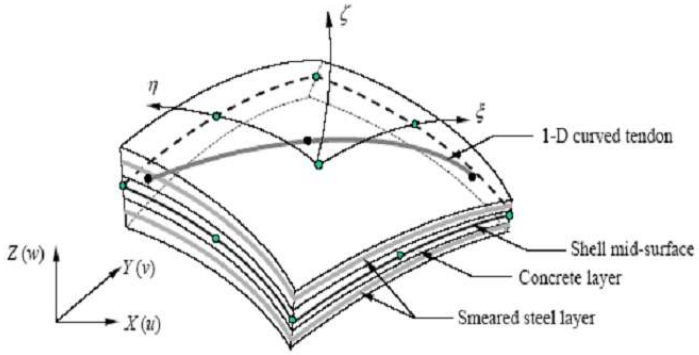

Figure 5-5 Multi-layered shell elements (Miao et al., 2006)

Based on principles of composite material mechanics, the multi-layered shell elements can be used for modelling the RC shear walls. The shell element is made up of many layers with different thickness, and different material properties are assigned

to various layers (see Figure 5-5). This means that the reinforcement rebars are smeared into one layer or more. During the finite element calculation, the axial strain and curvature of the middle layer can be obtained in one element. Then according to the assumption that plane sections remain plane, the strains and the curvatures of the other layers can be calculated and the corresponding stresses are calculated through the constitutive relations of the material assigned to each layer. From the above principles, it is seen that the structural performance of the shear wall can be directly related to the material constitutive law.

Multi-layered shell elements have been included in the finite element softwares such as LS-DYNA (Hallquist, 2005), ABAQUS (ABAQUS, 2005) and SAP2000 (SAP2000, 2002). They were used for the pushover analysis of RC frames with shear walls (Fahjan et al., 2012) and nonlinear analysis of various types of RC shell structures (Polak and Vecchio, 1993; Song et al., 2002). The FSI has been considered by employing the biaxial constitutive laws. Miao et al. (2006) developed a shell element that used the microplane model to simulate the concrete in shear, and predicted the coupled in-plane and out-of-plane bending failure of tall walls and the coupled in-plane bending-shear failure of short walls. The multi-layered shell models are efficient compared to the solid elements to simulate the nonlinear behavior of RC shear walls, but they still require great computational effort for large-scale structures.

5.4 Modelling RC shear walls using iAEM

After reviewing the various modelling methods, the nonlinear beam-truss model, a variant of the strut-and-tie model, is employed in the iAEM to analyse the structural response of RC shear walls. The beam-truss model was initially proposed by Panagiotou et al. (2012) to represent 2D shear walls in the FEM framework, and later extended to the 3D case by Lu and Panagiotou (2014). FSI is considered in this model by a biaxial material model for diagonal concrete truss. Though there are no

exact beam or truss elements in iAEM, the beam elements can be conceptually represented by iAEM elements connected by multiple pairs of normal and shear springs, and truss elements by only one pair. As a result, the name “beam-truss model” is still used in iAEM for ease of understanding.

5.4.1 Nonlinear beam-truss modelling approach

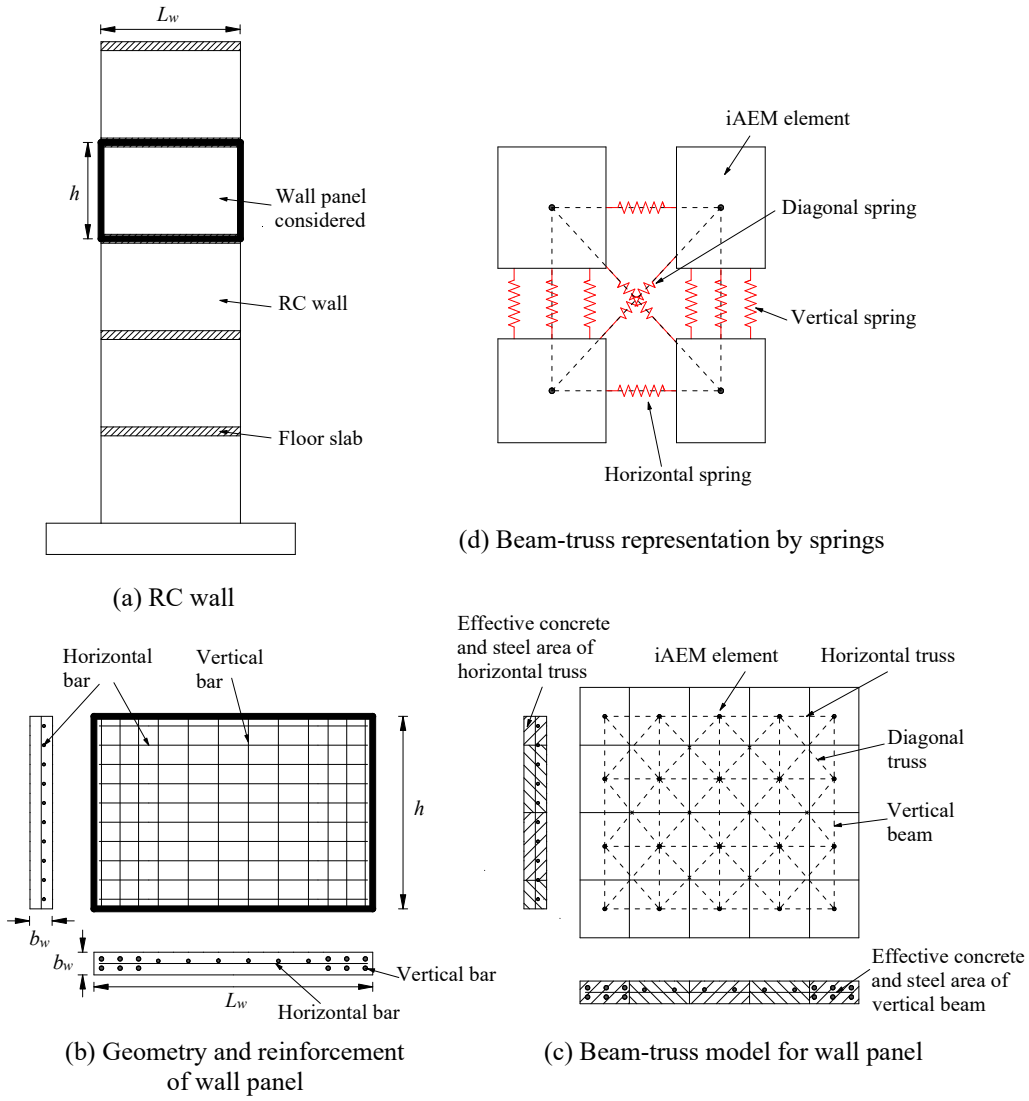

(a) RC wall

(d) Beam-truss representation by springs

(b) Geometry and reinforcement of wall panel

(c) Beam-truss model for wall panel

Figure 5-6 RC shear wall and beam-truss model for wall panel using iAEM

The FEM version of the beam-truss model uses nonlinear fiber beam elements in the vertical direction and nonlinear truss elements in the horizontal and diagonal directions. The diagonal nonlinear truss elements represent concrete only, and they

use a biaxial material model for concrete that accounts for the effect of normal tensile strain on the stress-strain relationship of concrete in compression (Vecchio and Collins, 1986).

To apply the beam-truss model in iAEM, consider the cantilever wall shown in Figure 5-6(a) where the wall length and storey height are L_w and h, respectively. The geometry and reinforcement of the wall panel considered are depicted in Figure 5-6(b). Figure 5-6(c) shows the beam-truss model for the wall panel in iAEM. The wall panel is divided into rows and columns of iAEM elements which are connected by three types of elements: (1) nonlinear fiber beam elements in the vertical direction; (2) nonlinear truss elements in the horizontal direction; and (3) nonlinear truss elements in the diagonal directions. The beam and truss elements are drawn by the dotted lines as they do not actually exist. Instead, they are represented in iAEM by using different number of normal and shear spring pairs at the iAEM element edges as shown in Figure 5-6(d). In both horizontal and diagonal directions, iAEM elements are connected by one spring pair to represent the horizontal and diagonal trusses, and the stiffnesses of the shear springs are set to zero. Truss springs are located along the dotted line of truss elements. In the vertical direction, iAEM elements are connected by multiple spring pairs (e.g. three pairs shown in Figure 5-6 (d)) to represent the vertical fiber beams, and the location of beam springs depend on reinforcement distribution and number of concrete fibers needed. Effective concrete and steel areas of each horizontal truss and vertical beam are expressed by the hatched areas in Figure 5-6(c). For the top and bottom rows of horizontal truss, only half of the concrete and steel areas are assigned as compared to those in the middle rows. The concrete area of diagonal truss is derived in the next paragraph by the panel-truss analogy.

Determination of the concrete area of diagonal trusses utilizes a panel-truss analogy. Assuming the classical shear stress-stain rule of $G = \tau\gamma$, and a uniform distribution of

shear stress across the shear area, the shear deformation of a concrete panel with width B and depth D as shown in Figure 5-7(a) can be derived as:

$$\Delta = \left(\frac{D}{B}\right)\left(\frac{V}{Gb_w}\right) \tag{5-1}$$

where V, G and b_w are the acting shear force, shear modulus of the concrete and thickness of the concrete panel, respectively. Meanwhile, the shear deformation of an equivalent truss system of the same geometry as shown in Figure 5-7(b) can be obtained as:

$$\Delta = \left(\frac{B^2 + D^2}{B^2}\right)\left(\frac{V}{k_d}\right) \tag{5-2}$$

where k_d is axial stiffness of the diagonal truss. By equating Equations (5-1) and (5-2), the axial stiffness of diagonal truss that gives the same shear deformation as the concrete panel can be calculated as:

$$k_d = \left(\frac{B^2 + D^2}{BD}\right)Gb_w \tag{5-3}$$

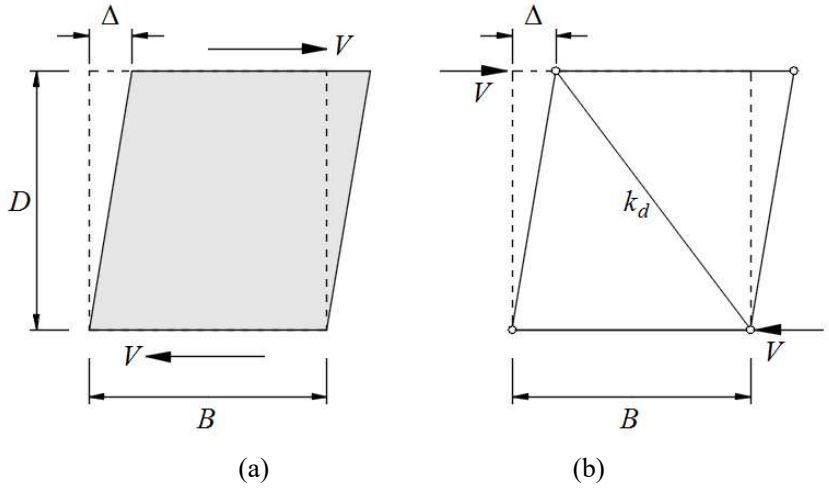

Figure 5-7 Derivation of concrete area of diagonal truss: (a) concrete panel and (b) equivalent truss model

As $G = E/\left[2\left(1+\nu\right)\right]$, where E is the Young's modulus of the material, $\nu = 0.2$ is Poisson's ratio of concrete, the axial stiffness of diagonal truss can be further expressed as:

$$k_d = \left(\frac{B^2 + D^2}{2.4BD}\right) E b_w \tag{5-4}$$

On the other hand, the axial stiffness of diagonal truss can also be expressed as:

$$k_d = EA_d / \sqrt{B^2 + D^2} \tag{5-5}$$

where A_d is concrete area of the diagonal truss. By equating Equations (5-4) and (5-5), concrete area of the diagonal truss is calculated as:

$$A_d = \frac{\left(B^2 + D^2\right)^{3/2} b_w}{2.4BD} \tag{5-6}$$

A relatively coarse mesh is used to determine the number elements or element width. A minimum number of four columns of beam elements as suggested by Lu and Panagiotou (2014) is adopted in the iAEM beam-truss model, and the number of columns can be adjusted according to the reinforcement distribution across the section. Then the number of rows of horizontal truss elements is determined in such a way that the inclination angle of the diagonal truss elements with respect to the horizontal lines is close to 45^0, so that the angle formed between the diagonal trusses and gauge elements is close to the suggested value of 90^0 as described in Section 5.2.2.2. The mesh-objectivity of the beam-truss model studied by Lu and Panagiotou (2014) showed that mesh refinement resulted in more accurate computation of strains (local response) while the overall force-displacement responses show no significant difference. Therefore, in the numerical examples by the iAEM beam-truss model, in order to simulate the global load-displacement

response other than the local strains and meanwhile to save the computational time, a relatively coarse mesh is used in the model.

5.4.2 Material constitutive models

5.4.2.1 Concrete model for vertical and horizontal elements

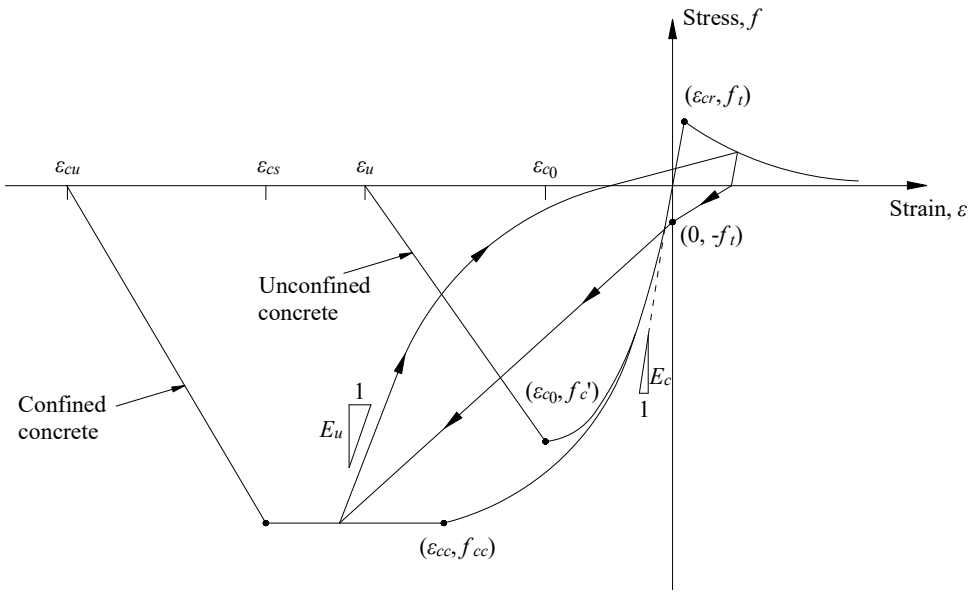

Figure 5-8 Stress-strain relationship of the concrete material

The stress-strain relationship of the concrete used for the vertical beam and horizontal truss elements is shown in Figure 5-8. For the unconfined concrete, the ascending part of concrete in compression is based on the Mander concrete model (Mander et al., 1988):

$$f(\varepsilon) = \frac{-f_c^{'} xr}{r - 1 + x^r} \tag{5-7}$$

where $f_c^{'}$ is the compressive strength of unconfined concrete at strain ε_{c0} = -0.2%, $x = \frac{\varepsilon}{\varepsilon_{c0}}$, ε is the compressive strain, $r = \frac{E_c}{E_c - E_{\sec}}$, $E_c = 5000\sqrt{f_c^{'}}$ (MPa) is the initial concrete modulus, and $E_{\sec} = \frac{f_c^{'}}{\varepsilon_{c0}}$ is the secant modulus. After reaching $f_c^{'}$, the

compressive stress decreases linearly until it becomes zero stress at strain ε_u. The value of ε_u accounts for the mesh size effects based on the notion of concrete fracture energy in compression (Bazant and Planas, 1998). ε_u is expressed as $\varepsilon_u = (1-\Lambda)\varepsilon_{c0} + (L_R/L)(0.2\% + \Lambda\varepsilon_{c0})$ (Lu and Panagiotou, 2014), where L is the element length of each beam or truss, L_R = 600 mm is the reference length considered in this study, which is based on the length over which average strains were measured in the concrete panel studies by Vecchio and Collins (1986). $\Lambda = f_c^{'}/\left[0.5\left(E_c\varepsilon_{c0} + f_c^{'}\right)\right]$ is a factor that considers the effect of unloading on the concrete fracture energy in compression.

For the confined concrete, the ascending part of concrete in compression is given by

$$f(\varepsilon) = \frac{-f_{cc}xr}{r-1+x^r} \tag{5-8}$$

where f_{cc} is the compressive strength of confined concrete at strain ε_{cc}, $x = \frac{\varepsilon}{\varepsilon_{cc}}$, $r = \frac{E_c}{E_c - E_{\sec}}$, and $E_{\sec} = \frac{f_{cc}}{\varepsilon_{cc}}$. The compressive stress remains constant and is equal to f_{cc} until the compressive strain reaches strain ε_{cs} at which softening initiates. The compressive stress softens linearly to zero at the strain ε_{cu}. f_{cc}, ε_{cc} and ε_{cs} can be calculated based on the equations by Mander et al. (1988). Accounting for mesh size effects, $\varepsilon_{cu} = (1-\Lambda)\varepsilon_{cs} + (L_R/L)(0.2\% + \Lambda\varepsilon_{cs})$, where $\Lambda = f_{cc}/\left[0.5\left(E_c\varepsilon_{cs} + f_{cc}\right)\right]$.

For compressive strain, the slope of the unloading branch is defined by Equation (5-9). After reaching zero stress, the material is re-stressed linearly to the point with the largest tensile strain that has occurred before.

$$E_u = 0.5\left(\frac{f}{\varepsilon}\right) + 0.5E_c \tag{5-9}$$

The tension envelope during loading is linear until it reaches the tensile strength of concrete $f_t = 0.33\sqrt{f_c'}$ in MPa. After this point, the concrete softens according to Equation (5-10) by Bentz (2005):

$$f(\varepsilon) = \frac{f_t}{1 + \sqrt{3.6M \cdot \varepsilon}} \tag{5-10}$$

where $M = \frac{A_c}{\sum d_b \pi}$ is the bond parameter in mm, A_c is the area of concrete effectively bonded to the bar, and d_b is the diameter of the bar in concrete stiffened area.

The material unloads from tension strain using a slope of E_c. After reaching zero stress, the material targets the point $(0, -f_t)$. Thereafter, the material is stressed linearly to the point where the peak compressive strain that previously occurred. In the case where the stress of this target point is less than f_t, the material reloads directly to the point where peak compressive strain that has occurred.

5.4.2.2 Concrete model for diagonal truss elements

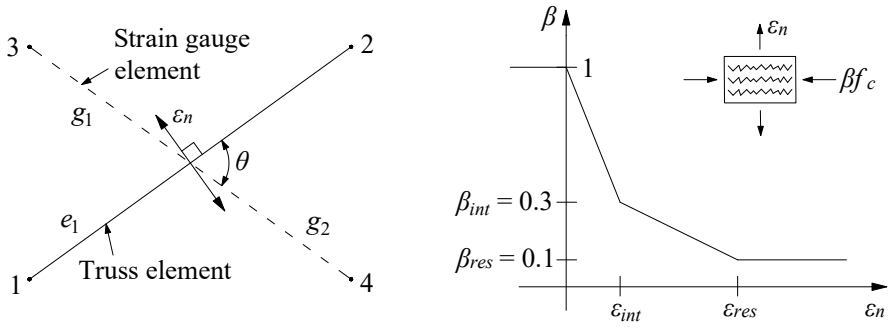

(a) (b)

Figure 5-9 (a) Truss element accounting for biaxial effects on the compressive stress-strain behavior of concrete; (b) reduction factor of concrete compressive stress β with respect to the lateral strain ε_n

The concrete model used for the diagonal truss elements is different from that for the vertical and horizontal elements in two aspects: (1) it has zero tensile strength and (2)

it accounts for the biaxial strain field on the concrete compressive behavior as described by Vecchio and Collins (1986). β factor is used to consider the reduction of concrete compressive stress due to the lateral strain ε_n. For truss element e_1 extending from node 1 to node 2 (see Figure 5-9(a)), lateral strain ε_n is computed using the zero-stiffness gauge element extending from the mid length of the element to nodes 3 and 4, g_1 and g_2, respectively, and it is calculated as:

$$\varepsilon_n = \frac{1}{\sin\theta}\left(\varepsilon_{34} - \varepsilon_{12}\cdot\cos\theta\right) \tag{5-11}$$

where ε_{12} is the strain of truss element e_1, ε_{34} is the average of the strain measured with the gauge elements g_1 and g_2 and θ is the angle formed between the truss and gauge elements of suggested value close to 90°. As shown in Figure 5-9(b), when $\varepsilon_n > 0$, the relationship between β and ε_n is trilinear. Therefore, the instantaneous compressive stress of element e_1 is multiplied by the factor β. For this study, the relation between β and ε_n depends on the length of the gauge elements, as first proposed by Panagiotou et al. (2012). Here, $\varepsilon_{int} = \left(600/L_g\right)\cdot 1\%$ and $\varepsilon_{res} = \left(600/L_g\right)\cdot 2.5\%$, where L_g is the total length of gauge elements g_1 and g_2. The values of ε_{int} and ε_{res} were chosen to be similar to that developed by Vecchio and Collins (1986).

5.4.2.3 Reinforcement model

The Menegotto-Pinto (MP) model (Menegotto and Pinto, 1973) with isotropic strain hardening (Filippou et al., 1983) is used to model the reinforcement in RC shear walls. The original MP model for characterizing response of reinforcement is defined by the following non-linear equation:

$$f^* = b\varepsilon^* + \frac{(1-b)\varepsilon^*}{\left(1+\varepsilon^{*R}\right)^{\frac{1}{R}}} \tag{5-12}$$

where $\varepsilon^* = (\varepsilon - \varepsilon_r)/(\varepsilon_0 - \varepsilon_r)$ and $f^* = (f - f_r)/(f_0 - f_r)$ are the effective strain and stress, respectively, f_0 and ε_0 are stress and strain at the point where two asymptotes of the branch under consideration meet, and f_r and ε_r are stress and strain at the point where the last strain reversal with stress of equal sign took place (see Figure 5-10). b is the strain hardening ratio. $R = R_0 - \frac{a_1\xi}{a_2 + \xi}$ is a parameter that defines the shape of the transition curve, where ξ is updated following a strain reversal (see Figure 5-11), R_0 is the value of parameter R during first loading, and a_1 and a_2 are experimentally determined parameters to be defined together with R_0.

In spite of the simplicity in formulation, the MP steel model can reproduce well experimental results with strain histories typical of structural steel. The major drawback of the model is that it fails to account for the isotropic strain hardening. To tackle this problem, Filippou et al. (1983) introduced a stress shift f_{st} parallel to the initial yield asymptote to this model, and it takes the following form:

$$\frac{f_{st}}{f_y} = a_3\left(\frac{\varepsilon_{\max}}{\varepsilon_y} - a_4\right) \tag{5-13}$$

where ε_y and f_y are the yield strain and stress, $\varepsilon_{\max}$ is the absolute maximum strain at the instant of strain reversal, and a_3 and a_4 are experimentally determined parameters. In this way, the isotropic strain hardening can be considered in this model. The parameters controlling the transition between the elastic to plastic branches in this study are as follows: $R_0 = 20$, $a_1 = 18.5$, $a_2 = 0.15$, $a_3 = 0.01$, and $a_4 = 7$ (Filippou et al., 1983). It is assumed that the geometric nonlinearity (bar buckling) and bond

slip between reinforcing steel and concrete as well as strain penetration in the base anchorage blocks are not considered.

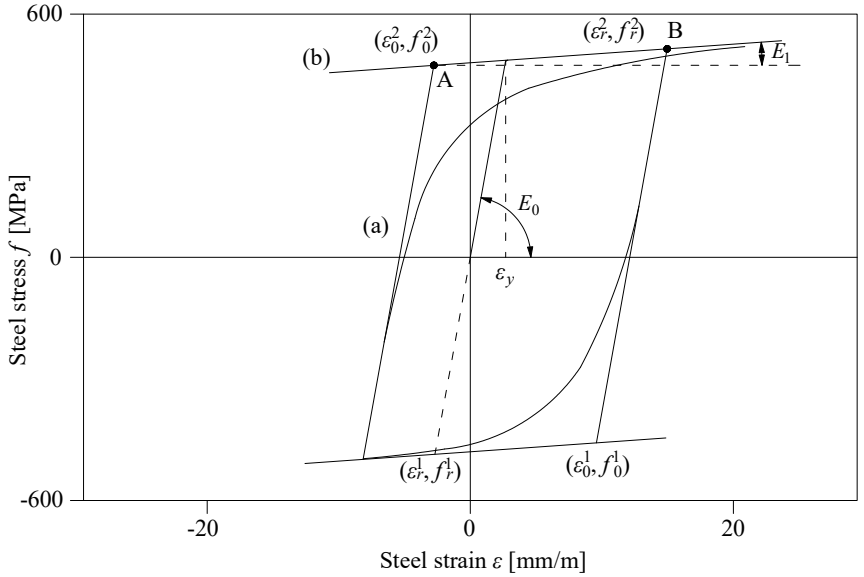

Figure 5-10 Menegotto-Pinto reinforcement model

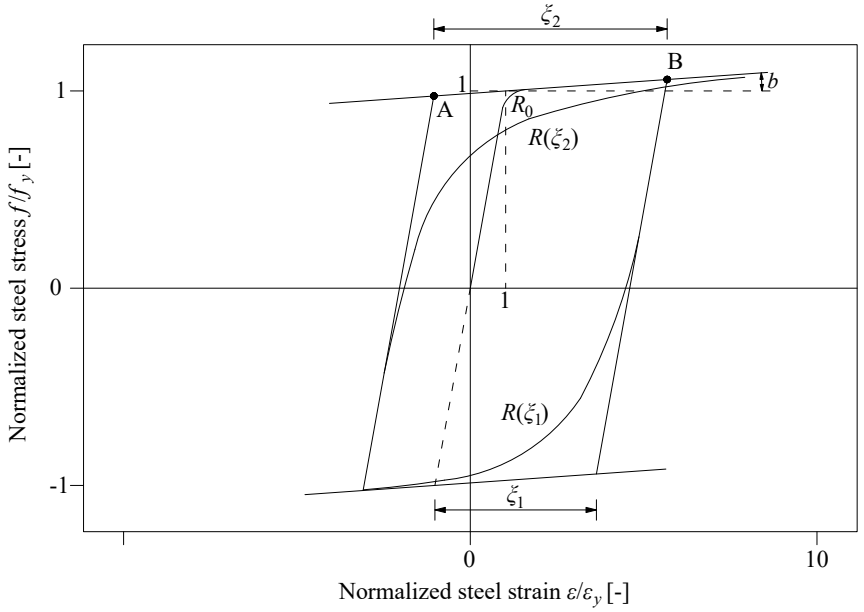

Figure 5-11 Definition of curvature parameter $R(\xi)$ in Menegotto-Pinto reinforcement model

5.5 Numerical examples

5.5.1 Thomsen and Wallace (1995) – Wall RW2

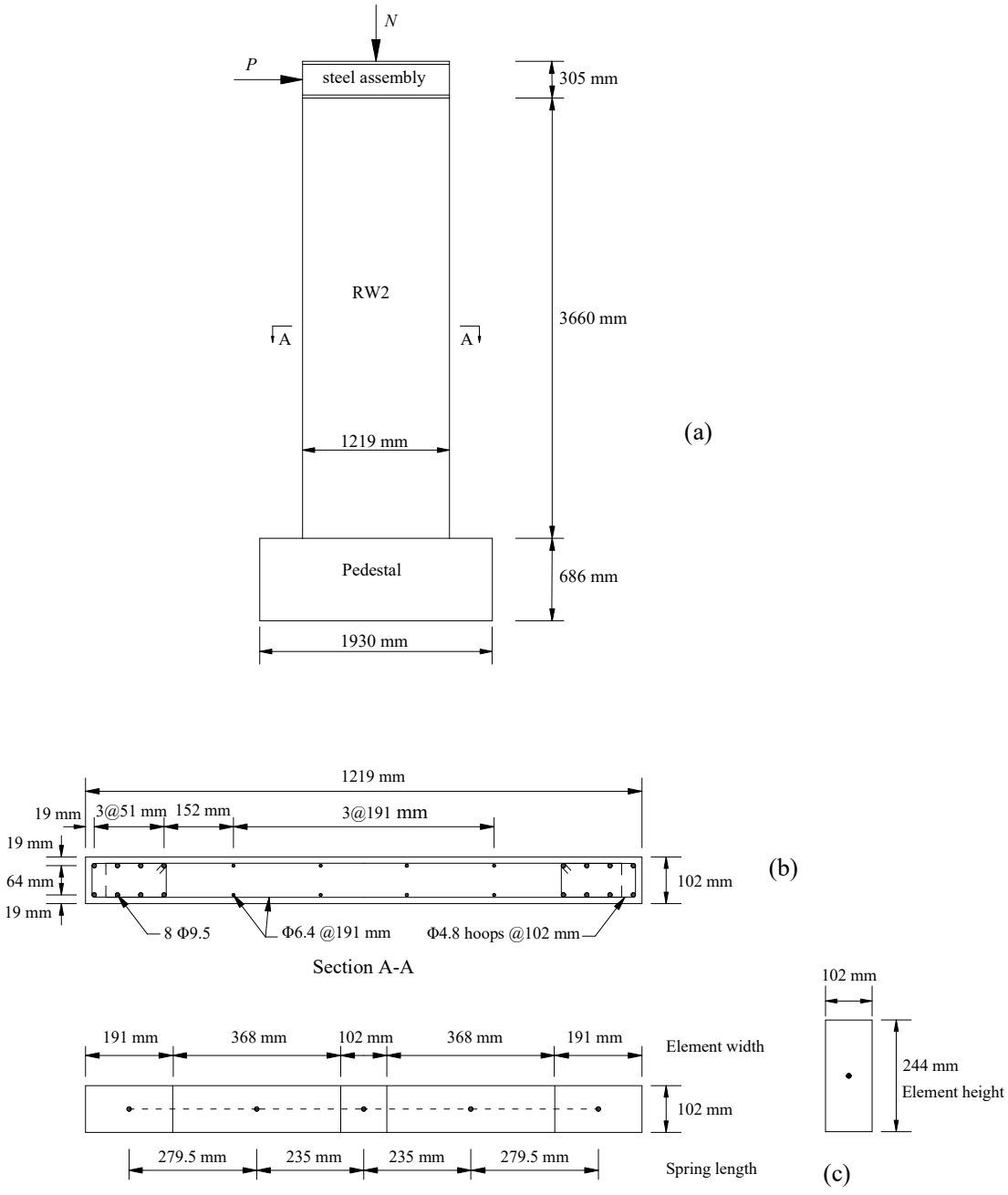

Figure 5-12 Wall specimen RW2 tested by Thomsen and Wallace (1995)

In the first numerical example, wall specimen RW2 tested by Thomsen and Wallace (1995) is considered (see Figure 5-12). This wall is moderately slender with its shear span ratio $M/VL_w = 3$, where M is the bending moment at the base of the wall, V is the base shear force, and L_w is the length of the wall in the horizontal direction. The longitudinal reinforcement ratios in the boundary elements and the web are $\rho_{lb} = 2.91\%$ and $\rho_{lw} = 0.30\%$, respectively. The transverse reinforcement ratio in the web is $\rho_{tw} =$ 0.33%. During the test, the axial and lateral loads were applied through a steel load transfer assembly that was placed at the top. The axial load ratio of the wall was $N/\left(f_c^{'}A_g\right) = 0.07$, where N is the vertical load applied at the centroid of the section, and A_g is the gross section area. Cyclic lateral load P was applied to the wall approximately 3.81 m above the base of the wall, while the vertical load N remained constant. A total of sixteen load cycles were applied in the test with two cycles at each drift level.

The beam-truss model for wall RW2 using iAEM is shown in Figure 5-13. The model consists of 85 (5×17) iAEM elements. The elements at the top two rows are connected rigidly in order to simulate the large steel beam at the top in the experiment. Cross section of the wall is divided into five fiber-beam sections, and the vertical spacing of horizontal trusses is 244 mm (see Figure 5-12(c)). Material properties of the wall RW2 for the analysis are listed in Table 5-1.

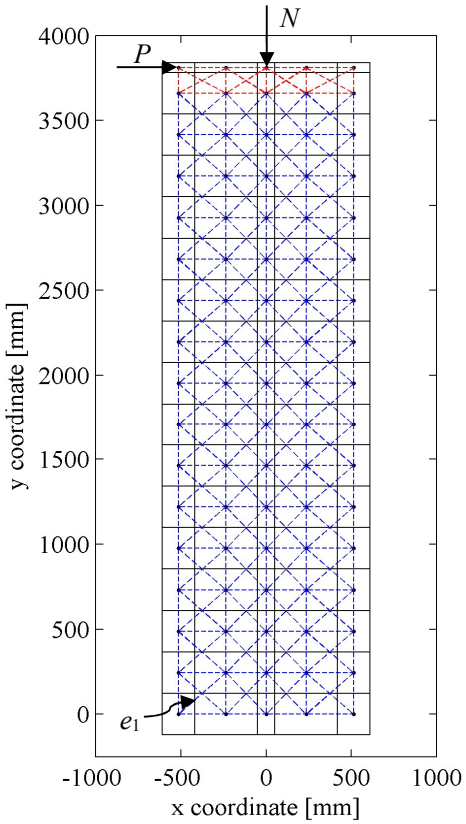

Figure 5-13 iAEM model of RW2

Table 5-1 Material properties of wall RW2

Unconfined concrete	$f_c^{'}$ (MPa)	ε_{c0}	f_t (MPa)
	-42.8	-0.2%	2.16
Confined concrete	f_{cc} (MPa)	ε_{cc}	
	-47.6	-0.30%	
Reinforcement	Type	f_y (MPa)	b
	Φ4.8	448	0.02
	Φ6.4	448	0.02
	Φ9.5	434	0.02

The lateral load versus top displacement curves from both iAEM analysis and the experimental tests are shown in Figure 5-14. In order to trace the cyclic response of the wall more clearly, the lateral load versus top displacement curves are plotted separately for every two cycles in Figure 5-15. It can be seen that the iAEM model computes the force-displacement response of the wall satisfactorily. The computed peak lateral strength in both directions is in excellent agreement with the experimentally measured response. The computed lateral strength at drift ratio of $\Theta =$ 1.0% is 1.06 times that of the experimental result. The drift ratio is defined as Δ / H, where Δ is the lateral displacement and H is the height where the lateral load is applied. For drift ratio larger than 1.5%, the computed lateral strength is almost the same as that of the experimental result for the first cycle at same drift level. The predominant mode of failure of this wall is the bar buckling which is not considered in the iAEM model. The computed peak diagonal compressive strain of the web measured in element e_1 is only 0.02% for the negative displacement (see Figure 5-13). This is in good agreement with the observed response in the experiment where no crushing of the diagonal compression field was observed.

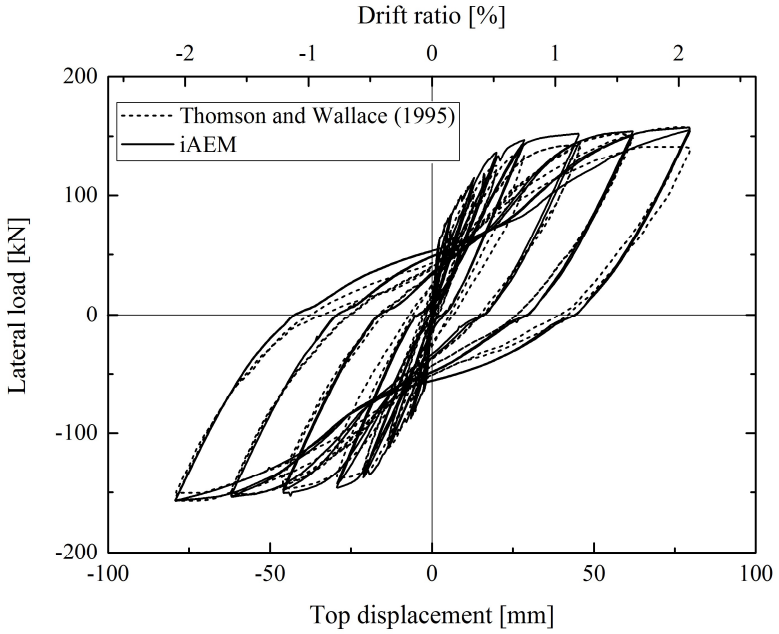

Figure 5-14 Lateral load versus top displacement curves of wall RW2

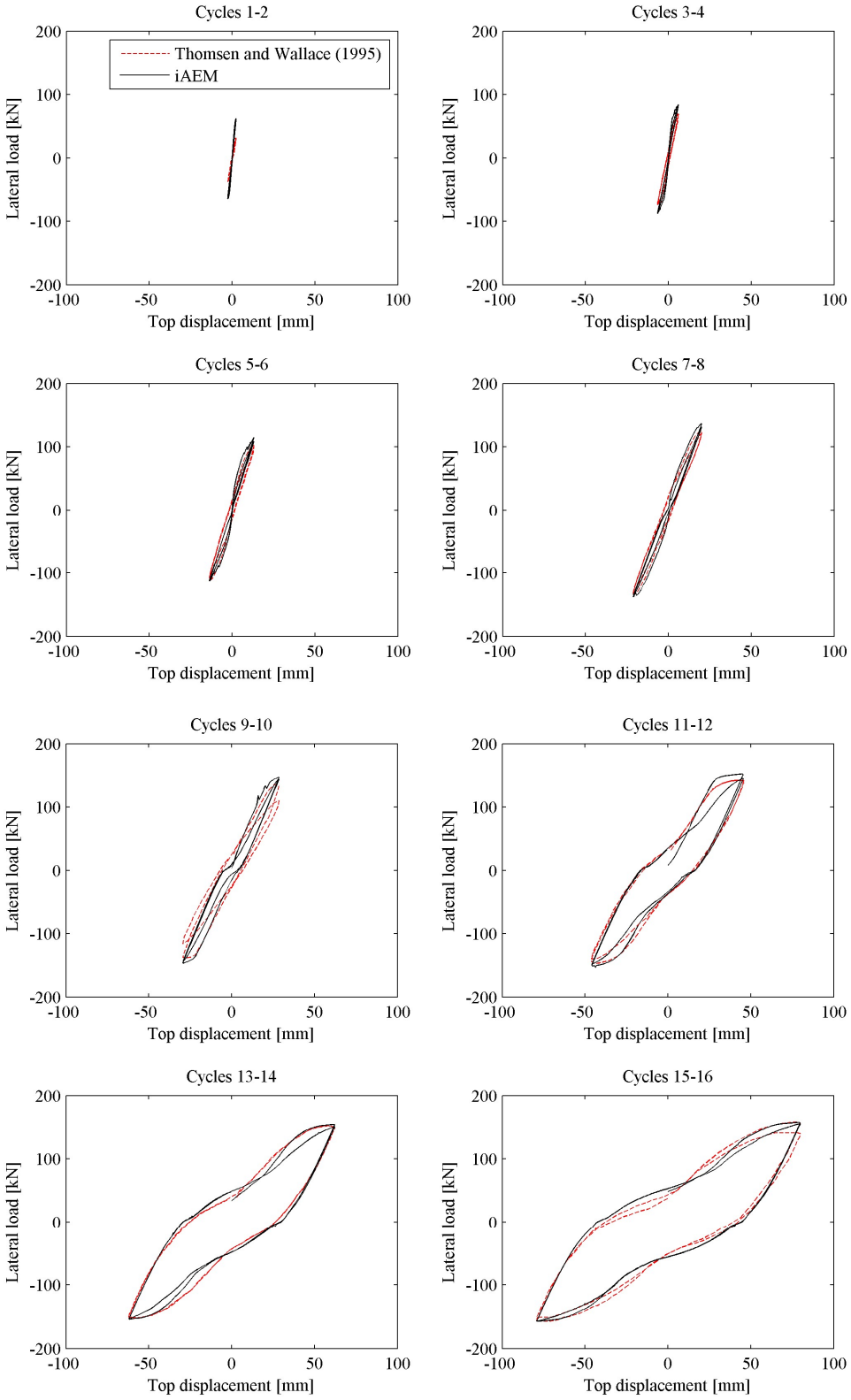

Figure 5-15 Lateral load versus top displacement curves of wall RW2 plotted every two cycles

5.5.2 Sittipunt et al. (2001) – Wall W2

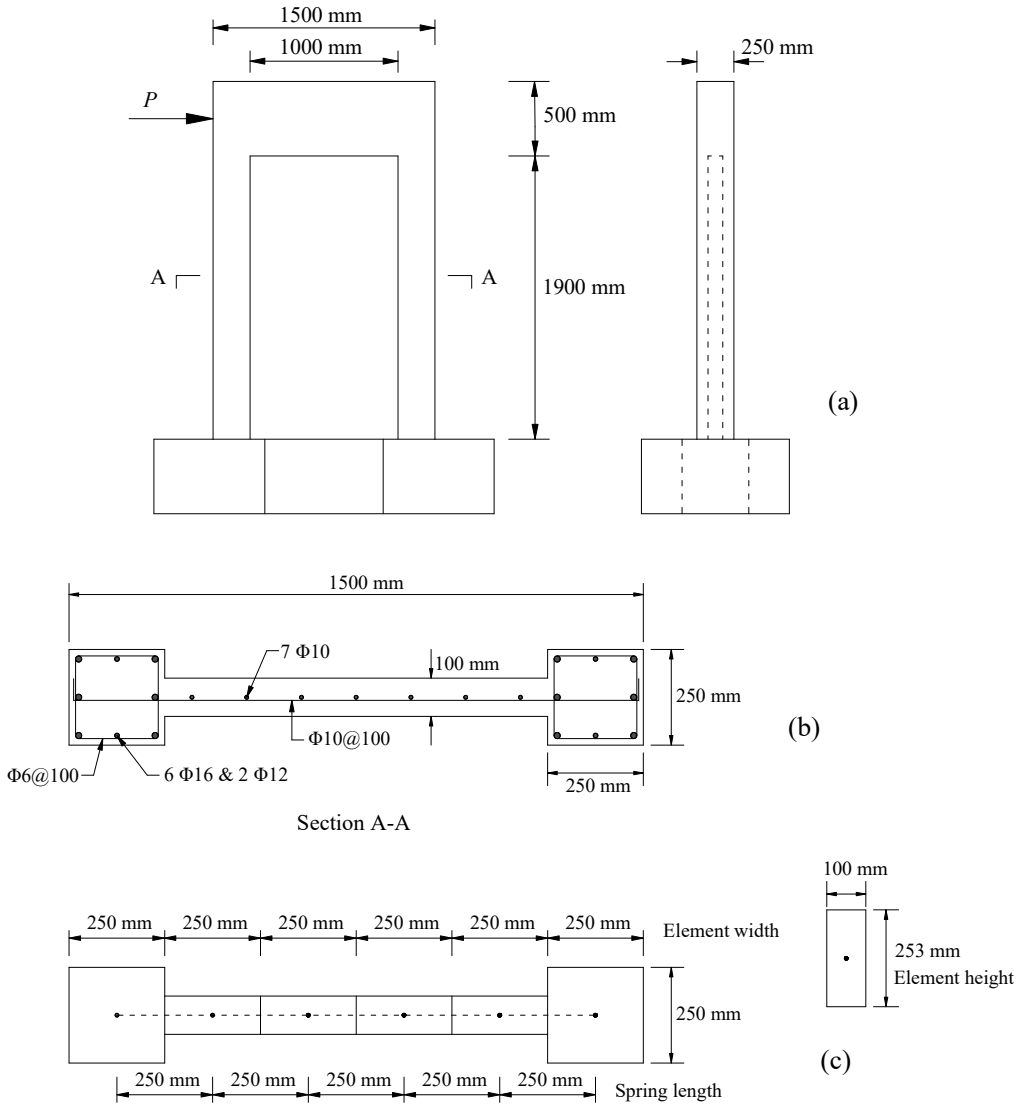

Figure 5-16 Wall specimen W2 tested by Sittipunt et al. (2001)

In this case study, wall specimen W2 tested by Sittipunt et al. (2001) (see Figure 5-16) is analysed using the beam-truss model in iAEM. This wall is considered squat with its shear span ratio of $M/VL_w = 1.4$. The longitudinal reinforcement ratios in the boundary elements and the web are $\rho_{lb} = 2.29\%$ and $\rho_{lw} = 0.52\%$, respectively. In the transverse direction, the reinforcement ratio in the web is $\rho_{tw} = 0.79\%$. In the test, cyclic lateral force P was applied at the top beam. This beam remained free

throughout the test. No axial load was applied to the wall in the test. A total of sixteen load cycles were applied in the test with three cycles at each drift level.

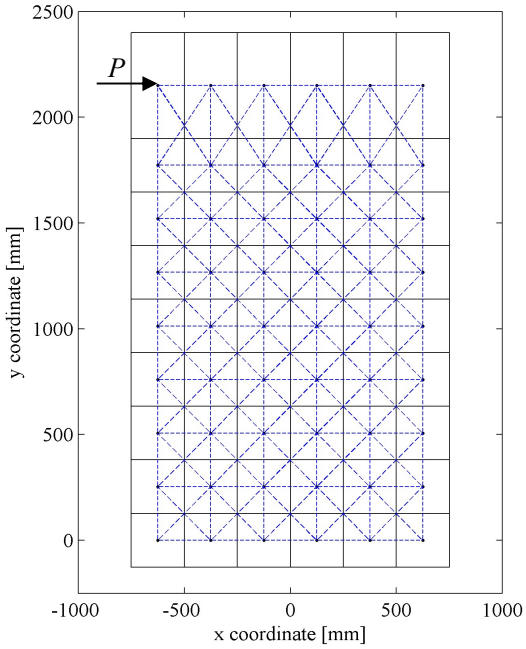

Figure 5-17 iAEM model of wall W2

Table 5-2 Material properties of wall W2

Unconfined concrete	$f_c^{'}$ (MPa)	ε_{c0}	f_t (MPa)
	-35.8	-0.2%	1.97
Confined concrete	f_{cc} (MPa)	ε_{cc}	
	-39.4	-0.30%	
Reinforcement	Type	f_y (MPa)	b
	Φ6	444	0.02
	Φ10	450	0.02
	Φ12	425	0.02
	Φ16	473	0.02

The beam-truss model for wall W2 using iAEM is shown in Figure 5-17. The model consists of 54 (6×9) iAEM elements. Cross section of the wall is divided into six

fiber-beam sections, and the vertical spacing of horizontal trusses is 253 mm (see Figure 5-16(c)). Material properties of the wall W2 in the analysis are listed in Table 5-2.

The lateral load versus top displacement curve from the iAEM analysis as well as the measured response by Sittipunt et al. (2001) are plotted in Figure 5-18. In order to trace the cyclic response of the wall more clearly, the lateral load versus top displacement curves are plotted every three cycles in Figure 5-19. It can be seen that the iAEM model computes the cyclic response of the wall in terms of strength, loading and unloading stiffnesses well. The computed peak lateral strength is 6.6% smaller than that of experimental result for the positive displacement response. In the test, the wall failed by web crushing at a top displacement of -35 mm, corresponding to a drift ratio of Θ = -1.6%. The iAEM model computes the initiation of compression softening and crushing of concrete diagonals at the drift ratio of Θ = -2.1% and -2.2%, respectively. This means iAEM model also predicts the failure mode of the wall as web crushing, but at a larger top displacement.

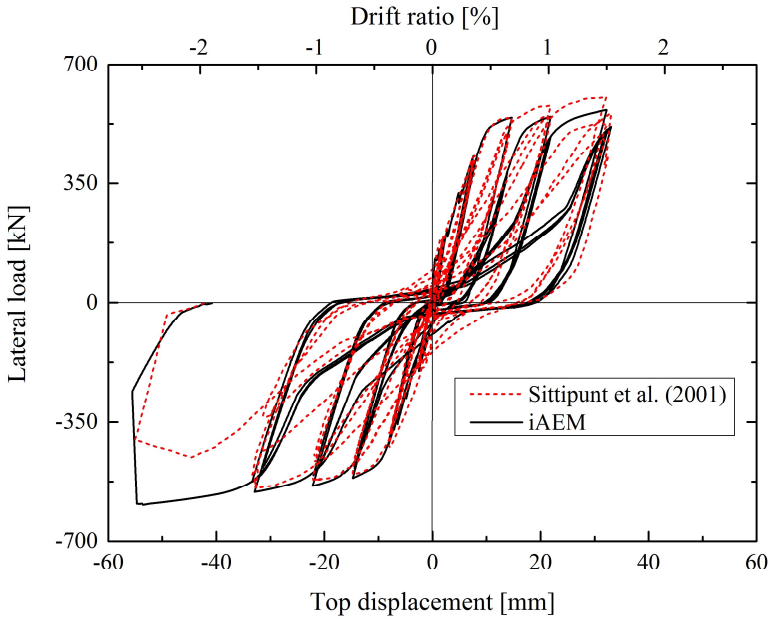

Figure 5-18 Lateral force versus top displacement curves of wall W2

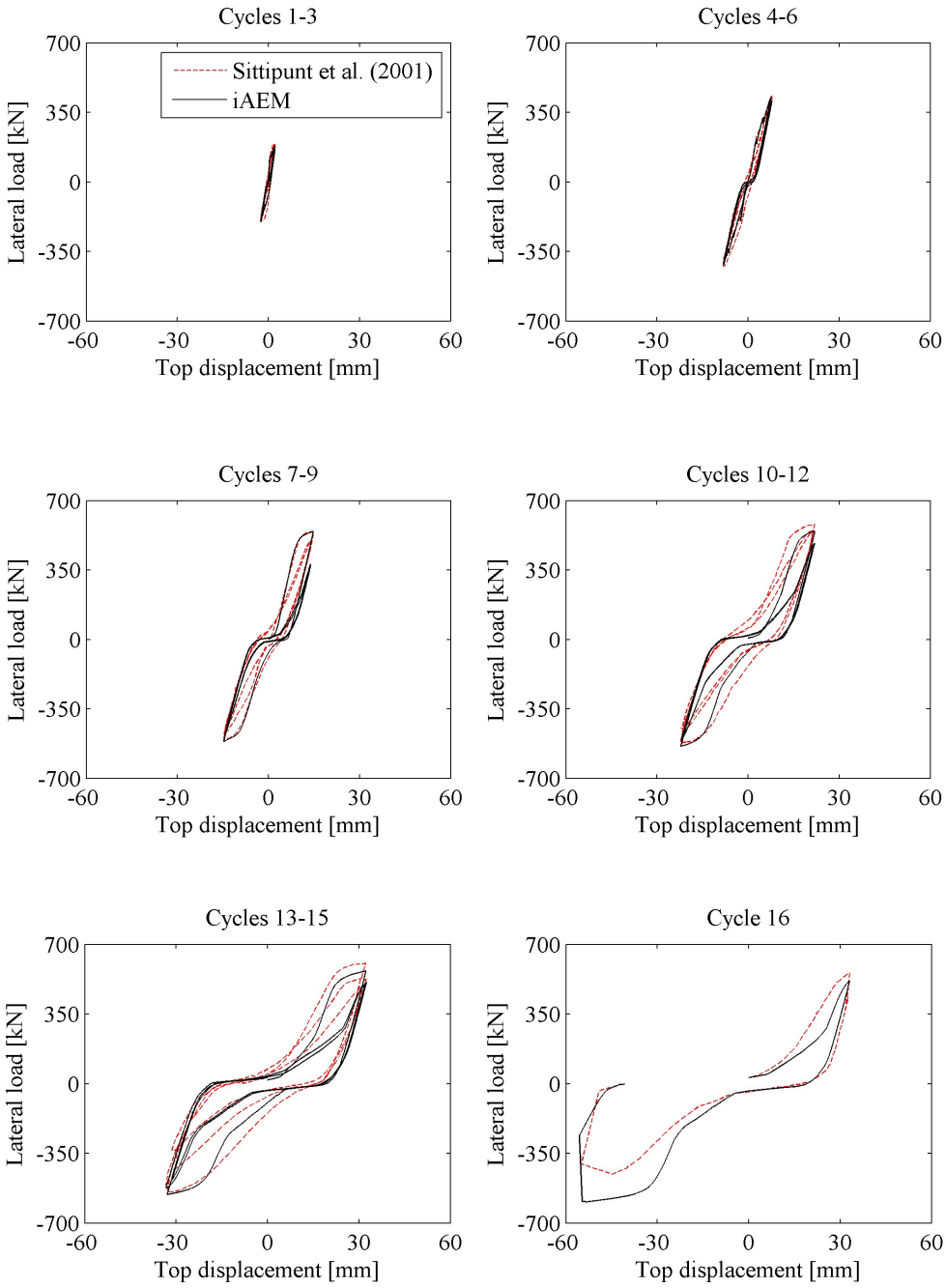

Figure 5-19 Lateral load versus top displacement curves of wall W2 plotted every three cycles

5.5.3 Shiu et al. (1981) – Wall PW1

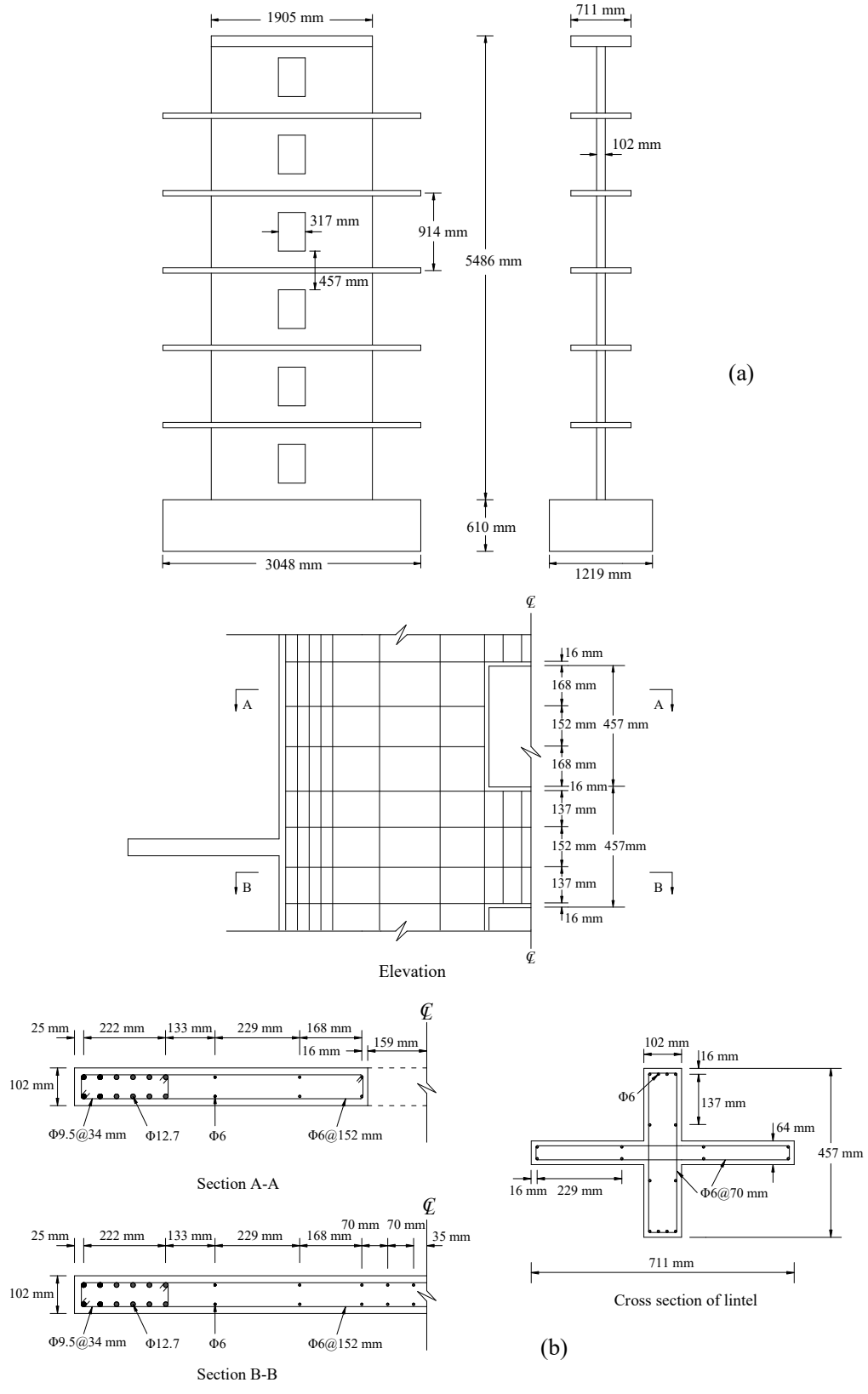

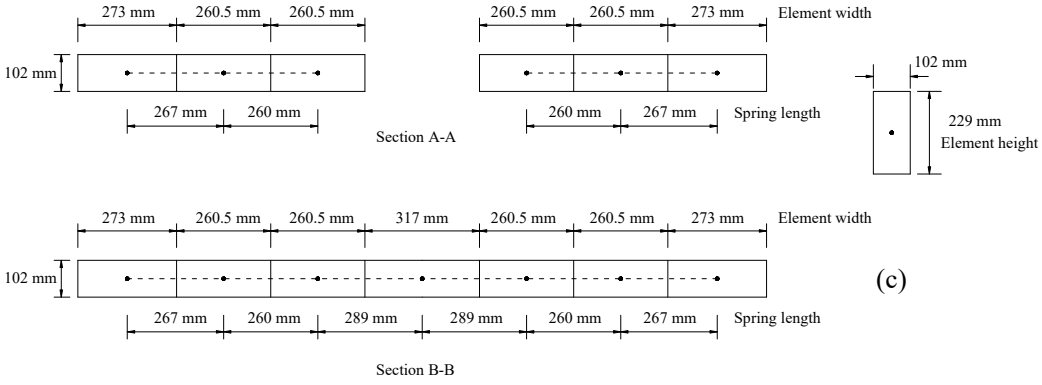

Figure 5-20 Wall specimen PW1 tested by Shiu et al. (1981)

In this numerical example, wall specimen PW1 tested by Shiu et al. (1981) is modelled by iAEM. This is a moderately slender wall with a shear span ratio of $M/VL_w = 2.9$, and it is a 1:3 scale representation of a six-storey RC wall with openings (see Figure 5-20). The longitudinal portion of the wall is heavily reinforced with reinforcement ratios in the boundary elements and web equal to $\rho_{lb} = 5.6\%$ and $\rho_{lw} = 0.3\%$, respectively. The transverse reinforcement ratio in the web is $\rho_{tw} = 0.4\%$. The longitudinal and transverse reinforcement ratios of the coupling beams are $\rho_{lcb} =$ 0.7% and $\rho_{tcb} = 0.9\%$, respectively. These beams were designed to be elastic and they remained elastic during the test. Cyclic lateral force P was applied at the top of the wall which was allowed to rotate freely by the test setup.

The beam-truss model for wall PW1 using the iAEM is shown in Figure 5-21. The model consists of 169 iAEM elements. Cross section of each longitudinal portion of the wall is represented by three fiber-beam sections. Cross section of the coupling beams in the longitudinal direction is represented by one fiber-beam section. The vertical spacing of horizontal trusses is 229 mm (see Figure 5-20(c)). Material properties of wall PW1 in the analysis are listed in Table 5-4.

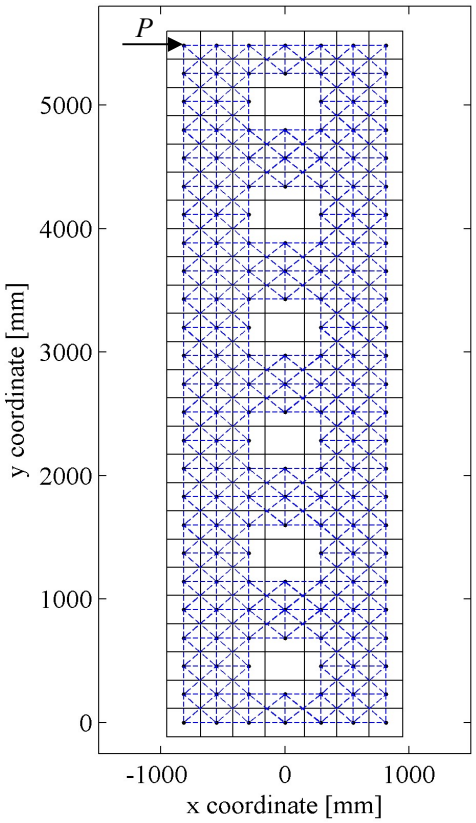

Figure 5-21 iAEM model of wall PW1

Table 5-3 Material properties of wall PW1

Unconfined concrete	$f_c^{'}$ (MPa)	ε_{c0}	f_t (MPa)
	-21.0	-0.2%	1.51
Confined concrete	f_{cc} (MPa)	ε_{cc}	
	-33.7	-0.80%	
Reinforcement	Type	f_y (MPa)	b
	Φ6	462	0.05
	Φ9.5	538	0.05
	Φ12.7	416	0.05

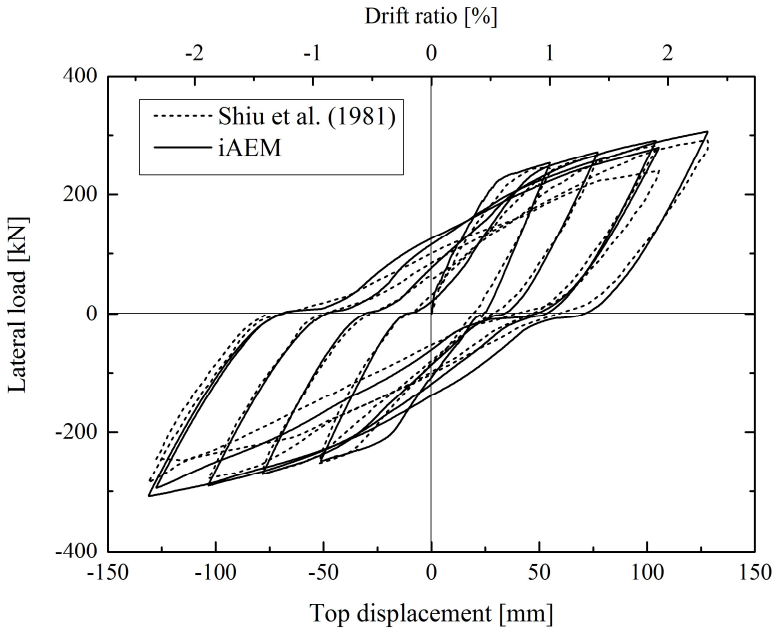

Figure 5-22 Lateral load versus top displacement curves of wall PW1

The lateral load versus top displacement curve of the wall PW1 from the iAEM analysis as well as the one measured by Shiu et al. (1981) are plotted in Figure 5-22. From the figure, it can be seen that the iAEM model satisfactorily computes the overall cyclic response of the wall in terms of strength, loading and unloading stiffness. The computed peak lateral force is 307 kN which is 5.0% larger than that of the experiment result for the positive displacement response. In the experiment, the compression-shear failure was observed in the boundary element of the first storey in the last cycle. However, from iAEM analysis, the diagonal concrete does not reach ε_{c0}, and there is no compression softening. This is probably because compression-shear failure is quite local for this moderately slender wall, and more refined iAEM mesh may be needed to properly connect the longitudinal portions and the coupling beams.

5.5.4 Massone (2006) – Wall WP1105-8

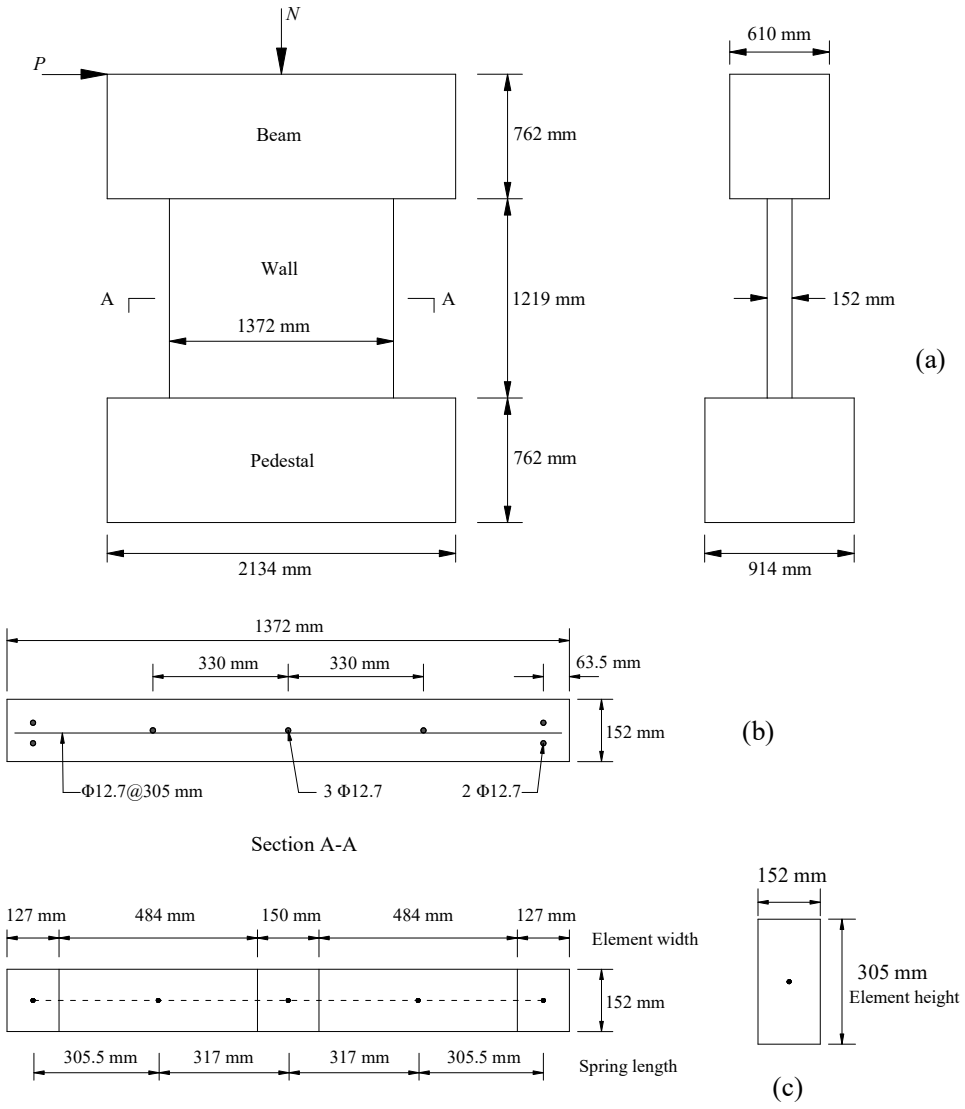

Figure 5-23 Wall specimen WP1105-8 tested by Massone (2006)

In this numerical example, a very squat wall specimen WP1105-8 tested by Massone (2006) (see Figure 5-23) is modelled by iAEM. Its shear span ratio is $M/VL_w = 0.45$. The wall is lightly reinforced in the longitudinal and transverse directions. The wall's longitudinal and transverse reinforcement ratios are $\rho_l = 0.43\%$ and $\rho_t = 0.27\%$, respectively. As in the previous examples, cyclic lateral force P was applied to the wall via a top beam in the test, and the top beam was restrained from rotating,

resulting in a point of inflection at the wall's midheight. The compressive axial load ratio was $N/\left(f_c^{'}A_g\right)=0.05$, and it remained constant during the test.

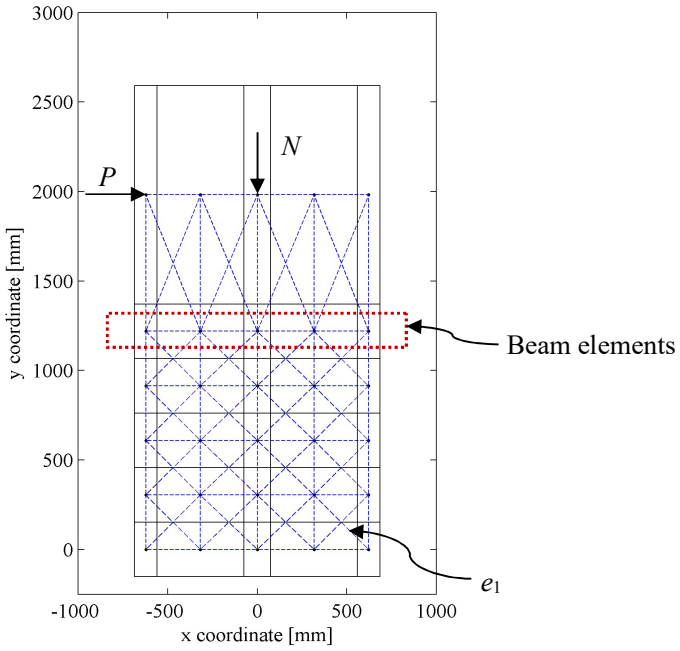

Figure 5-24 iAEM model of wall WP1105-8

Table 5-4 Material properties of wall WP1105-8

Unconfined concrete	$f_c^{'}$ (MPa)	ε_{c0}	f_t (MPa)
	-35.8	-0.2%	1.97
Reinforcement	Type	f_y (MPa)	b
	Φ12.7	444	0.02

The beam-truss model for wall WP1105-8 in iAEM is shown in Figure 5-24. The model consists of 30 (5×6) iAEM elements. Cross section of the wall is divided into five fiber-beam sections. In order to transfer the moment due to zero-rotation at the top beam, flexural behavior of the top beam should not be ignored in the iAEM modeling, therefore, instead of using horizontal truss elements, horizontal beam elements with the same flexural stiffness as the top beam are used to connect the iAEM elements at the 5th row, while the elements of 5th and 6th rows are rigidly

connected. The vertical spacing of the elements at the 5th and 6th rows is 762 mm while the vertical spacing between other horizontal trusses is 305 mm (see Figure 5-23(c)). Material properties of the wall WP1105-8 in the analysis are listed in Table 5-4.

The monotonic pushover analysis is first performed for the wall to validate the beam assumption at the 5th row. The lateral load versus top displacement curve from iAEM analysis is shown in Figure 5-25 together with the experimental result. The wall response when the horizontal truss elements are used to connect the elements at the 5th row is also plotted for comparison. It can be seen that the result from the model with the beam assumption agree well with the backbone curve of the experimental result by Massone (2006), whereas the model with the truss assumption predicts much smaller lateral strength. Since rotation of this wall is restrained, bending moment due to *P* at the top beam should be transferred, and horizontal beam elements therefore should be used.

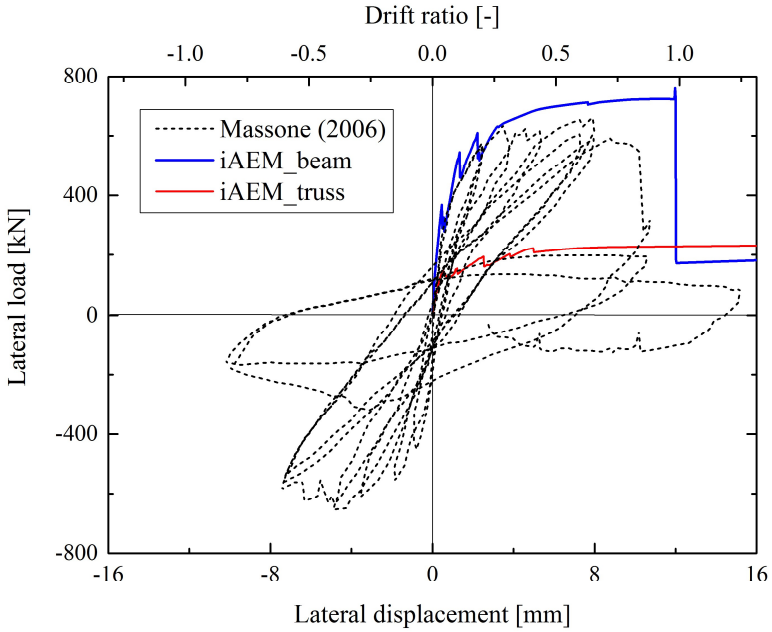

Figure 5-25 Lateral load versus top displacement curves of wall WP1105-8 under monotonic pushover analysis

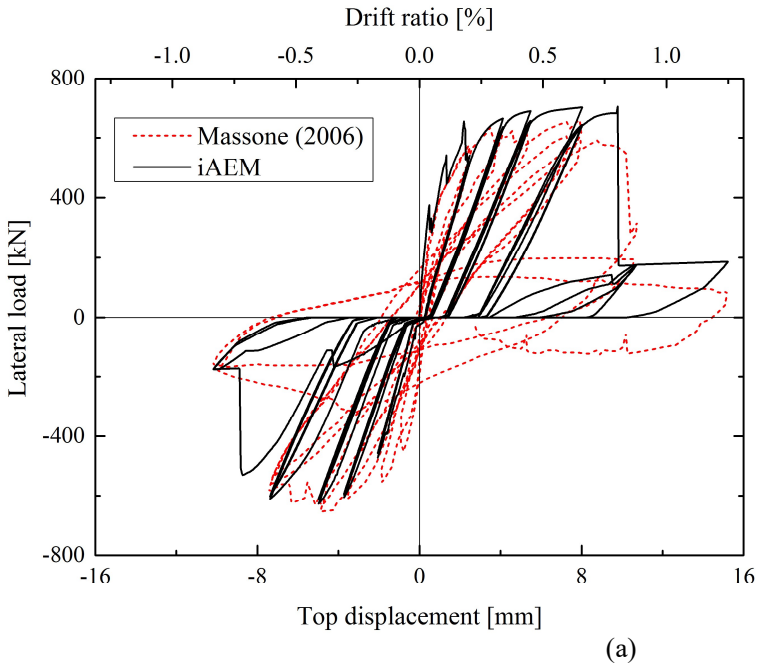

(a)

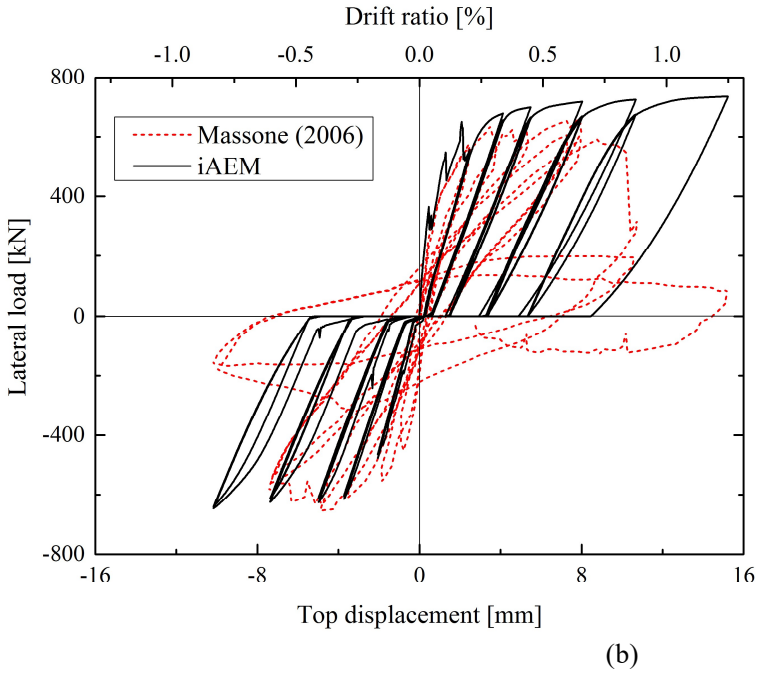

(b)

Figure 5-26 Lateral load versus top displacement curves of wall WP1105-8 under cyclic pushover analysis (a) with FSI (b) without FSI

The cyclic pushover analysis is then carried out. The lateral load versus top displacement curve from the iAEM analysis is shown in Figure 5-26(a) together with the one measured by Massone (2006). From this figure, it can be seen that the overall response from iAEM compares well with the one by Massone (2006) in terms of

strength, loading and unloading stiffness. The computed peak lateral strength is 6.5% larger than the experimentally measured one for the positive displacement response. In the test, diagonal crushing of the concrete and loss of gravity load resistance were observed at $\Theta = 0.84\%$ before the wall reached its flexural strength. The drift ratio of $\Theta = 0.80\%$ corresponding to the sudden drop in the lateral force is accurately computed by iAEM. The initiation of compression softening and crushing of concrete diagonal e_1 (see Figure 5-24) from iAEM analysis occurs at the drift ratios $\Theta = 0.77\%$ and $\Theta = 0.84\%$, respectively. Thus, for this very squat shear wall, compression-shear failure is captured by the beam-truss model with FSI in iAEM.

If the FSI is not considered for this wall by setting the reduction factor of compressive stress of diagonal trusses β equal to 1, the lateral load versus top displacement curve from the iAEM analysis is plotted in Figure 5-26(b) together with the experimental result. It can be seen that when FSI is not considered, lateral strength of the wall keeps increasing when the horizontal displacement increases, and sudden drop of the load displacement curve due to crushing of concrete diagonal cannot be predicted. When the drift ratio reaches 1.25%, the computed maximum compressive strain of the diagonal trusses from the iAEM analysis is only 0.0007 which is much smaller than the strain of 0.002 when softening of the concrete initiates, the wall hasn't failed. Therefore, it is important to consider FSI in the modeling in order to predict accurate wall response.

5.5.5 Ono et al. (1976) – Wall W7502

In the last numerical example, a two-storey I-shaped squat shear wall specimen W7502 tested by Ono et al. (1976) (see Figure 5-27) is modelled by iAEM. Shear span ratio of the wall is $M/VL_w = 0.94$. The longitudinal and transverse reinforcement ratios in the boundary columns are $\rho_{lc} = 1.6\%$ and $\rho_{tc} = 0.22\%$, respectively. The longitudinal and transverse reinforcement ratios in the web are

equal with $\rho_w = 0.24\%$. The longitudinal and transverse reinforcement ratios in the beams are $\rho_{lb} = 0.8\%$ and $\rho_{tb} = 0.22\%$, respectively. In the test, a total vertical load of $N = 368$kN with $N/2$ at each column was applied to this wall. The lateral load P was applied to the top beam while the vertical load remained constant during the test.

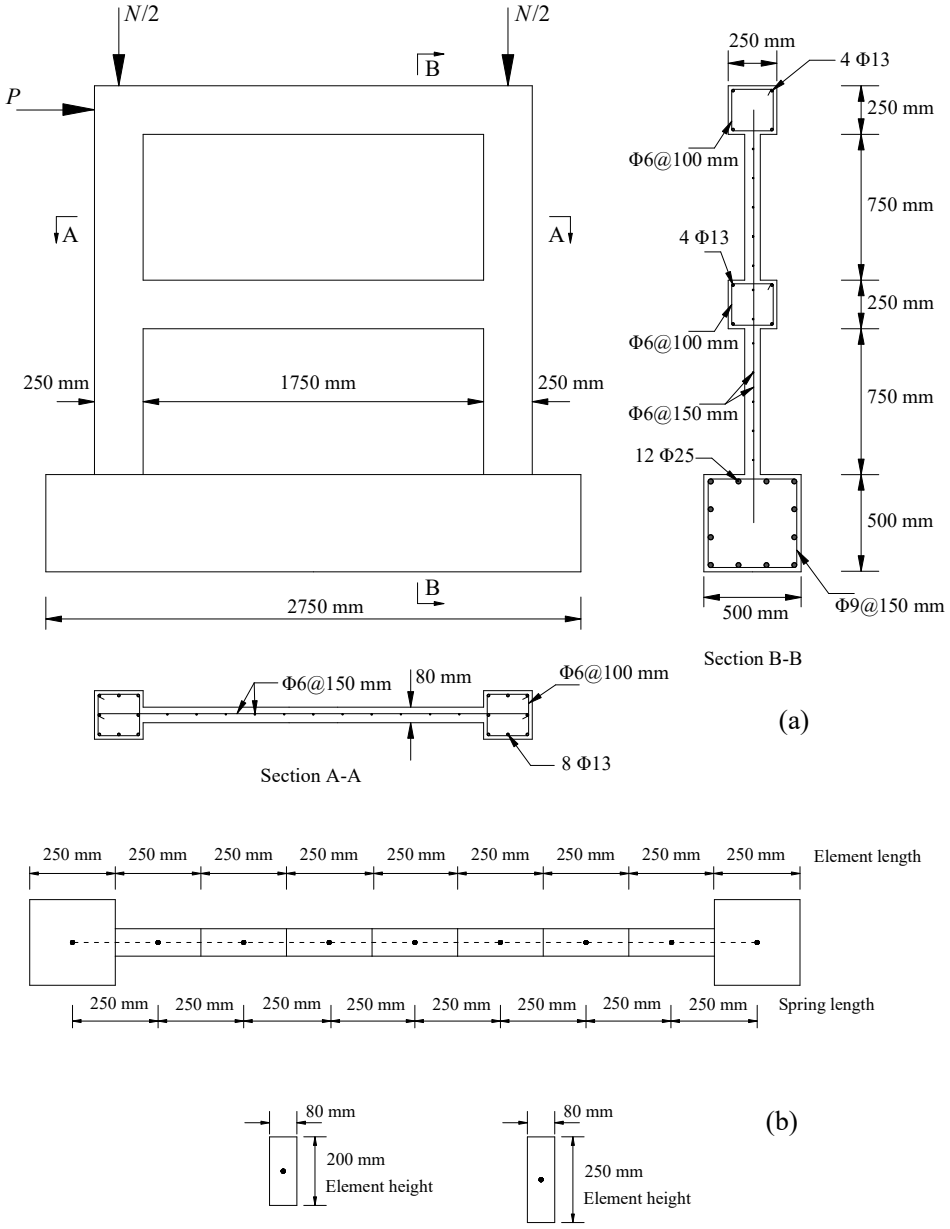

Figure 5-27 Wall specimen W7502 tested by Ono et al. (1976)

The beam-truss model for wall W7502 in iAEM is shown in Figure 5-28. The model consists of 81 (9×9) iAEM elements. Cross section of the wall is divided into nine fiber-beam sections. As the cross section of the horizontal beams at the first and second stories is considered large compared to the storey height and web thickness, flexural behavior of the horizontal beams should not be ignored in the iAEM modelling. Therefore, horizontal beam elements instead of horizontal trusses are used to represent these two beams. The vertical spacing of horizontal trusses for the first and second stories of the wall is 200 mm and 250 mm, respectively (see Figure 5-27(b)). Material properties of the wall W7502 in the analysis are listed in Table 5-5.

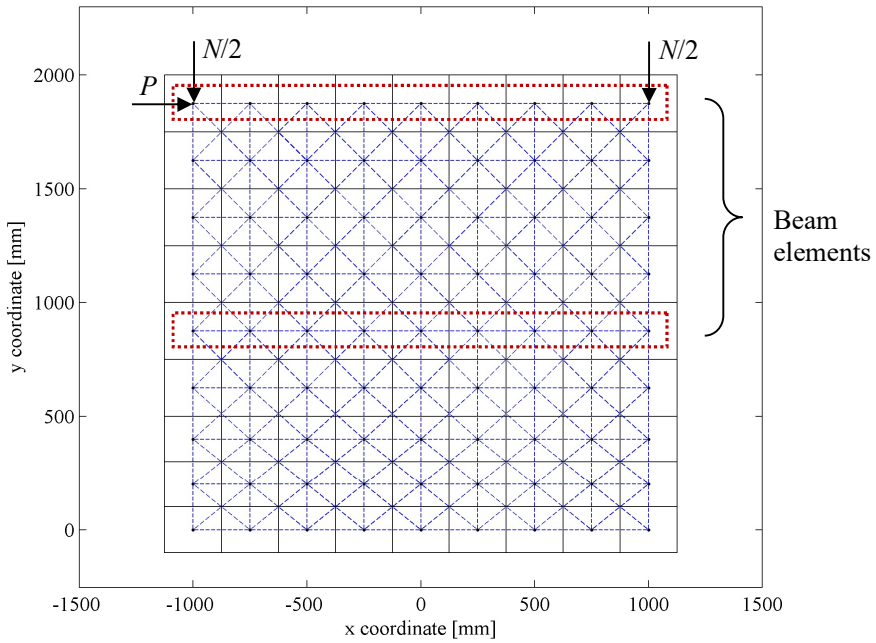

Figure 5-28 iAEM model of wall W7502

Table 5-5 Material properties of wall W7502

Unconfined concrete	$f_c^{'}$ (MPa)	ε_{c0}	f_t (MPa)
	-22.86	-0.2%	1.58
Confined concrete	f_{cc} (MPa)	ε_{cc}	
	-27.07	-0.38%	

	Type	f_y (MPa)	b
Reinforcement	Φ6	367	0.02
	Φ13	318	0.02

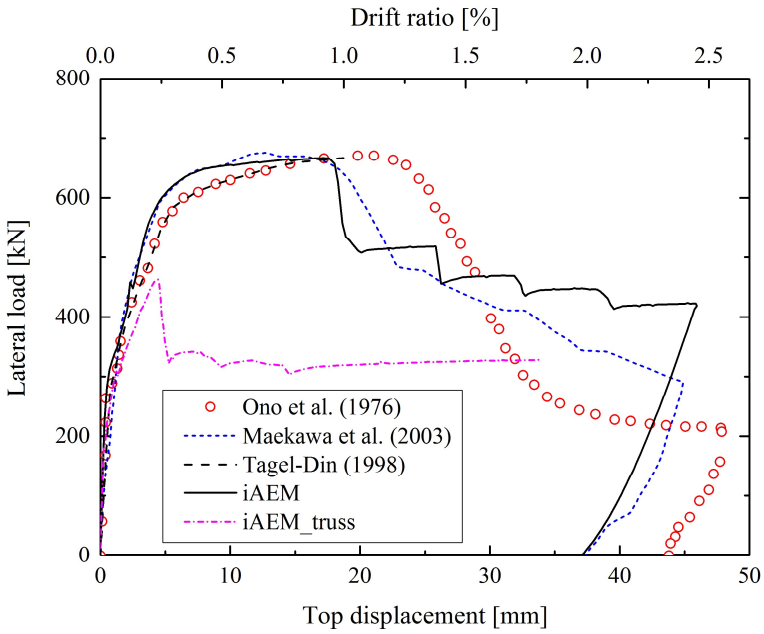

Figure 5-29 Lateral load versus top displacement curves of wall W7502

The result in terms of lateral load versus top displacement from the iAEM analysis is shown in Figure 5-29, in comparison with the one measured by Ono et al. (1976) and those analysed by Maekawa et al. (2003) using FEM and Tagel-Din (1998) using conventional AEM. It should be mentioned that, in the figure, the curve by the conventional AEM gives only the load displacement curve up to the peak strength, while the other three curves contain the loading, softening and unloading paths. From this figure, it can be seen that the overall load displacement curve from iAEM compares well with the published results. The computed peak lateral load from iAEM is 669 kN which is only –0.3% and –0.4% than the experimentally measured one by Ono et al. (1976) and the one predicted by Maekawa et al. (2003) using FEM, respectively. From the iAEM analysis, the failure of the wall specimen is due to crushing of the concrete diagonals of the wall after it reaches peak strength. The

failure observed in the experiment is initiated by the shear compression failure of the column at the compression side followed by the compression failure of the wall. Thus, for this very squat shear wall, compression-shear failure is captured by the beam-truss model with FSI in iAEM.

In the same figure, the iAEM model with truss elements instead of beam elements for the two large-sized beams is also plotted. It can be seen that the model with truss assumption for two large-sized beams predicts lateral strength of the wall as only 460 kN which is 31.2% smaller than that from the model with beam assumption. Therefore, for the horizontal beams with considerable size, their flexural behavior should be considered by using the beam elements in the modeling.

To model this shear wall, only 81 iAEM elements are used as compared to 1800 conventional AEM elements (Tagel-Din, 1998). The computational demand is estimated as N^2, where N is the number of degrees of freedom of a numerical model. For both iAEM and conventional AEM, each element has 3 degrees of freedom for the two-dimensional case. Therefore, the conventional AEM requires approximately 500 times more computational demand than the iAEM model. The estimation ignores the influence of stress update of spring pairs on the computational demand in the nonlinear analysis. It is known that stress update of a large number of springs constitutes a significant portion of total computational demand. For this wall, 656 spring pairs are used to connect the iAEM elements while approximately 36000 spring pairs are used by the conventional AEM. Therefore, the estimation is deemed conservative and much more efficient analysis of RC shear wall is performed by the iAEM.

5.6 Summary

In this chapter, a review on the modelling methods for RC shear walls is first briefly presented. Then the beam-truss model to simulate the RC shear walls in iAEM is

described. The FSI is considered in this model through compression-only diagonal truss elements which account for the effect of lateral tensile strain on the stress-strain relationship of concrete in compression. Finally, the beam-truss model is used in iAEM to analyse five tested RC shear walls with shear span ratio ranging from 0.45 to 3. The calculated load displacement curves from iAEM agree well with those from the tests. It is found that the beam-truss model can properly capture different failure modes for the walls with different shear span ratios, and compression-shear failure is predicted for the squat walls where strong FSI exist. It is also found that for shear walls which contain horizontal beams with considerably large cross section (Ono et al., 1976) or transfer the bending moments due to zero rotation (Massone, 2006), flexural behavior of these beams should not be ignored. Therefore, horizontal beam elements should be used in iAEM in order to predict more accurate wall response. Compared with the conventional AEM, by using the beam-truss model in iAEM, the compression-shear failure of the squat wall can be predicted with high efficiency.

6 System-level Case Studies

In Chapters 3 and 4, extension of the iAEM to consider initial imperfections and semi-rigid connection behavior of real steel structures is presented. In Chapter 5, application of the iAEM to model RC shear walls is performed using the beam-truss model. In this chapter, these modelling features in iAEM are integrated for system-level case studies of two multi-storey buildings. The first building is the 6-storey 2-bay Vogel frame for which the initial imperfections and semi-rigid connections are considered. The second building is a 14-storey hybrid structure for which the steel frames and RC shear wall are modelled together using iAEM.

6.3 6-storey 2-bay Vogel frame

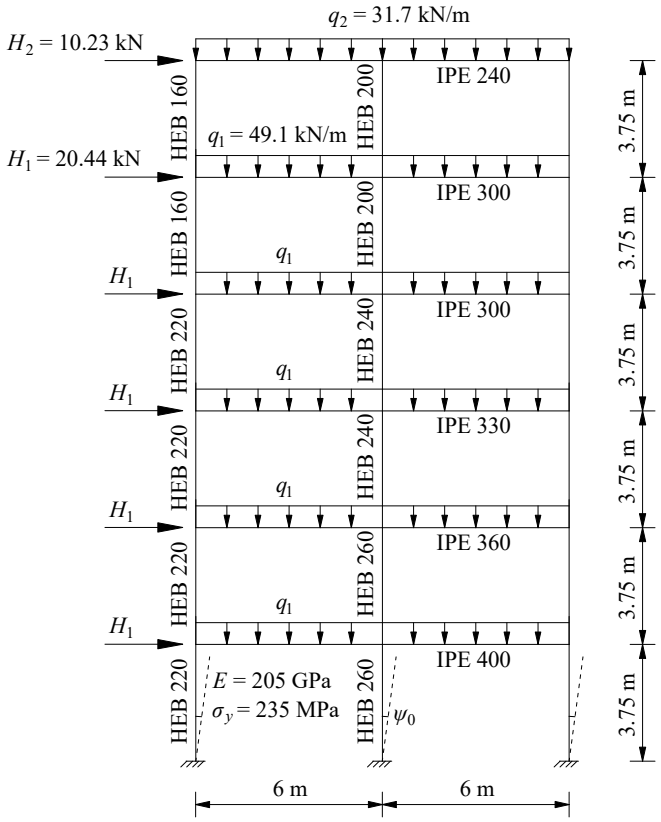

Figure 6-1 6-storey 2-bay Vogel frame

In the first case study, nonlinear static analysis is performed for the 6-storey 2-bay Vogel frame with semi-rigid connection behavior studied by Chan and Chui (2000). The detailed description of the frame can be referred to Section 3.3.4 where the same frame with rigid connection has been studied. Here the top and seat with web angles (TSWA) connection is considered for the iAEM analysis. In the study of Chan and Chui (2000), rotational springs were used to consider the semi-rigid connection behavior. Chen-Lui exponential model (Lui and Chen, 1986; Lui and Chen, 1988) was used to represent the nonlinear moment-rotation curve of the semi-rigid connections, and the function parameters are given in Table 6-1 to fit one of the eighteen experimental tests by Azizinamini (1985). In order to apply the component method as described in Chapter 4 in iAEM, specific connection details should be known to define the load deformation relation of each component. Therefore, it is necessary to know the curve by Chen-Lui exponential model is fitted for which of the experimental tests by Azizinamini (1985) .

The Chen-Lui exponential model takes the following form:

$$M = M_o + \sum_{j=1}^{n} C_j \left[1 - \exp\left(\frac{-|\Phi_c|}{2j\alpha} \right) \right] + R_{kf} |\Phi_c| \tag{6-1}$$

and its tangent connection stiffness S_c is given by:

$$S_c = \sum_{j=1}^{n} \frac{C_j}{2j\alpha} \exp\left(\frac{-|\Phi_c|}{2j\alpha} \right) + R_{kf} \tag{6-2}$$

with the initial stiffness S_c^o obtained as:

$$S_c^o = \sum_{j=1}^{n} \frac{C_j}{2j\alpha} + R_{kf} \tag{6-3}$$

where M is the moment in the connection, $|\Phi_c|$ is the absolute value of the rotational deformation of the connection, M_o is the initial moment, R_{kf} is the strain-

hardening stiffness of the connection, α is the scaling factor, C_j is the curve-fitting coefficient and n is the number of terms considered.

Table 6-1 Connection parameters for the TSWA connection in Chen-Lui exponential model

M_o	0	R_{kf}	0.43169×10^{3}	α	0.31425×10^{-3}
C_1	-0.34515×10^{-3}	C_2	0.52345×10^{4}	C_3	-0.26762×10^{5}
C_4	0.61920×10^{5}	C_5	-0.65115×10^{5}	C_6	0.25506×10^{5}
S_c^o	0.95219×10^{5}				

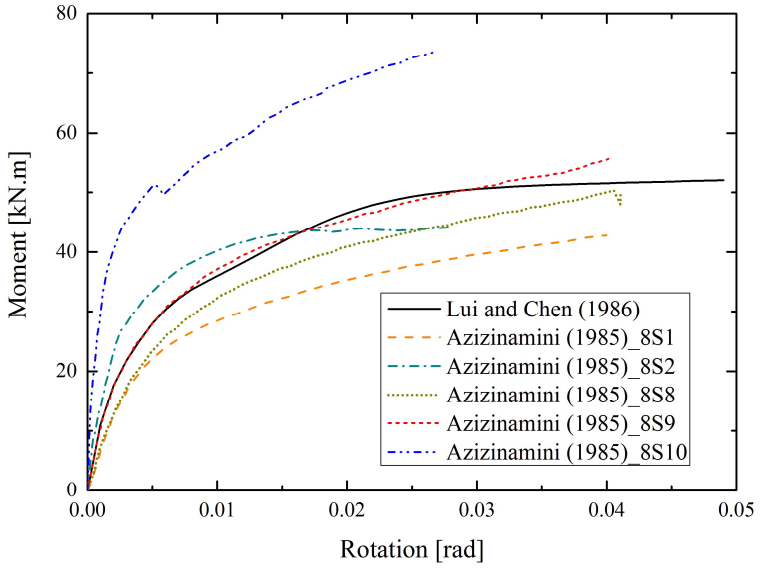

Figure 6-2 Moment rotation curves from the Chen-Lui exponential model and the tests by Azizinamini (1985)

By comparing the moment rotation curve from the Chen-Lui exponential model with those from the selected tests by Azizinamini (1985) in Figure 6-2, it is found that Chen-Lui exponential model best fits the result of the test with connection specimen 8S9. Hence, it can be deduced that it is the test result of specimen 8S9 that the Chen-Lui's model aimed to fit. Therefore, specimen 8S9 is used for connection modelling by the component method in iAEM.

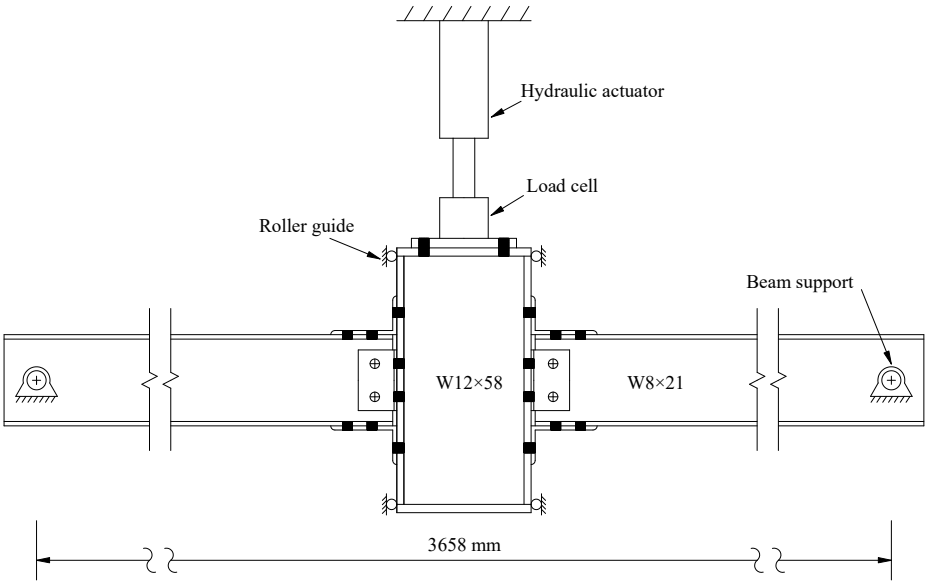

Figure 6-3 Test setup of the static connection test for specimen 8S9

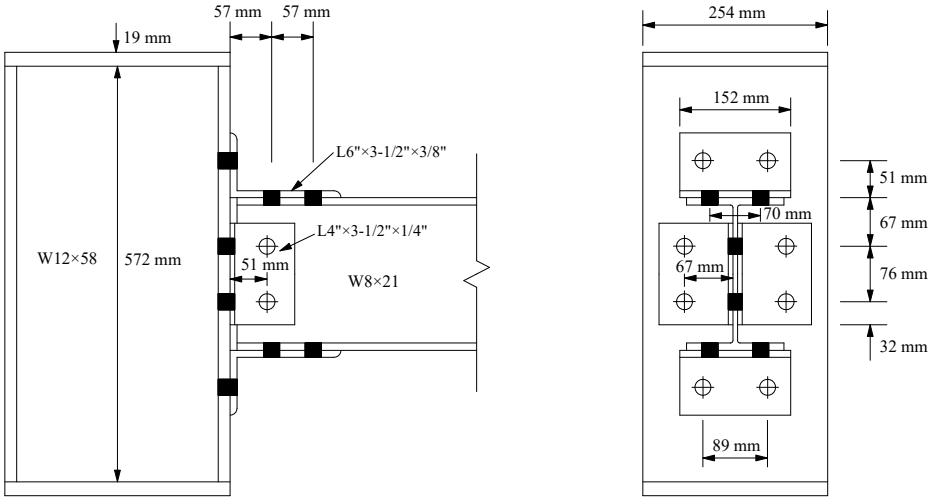

Figure 6-4 Details of the connection specimen 8S9

The test setup of the static connection test by Azizinamini (1985) for specimen 8S9 is illustrated in Figure 6-3. The test members consist of a pair of W8×21-section (equivalent UB203×133×31) beams attached to a centrally positioned W12×58-section (equivalent UB305×254×86) stub column. The distance between the two pin supports is 3658 mm. Displacement control is used for the test. Details of the

connection specimen 8S9 are shown in Figure 6-4. The top and seat angle size is L6"×3-1/2"×3/8" (equivalent L150×90×10 in mm), and the web angle size is L4"×3-1/2"×1/4" (equivalent L100×90×6). ASTM A36 steel is used for the members and connection elements. The fasteners are 7/8" (22.2 mm) diameter ASTM A325 heavy-hex high-strength bolts and nuts, with A325 hardened washers used under the turned elements. Azizinamini (1985) tests were terminated when the preset displacement limit was reached and significant nonlinear deformations were developed, but connection failures did not occur.

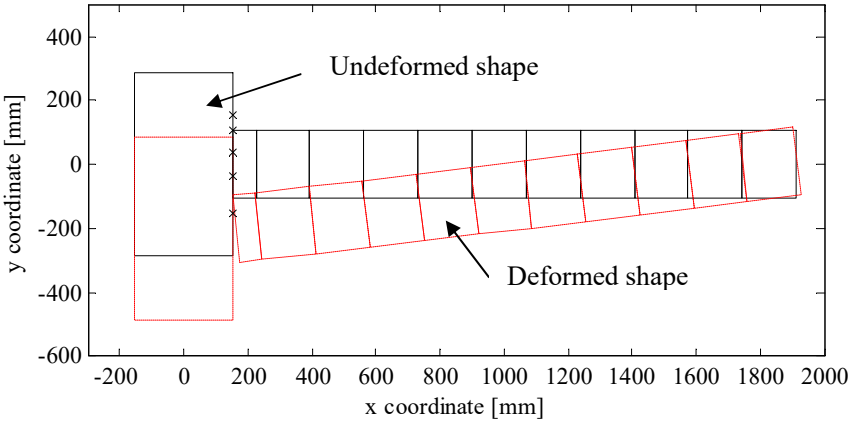

Figure 6-5 iAEM model of connection specimen 8S9

The iAEM model of the double-span test beam with connection specimen 8S9 is shown in Figure 6-5, and only half of the test structure is modelled due to symmetry. Five springs are used to model the beam-to-column connection (see Figure 6-5). The bottom spring represents the seat angle component, and the 2nd and 3rd springs from the bottom represent the two web angle components at each bolt row. To represent the top angle component, two springs are used at the top (or compression side) in case of a change of spring force from compression to tension. Bolt-slippage is not considered in the iAEM model as it was not observed in the test.

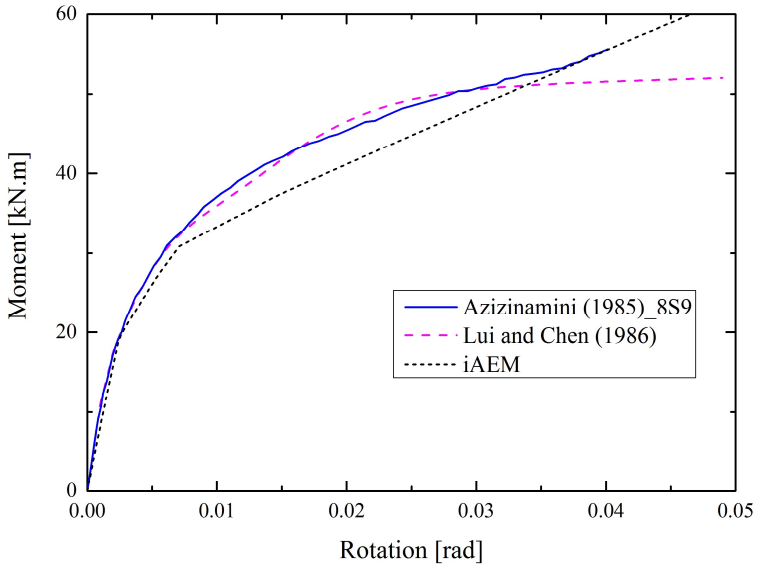

Figure 6-6 Moment rotation curves for connection specimen 8S9

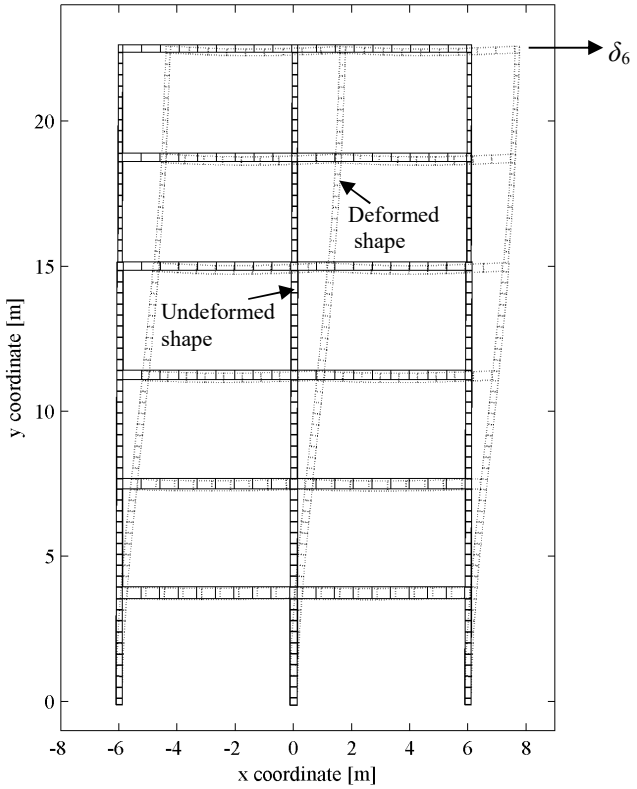

Figure 6-7 iAEM model of the 6-storey 2-bay Vogel frame

The moment rotation curve from iAEM analysis is shown in Figure 6-6 together with those from Chen-Lui exponential model and test of specimen 8S9 by Azizinamini

(1985). According to this figure, it can be seen that moment rotation curve predicted by the component-based model in iAEM agrees generally well with those from the experiment and the Chen-Lui exponential model until the rotation of 0.035 rad. Then this connection model in iAEM is applied to the 6-storey 2-bay Vogel frame.

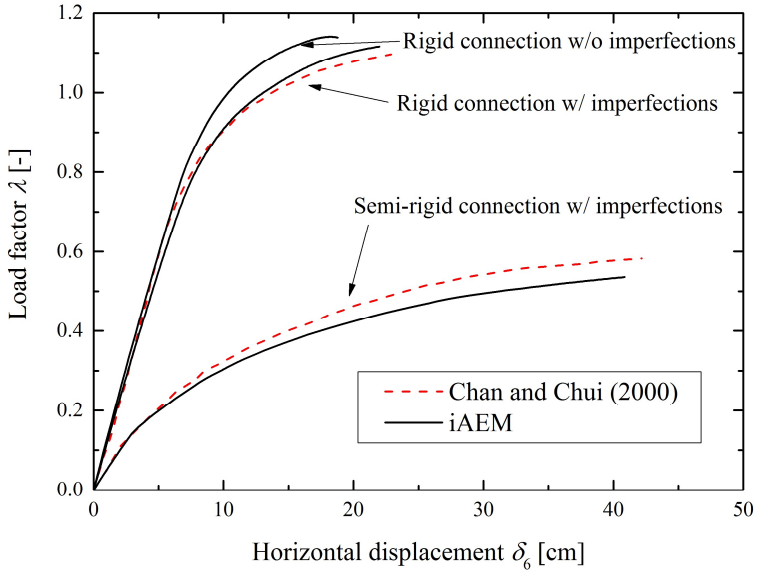

Figure 6-8 Load factor versus horizontal displacement curves of the Vogel frame

As shown in Figure 6-7, a total of 291 iAEM elements are used to model the frame, and the explicit modelling methods as proposed in Chapter 3 are adopted to account for the frame's initial geometric imperfections and residual stresses. In addition, to simulate the semi-rigid connection behavior, the validated connection behavior for TSWA-typed specimen 8S9 using the component method as described in Chapter 4 is applied for the frame. The load factor versus top-storey displacement δ_6 curve from iAEM analysis is shown in Figure 6-8. The corresponding result predicted by Chan and Chui (2000) is also plotted for comparison. In the same figure, the results from rigid connection assumption with and without considering initial imperfections are also plotted. From this figure, it can be seen that the curves from iAEM analysis agree generally well with those given by Chan and Chui (2000). In the rigid connection condition, the frame with initial imperfections yields earlier, and has a smaller

ultimate load factor of 1.113 as compared to 1.141 for the frame without initial imperfections. When the semi-rigid connection behavior of specimen 8S9 is considered, it is found that the ultimate load factor of the frame from iAEM analysis reduces significantly to 0.536. It is concluded that, in order to get more accurate structural behavior of real steel structures, modelling of initial imperfections and semi-rigid connection behavior is necessary.

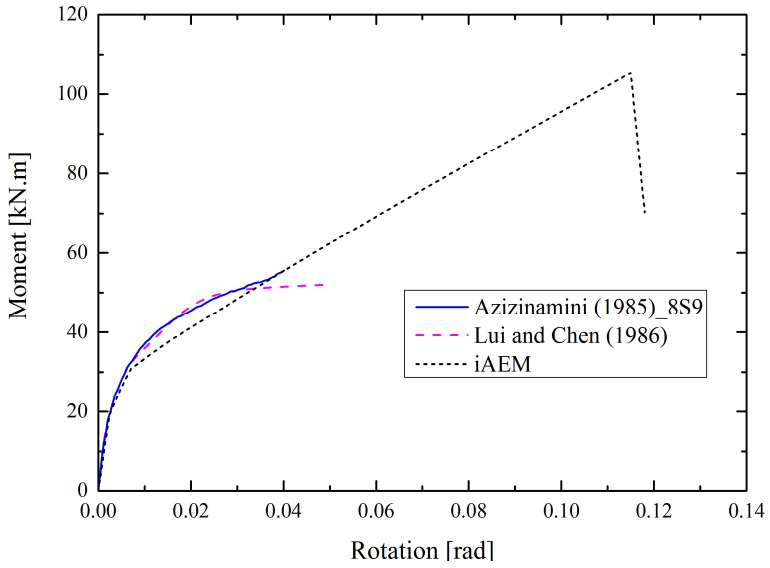

Figure 6-9 Extended moment rotation curves for connection specimen 8S9

For this 6-storey 2-bay frame, both Chen-Lui exponential model and iAEM component-based model predict very similar moment rotation curves when the connection rotation is still small, i.e. less than 0.04 rad. But by extending the moment rotation curve beyond 0.04 rad by iAEM for the connection specimen 8S9 (see Figure 6-9), it can be seen that the Chen-Lui's curve flattens while the component-based model in iAEM predicts increasing moment consistent with the experimental observation by Yang and Tan (2013b). Therefore, Chen-Lui's model is not suitable for progressive collapse analysis involving very large deformation in which the moment will increase due to material hardening and large geometric nonlinearities. In addition, with the defined failure load and displacement, the component-based model in iAEM has the ability of simulating the gradual connection failure with

the progressive fracture of component springs, while the Chen-Lui exponential model using the rotational spring in this case study fails to do so. Therefore, the advantages of the component-based model in iAEM over the rotational spring model in Chen Lui's model are demonstrated for progressive collapse analysis.

6.4 14-storey hybrid structure

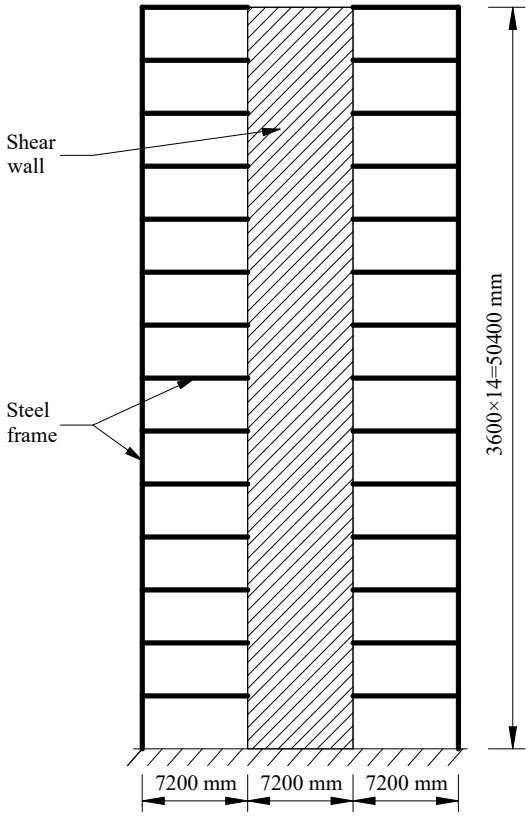

Figure 6-10 14-storey hybrid structure

Table 6-2 Section size and reinforcement distribution

Member type	Section size	Reinforcement distribution
Steel column	Boxed-shaped 550×550×20	-
Steel beam	I-shaped 500×200×14×20	-
RC shear wall	Wall thickness = 350 mm	Double layered Φ12 @150 mm in both directions

In this case study, the 14-storey hybrid structure as shown in Figure 6-10 studied by Zhang (2006) is considered. The efficient hybrid structure is widely used for high-rise buildings as it has advantages of fast construction from steel and large structural stiffness and low cost from concrete. This hybrid structure is fixed at its base, and it is composed of an RC shear wall in the middle bay and steel frames in the perimeter bays. The storey height and bay length of the structure is 3.6 m and 7.2 m,

respectively. The section sizes of the members and reinforcement distribution of the wall are given in Table 6-2. It is assumed that the steel beams are rigidly connected to the steel columns and the RC shear wall. The concrete material has the compressive strength of $f_c^{'} = 35$ MPa and Young's modulus of $E_c = 31.5$ GPa. The steel material and reinforcement have the same yield strength of $f_y = 235$ MPa and Young's modulus of $E_s = 206$ GPa, and it is assumed that strain hardening ratio is 0.3%. Two types of analyses are performed for this structure in the iAEM, i.e. pushover analysis and nonlinear dynamic analysis, and they are described in the following two sections.

6.4.1 Pushover analysis of the hybrid structure

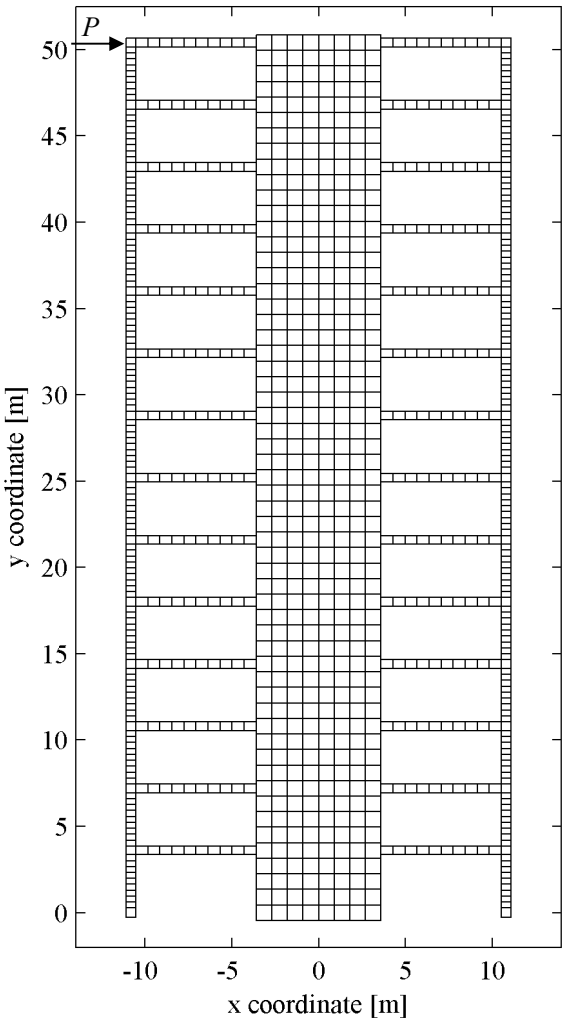

Figure 6-11 iAEM model of the hybrid structure

The iAEM model of the hybrid structure is shown in Figure 6-11. A total of 1018 elements are used in the model with 562 elements for the steel frames and 456 elements for the RC shear wall. The beam-truss model as proposed in Chapter 5 is used to simulate the RC shear wall. Cross section of the wall is divided into eight fiber-beam sections, and the vertical spacing of horizontal trusses is 900 mm. As shown in Figure 6-12, the rigid beam-to-wall connection is modelled with 10 pairs of shear and normal springs between each beam and the wall. Self-weight is first applied to the structure to obtain its initial deformation and stresses. Then a horizontal load P is applied at the top of the structure for pushover analysis.

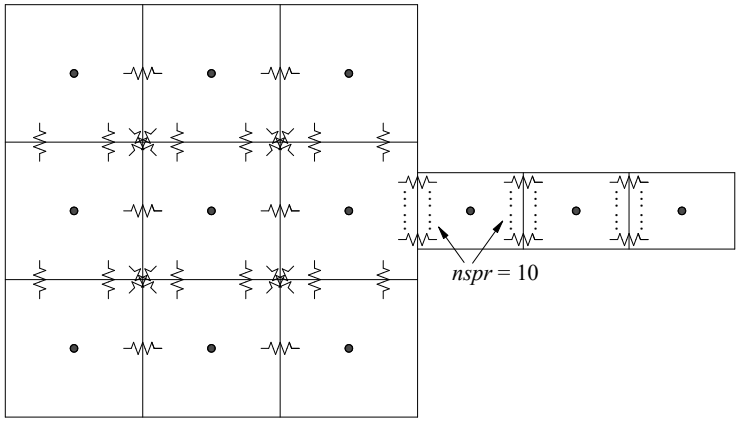

Figure 6-12 Rigid beam-to-wall connection

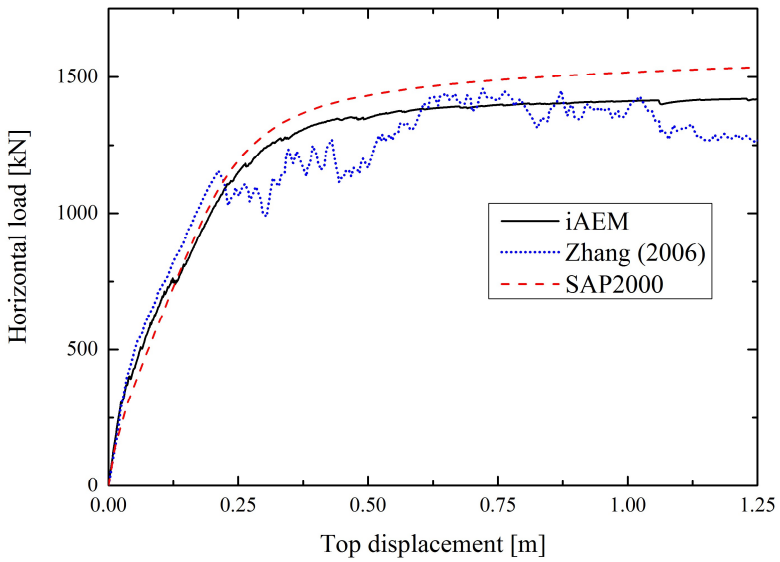

Figure 6-13 Horizontal load versus top displacement curves of the structure

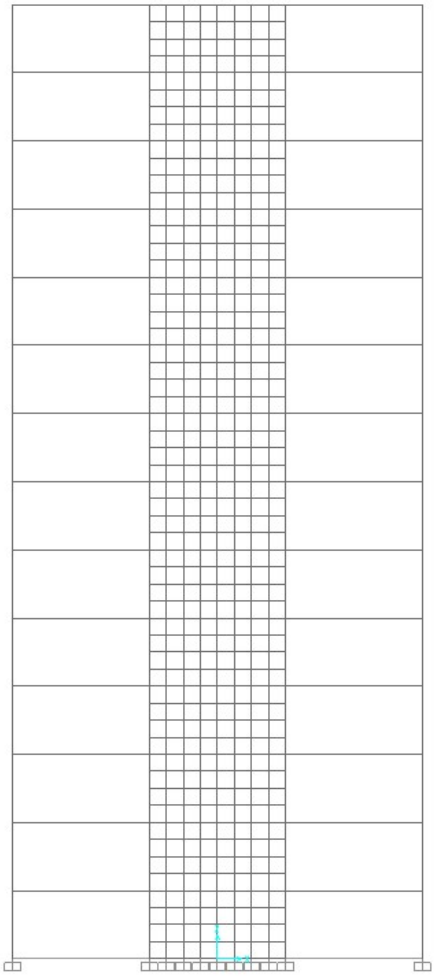

Figure 6-14 FEM model of the hybrid structure in SAP2000

The horizontal load versus top displacement curve from the pushover analysis in iAEM is shown in Figure 6-13, together with that predicted by Zhang (2006) in a pseudo-static way using the explicit dynamic analysis in ABAQUS. Nevertheless, Zhang (2006)'s result contains considerable fluctuations due to numerical convergence problem and may not be accurate. Hence, the load-displacement curve from pushover analysis by SAP2000 is also plotted in Figure 6-13 for comparison. The FEM model of the hybrid structure in SAP2000 is shown in Figure 6-14. Fiber-beam and multi-layered shell elements are used to model the steel frames and RC shear wall, respectively. To simulate the rigid beam-to-wall connection, the steel beams are embedded into the RC shear wall by 900 mm such that they extend the

length of the shell element and connect to two nodes of the shell element. This is because the stiffness properties of drilling DOF, which are normal to shell surfaces, are not accurate for the connection of beam elements (Kalny, 2014). As the mesh is refined, the connection of the beam and shell elements becomes increasingly flexible. By extending the beam elements to connect to two nodes of the shell element, the moments between the beams and RC shear wall are correctly transferred. According to Figure 6-13, it can be seen that the result from iAEM analysis generally agree well with those by Zhang (2006) and SAP2000 analysis. The three curves have almost the same initial stiffness. The computed ultimate load from iAEM is 1417 kN which is -2.7% and -7.8% than those predicted by Zhang (2006) and SAP2000, respectively.

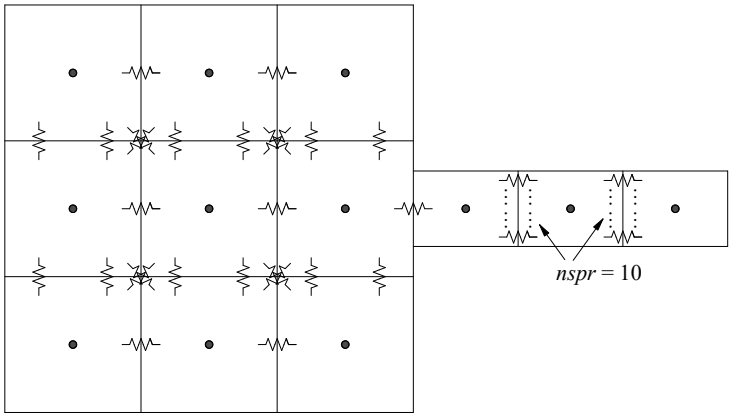

Figure 6-15 Pinned beam-to-wall connection

The pushover analysis assuming pinned beam-to-wall connection is then performed for this structure in both iAEM and SAP2000. To simulate the pinned beam-to-wall connection, only one pair of normal and shear springs is used in iAEM to connect each beam and the wall (see Figure 6-15). In SAP2000, the beam ends are directly connected to the wall boundaries. The load displacement curves are shown in Figure 6-16 together with those assuming the rigid beam-to-wall connection. This figure shows that when the beam-to-wall connection is pinned, the result from iAEM also compares well with that from SAP2000. The computed ultimate load from iAEM is

948 kN which is -33.1% than that from rigid beam-to-wall connection assumption. It is therefore important to appropriately model the beam-to-wall connection to obtain more accurate structural response.

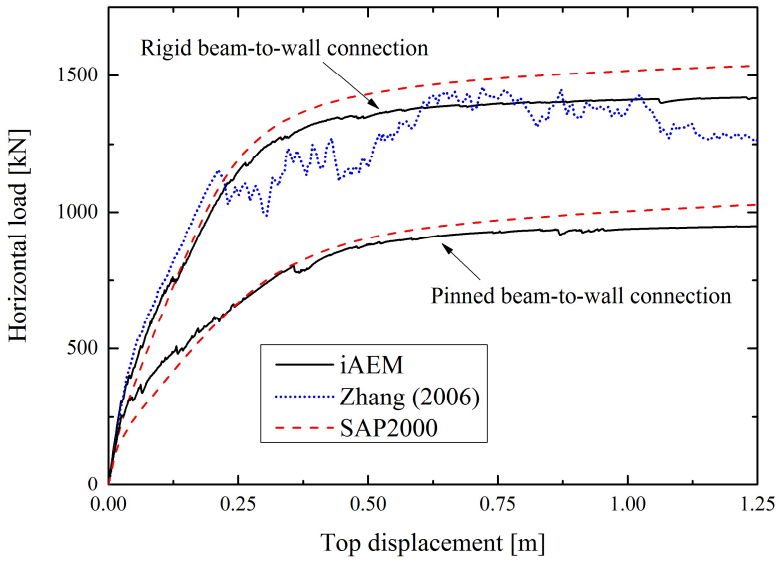

Figure 6-16 Horizontal load versus top displacement curves of the structure with different beam-to-wall connections

6.4.2 Nonlinear dynamic analysis of the hybrid structure

After verification of the iAEM model through pushover analysis, nonlinear dynamic analysis is performed for this hybrid structure to study its structural behavior during progressive collapse. The alternate path method (APM) is adopted by removing the right column of the first storey instantly. It is assumed that the structure is designed for office use with 200 mm thick slab spanning 5.4 m on the frame. According to Eurocode (2002), the dead load (DL) and live load (LL) imposed on the beams is 26.46 kN/m and 13.5 kN/m, respectively. Under the column removal scenario, load combination of 1.2DL+0.5LL recommended by GSA (2013) is employed for the nonlinear dynamic analysis. Therefore, the combined uniformly distributed load (UDL) can be obtained as $w = 38.50$ kN/m.

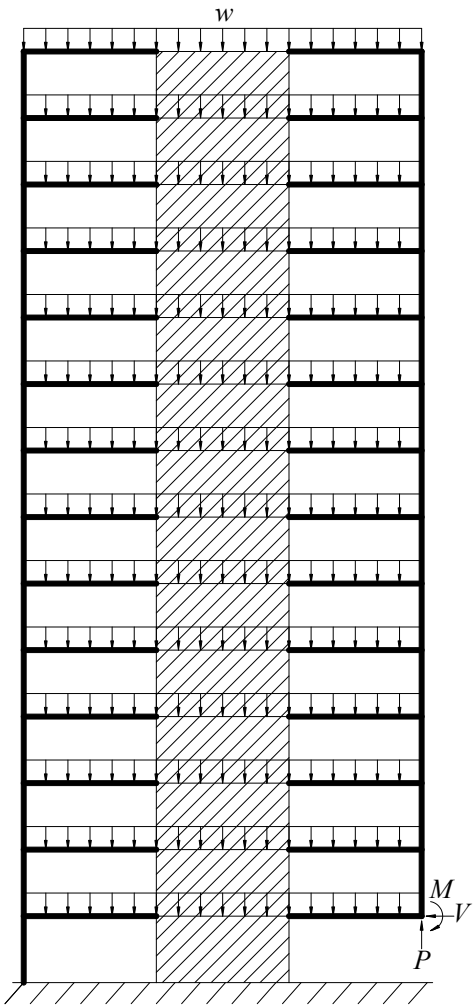

Figure 6-17 Column removal of the hybrid structure

The loading sequence of the nonlinear dynamic analysis of this structure in iAEM is similar to that used in sudden column removal analysis of the moment frames in Chapter 2. As shown in Figure 6-17, w is the UDL acting on each floor, and equivalent reaction forces (i.e. axial force P, shear force V and bending moment M) are used to represent the column that is to be removed. Two-phase analysis approach is employed to analyse the structure. Firstly, static analysis is performed until both sets of the forces (i.e. UDL and reaction forces) are gradually increased to the applied amount. The gradual increase of forces considers both material and geometric nonlinearities. Then with the developed initial deformation and internal forces of the structure, dynamic time history analysis is performed by reducing the reaction forces

to zero over a short period of time. As recommended by DoD (2009), the removal duration of 0.02 s is adopted, which is smaller than one tenth of the period associated with the modal response of the bays above the removed column in vertical direction.

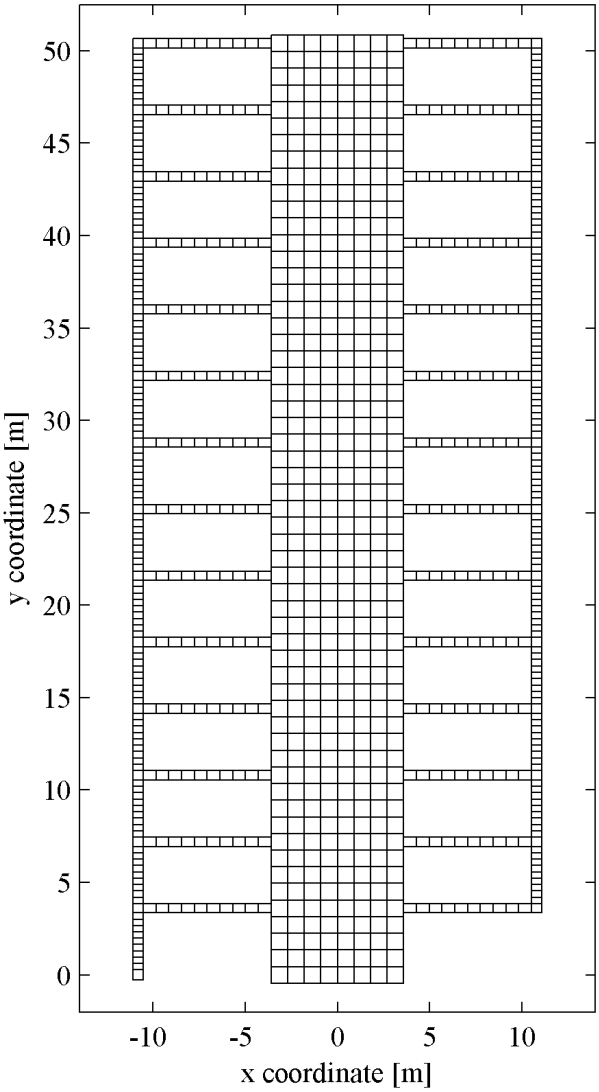

Figure 6-18 iAEM model of the hybrid structure under a column removal scenario

The iAEM model under column removal scenario is shown in Figure 6-18. The displacement time history from iAEM analysis is shown in Figure 6-19 along with that from SAP2000 for comparison. From this figure, it can be seen that for the first 0.4 s, the curve by iAEM agrees very well with that obtained by SAP2000.

Consequently, the iAEM curve has a similar pattern to the SAP2000 curve, but the displacement magnitude is larger. It is observed that iAEM consistently shows more flexible behavior than SAP2000 in dynamic analysis, as seen in the pushover analysis. The largest vertical displacement from iAEM analysis is 263 mm which is 10.5% larger as compared to 238 mm from SAP2000 analysis. For both iAEM and SAP2000 models, the free vibration period measured from one peak to next peak on the displacement time history curve is close to the fundamental period from the modal analysis, that is, 1.27 s compared to 1.21 s in iAEM and 1.35 s compared to 1.32 s in SAP2000. According to DoD (2009), the allowable vertical displacement at the top of removed column is $3\theta_y L_b$ for collapse prevention, where θ_y is the yield chord rotation of the beam at the top of the removed column and L_b is the beam length. The allowable displacement is calculated to be 237 mm, which is exceeded by 263 mm from iAEM analysis. Therefore, the structure is deemed to be unable to resist the progressive collapse due to removal of the bottom column.

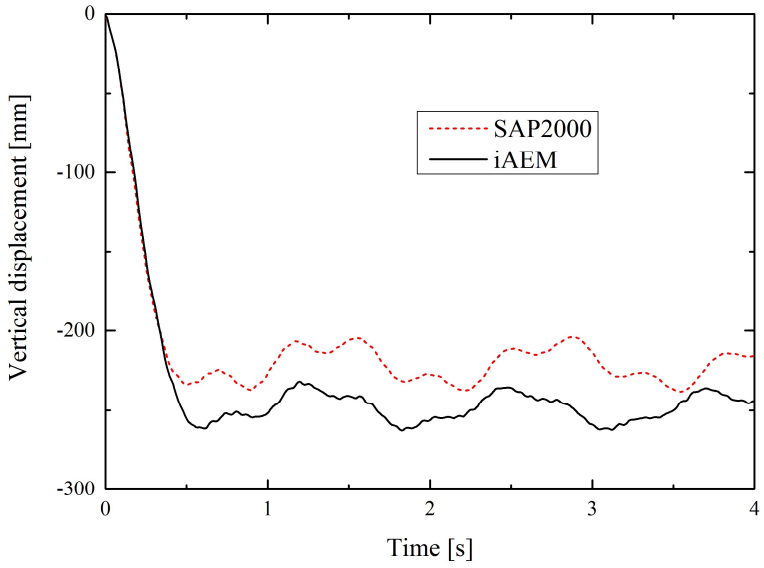

Figure 6-19 Displacement time histories of the hybrid structure under the column removal scenario

However, the collapse prevention criterion of the connection in DoD (2009) is based on the ductility requirement. By checking the strains of the beam-to-wall connection springs, it is found that the maximum tensile strain is still smaller than the assumed ultimate strain of $100\varepsilon_y$, where ε_y is the yield strain of steel material, and all the connection springs haven't failed. Therefore, as shown in Figure 6-19, the iAEM model can keep predicting the transient displacement time histories by assuming rigid beam-to-wall connections in the analysis.

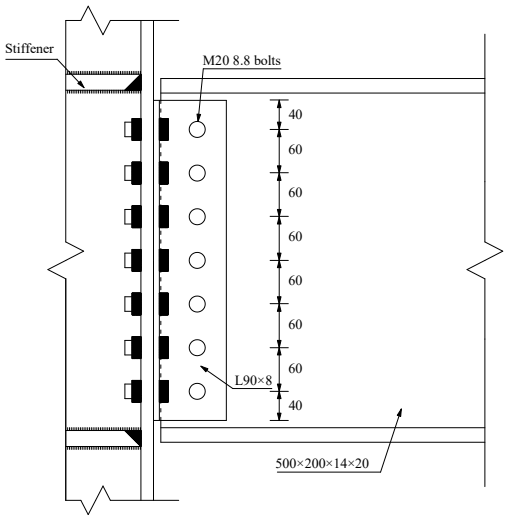

Figure 6-20 Semi-rigid connection for beam-to-wall

In order to see the influence of failure of the connection springs on the dynamic behavior of the structure, the beam-to-wall connections are modified to have smaller rigidity. The beam-to-column connection as shown in Figure 6-20 is used to represent the beam-to-wall connection of the hybrid structure. This representation is deemed appropriate as the column deformation is negligible as the RC wall because the column is stiffened by thick steel plates. This connection details is adapted from specimen W-8 in the static connection test by Yang and Tan (2013b), and the angle length is increased to accommodate seven rows of bolts based on the beam depth of 500mm. The same angle size of L90×8, bolt size of Grade 8.8 M20 bolts and steel

materials are used for this connection. The component method is applied to model the beam-to-wall connection in iAEM, and nine connection springs are used at each connection. Two rigid-plastic springs are located at the top and bottom beam flanges, and seven bolted-angle connection springs are in between. The displacement time history of the structure under sudden column removal scenario is plotted in Figure 6-21 together with the one with rigid beam-to-wall connection assumption. It can be seen that the vertical displacement time history curve keeps going down without turning back. This is because in the iAEM analysis, the connection springs fail one by one at each beam-to-wall connection on the right-hand side of the wall after they reach the failure strain. The beam-to-wall connection cannot sustain the load acting on the structure, resulting in persistent increase of the vertical displacement. In the analysis, eventually the wall and beam elements are disconnected when all the connections springs connecting them fail. From this study, it can be seen that influence of the connection rigidity on the structural behavior is very significant, and should be properly considered in order to predict correct structural behavior.

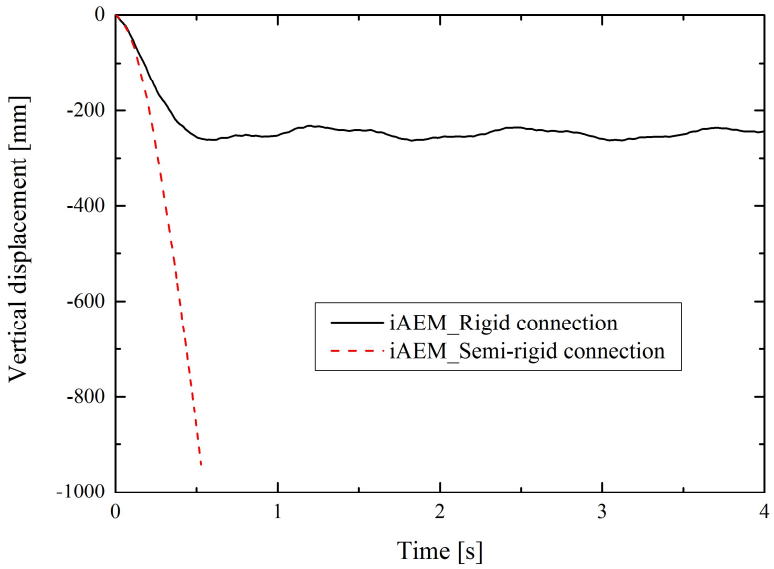

Figure 6-21 Displacement time histories of the hybrid structure under the sudden column removal scenario with different beam-to-wall connections

6.5 Summary

In this chapter, two multi-storey buildings are studied to demonstrate that the developed modelling features in iAEM can readily be integrated for nonlinear analysis of buildings. The first building is the 6-storey 2-bay Vogel frame. By accounting for the initial imperfections (i.e. geometric imperfections and residual stresses) and semi-rigid connection behavior, the load displacement curve from nonlinear static analysis in iAEM matches well with the one predicted by Chan and Chui (2000). The second building is a 14-storey hybrid structure composed of steel frames and an RC shear wall. The beam-truss model is used to simulate the RC shear wall. The predicted responses from iAEM analysis agree generally well with those from SAP2000 analysis for both pushover and nonlinear dynamic analyses under sudden column removal scenario. By changing the rigid beam-to-wall connection to one semi-rigid type, gradual failure of the connection is observed with progressive failure of the connection springs, which results in persistent increase of the vertical displacement. Therefore, proper beam-to-wall connections should be considered in the analysis in order to obtain accurate structural behavior.

7 Conclusions and Recommendations

This thesis focuses on enhancing the iAEM to simulate nonlinear dynamic analysis with efficiency and accuracy. The enhancements include modelling of initial imperfections and semi-rigid connections of steel structures, as well as modelling of RC shear walls using the efficient beam-truss method. These capabilities are validated in numerical examples by comparing with published experimental and numerical results, and the results obtained from the established commercial software SAP2000. Lastly, the enhanced features are integrated in iAEM at the system level to model the 6-storey Vogel frame and a 14-storey hybrid structure. The key findings from the numerical studies are presented below.

7.3 Conclusions

7.3.1 Modelling of initial imperfections of steel frames

The explicit modelling methods are used to account for initial geometric imperfections and residual stresses in iAEM. To model the single members with initial geometric imperfections including both member out-of-straightness and out-of-plumbness, the members are modelled explicitly according to their initial deformed shapes using non-rectangular iAEM elements. Non-rectangular joint elements are also introduced to accommodate the beams and columns with geometric imperfections. To model the residual stresses of the structure in iAEM, the approach as used for the plastic-zone method is adopted by dividing the cross section into grids of fibers (or springs). Implementation of these explicit modelling methods in iAEM is straightforward without changing the element formulation. Compared to the other imperfection modelling methods adopted in advanced analysis of steel structures such

as the equivalent notional load or reduction of the tangent modulus (Kim and Chen, 2005), the explicit modelling methods directly and physically account for imperfections of the structure. Using non-rectangular iAEM elements, the members that non-perpendicularly join at a common point as often seen in the braced steel structures, domes and arch structures can be readily modeled.

Accuracy of the imperfection modelling in iAEM is validated against the published results and those from FEM plastic-zone analysis through four numerical examples. It is found that, with the increase of out-of-straightness or the out-of-plumbness, structural strength is reduced significantly. When the out-of-straightness is considered, the buckling and post-buckling behavior of the column is predicted. When residual stresses are accounted for, earlier yielding of the structure occurs which has to be captured for nonlinear analysis. In the example of the Vogel portal frame (Vogel, 1985), the significant difference of structural response with and without both initial imperfections demonstrates the importance of imperfection modelling for real steel frames using iAEM.

7.3.2 Modelling of semi-rigid connections of steel frames

To more accurately simulate the structural behavior of real steel frames, the component method is incorporated in iAEM to consider the semi-rigid bolted-angle connections. This method is not only effective in predicting the complex connection behavior, but also consistent with the usage of springs in iAEM. The monotonic load deformation behavior is described for the three components including bolted angle under tension, bolt in shear and plate in bearing. The fracture load and displacement for each component are defined so that gradual failure of the connection can be simulated at the large displacement stage during progressive collapse. The unloading and reloading paths are also defined to consider the cyclic connection behavior in the dynamic analysis.

Comparison with the experimental results in the literature shows reasonable accuracy of the component method in predicting the structural response. The example of pseudo-static column-removal test by Yang and Tan (2013b) reveals that the component-based models is able to simulate the key responses of bolted-angle connections during progressive collapse, including the formation of flexural action at small deformation stage, the development of catenary action at large deformation stage, and the fracture of connection components at the last stage. In the example of the two-storey single-bay frame by Stelmack et al. (1986), the frame with semi-rigid connection modelled by the component method predicts much more flexible load displacement response than that with the rigid connection, indicating the importance of semi-rigid connection modelling in iAEM. In the example of the dynamic connection test by Liu et al. (2013), the displacement time histories predicted by iAEM agrees reasonably well with those from the experiment.

7.3.3 Modelling of RC shear walls

RC shear walls extensively used as the lateral resisting systems in the steel buildings are subjected to axial forces, bending moments and shear forces, and their responses are often significantly affected by FSI. The use of conventional AEM to model the RC shear walls is not only time-consuming but also inaccurate, because many small brick-type elements are needed in the model, and FSI is not well considered for squat walls. The use of macromodel-based nonlinear beam-truss model in iAEM can provide both efficient and accurate analysis of RC shear walls. In the beam-truss model, the wall panel is divided into rows and columns of iAEM elements connected by nonlinear vertical fiber beams, horizontal and diagonal trusses. The FSI is represented in this model through compression-only diagonal truss elements which account for the effect of lateral tensile strain on the stress-strain relationship of concrete in compression.

The nonlinear beam-truss model in iAEM is verified by comparing the computed and experimental results of five RC shear walls with shear span ratio ranging from 0.45 to 3. The proposed model computes the post-cracking cyclic load displacement response of RC shear walls in terms of strength and stiffness reasonably well, and it can predict different failure modes for the walls with different shear span ratios. Using the compression-only diagonal trusses, compression-shear failure is captured for the squat walls tested by Massone (2006), Ono et al. (1976) and Sittipunt et al. (2001) where significant FSI exists. The study shows that for shear walls which contain horizontal beams with considerably large cross section (Ono et al., 1976) or need to transfer the bending moments due to zero rotation (Massone, 2006), flexural behavior of these beams should not be ignored. Therefore, horizontal beam elements instead of truss elements should be used for these walls in iAEM in order to predict more accurate wall response. The accuracy and efficiency of iAEM over conventional AEM is demonstrated for the shear wall tested by Ono et al. (1976). The beam-truss model in iAEM can reasonably predict the loading, softening and unloading paths while the conventional AEM model can only show the loading path, and the subsequent softening path due to significant FSI is not provided. The beam-truss model uses only 81 elements while the conventional AEM model uses 1800 elements, significant reduction of computational time by iAEM is evident.

7.3.4 System-level case studies

Two multi-storey buildings are presented to demonstrate that the developed modelling features in iAEM can readily be integrated for nonlinear analysis of buildings. The first building is the 6-storey 2-bay Vogel frame. Comparison of the structural behavior with and without considering the initial imperfections and semi-rigid connections again reveals the significance of considering these effects in iAEM. The second building is a 14-storey hybrid structure where the RC shear wall is simulated by the proposed beam-truss model. Compared with the results from

literature (Zhang, 2006) and SAP2000, the iAEM model predicts reasonably well the structural response in both pushover and nonlinear dynamic analyses. By changing the rigid beam-to-wall connection to one semi-rigid type, gradual failure of the connection is observed with progressive failure of the connection springs, which results in persistent increase of the vertical displacement. Therefore, different beam-to-wall connections can result in different structural behavior, and proper beam-to-walls should be considered in the analysis.

7.4 Recommendations for future research

Future research work is recommended below for more advanced analysis using the iAEM:

1 Initial geometric imperfections of steel frames have been considered by the explicit modelling methods. Non-rectangular joint elements are created to accommodate the beams and columns with geometric imperfections. For future study, braced steel frames, domes or more irregular steel structures can be modelled, and their structural behavior during progressive collapse can be investigated.

2 Semi-rigid bolted-angle type of steel connections has been modelled by the component method in iAEM. Further research can be expanded by modeling more types of connections such as end plate connections and T-stub connections, and propose a method for efficient establishment of the semi-rigid connection model in iAEM.

3 The modelling features developed in this study are in the framework of two dimensional version of iAEM and should be extended to three dimensional analysis for real buildings. The lateral-torsional beam buckling as often seen for steel structures can be modeled by the iAEM in a proper way. Some researchers have also reported that floor slabs have significant influence on

the progressive collapse resistance of the buildings (Sadek et al., 2008; Yu et al., 2010). Therefore, appropriate modelling of floor slabs in the iAEM to capture their key structural behaviors such as bending and membrane actions during progressive collapse is needed.

4 The whole process leading to total collapse of structures is not simulated in this study due to time constraint. In future research, along with the developed modelling features in iAEM, the simulation of subsequent fragmentation and impact of structural elements should be performed after the collapse is initiated (a key element breaks off from the structure). In this way, the entire failure process of the structure can be traced, the damage area during collapse can be assessed and appropriate remedial measures may be taken to mitigate or prevent the collapse.

References

ABAQUS. (2005). ABAQUS/Standard user's manual (Version 6.5). Providence, RI: Dassault Systèmes Simulia Corp.

ACI. (2014). Building code requirements for structural concrete (ACI 318-14) and commentary (ACI 318R-14). Farmington Hills, MI: American Concrete Institute.

Alashker, Y., Li, H., El-Tawil, S. (2011). Approximations in progressive collapse modeling. *Journal of Structural Engineering, 137*(9), 914.

ASCE. (2010). Minimum design loads for buildings and other structures, SEI/ASCE 7-10. Reston, VA.

Azizinamini, A. (1985). *Cyclic characteristics of bolted semi-rigid steel beam-to-column connections.* (Ph.D. Dissertation), University of South Carolina, Ann Arbor, MI. ProQuest Dissertations & Theses Global database.

Bao, Y., Kunnath, S. K. (2010). Simplified progressive collapse simulation of RC frame–wall structures. *Engineering Structures 32*(10), 3153-3162.

Baron, M. L., Bleich, H. H., Weidlinger, P. (1961). Dynamic elastic-plastic analysis of structures. *Engineering Mechanics Division, ASCE, 87*, 23-42.

Bathe, K.-J. (2007). Conserving energy and momentum in nonlinear dynamics: A simple implicit time integration scheme. *Computers & Structures, 85*(7–8), 437-445.

Bathe, K. J. (1996). *Finite element procedures*. Upper Saddle River, New Jersey: Prentice Hall.

Batoz, J.-L., Dhatt, G. (1979). Incremental displacement algorithms for nonlinear problems. *International Journal for Numerical Methods in Engineering 14*(8), 1262-1267.

Bazant, Z. P., Planas, J. (1998). *Fracture and size effect in concrete and other quasibrittle materials*. Boca Raton, FL: CRC Press.

Bažant, Z. P., Verdure, M. (2007). Mechanics of progressive collapse: Learning from World Trade Center and building demolitions. *Journal of Engineering Mechanics, 133*(3), 308-319.

Bentz, E. C. (2005). Explaining the riddle of tension stiffening models for shear panel experiments. *Journal of Structural Engineering, 131*(9), 1422-1425.

Bićanić, N. (2004). Discrete Element Methods *Encyclopedia of Computational Mechanics*: John Wiley & Sons, Ltd.

Bolander, J. J., Yoshitake, K., Thomure, J. (1999). Stress analysis using elastically homogeneous rigid-body spring networks. *Structural Eng./Earthquake Eng., JSCE, 16*(2), 125-132.

Breen, J. E. (1975). Research workshop on progressive collapse of building structures held at the University of Texas at Austin. Washington, D.C.: National Bureau of Standards.

CEB-FIP. (2013). *fib model code for concrete structures 2010* Lausanne, Switzerland: International Federation for Structural Concrete (fib).

Chan, E. C.-Y. (1983). *Nonlinear geometric, material and time dependent analysis of reinforced concrete shells with edge beams.* (Ph.D. Dissertation), University of California, Berkeley.

Chan, S. L., Chui, P. P. T. (2000). *Non-linear static and cyclic analysis of steel frames with semi-rigid connections*. New York: Elsevier.

Chao, S., Khandelwal, K., El-Tawil, S. (2006). Ductile Web Fracture Initiation in Steel Shear Links. *Journal of Structural Engineering, 132*(8), 1192-1200.

Chen, W.-F., Goto, Y., Liew, J. Y. R. (1996). *Stability design of semi-rigid frames* (Vol. 886419). New York: John Wiley & Sons, Inc.

Choi, J.-h., Chang, D.-k. (2009). Prevention of progressive collapse for building structures to member disappearance by accidental actions. *Journal of Loss Prevention in the Process Industries 22*(6), 1016-1019. doi: http://dx.doi.org/10.1016/j.jlp.2009.08.020

Clarke, M. J., Bridge, R. Q., Hancock, G. J., Trahair, N. S. (1992). Advanced analysis of steel building frames. *Journal of Constructional Steel Research 23*(1-3), 1-29.

Colotti, V. (1993). Shear Behavior of RC Structural Walls. *Journal of Structural Engineering, 119*(3), 728-746.

Corley, W., Mlakar, P. F., Sozen, M. A., Thornton, C. H. (1998). The Oklahoma City bombing: summary and recommendations for multihazard mitigation. *Journal of Performance of Constructed Facilities, 12*(3), 100-112.

Corley, W. G. (2004). Lessons learned on improving resistance of buildings to terrorist attacks. *Journal of Performance of Constructed Facilities, 18*(2), 68-78.

Cundall, P. A. (1971). *A computer model for simulating progressive, large-scale movements in blocky rock systems.* Paper presented at the Proceedings of the International Symposium on Rock Mechanics, Nancy, France.

DIANA. (2007). Finite element analysis, release 9.2: TNO building and construction research, Delft(The Netherlands).

Díaz, C., Martí, P., Victoria, M., Querin, O. M. (2011). Review on the modelling of joint behaviour in steel frames. *Journal of Constructional Steel Research 67*(5), 741-758.

DoD. (2009). Design of buildings to resist progressive collapse, unified facilities criteria (UFC) 4-023-03.

Dusenberry, D. O., Juneja, G. (2002). *Review of existing guidelines and provisions related to progressive collapse*. Paper presented at the Workshop on Prevention of Progressive Collapse.

ECCS. (1984). Ultimate limit state calculation of sway frames with rigid joints (1 ed., pp. 20). Rotterdam: European Convention for Constructional Steelwork.

Elkholy, S., Meguro, K. (2004). *Numerical simulation of high-rise steel buildings using improved applied element method*. Paper presented at the 13th World Conference on Earthquake Engineering, Vancouver, B.C. Canada.

Elkholy, S. A. (2004). *Improved applied element method for numerical simulations of structural failure and collapse.* (Ph.D. Dissertation), University of Tokyo, Tokyo, Japan.

Ellingwood, B. R., Dusenberry, D. O. (2005). Building Design for Abnormal Loads and Progressive Collapse. *Computer-Aided Civil and Infrastructure Engineering, 20*(3), 194-205.

Ellingwood, B. R., Smilowitz, R., Dusenberry, D. O., Duthinh, D., Lew, H. S., Carino, N. J. (2007). Best Practices for Reducing the Potential for Progressive Collapse in Buildings.

ELS. (2006). Extreme loading for structures technical manual. Raleigh, NC: Applied Science International, LLC.

Elsanadedy, H. M., Almusallam, T. H., Alharbi, Y. R., Al-Salloum, Y. A., Abbas, H. (2014). Progressive collapse potential of a typical steel building due to blast attacks. *Journal of Constructional Steel Research 101*, 143-157. doi: http://dx.doi.org/10.1016/j.jcsr.2014.05.005

Eurocode. (2002). Eurocode 1 - Actions on structures - Part 1-1: General actions - Densities, self-weight, imposed loads for buildings. Brussels.

Eurocode. (2005). Eurocode 3 - Design of steel structures - Part 1-8: Design of joints. UK: British Standards Institution.

Eurocode. (2006). Eurocode 1 - Actions on structures - Part 1-7: General actions - Accidental actions. Brussels.

Faella, C., Piluso, V., Rizzano, G. (2000). *Structural steel semirigid connections: theory, design and software*. Boca Raton, FL: CRC Publishers.

Fahjan, Y., Doran, B., Akbas, B., Kubin, J. (2012). *Pushover analysis for performance based-seismic design of RC frames with shear walls*. Paper presented at the 15th World Conference on Earthquake Engineering, Lisbon, Portugal.

FEMA. (1996). The Oklahoma City bombing: Improved building performance through multi-hazard mitigation (pp. 116). Washington, DC: FEMA 277.

FEMA. (2002). World Trade Center building performance study: data collection, preliminary observations, and recommendations. Washington, DC: FEMA 403.

Filippou, F. C., Popov, E. P., Bertero, V. V. (1983). Effects of bond deterioration on hysteretic behavior of reinforced concrete joints: Earthquake Engineering Research Center, University of California, Berkeley.

Fintel, M., Schultz, D. M. (1979). Structural integrity of large panel buildings. *ACI Journal Proceedings, 76*(5), 583-620.

Fischinger, M., Vidic, T., Fajfar, P. (1992). Nonlinear seismic analysis of structural walls using the multiple-vertical-line-element model. In P. Fajfar & H. Krawinkler (Eds.), *Nonlinear Seismic Analysis and Design of Reinforced Concrete Buildings* (pp. 226-240). New York, NY: Elsevier Applied Science.

Fu, F. (2009). Progressive collapse analysis of high-rise building with 3-D finite element modeling method. *Journal of Constructional Steel Research 65*(6), 1269-1278.

Galal, K., El-Sawy, T. (2010). Effect of retrofit strategies on mitigating progressive collapse of steel frame structures. *Journal of Constructional Steel Research, 66*(4), 520-531.

Galambos, T. V. (2000). Recent research and design developments in steel and composite steel–concrete structures in USA. *Journal of Constructional Steel Research 55*(1–3), 289-303.

Giberson, M. F. (1967). *The response of nonlinear multi-story structures subjected to earthquake excitation.* (Ph.D. Dissertation), California Institute of Technology, Pasadena, California.

Griffiths, H., Pugsley, A. G., and Saunders, O. (1968). Report of the inquiry into the collapse of flats at Ronan Point, Canning Town. London: Her Majesty's Stationery Office.

Groger, T., Tuzun, U., Heyes, D. (2002). *Shearing of wet particle systems-Discrete element simulations*. Paper presented at the First International PFC Symposium, Itasca.

GSA. (2013). Alternate path analysis and design guidelines for progressive collapse resistance: General Services Administration.

Guragain, R., Worakanchana, K., Mayorca, P., Meguro, K. (2006). Simulation of brick masonry wall behavior under cyclic loading using applied element method. *SEISAN KENKYU, 58*(6), 45-48.

Hakuno, M., Meguro, K. (1993). Simulation of concrete ‐ frame collapse due to dynamic loading. *Journal of Engineering Mechanics, 119*(9), 1709-1723.

Hallquist, J. (2005). LS-DYNA. Livermore, California: Livermore Software Technology Corp.

Hayes Jr, J. R., Woodson, S. C., Pekelnicky, R. G., Poland, C. D., Corley, W. G., Sozen, M. (2005). Can strengthening for earthquake improve blast and progressive collapse resistance? *Journal of Structural Engineering, 131*(8), 1157-1177.

Helmy, H., Salem, H., Mourad, S. (2012). Progressive collapse assessment of framed reinforced concrete structures according to UFC guidelines for alternative path method. *Engineering Structures 42*, 127-141.

Hidalgo, P. A., Jordan, R. M., Martinez, M. P. (2002). An analytical model to predict the inelastic seismic behavior of shear-wall, reinforced concrete structures. *Engineering Structures 24*(1), 85-98.

HMG. (2013). The Building Regulations 2010: Approved Document A - Structure (2004 Edition incorporating 2010 and 2013 amendments): NBS.

Izzuddin, B. A., Vlassis, A. G., Elghazouli, A. Y., Nethercot, D. A. (2008). Progressive collapse of multi-storey buildings due to sudden column loss - Part I: Simplified assessment framework. *Engineering Structures 30*(5), 1308-1318.

Jiang, X.-M., Chen, H., Liew, J. Y. R. (2002). Spread-of-plasticity analysis of three-dimensional steel frames. *Journal of Constructional Steel Research 58*(2), 193-212.

Jin, J., El-Tawil, S. (2005). Evaluation of FEMA-350 seismic provisions for steel panel zones. *Journal of Structural Engineering, 131*(2), 250-258.

Kabeyasawa, T., Shiohara, H., Otani, S., Aoyama, H. (1983). Analysis of the full-scale seven-story reinforced concrete test structure. *Journal(B), the Faculty of Engineering, University of Tokyo, XXXVII*(2), 432-478.

Kaewkulchai, G. (2003). *Dynamic progressive collapse of frame structures.* (Ph.D. Dissertation), The University of Texas at Austin

Kaewkulchai, G., Williamson, E. B. (2004). Beam element formulation and solution procedure for dynamic progressive collapse analysis. *Computers and Structures, 82*(7-8), 639-651.

Kaewkulchai, G., Williamson, E. B. (2006). Modeling the impact of failed members for progressive collapse analysis of frame structures. *Journal of Performance of Constructed Facilities, 20*(4), 375-383.

Kalny, O. (2014). Connecting frame, shell, and solid elements. Retrieved April 15, 2016, from https://wiki.csiamerica.com/display/kb/Connecting+frame,+shell,+and+solid+elements

Kawai, T. (1977). New element models in discrete structural analysis. *Journal of the Society of Naval Architects of Japan* (141), 174-180.

Khandelwal, K., El-Tawil, S. (2006). *Catenary action during collapse of steel MRF buildings*. Paper presented at the Proceedings of the Structures Congress and Exposition, St. Louis, Missouri.

Khandelwal, K., El-Tawil, S., Kunnath, S. K., Lew, H. S. (2008). Macromodel-based simulation of progressive collapse: Steel frame structures. *Journal of Structural Engineering, 134*(7), 1070-1078.

Kim, J., An, D. (2009). Evaluation of progressive collapse potential of steel moment frames considering catenary action. *Structural Design of Tall and Special Buildings, 18*(4), 455-465.

Kim, J., Kim, T. (2009). Assessment of progressive collapse-resisting capacity of steel moment frames. *Journal of Constructional Steel Research 65*(1), 169-179.

Kim, S. E., Chen, W.-F. (2005). Steel frame design using advanced analysis. In W.-F. Chen & E. M. Lui (Eds.), *Handbook of structural engineering*. Boca Raton, FL: CRC Press.

Kunieda, M., Ogura, H., Ueda, N., Nakamura, H. (2011). Tensile fracture process of strain hardening cementitious composites by means of three-dimensional meso-scale analysis. *Cement and Concrete Composites 33*(9), 956-965.

Kwasniewski, L. (2010). Nonlinear dynamic simulations of progressive collapse for a multistory building. *Engineering Structures 32*(5), 1223-1235.

Lee, C. H., Kim, S., Han, K. H., Lee, K. (2009). Simplified nonlinear progressive collapse analysis of welded steel moment frames. *Journal of Constructional Steel Research 65*(5), 1130-1137.

Lemonis, M. E., Gantes, C. J. (2009). Mechanical modeling of the nonlinear response of beam-to-column joints. *Journal of Constructional Steel Research 65*(4), 879-890.

Li, G. Q., Li, J.-J. (2007). *Advanced analysis and design of steel frames*: John Wiley and Sons.

Liew, J. Y. R., Punniyakotty, N. M., Shanmugam, N. E. (1997). Advanced analysis and design of spatial structures. *Journal of Constructional Steel Research 42*(1), 21-48.

Liu, C., Tan, K. H., Fung, T. C. (2013). Dynamic behaviour of web cleat connections subjected to sudden column removal scenario. *Journal of Constructional Steel Research 86*, 92-106.

Liu, C., Tan, K. H., Fung, T. C. (2015). Component-based steel beam–column connections modelling for dynamic progressive collapse analysis. *Journal of Constructional Steel Research 107*, 24-36.

Liu, J. L. (2010a). Preventing progressive collapse through strengthening beam-to-column connection, Part 1: Theoretical analysis. *Journal of Constructional Steel Research 66*(2), 229-237.

Liu, J. L. (2010b). Preventing progressive collapse through strengthening beam-to-column connection, Part 2: Finite element analysis. *Journal of Constructional Steel Research 66*(2), 238-247.

Liu, S. C., Lin, T. H. (1979). Elastic-plastic dynamic analysis of structures using known elastic solutions. *Earthquake Engineering & Structural Dynamics, 7*(2), 147-159.

Lorig, L. J., Cundall, P. A. (1989). Modeling of Reinforced Concrete Using the Distinct Element Method. In S. Shah & S. Swartz (Eds.), *Fracture of Concrete and Rock* (pp. 276-287): Springer New York.

Lu, Y., Panagiotou, M. (2014). Three-dimensional cyclic beam-truss model for nonplanar reinforced concrete walls. *Journal of Structural Engineering, 140*(3), 04013071.

Lui, E. M., Chen, W. F. (1986). Analysis and behaviour of flexibly-jointed frames. *Engineering Structures 8*(2), 107-118.

Lui, E. M., Chen, W. F. (1988). Behavior of braced and unbraced semi-rigid frames. *International Journal of Solids and Structures 24*(9), 893-913.

Maekawa, K., Pimanmas, A., Okamura, H. (2003). *Nonlinear mechanics of reinforced concrete*. New York, NY: Spon Press.

Mander, J., Priestley, M., Park, R. (1988). Theoretical stress‐strain model for confined concrete. *Journal of Structural Engineering, 114*(8), 1804-1826.

Masoero, E., Wittel, F., Herrmann, H., Chiaia, B. (2010). Progressive collapse mechanisms of brittle and ductile framed structures. *Journal of Engineering Mechanics, 136*(8), 987-995.

Massone, L. M. (2006). *RC wall shear-flexure interaction: analytical and experimental responses.* (Ph.D. Dissertation), University of California, Los Angeles.

Mayorca, P., Meguro, K. (2003). Modeling Masonry Structures using the Applied Element Method. *SEISAN KENKYU, 55*(6), 123-126.

McGuire, W., Leyendecker, E. V. (1974). Analysis of non-reinforced masonry building response to abnormal loading and resistance to progressive collapse (pp. 66). Washington, D.C.: U. S. Department of Commerce, National Bureau of Standards.

McKenna, F., Fenves, G. L., Scott, M. H. (2000). Open system for earthquake engineering simulation. Berkerly, CA: University of California.

Meguro, K., Tagel-Din, H. (1997). A new efficient technique for fracture analysis of structures. *Bulletin of Earthquake Resistant Structure Research Center, Institute of Industrial Science, University of Tokyo*(30), 103-116.

Meguro, K., Tagel-Din, H. (2000). Applied element method for structural analysis: theory and application for linear materials. *Structural Eng./Earthquake Eng. JSCE, 17*(1), 21s-35s.

Meguro, K., Tagel-Din, H. (2001). Applied element simulation of RC structures under cyclic loading. *Journal of Structural Engineering, 127*(11), 1295-1305.

Meguro, K., Tagel-Din, H. (2002). Applied Element Method Used for Large Displacement Structural Analysis. *Journal of Natural Disaster Science, 24*(1), 25-34.

Menegotto, M., Pinto, P. E. (1973). *Method of analysis for cyclically loaded RC plane frames including changes in geometry and non-elastic behavior of elements under combined normal force and bending*. Paper presented at the Symposium of Resistance and Ultimate Deformability of Structures Acted on by Well-Defined Repeated Loads, Lisbon, Portugal.

Miao, Z. W., Lu, X. Z., Jiang, J. J., Ye, L. P. (2006). *Nonlinear FE Model for RC Shear Walls Based on Multi-layered microplane constitutive model.* Paper presented at the Computational Methods in Engineering and Science, EPMESC X, Sanya, Hainan, China.

Mohamed, O. A. (2006). Progressive collapse of structures: Annotated bibliography and comparison of codes and standards. *Journal of Performance of Constructed Facilities, 20*(4), 418-425.

Mondkar, D. P., Powell, G. H. (1978). Evaluation of solution schemes for nonlinear structures. *Computers & Structures, 9*(3), 223-236.

Monti, G., Spacone, E. (2000). Reinforced Concrete Fiber Beam Element with Bond-Slip. *Journal of Structural Engineering, 126*(6), 654-661.

Nagarajan, S., Popov, E. P. (1974). Elastic-plastic dynamic analysis of axisymmetric solids. *Computers & Structures, 4*(6), 1117-1134.

Nakagawa, T., Narafu, T., Imai, H., Hanazato, T., Ali, Q., Minowa, C. (2011). Collapse behavior of a brick masonry house using a shaking table and numerical simulation based on the extended distinct element method. *Bulletin of Earthquake Engineering* 1-15.

NIST. (2005). Federal building and fire safety investigation of the World Trade Center disaster: Final report of the National Construction Safety Team on the collapses of the World Trade Center Towers. Gaithersburg, MD: NIST NCSTAR 1.

NIST. (2006). Best practice for reducing potential for progressive collapse in buildings.

Oesterle, R. G., Aristizabal-Ochoa, J. D., Shiu, K. N., Corley, W. G. (1984). Web crushing of reinforced concrete structural walls. *ACI Journal Proceedings, 81*(3), 231-241.

Ono, H., Adachi, H., Nakanishi, S., Shimizu, Y., Sugiyama, K. (1976). General studies on seismic performance of reinforced concrete shear wall, No. 7, Loading paths and lateral ties of columns. *Summaries of Annual Meeting, Architectural Institute of Japan*, 1601-1602.

Panagiotou, M., Restrepo, J. I., Schoettler, M., Geonwoo, K. (2012). Nonlinear cyclic truss model for reinforced concrete walls. *ACI Structural Journal, 109*(2), 205-214.

Park, A. Y., Wang, Y. C. (2012). Development of component stiffness equations for bolted connections to RHS columns. *Journal of Constructional Steel Research 70*, 137-152.

Park, H., Eom, T. (2007). Truss Model for Nonlinear Analysis of RC Members Subject to Cyclic Loading. *Journal of Structural Engineering, 133*(10), 1351-1363.

Park, R., Kent, D. C. S., Richard A. . (1972). Reinforced Concrete Members with Cyclic Loading. *Journal of the Structural Division, 98*(7), 1341-1360.

Paz, M., Leigh, W. (2004). *Structural dynamics: theory and computation* (5 ed.): Springer Science and Business Media New York.

Pearson, C., Delatte, N. (2005). Ronan point apartment tower collapse and its effect on building codes. *J. Perform. Constr. Facil., 19*(2), 172.

Peng, W., Pan, R., Dai, F. (2015). Theoretic Framework and Finite Element Implementation on Progressive Collapse Simulation of Masonry Arch Bridge. *Mathematical Problems in Engineering, 2015*, 12. doi: 10.1155/2015/707269

Petrangeli, M., Pinto, P., Ciampi, V. (1999). Fiber element for cyclic bending and shear of RC structures. I: Theory. *Journal of Engineering Mechanics, 125*(9), 994-1001.

Pham, X. D., Tan, K. H. (2013). Membrane actions of RC slabs in mitigating progressive collapse of building structures. *Engineering Structures 55*, 107-115.

Polak, M., Vecchio, F. (1993). Nonlinear Analysis of Reinforced ‐ Concrete Shells. *Journal of Structural Engineering, 119*(12), 3439-3462.

Quintiere, J. G., di Marzo, M., Becker, R. (2002). A suggested cause of the fire-induced collapse of the World Trade Towers. *Fire Safety Journal 37*(7), 707-716.

Ramancharla, P. K., Meguro, K. (2001). A study on the attenuation characteristics of peak responses in the near-fault region using applied element method. *SEISAN KENKYU, 53*(11-12), 11-15.

Rex, C. O., Easterling, W. S. (2003). Behavior and modeling of a bolt bearing on a single plate. *Journal of Structural Engineering, 129*(6), 792-800.

Ross, S. (1984). *Construction disasters: Design failures, causes, and prevention*. New York: McGraw-Hill.

Saatcioglu, M., Derecho, A. T., Corley, W. G. (1983). Modelling hysteretic behaviour of coupled walls for dynamic analysis. *Earthquake Engineering and Structural Dynamics, 11*(5), 711-726.

Sadek, F., El-Tawil, S., Lew, H. S. (2008). Robustness of composite floor systems with shear connections: modeling, simulation, and evaluation. *Journal of Structural Engineering, 134*(11), 1717-1725.

Sadek, F., Main, J. A., Lew, H. S., Bao, Y. (2011). Testing and analysis of steel and concrete beam-column assemblies under a column removal scenario. *Journal of Structural Engineering, 137*(9), 881.

Salmon, C. G., Johnson, J. E. (1996). *Steel structures: design and behavior - emphasizing load and resistance factor design* (4th ed.): Harper Collins College Publishers.

SAP2000. (2002). Version 8, analysis reference manual. Berkerley, CA: Computers and Structures, Inc.

Sarraj, M. (2007). *The behavior of steel fin plate connections in fire.* (Ph.D. Dissertation), University of Sheffield, UK.

Sasani, M. (2008). Response of a reinforced concrete infilled-frame structure to removal of two adjacent columns. *Engineering Structures, 30*(9), 2478-2491.

Schlaich, J., Schäfer, K. (1984). Towards a consistent design of reinforced concrete structures. *IABSE congress report 12*, 887-894.

Scott, M., Fenves, G. (2010). Krylov Subspace Accelerated Newton Algorithm: Application to Dynamic Progressive Collapse Simulation of Frames. *Journal of Structural Engineering, 136*(5), 473-480. doi: doi:10.1061/(ASCE)ST.1943-541X.0000143

Shen, J., Astaneh-Asl, A. (2000). Hysteresis model of bolted-angle connections. *Journal of Constructional Steel Research 54*(3), 317-343.

Shiu, K. N., Daniel, J. I., Aristizabal-Ochoa, J. D., Fiorato, A. E., Corley, W. G. (1981). Earthquake resistant structural walls - tests of walls with and without openings (pp. 123). Skokie, Illinois: Construciton Technology Laboratories, Portland Cement Association.

Sittipunt, C., Wood, S. L., Lukkunaprasit, P., Pattararattanakul, P. (2001). Cyclic behavior of reinforced concrete structural walls with diagonal web reinforcement. *ACI Structural Journal, 98*(4), 554-562.

Song, H., Shim, S., Byun, K., Maekawa, K. (2002). Failure analysis of reinforced concrete shell structures using layered shell element with pressure node. *Journal of Structural Engineering, 128*(5), 655-664.

Sozen, M. A., Thornton, C. H., Corley, W. G., Mlakar, P. F. (1998). The Oklahoma City bombing: structure and mechanisms of the Murrah Building. *Journal of Performance of Constructed Facilities, 12*(3), 120-136.

Stelmack, T., Marley, M., Gerstle, K. (1986). Analysis and tests of flexibly connected steel frames. *Journal of Structural Engineering, 112*(7), 1573-1588.

Szyniszewski, S., Krauthammer, T. (2012). Energy flow in progressive collapse of steel framed buildings. *Engineering Structures 42*, 142-153.

Tagel-Din, H., Meguro, K. (2000). Nonlinear simulation of RC structures using applied element method *Structural Eng./Earthquake Eng., JSCE, 17*(2), 137-148.

Tagel-Din, H. S. (1998). *A new efficient method for nonlinear, large deformation and collapse analysis of structures.* (Ph.D. Dissertation), The University of Tokyo, Tokyo, Japan.

Takeda, T., Sozen, M. A., Nielsen, N. N. (1970). Reinforced concrete response to simulated earthquakes. *Journal of the Structural Division, 96*(12), 2557-2573.

Tan, S., Astaneh-Asl, A. (2003). Cable-based retrofit of steel building floors to prevent progressive collapse. Berkeley: University of California.

Tan, S., Astaneh-Asl, A. (2003). *Use of steel cables to prevent progressive collapse of existing buildings.* Paper presented at the Sixth Conference on Tall Buildings in Seismic Regions, Los Angeles, CA.

Tay, C. G. (2013). *Efficient progressive collapse analysis for robustness evaluation and enhancement of steel-concrete composite buildings.* (Ph.D. Dissertation), National University of Singapore.

Taylor, R. G. (1977). *The nonlinear seismic response of tall shear wall structures.* (Ph.D. Dissertation), University of Canterbury, Christchurch, New Zealand

Thomsen, J. H., Wallace, J. W. (1995). Displacement-based design for reinforced concrete structural walls: an experimental investigation of walls for rectangular and T-shaped cross-sections. Potsdam, New York: Clarkson University.

To, N. H. T., Ingham, J. M., Sritharan, S. (2001). Monotonic nonlinear strut-and-tie computer models. *Bulletin of the New Zealand Society for Earthquake Engineering 34*(3), 169-190.

Usmani, A. S., Chung, Y. C., Torero, J. L. (2003). How did the WTC towers collapse: a new theory. *Fire Safety Journal 38*(6), 501-533.

Vecchio, F. J., Collins, M. P. (1986). The modified compression-field theory for reinforced concrete elements subjected to shear. *Journal Proceedings of ACI, 83*(2), 219-231.

Vecchio, F. J., Collins, M. P. (1988). Predicting the response of reinforced concrete beams subjected to shear using the modified compression field theory. *ACI Structural Journal, 85*, 258-268.

Vlassis, A. G., Izzuddin, B. A., Elghazouli, A. Y., Nethercot, D. A. (2009). Progressive collapse of multi-storey buildings due to failed floor impact. *Engineering Structures 31*(7), 1522-1534.

Vogel, U. (1985). Calibrating frames. *Stahlbau*, 295-301.

Vulcano, A., Bertero, V. V., Colotti, V. (1988). *Analytical modeling of R/C structural walls*. Paper presented at the Proceedings of 9th World Conference on Earthquake Engineering Tokyo-Kyoto, Japan.

Wales, M. W., Rossow, E. C. (1983). Coupled moment-axial force behavior in bolted joints. *Journal of Structural Engineering, 109*(5), 1250-1266.

Worakanchana, K., Mayorca, P., Guragain, R., Navaratnanaj, S., K., M. (2008). *3-D Applied element method for PP-band retrofitted masonry*. Paper presented at the The 14th World Conference on Earthquake Engineering, Beijing, China.

Worakanchana, K., Meguro, K. (2006). Voronoi applied element method for analysis of the soil deposit under the fault action. *SEISAN KENKYU, 58*(6), 535-540.

Xu, G., Ellingwood, B. R. (2011). Disproportionate collapse performance of partially restrained steel frames with bolted T-stub connections. *Engineering Structures 33*(1), 32-43.

Yang, B., Tan, K. H. (2012a). *Component-based model of bolted-angle connections subjected to catenary action*. Paper presented at the Proceedings of the 10th International Conference on Advances in Steel Concrete Composite and Hybrid Structures, Singapore.

Yang, B., Tan, K. H. (2012b). Numerical analyses of steel beam–column joints subjected to catenary action. *Journal of Constructional Steel Research 70*, 1-11.

Yang, B., Tan, K. H. (2013a). Experimental tests of different types of bolted steel beam–column joints under a central-column-removal scenario. *Engineering Structures 54*, 112-130.

Yang, B., Tan, K. H. (2013b). Robustness of bolted-angle connections against progressive collapse: experimental tests of beam-column joints and development of component-based models. *Journal of Structural Engineering, 139*(9), 1498-1514.

Yang, B., Tan, K. H. (2013c). Robustness of bolted-angle connections against progressive collapse: mechanical modelling of bolted-angle connections under tension. *Engineering Structures 57*, 153-168.

Yim, H. C., Krauthammer, T. (2012). Mechanical properties of single-plate shear connections under monotonic, cyclic, and blast loads. *Engineering Structures 37*, 24-35.

Yu, H., Burgess, I. W., Davison, J. B., Plank, R. J. (2009). Tying capacity of web cleat connections in fire, Part 2: Development of component-based model. *Engineering Structures 31*(3), 697-708.

Yu, H., Hwang, S. (2005). Evaluation of softened truss model for strength prediction of reinforced concrete squat walls. *Journal of Engineering Mechanics, 131*(8), 839-846.

Yu, M., Zha, X., Ye, J. (2010). The influence of joints and composite floor slabs on effective tying of steel structures in preventing progressive collapse. *Journal of Constructional Steel Research 66*(3), 442-451.

Zhang, X. (2006). *Nonlinear finite element analysis of steel frame-RC corewall hybrid structure.* (M.S. Thesis), Hunan University.

Zhang, Z., Li, H., Li, G., Wang, W., Tian, L. (2013). The numerical analysis of transmission tower-line system wind-induced collapsed performance. *Mathematical Problems in Engineering, 2013*, 11.